Modelling a pebble bed High Temperature Gas-cooled Reactor using a system-CFD approach

Hermanus Johannes van Antwerpen

M.Ing (Mechanical)

Thesis submitted in partial fulfilment of the requirements for the degree

Philosophae Doctor

at the

School of Mechanical Engineering,

Potchefstroom Campus of the Northwest University

Promoter: Professor G.P. Greyvenstein

Potchefstroom

2007

Abstract

The objective of this study was the development of a systems-CFD model of the PBMR reactor that used the minimum number of grid points to achieve grid independence. The number of grid points is reduced by increasing the accuracy of the discretisation scheme in the reactor model. Any reduction in the number of grid points leads to an increase in calculation speed, which is critical for systems simulation codes that are used for optimisation or transient simulations.

While some previous reactor models had been developed for systems simulation codes, their discretisation schemes have not been optimised to use the minimum number of grid points and some heat transfer phenomena were neglected without knowing the effect. Therefore, there was a need to optimise discretisation schemes as well as investigate the effect of including certain heat transfer mechanisms.

Modelling methods for several phenomena were developed and implemented in a reactor model in the *Flownex* systems simulation code, which is used to simulate the PBMR. Subjects of investigation included pebble bed convection discretisation, fuel sphere discretisation, the effect of the radiation heat transfer modelling approach as well as conjugate conduction and radiation across the helium riser channels in the reactor side reflector. After testing the phenomenological models in isolation, the comprehensive reactor model was tested by simulating the SANA experiment and HTR-10 reactor experiments published by the IAEA. Several sensitivity studies were performed to assess the effect of physical as well as numerical parameters.

Two reactor discretisation schemes were also evaluated, namely the control-volume based scheme and the element-based scheme. The control-volume based scheme was found to provide a simpler and more intuitive framework for implementing mathematical models, but not to increase accuracy directly.

The most significant finding was that the newly developed second-order accurate convection heat transfer scheme gives the greatest improvement in calculation speed by requiring the least number of pebble bed increments. The other important finding was that the methods currently used in many reactor simulation codes for fuel sphere discretisation and radiation heat transfer approximation are appropriate and give adequate accuracy.

Bedankings/Acknowledgements

Alle lof aan ons Hemelse Vader, vir sy oneindige genade en seëninge! Vir die mense en die geleenthede wat Hy op my pad gestuur het. Vir die voorreg om die afgelope tyd aan hierdie navorsing te kon werk.

Baie dankie aan my promotor, Professor Gideon Greyvenstein, wat op hierdie interessante onderwerp afgekom het en my daaraan bekend gestel het.

Hartlike dank ook aan PBMR (Edms) Bpk. wie se finansiële steun hierdie studie moontlik gemaak het. Mag die PBMR projek net van krag tot krag gaan!

Die "Garage" by M-Tech Industrieel, asook die ander personeel by Mtech. Dankie vir baie dae se gesprekke, belangstelling en `n heerlike omgewing om in te werk.

Frieda, dankie vir jou bankvaste ondersteuning en aanmoediging deur die loop van hierdie studie! Baie dankie vir vele naweke en aande wat jy opgeoffer het om saam met my te werk.

Table of contents

Abstract ... ii
Bedankings/Acknowledgements ... iii
Table of contents ... iv
List of Figures ... viii
Nomenclature ... xix

1 INTRODUCTION ... 1

1.1 INTRODUCTION ... 1
1.2 THE HTR IN THE CONTEXT OF THE NUCLEAR RENAISSANCE ... 2
1.3 DESCRIPTION OF THE PBMR ... 4
1.4 PROBLEM STATEMENT ... 7
1.5 OBJECTIVE OF THIS STUDY ... 8
1.6 OUTLINE OF THIS THESIS ... 9

2 BACKGROUND TO HTR OPERATION ... 11

2.1 INTRODUCTION ... 11
2.2 THE NUCLEAR FISSION REACTION: IMPLICATIONS FOR HTR FUEL ... 11
2.3 FUEL DESIGN: CONTAINMENT, MODERATOR AND COOLING ... 12
2.4 REACTOR LAYOUT ... 13
2.5 DETAILED HEAT REMOVAL PATHS FROM THE REACTOR ... 15
2.6 PREVIOUS PEBBLE BED HTRS ... 16
2.7 CONCLUSION ... 18

3 LITERATURE STUDY OF REACTOR SIMULATION ... 20

3.1 INTRODUCTION ... 20
3.2 REACTOR MODELLING AND SYSTEMS SIMULATION ... 20
3.3 PREVIOUS HTR REACTOR MODELS ... 23
3.4 DETAILED REACTOR MODEL/SYSTEMS CODE COUPLING ... 26
3.5 INTEGRATED SYSTEMS SIMULATION REACTOR MODELS ... 27
3.6 LIMITATIONS IN CURRENT APPROACHES ... 28
3.7 CONCLUSIONS ... 29

4 BACKGROUND THEORY ... 30

4.1 INTRODUCTION 30
4.2 THE NETWORK OR SYSTEM CFD APPROACH 30
4.3 DEVELOPMENT OF REACTOR MODELS WITH THE NETWORK APPROACH 35
4.4 GENERATION III REACTOR MODEL CONSERVATION EQUATIONS 39
4.5 GENERATION III REACTOR MODEL DISCRETISATION 40
4.6 PROPERTIES OF THE GENERATION III REACTOR MODEL DISCRETISATION 45
4.7 ALTERNATIVE NETWORK TOPOLOGIES 49
4.8 FLUID AND HEAT FLOW ELEMENTS FOR CONTROL-VOLUME BASED DISCRETISATION 51
4.9 NETWORK TOPOLOGIES FOR CONTROL-VOLUME TYPES 62
4.10 ASSEMBLY OF REACTOR ZONES 67
4.11 CONCLUSION 70

5 CORRELATIONS 71

5.1 INTRODUCTION 71
5.2 OVERVIEW OF HEAT TRANSFER MECHANISMS IN A PEBBLE BED REACTOR 71
5.3 HEAT GENERATION IN A PEBBLE BED REACTOR 72
5.4 PEBBLE BED POROSITY 76
5.5 PEBBLE BED PRESSURE DROP CORRELATION 78
5.6 CONVECTION HEAT TRANSFER CORRELATION 79
5.7 DISPERSION HEAT TRANSFER 80
5.8 PEBBLE BED CONDUCTION 84
5.9 CONCLUSION 86

6 EXTENSIONS AND REFINEMENTS 87

6.1 INTRODUCTION 87
6.2 SPHERE DISCRETISATION 87
6.3 CONVECTION HEAT TRANSFER DISCRETISATION 90
6.4 PEBBLE BED/WALL HEAT TRANSFER CORRELATIONS 106
6.5 HEAT TRANSFER THROUGH THE SIDE REFLECTOR 109
6.6 RADIATION HEAT TRANSFER 117
6.7 CONCLUSION 119

CHAPTER 7 120

7 RESULTS 120

7.1 INTRODUCTION 120
7.2 SANA EXPERIMENT 120
7.3 HTR-10 STEADY STATE 129
7.4 HTR-10 LOSS-OF-FLOW TRANSIENT 140
7.5 HTR-10 CONCEPTUAL GEOMETRY TO QUANTIFY SPHERE AND CONVECTION DISCRETISATION GRID DEPENDENCE 154
7.6 CONCLUSION 159

8 CONCLUSIONS AND RECOMMENDATIONS 161

8.1 EXECUTIVE SUMMARY 161
8.2 CONCLUSIONS 162
8.3 RECOMMENDATIONS FOR FUTURE WORK 162

REFERENCES 164

APPENDIX A: HEAT GENERATION DISTRIBUTION 172

APPENDIX B: THE SYSTEM CFD APPROACH APPLIED TO A PEBBLE BED REACTOR CORE 175

APPENDIX C: HEAT TRANSFER ACROSS A HOLED SOLID 191

APPENDIX D: EVALUATION OF A DETAILED RADIATION HEAT TRANSFER MODEL IN A HIGH TEMPERATURE REACTOR SYSTEMS SIMULATION MODEL 195

1. ABSTRACT 195
2. NOMENCLATURE 196
3. INTRODUCTION 196
4. SIGNIFICANCE OF RADIATION SPATIAL EFFECTS 198
5. CALCULATION MODEL 199
6. CASE STUDIES 208
7. HTR-10 PLOFC 210
8. 268MW PBMR DLOFC 211
9. REDUCTION OF ELEMENT NUMBER 212
10. CONCLUSION 215
11. ACKNOWLEDGMENTS 216

12. REFERENCES 216

APPENDIX E: ADDITIONAL RADIATION VIEW FACTOR DERIVATIONS AND IMPLEMENTATION 218

E.1 IMPLEMENTATION 218

E.2 ADDITIONAL DERIVATIONS: DISCRETISED SURFACES 219

APPENDIX F: SPHERE DISCRETISATION SCHEMES 226

ABSTRACT 226

F.1 ABBREVIATIONS AND ACRONYMS 226

F.2 NOMENCLATURE 226

F.3 INTRODUCTION 228

F.4 PREVIOUS WORK 228

F.5 THEORY 229

F.6 GEOMETRY 230

F.7 SPHERE DISCRETISATIONS 234

F.8 SUBDIVIDED SPHERE DISCRETISATION SCHEMES 238

F.9 STEADY-STATE GRID DEPENDENCE TESTS 243

F.10 TRANSIENT GRID DEPENDENCE TESTS 246

F.11 SUMMARY AND CONCLUSIONS 257

F.12 BIBLIOGRAPHY 258

List of figures

Figure 1.1. Vertical and horizontal cross-sections of the PBMR pressure vessel and core internals. (Matzner 2004, Koster *et al.* 2003) 5

Figure 1.2. The PBMR power conversion unit. (Matzner, 2004) 6

Figure 1.3. Schematic layout of the PBMR gas turbine power cycle. 6

Figure 2.1. Fuel design for the PBMR (Van Staden *et al.* 2002). 12

Figure 2.2. The general layout of the PBMR (Matzner, 2004) 14

Figure 2.3. Various pebble bed reactors, from left to right: the AVR, the THTR and the HTR-10 (not to scale) (Kugeler *et al.* 2003, IAEA 2006). 16

Figure 2.4. A cutaway view of the HTTR. 18

Figure 3.1. A network discretisation of the PBMR reactor. 28

Figure 4.1. Various heat transfer paths to and from a control volume. 31

Figure 4.2. Illustration of the discretisation of a pipe in to control volumes, showing the network representation as well. 32

Figure 4.3. A setup with two dams, a pump, a pipeline and a orifice flow meter represented with the network approach on the right. Heat transfer is also treated efficiently. 33

Figure 4.4. The layout of a typical finned tube heat exchanger, commonly used for water/air heat exchange 34

Figure 4.5. The flow paths of a typical finned tube heat exchanger on the right, with the network representation of the shaded part on the left (Swift, 2006). 35

Figure 4.6. A first-generation pebble bed reactor model for systems simulation 36

Figure 4.7. The network discretisation in the Generation II Flownex reactor model 37

Figure 4.8. The 268MW PBMR and its geometrical zones input for a reactor thermal-fluid model. 38

Figure 4.9. The staggered grid discretisation in CFD, showing the primary conservation variables of total pressure and total temperature on the nodes and velocity (for momentum) on staggered control volumes between nodes. The network representation is on the right-hand side. 41

Figure 4.10. Methods of dealing with change in material properties across control volumes, using the discretisation of a solid zone as example (Swift, 2006). Each coloured zone represents a different material type. Node mass calculation is explained in greater detail in Figure 4.11. 43

Figure 4.11 The method by which node mass is calculated from the elements. Note that volume is assigned only to the vertical conduction elements and then divided between nodes. Each coloured zone represents a different material type. 43

Figure 4.12. The network topology for a single *Pebble Bed* zone. 44

Figure 4.13. The network topology of assembled *Pebble Bed* and *Solid* zones, as it occur at the pebble bed/side reflector interface. 44

Figure 4.14. A typical combination of zones encountered in the solids around a pebble bed reactor core, with the Generation III network layout. 45

Figure 4.15. Pebble bed topologies that were used to test the transient response validity, as calculated with the Generation III network topology, referred to as the "sphere topology" in this figure. 46

Figure 4.16. An illustration of the creation of artificial natural circulation paths in the Generation III reactor model topology for *Solid with 1-D Flow.* 47

Figure 4.17. The Generation III network topology at the pebble bed/wall interface. 48

Figure 4.18. Methods of dealing with change in material properties across control volumes, using the discretisation of a solid zone as example. 50

Figure 4.19. Discretisation of the flow path at an interface, according to the control-volume based and the element-based approaches. 52

Figure 4.20. Graphic description of some composite flow element inputs in axially symmetric coordinates. 52

Figure 4.21. Discretisation of the heat flow path at an interface, according to the control-volume based and the element-based approaches. 54

Figure 4.22. Illustration of the symbols for heat flux calculation between two control volumes. 54

Figure 4.23. Conduction heat transfer topology for using conductivity at average temperature. 55

Figure 4.24. Conduction heat transfer topology for using conduction resistances in series. 55

Figure 4.25. Conduction topology for using the weighted average for conductivity. 56

Figure 4.26. Geometry used for studying the contribution of varying conductivity to grid dependence. The grid on the left has one subdivision and the one the right shows the general subdivision scheme. 57

Figure 4.27. Grid dependence attributed to temperature dependent conductivity. The grid-independent result of all cases are equal and are used as reference. 57

Figure 4.28. Topology in which a convection element is used. 58

Figure 4.29. Topology of the radiation and conduction network around a cavity..... 60

Figure 4.30. Illustration of the view factor integral variables. 61

Figure 4.31. Network representation of a solid type control volume. 62

Figure 4.32. Nodes and elements used to represent a solid with one-dimensional flow through it. 63

Figure 4.33. Network topologies for two types of two-dimensional flow through control volumes. 64

Figure 4.34 Assembly of nodes and elements representing a pebble bed zone..... 64

Figure 4.35. A first alternative pebble bed/wall topology for the Generation III reactor model.65

Figure 4.36. The pebble bed/wall topology for the control-volume based discretisation, assuming a homogeneous porous solid up to the wall..... 66

Figure 4.37. The pebble bed/wall topology for the control-volume based discretisation. 66

Figure 4.38. Network topology used to represent a single cavity, radiation spatial elements omitted. 67

Figure 4.39. The discretisation process for a pebble bed type reactor with a central column.... 69

Figure 5.1 Flow diagram of reactor heat removal paths. 72

Figure 5.2. Volume-based radial variation in porosity for various peel thicknesses for an annular packed bed. The annular height is 14 sphere diameters. (Du Toit, 2004). 77

Figure 6.1. Network layout for the "Analytical Sphere" discretisation. 88

Figure 6.2. A one-dimensional discretisation of fluid passing through a heated solid with the domain discretisation on the left and the control-volume detail on the right. 90

Figure 6.3. Temperature rise in a control volume, as well as solid/fluid temperature difference when Eq.(6.8) is used for calculating solid temperature. 91

Figure 6.4. A convection heat transfer scheme that is second-order accurate..... 91

Figure 6.5. Temperature rise and solid/fluid temperature difference when the fluid average temperature is used. 92

Figure 6.6. When solid temperature is coupled to fluid average fluid temperature, the fluid exit temperature is larger than solid temperature when $1/(hA) < 1/(2mc_p)$. 93

Figure 6.7. Temperature oscillations in a constant wall temperature heat exchanger due to the unboundedness of solid/average fluid temperature coupling. 94

Figure 6.8. Temperature relations for a bounded solution by modifying the convection heat transfer resistance. 95

Figure 6.9. Error (per control volume) as calculated with Eqs.(6.12) and (6.15), as a function of increment size for the PBMR pebble bed core at full power and mass flow. $hA/2mc_p$ equals one at an increment length of 1.033m. 96

Figure 6.10. Data from Figure 6.9, in the form of a typical grid dependence test. 96

Figure 6.11. Number of axial increments for the PBMR core (400 MW, full mass flow) as a function of the desired error. In general, solution time is proportional to the number of increments. 97

Figure 6.12. Nodes for explaining the treatment of convection heat transfer in two dimensions. 98

Figure 6.13. Division of the convection heat transfer between two flow streams according to mass flow. Left and Right are used for ease of explanation, but the method of division holds for any number of inlet flow streams to node 3. 99

Figure 6.14. The network topology for an implicit implementation of second-order accurate convection heat transfer in two dimensions. Note that when a convection heat transfer element links the solid node to an outflow node, its convection heat transfer coefficient is set to zero. 101

Figure 6.15. Maximum grid length values for which convection heat transfer can be calculated unconditionally stable to second-order accuracy, as a function of superficial mass flux for a helium-cooled pebble bed HTR core at four different fluid temperatures 105

Figure 6.16. A demonstration of the grid dependence of numerical diffusion in a convective heat transport problem. It shows fluid temperature on the diagonal line AB, for three grid refinements. 106

Figure 6.17. The pebble bed/wall topology for the control-volume based discretisation. Mathematical descriptions of $h_{sw,}$ and h_{fw} are given in Eqs. (6.37) and (6.38). 107

Figure 6.18. Heat transfer phenomena at the pebble bed/wall interface. 107

Figure 6.19. Geometry of the side reflector with holes, as well as a piece of simplified geometry. 110

Figure 6.20. Nodes and elements used to represent a solid with one-dimensional flow through it (Figure 4.32 repeated for clarity)..... 110

Figure 6.21. Schematic illustration of symbols, as well as the approximations used for the basic geometry of an annular shell with axial holes..... 112

Figure 6.22. Approximation of circular geometry with rectangular geometry..... 113

Figure 6.23. Rectangular geometry..... 113

Figure 6.24. Geometries used for parametric studies into the accuracy of the one-block and three-block approximations..... 114

Figure 6.25. CFD grids for evaluating conduction form factors..... 114

Figure 6.26. Typical temperature distributions across solids with axial holes..... 115

Figure 6.27. Parametric study results for rectangular geometry..... 115

Figure 6.28. Parametric study results for radial geometry with a r_p/r ratio of 30 and r_p 1.987m 116

Figure 7.1. Cutaway and axi-symmetric views of the SANA experiment..... 120

Figure 7.2. The zones and increment sizes for a 7x7 pebble bed simulation of the SANA experiment. Zones:1: Heating element; 2: Outer shell with fixed temperatures; 4: Insulation boundary; 8: Pebble bed..... 121

Figure 7.3. Grid dependence calculations with three pebble bed grid sizes. Shown here are radial temperature profiles at three different vertical positions in the SANA experiment, operating at 10kW, using nitrogen and 60mm graphite balls. For this case, a bed/wall parameter C_{sw} of 0.5 was used while the value of C_{fw}=0.1 had negligible effect./..... 122

Figure 7.4. Solution time for the various grid sizes..... 123

Figure 7.5. Fluid velocity vectors in the SANA experiment, calculated with the Generation IV reactor model..... 123

Figure 7.6. The pebble bed/wall heat transfer model used in this study. KS and ZS refer to Kugeler-Schulten and Zehner-Schlunder respectively, while the factor 0.5 for solid conduction was estimated from the SANA simulations. 124

Figure 7.7. The effect of dispersion heat transfer, as shown on this simulation of the SANA experiment with 4.34kW and Nitrogen. Dispersion is more important here than with the 10kW case..... 125

Figure 7.8. SANA results for Nitrogen, 35kW heat input over the full height of the pebble bed. 126

Figure 7.9. Comparison between the Generation IV reactor model and the Generation III reactor model as it is implemented in Flownex. The Generation IV result is for a 15x15 grid while the Generation III result is for a grid with 60 axial increments and 40 radial increments. The SANA experiment with 4.34kW heat addition and nitrogen was simulated..... 127

Figure 7.10. Results from the SANA experiment, Generation IV and Generation III reactor models for grid sizes of 7x7 increments and 35x28 increments..... 128

Figure 7.11. Vertical cross-section of the HTR-10. (IAEA, 2006) 130

Figure 7.12. Schematic layout of the flow path through the HTR-10 reactor. 131

Figure 7.13. Zones and dimensions for describing the reactor geometry and input values. 132

Figure 7.14. Porosity, permeability, hydraulic diameter and number of flow channels for porous flow regions. Some permeabilities and hydraulic diameters were adjusted to obtain the correct flow distribution. 133

Figure 7.15. HTR-10 core heat distribution. The highest heat generation is near the outer reflector, where the thermal neutron flux is the highest. 135

Figure 7.16. Radial temperature profile in the side reflector, 5.76m above the reactor bottom. 136

Figure 7.17. Radial temperature profile in the sidereflector, 4.88m above the reactor bottom.136

Figure 7.18. Temperatures in core structures, as listed in Table 7-4..... 137

Figure 7.19. The influence of the convection discretisation on the radial solid temperature profile at 4.94m, near the bottom of the pebble bed. 138

Figure 7.20. Reflector radial temperature profiles at a height of 4.94m (0.8m from the core top) for two values of C_{fw}. When Figure 7.21 is taken into account as well, a value of 0.1 is considered the most accurate. 139

Figure 7.21. Reflector radial temperature profiles at a height of 5.85m (1.7m from the core top) for two values of C_{fw}. Side reflector radial temperature profile at two heights in the reactor, showing the effect of fluid/wall empirical factor C_{fw}. 139

Figure 7.22. Flattening of the pebble bed gas temperature profile due to dispersion heat transfer. 140

Figure 7.23. Decay heat for the HTR-10, as calculated by INET. 143

Figure 7.24: Generation III model of the HTR-10 for simulating a transient in Flownex. The grid is not to scale but is equally spaced grid for display purposes (Van Antwerpen, 2006). 144

Figure 7.25. Normalised power versus time shortly after stopping coolant flow in the HTR10. 145

Figure 7.26 Normalised power after stopping coolant flow in the HTR-10, showing recriticality at about 4300 seconds. 145

Figure 7.27. Flow vectors in the HTR-10 after a LOFC incident. Note that flow direction is indicated by lines pointing away from the black dots, which indicate node positions..... 147

Figure 7.28. Topology of the circulation cells in the HTR10 LOFC case..... 147

Figure 7.29. The networks for the cavity above the pebble bed as a single cavity (left) or as a series of open vertical flow zones (right). 149

Figure 7.30. Relative power for the two different cavity networks in Figure 7.29. 149

Figure 7.31. The effect of top reflector cavity convection heat transfer coefficient. 150

Figure 7.32. Reactivity as a function of time for three different choices of side reflector zones, showing the importance of proper zone specification. 151

Figure 7.33. Two zone sets that were used to calculate the reflector average temperature for reactivity feedback. Zone 2 gave the best agreement with experimental result. The scale of the reactor grid in the background is distorted to display all cells the same size. 152

Figure 7.34. Relative power for two different convection discretisation methods..... 153

Figure 7.35. Simplified reactor geometry for quantifying the effect of convection and sphere discretisation with six pebble bed axial increments. 155

Figure 7.36. Steady-state average fuel temperature or baseline temperature as function of increment length for the modified HTR-10 case in Figure 7.35..... 156

Figure 7.37. Steady-state average fuel temperature or baseline temperature as function of the number of axial increments for first order and second order accuracy convection heat transfer discretisation. 156

Figure 7.38. Time of recriticality and the time required for simulating 100 timesteps for various grid sizes and both first order and second order convection discretisation. 157

Figure 7.39. Average fuel temperature and normalised difference with the "Analytical Sphere" scheme for various sphere discretisations. The difference between sphere center temperature (T_{max}) and surface temperature (T_{surf}) was six degrees Celcius..... 158

Figure A.8.1. Power distribution zones for the reactor model presented in this document..... 172

Figure A.8.2. A radial power distribution with indication of the control volume locations. ... 173

Figure F.8.3. A spherical shell without heat generation. T^* is the average temperature of the shell, located at r^*..... 231

Figure F.8.4. Left: possible sphere internal node placement, right: node placement required at a surface..... 233

Figure F.8.5. A simple calculational setup for maximum temperature in a sphere with heat generation. 236

Figure F.8.6. A sphere model that provides maximum and average temperatures analytically in the context of the network approach. 237

Figure F.8.7. Successive sphere shells without heat generation, if transient simulation accuracy requires it. 237

Figure F.8.8. Network layout for a simple analytical fuel sphere model. 238

Figure F.8.9. Node and element placement for the Numerical discretisation scheme. 239

Figure F.8.10. Node and control volume placement for staggered volume discretisation. 241

Figure F.8.11. The negligible grid dependence of the maximum fuel temperature as calculated with the Numerical and Staggered Volume schemes. k(w) denotes the weighted method for temperature dependent conductivity. 244

Figure F.8.12. Average temperature grid dependence for three sphere modelling approaches, as well as constant and temperature dependent conductivity. 244

Figure F.8.13. Surface layer average temperature grid dependence for two discretisation schemes. The test is for a spherical layer between 25mm and 30mm without heat generation. 246

Figure F.8.14. Sphere subdivision, with n the number of inner divisions and m the number of shell divisions. 248

Figure F.8.15. The average temperature percentage difference with a reference case. The Staggered Volume scheme is denoted by SV and the Numerical scheme by N. Results from a SVn20m10 simulation with temperature dependent conductivity were used as reference. 248

Figure F.8.16. The average temperature response relative difference with reference case SVn20m10 for a sudden step in gas temperature. Conductivity is temperature dependent. AS denotes the Analytical Sphere model. Surface division (m) has the largest effect on the initial response. 250

Figure F.8.17. The average temperature response relative difference with reference case SVn20m10 for a sudden drop in power with constant gas temperature. Conductivity is temperature dependent. 251

Figure F.8.18. Maximum temperature response to a step power increase. Conductivity is temperature dependent and a reference of 700°C is used, i.e. conductivity at 40°C on the graph is calculated at 740°C. 254

Figure F.8.19. Maximum temperature response, difference with the SVn20m10 reference case. 254

Figure F.8.20. The average temperature response relative difference with reference case SVn20m10 for a step increase in power with constant gas temperature. 255

Figure F.8.21. Gas outlet temperature transient response and relative difference between one and ten surface layer increments, showing negligible difference. 257

Nomenclature

Roman lettering (lower case)

Symbol	Units	Description
b	-	Modelling constant
b	m	Block width
d	m	Diameter
e	m	Surface roughness
e	J/kgK	Enthalpy
f	-	Friction factor
g	m/s^2	Gravitational acceleration
g_{rad}	-	Radiation increase factor
h	W/m^2K	Heat transfer coefficient
k	W/mK	Conductivity
m	kg	Mass
p	Pa or bar	Pressure
q'''	W/m^3	Volumetric heat generation
r	m	Radius
t	s	Time
u	m/s	Velocity
w	-	Denotes weighted method for conductivity calculation
x	m	Horizontal position
x	-	Ratio between total and nominal reactor power
z	m	Vertical or axial position
y	m	Vertical or axial position

Roman lettering (uppercase)

A	m^2	Area
B	-	Modelling constant
B	$kg.m/s^2$	Body force
C		Modelling constant or Precursor concentration
c_p	J/kgK	Constant-pressure heat capacity
D	m	Diameter
D	-	Concentration of decay-heat producing isotope
E	GPa	Modulus of elasticity

E	J	Energy release per fission
E	J/kg	Total specific energy
F	m	Conduction shape factor
F_{12}	-	Radiation view factor from surface 1 to surface 2
H	m	Height
K	-	Dispersion shape factor
K	-	Pressure loss factor
L	m	Length
N		Modelling constant
N		Node
N	-	Number of holes
P	W	Power
Q	m^3/s	Volume flow rate
Q	W	Heat
R	J/kgK	Gas constant
R	m	Radius
R	K/W	Thermal resistance
T	°C or K	Temperature
V	m/s	Velocity
$\not{V}$	m^3	Volume
W	W	Work

Dimensionless numbers

These numbers are never written in Italics.

Bi	Biot number	Ratio between convection and conduction thermal resistance
Eu	Euler number	Ratio between inertial forces and the pressure gradient
Nu	Nusselt number	Dimensionless fluid temperature gradient at a solid interface
Pe	Peclet number	Ratio between convective and diffusive transport
Pr	Prandtl number	Ratio between momentum and thermal diffusivity
Re	Reynolds number	Ratio between inertial and viscous forces
Λ	Planck number	Ratio between radiation and conduction heat transfer
St	Stanton number	Ratio between convection heat resistance and fluid stream heat capacity

Subcripts

0	Stagnation property
0	Superficial velocity
∞	Environment or reference
a	Air
amb	Ambient condition
atm	Atmospheric condition
ave	Average
b	Bed or Bulk
c	Cylinder
ch	Core hydraulic diameter
cond	Conduction
conv	Convection
dec	Decay heat
DS	Downstream
e	East
eff	Effective
F	Control volume face
F	Fluid
feff	Fluid effective
fs	From fluid to solid
fw	Fluid-wall
g	Gas
gen	Generated
h	Helium
i	Index, mostly for radial increments
in	Inflow or inlet
j	Index, mostly for axial increments
k	Index, mostly for neutron precursor groups
KS	Kugeler-Schulten
min	minimum
mol	molecular
n	North or normalised
N	Node
nom	Nominal

out	Outlet or outflow
p	Denotes constant pressure in specific heat c_p or Particle or Control Volume Center or Pitch Circle
r	Radial
rad	Radiation
R	Radius
ref	Reference
s	South or Solid
S	Sphere
$	Denotes the radial position of the boundary between sphere surface control volumes.
sf	From solid to fluid
sh	Shell
sp	Spatial
sph	Sphere
SS	Steady-state
sw	Solid-wall
tot	Total
US	Upstream
VM	Vortmeyer-Le Mong
w	Wall or West
z	Axial
ZS	Zehner-Schlunder
θ	Tangential

Greek letters

β	-	Delayed neutron fraction or isotope production constant
ϕ_T	#/s.m^2	Thermal neutron flux
ε	-	Porosity
ε_r	-	Emissivity
γ	-	Ratio of specific heat
Δ	-	Difference
η	-	Efficiency
θ	-	Angle

θ	-	Time
λ		Conductivity ratio or Decay constant or Ratio between fluid and particle conductivity
Λ	- or s	Planck number/Average neutron lifetime
μ	kg/ms	Viscosity
ν	m^2/s	Kinematic viscosity
ρ	kg/m^3	Density or Reactivity
σ	W/m^2K^4	Stefan-Boltzmann constant
Σ_f	m^2/m^3	Macroscopic fission cross-section
ψ	-	Ergun pressure loss parameter

Abbreviations

AVR	Arbeitsgemeinschaft Versuchs Reaktor
BISO	Bistructural-isotropic
CFD	Computational Fluid Dynamics
CRP	Coordinated Research Procject
CTL	Coal To Liquid
DLOFC	Depressurised Loss of Forced Cooling
GTL	Gas To Liquid
GT-MHR	Gas Turbine Modular High Temperature Reactor
HEU	Highly Enriched Uranium
HTR	High Temperature Gas-cooled Reactor
HTTF	Heat Transfer Test Facility
HTTR	High Temperature Test Reactor
IAEA	International Atomic Energy Agency
INEEL	Idaho National Energy and Environmental Laboratory
INET	Institute for Nuclear Energy Technology (Beijing, China)
IPCM	Implicit Pressure Correction Method
KS	Kugeler-Schulten
KTA	Kern Technisches Ausschuss
LEU	Low Enriched Uranium
LOFC	Loss Of Forced Cooling
LWR	Light Water Reactor
MEDUL	Mehrfach Durchlauf (Multiple pass)

NTU	Number of Transfer Units
PBMR	Pebble Bed Modular Reactor
PCU	Power Conversion Unit
RANS	Reynolds-Averaged Navier Stokes
RCCS	Reactor Cavity Cooling System
RCFR	Rated Coolant Flow Rate
SANA	Selbsttätigen Abfuhr von Nachwärme
SAS	Small Absorber Spheres
SCFD	Systems Computational Fluid Dynamics
SPECTRA	Sophisticated Plant Evaluation Code for Thermal-hydraulic Response Assessment
THTR	Thorium High Temperature Reactor
TINTE	TIme-dependent Neutronics and Temperatures
TRISO	Tristructural-isotropic
VSOP	Very Superior Old Programs
ZS	Zehner-Schlünder

Chapter 1

Introduction

1.1 Introduction

With the worldwide increase in the demand for energy and the threat that CO_2 emission poses to global warming, many countries, previously opposed to nuclear power, are now starting to consider nuclear power as an option for future power generation.

According to authoritative estimates the world needs to increase its current fleet of 440 power reactors by a factor of at least ten in the next fifty to hundred years to avoid economic and environmental disaster (Ritch, 2005). The case for nuclear power has become so strong that leading environmentalists, such as James Lovelock and Patrick Moore, have expressed support for nuclear power. (Moore, 2005; Lovelock, 2004).

One of the most promising reactor concepts of the Nuclear Renaissance is the High Temperature Gas-Cooled Reactor (HTR), which offers advantages such as inherent safety, improved economics, shorter construction times, distributed generation and high temperature availability, which makes it suitable for process heat applications such as hydrogen production.

Presently, several projects on HTR technology are under way all-over the world, such as the HTR10 research reactor in China and the HTTR project in Japan. The project that has progressed the furthest commercially, is the Pebble Bed Modular Reactor (PBMR) project, described by Dr. Bill Nuttall in his book "*Nuclear Renaissance*" as "*the most talked about HTGR project positioned to contribute to the nuclear renaissance*". At the recent PBMR Supplier's Conference, the South African Government announced plans to commission a demonstration plant by 2011, with Eskom indicating that it will order a number of PBMR plants once the demonstration project has been successfully completed.

One of the greatest challenges in the design of the PBMR is the prediction of the flow and heat transfer in the reactor. The capability to accurately predict the flow and heat transfer in the reactor is of great importance as it is extremely difficult (i.e. expensive) to design such a reactor experimentally, due to high radiation and temperatures in and around the reactor. Furthermore,

the flow and heat transfer mechanisms in the PBMR are very complex, setting high demands on computational methods.

Considerable work has already been done on the simulation of flow and heat transfer phenomena in pebble bed reactors, but it dates from the 1970s and focuses mainly on the reactor as a component separated from the plant. Even though simulation codes like VSOP and TINTE currently play an important role in the design of the PBMR, they are slow and difficult to operate. Most of these codes were also written in Fortran and they are poorly documented.

The reactor is, however, part of an intricate plant and events elsewhere in the plant also influence the reactor. This interdependence led to the development of system codes that attempt to simulate the plant as a whole with the reactor as a fully integrated subsystem. Currently, system simulation codes play an important role in the design of power plants as they allow tasks that are impossible with separate specialised reactor codes, such as sensitivity analyses, accident analyses and optimisation.

Detailed reactor models like VSOP and TINTE are not suitable for inclusion in system simulation codes due to numerical difficulties and the calculation speed penalty of interfacing different codes. Also, the level of detail included in these codes is more than what is needed for integrated system simulation. This has led to the development of simplified reactor models such as those of Stempniewicz (2002) and Du Toit *et al.*(2003).

The subject of this study is the development of a more advanced reactor model for integration into the system simulation code *Flownex*. This model attempts to find a balance between speed and accuracy and takes important phenomena, not included in the present *Flownex* reactor model, into account.

1.2 The HTR in the context of the nuclear renaissance

Because of its unique safety features, the high temperature gas-cooled reactor (HTR) features strongly in discussions on the nuclear renaissance. It has been included as one of six reactor types for further development by the Generation IV International Forum, a joint research effort between ten countries (Marcus, 2003).

In general, a HTR is a helium-cooled graphite-moderated reactor with low enriched uranium fuel in the form of TRISO-coated particles dispersed in the moderator. This composition has

thermal and neutronic properties which make inherently safe designs feasible, as well as, offering high proliferation resistance, due to difficult reprocessing and low plutonium yield (Kugeler *et al.* 2003).

Apart from the abovementioned advantages, high temperature gas-cooled gas reactors are also very promising suppliers of process heat, due to the high reactor outlet temperature. High temperature gas-cooled reactors are the only non-fossil fuel energy source capable of providing heat at temperatures above 800°C required by processes such as thermochemical water splitting to produce hydrogen (Kugeler *et al.*, 2003; IAEA, 2001). Other promising applications of HTRs are the supply of process heat for Coal-To-Liquid (CTL) synfuel production, as well as steam generation for oil-sands extraction. Both CTL and oil-sands extraction will serve to reduce the CO_2 emissions of carbon-based energy in the short term.

The core layout of an HTR can be either prismatic block-type, or pebble bed-type. In prismatic block core layouts, the TRISO fuel particles are embedded in graphite fuel pins that are inserted into fuel holes alongside control rod and coolant holes in the graphite moderator blocks. The core is made up of several layers of these blocks. Prismatic block-type fuel was used by General Atomics (GA) in the Fort St. Vrain gas-cooled reactor in the USA, by the Japanese in the High Temperature Test Reactor (HTTR), as well as in the GT-MHR being developed jointly by GA and MINATOM of Russia (GA, 1999).

Pebble bed reactor technology, as it is known today, was mostly developed by the German research programme at Jülich which spanned more than thirty years. During that time, a demonstration and research pebble bed reactor, the Arbeitsgemeinschaft Versuchs Reaktor (AVR) was built and successfully operated for twenty years between 1965 and 1988 (Kugeler *et al.*, 2003). The AVR demonstrated the inherent safety that is possible with HTRs, as well as the reliable performance of pebble fuel.

The pebble bed core layout was also used in the Thorium High Temperature Reactor (THTR) that operated at Schmehausen in Germany. After some difficulties during construction and startup, it performed well but was closed down in 1988 due to an unfortunate course of financial and political events following the Chernobyl disaster (Kugeler *et al.* 2003).

Currently the only operating pebble bed type reactor is the 10MW Chinese HTR-10, started in 2000 as a demonstration and research facility for pebble bed HTR technology. The HTR that is the nearest to commercial deployment, is the South African Pebble Bed Modular Reactor

(PBMR), of which the construction of a prototype is expected to start in 2008 at Koeberg in the Western Cape.

1.3 Description of the PBMR

1.3.1 The reactor

The reactor used in the PBMR power plant has a tall annular core geometry. The annular core volume for approximately 400 000 fuel spheres is formed between the graphite central and outer reflectors as shown in Figure 1.1. The annular core is used to meet the passive safety requirement while maximising the reactor power output. The passive safety feature of the PBMR relies on limiting the reactor core power density and the core diameter, so that decay heat can escape from the reactor by radial conduction through the pressure vessel. To increase the core cross-sectional area and, therefore, thermal power without increasing the thermal resistance for decay heat removal, an annular core geometry is used instead of a cylindrical core.

A neutronics advantage of an annular core is a more uniform neutron flux distribution in the reactor which leads to a more even power distribution and fuel burnup. An annular core also makes more effective control rod placement possible. The outer reflector houses the operating control rods, while the central reflector has holes for the reactor shutdown system, the small absorber sphere (SAS) system, as well as a central hole for the neutron source used to start up the reactor. These are shown on the right-hand diagram in Figure 1.1.

To limit radial heat losses under full power operation and to cool down the outer reflector, helium riser channels are placed around the perimeter of the central reflector. They run from the inlet manifold at the bottom to core inflow slots above the pebble bed.

Another neutronic property of HTRs is that the reactor can shut itself down in the event of a loss of coolant flow or a sudden control rod ejection, as demonstrated in the AVR in Germany and the HTR-10 in China. This behaviour of the reactor is due to the strong negative temperature coefficient combined with the low power density (2 to 6 MW/m^3). The high thermal mass of the reactor core limits the temperature rise in such events.

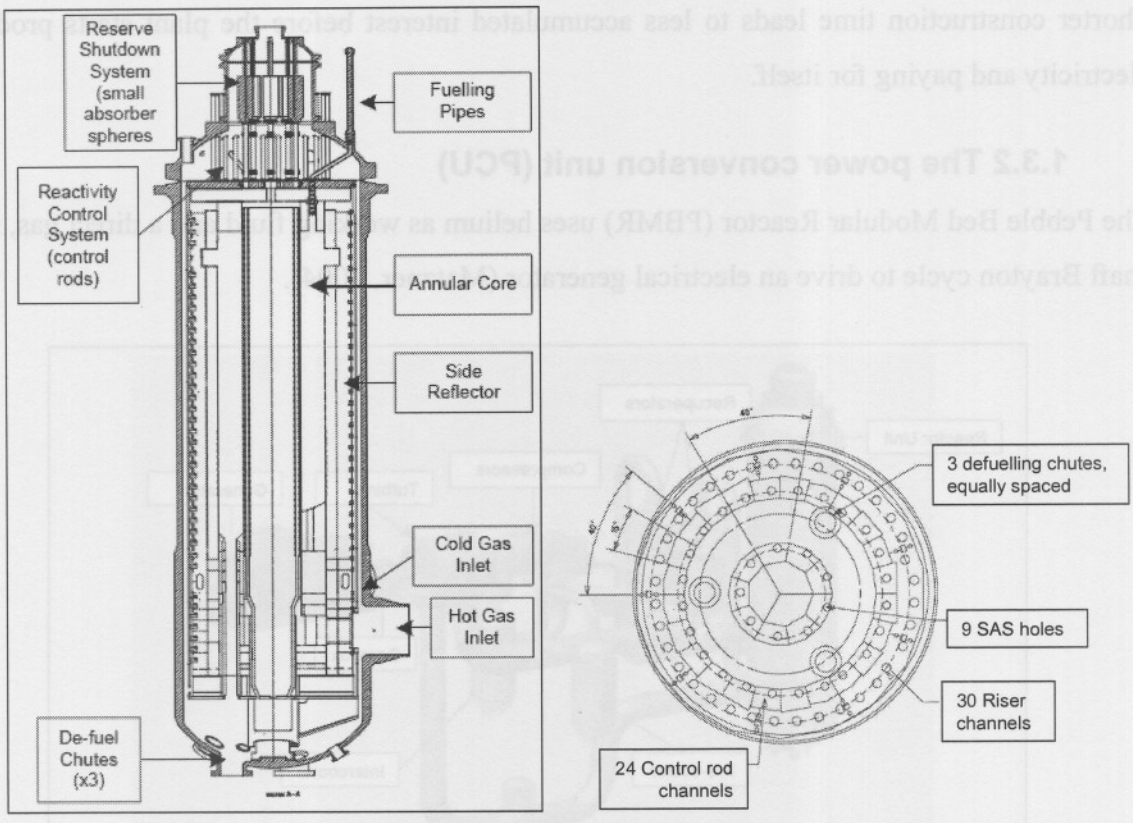


Figure 1.1. Vertical and horizontal cross-sections of the PBMR pressure vessel and core internals. (Matzner 2004, Koster *et al.* 2003)

The PBMR operates on the MEDUL (German acronym for multiple pass) fuel cycle, in which each sphere is passed through the core several times until it reaches the maximum burnup level. Spheres are inserted at the top, gradually move downward through the core and are extracted through one of three defuelling chutes at the bottom of the pressure vessel. The core bottom reflector is porous, so that the core coolant is separated from the pebble bed into the hot gas manifold, from where it passes to the high-pressure turbine. The online refuelling capability of the PBMR enables operational periods of up to six years between maintenance shutdowns (Ion *et al.*, 2003), as compared with LWR reactors which have to shut down and open up for fuel changes every two years.

As shown in Figure 1.1 all the fixed core components, like the reflectors (central, side, top and bottom) and gas manifolds, are made of interlocking graphite bricks. Thus no meltable metal or corrosive fluids are used in the reactor core. These are all contained in a steel pressure vessel.

The size limit imposed by safety considerations on the reactor, also limits the financing cost of constructing the power plant, as smaller units generally have a shorter construction time.

Shorter construction time leads to less accumulated interest before the plant starts producing electricity and paying for itself.

1.3.2 The power conversion unit (PCU)

The Pebble Bed Modular Reactor (PBMR) uses helium as working fluid and a direct gas, single shaft Brayton cycle to drive an electrical generator (Matzner, 2004).

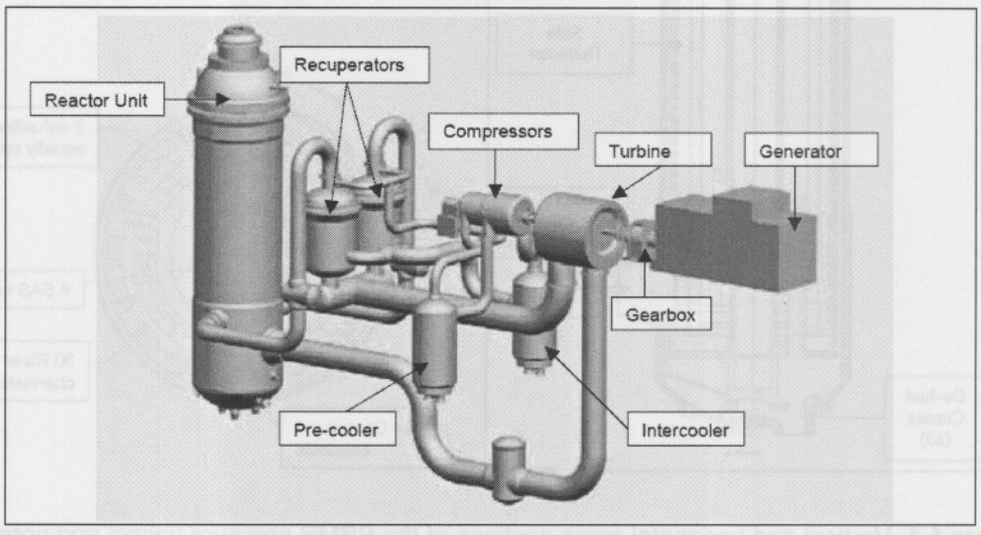


Figure 1.2. The PBMR power conversion unit. (Matzner, 2004)

Figure 1.2 shows the latest planned physical layout of the PBMR reactor and power conversion unit, which includes turbomachinery, heat exchangers and the generator. The schematic layout of the system is shown in Figure 1.3.

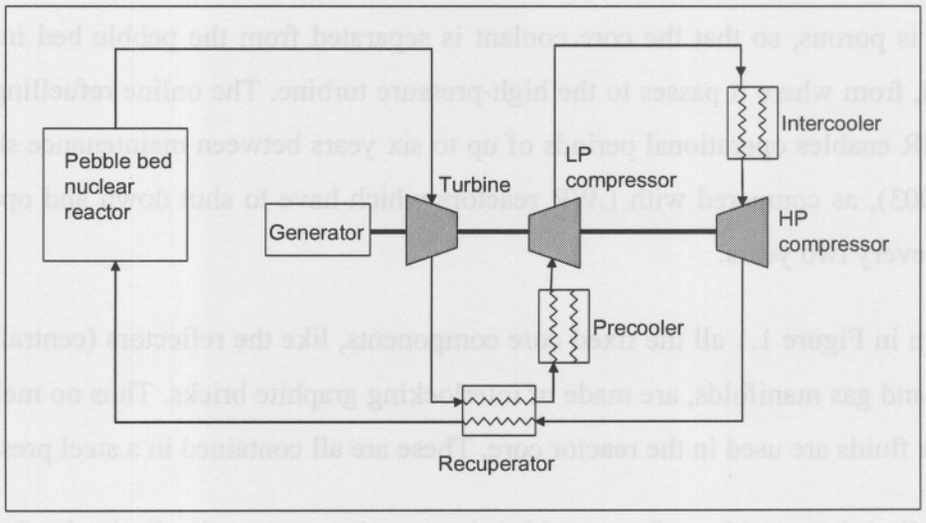


Figure 1.3. Schematic layout of the PBMR gas turbine power cycle.

This PCU configuration uses a single shaft for the generator, power turbine and compressors, enabling the generator to be used as a motor for startup. The prototype PBMR power plant is planned for construction at the Koeberg site, alongside the existing PWR power plant.

1.4 Problem statement

Because of the direct closed gas cycle of this power plant, the reactor behaviour is strongly coupled to the rest of the power conversion system. This strong coupling makes it necessary to treat the reactor as part of the overall system for steady-state as well as transient events.

For steady-state operation, the combination of reactor, heat exchangers and turbomachinery in the main power system must be optimised for best economy and controllability without compromising safety. During transient events like startup, load following or loss of coolant accidents, reactor component temperatures interact closely with system flow rates and turbo/generator shaft speed, so that proper event procedures can only be established by taking this interaction into account.

The most cost-effective way to match all system components for steady-state operation is to do integrated computer simulations of the system, instead of testing with physical equipment. For transient events as well, it would be difficult and expensive to establish proper operating procedures without integrated system simulations. Transient system simulations are also needed to characterise the dynamic behaviour of the system in order to design controllers.

The development of a comprehensive system simulation is, however, not a simple task because of the complex phenomena encountered in the reactor. One solution is to link either a Computation Fluid Dynamics (CFD) or a detailed reactor model to a system simulation code, such as the work by Verkerk (2000) and Kikstra (2001). Specialised HTR models were developed during the 1980s, namely the German THERMIX and TINTE codes. Both these codes use a finite difference discretisation of two-dimensional axi-symmetric geometry with separate functions to calculate solid conduction, gas flow, convection and convective heat transfer. During one timestep, these functions are iterated until convergence is obtained. These codes are not system simulation codes, but focused on detailed reactor modelling.

The approach to link a detailed reactor model to a system simulation code presents two specific challenges. Firstly, it is difficult to maintain mass and energy conservation across the interface

between the codes. Secondly, the explicit interface imposes a stability limit on the time step in transient simulations (Aumiller *et al.* 2001).

This led to the creation of "first generation" reactor models in system simulation codes such as those Stempniewicz (2002), created for the SPECTRA code and Du Toit *et al.* (2003) developed for the code *Flownex.* In these reactor models, calculation models available in the system simulation code are used to assemble a sub-network representing the reactor. These reactor models are first-of-a-kind systems simulation models which work well and give useful results.

But as the main objective of these developments was simply to get working calculation models, many simplifying assumptions were made and many detail heat transfer phenomena were disregarded. Therefore, obtaining accurate grid-independent results with these reactor models requires considerable grid refinement, thereby slowing down the simulation. These traits severely limit the application of these reactor models.

As the limitations of present reactor models are due to the fact that the discretisation methods used, are not yet well-investigated, there is a need to study the optimal numerical schemes for these reactor models, as well as the inclusion of more detailed heat transfer mechanisms. There is also a possibility of gaining calculation speed when more efficient discretisation schemes are used.

1.5 Objective of this study

The objective of this study is to find methods to increase the accuracy and speed of simplified reactor models, intended for use in system CFD codes. Excessive grid refinement is to be avoided as it increases the calculation time and computing requirements.

The objective is also to include heat transfer mechanisms that are not taken into account in present reactor models. These include radiation heat transfer in cavities and conjugate radiation and conduction heat transfer through the holed side reflector.

The focus will, therefore, be on a thermal-fluid model, using a coarse finite-volume discretisation of a pebble bed type high temperature gas-cooled nuclear reactor. Neutronic heat generation is obtained from a point-kinetic neutronics model and a power distribution profile. The systems simulation code *Flownex* will be used as calculational platform for this study. A

research version of *Flownex*, previously referred to as *Flownet 5*, is currently used as an academic research tool at the North-West University.

The approach followed in this study is to develop a thorough understanding of all phenomena involved and reduce all calculation models to capture only crucial phenomena. Even though some of the simplifications bring slight inaccuracy, the gain in speed and the ability to do fast parametric studies on a combined system are expected to outweigh the loss in accuracy. While CFD simulations frequently tend to lead designers astray in component detail, a comprehensive system simulation enables designers to keep a broad engineering perspective on the system. Such a balanced perspective is vital to identify the significant parameters and to make sound high-level technical decisions.

1.6 Outline of this thesis

Chapter 2 provides background on the nuclear fission reaction and how the requirements for safely sustaining such a reaction are met by the design of a pebble bed HTR. As a recent example of a pebble bed HTR, the general layout and operation of the PBMR are described. Some previous HTRs are also described.

Chapter 3 presents a literature study of previous simulation models of HTRs. This chapter discusses various simulation tools with specific consideration of reactor models for systems simulation. The strengths and limitations of the various existing methods are pointed out.

In Chapter 4, the background theory for a systems simulation reactor thermal-fluid model is described. This entails the conservation equations, as well as the network or systems CFD approach for discretising a thermal-fluids system such as a nuclear reactor. The properties of an existing reactor model are described, together with the network topologies that cause the properties. Alternative network topologies and room for improvement are also highlighted.

Chapter 5 describes correlations for many phenomena that are not explicitly treated in a systems simulation reactor model. The correlations in this chapter are well-established and known to give accurate results.

Chapter 6 deals with the extensions and refinements to the systems simulation reactor model developed during this study. These include investigations into the fuel sphere discretisation,

convection heat transfer discretisation, pebble bed/wall interface network topology, radiation heat transfer model and calculation of conduction heat transfer across the holed side reflector.

The results obtained with the comprehensive reactor model are presented in Chapter 7. It is tested by firstly calculating the temperature profiles in the relatively simple SANA experiment. After that, a benchmark case presented by the IAEA on the Chinese HTR-10 reactor is used to test the reactor model.

Chapter 8 presents an executive summary of the thesis and discusses some of the conclusions reached in the study. Recommendations for further work regarding various modelling methods required by reactor thermal-fluid simulation models are also made.

Chapter 2

Background to HTR operation

2.1 Introduction

This chapter starts by describing the various requirements and consequences of the nuclear fission reaction and how these are met by the unique design of pebble bed HTRs. The properties of coated particle fuel are discussed, as well as the design principles for an inherently safe nuclear reactor. Earlier examples of pebble bed HTRs are also discussed.

2.2 The nuclear fission reaction: implications for HTR fuel

The reasons for the unique layout of High Temperature Gas Reactors are found in the detail of the heat-producing nuclear fission reaction. A fission reaction starts when a fissionable nucleus such as U^{235} absorbs a neutron, becomes unstable and decomposes. The decomposition products are two new nuclei, each with about half the mass of the original U^{235} nucleus, two or three high-energy neutrons and an amount of energy in the form of gamma rays. The largest part of energy from the nuclear reaction is imparted to the two newly formed nuclei in the form of kinetic energy, which appears as heat generation in the fuel. This necessitates cooling of the fuel components in the reactor core.

The neutrons emanating from the fission reaction have too much energy to be readily absorbed by U^{235} nuclei and thus have to be slowed down. This slowing down, or moderation of neutrons is done most efficiently by colliding the neutrons with a relatively light nucleus such as hydrogen, carbon or a heavier isotope of hydrogen, called deuterium. Therefore, typical moderator materials are water, heavy water and graphite.

The nuclei resulting from the splitting reaction are usually highly unstable isotopes which decay into other elements, producing still more heat, some neutrons, as well as alpha, beta and gamma rays. As many fission products are environmentally damaging and have long half-lives, it is crucial to contain the fuel and fission products effectively.

Therefore, a nuclear reactor core requires coolant, moderator and a method to contain the radioactive fission products. With these requirements in mind, the fuel of a pebble bed HTR is described.

2.3 Fuel design: Containment, moderator and cooling

Containment of radioactive fission products is the driving force behind reactor safety. Therefore, TRISO ceramic-coated particle fuel was developed in Germany and the USA during the 1960s and 1970s (IAEA, 2002). TRISO particle fuel can withstand extremely high temperatures and chemical attack without releasing fission products. This makes HTRs much safer than other reactor types that contain the fuel in zirconium (Light Water Reactors such as Koeberg) or stainless steel metal tubes (Sodium Cooled Fast Reactors), as metal tubes can melt or corrode.

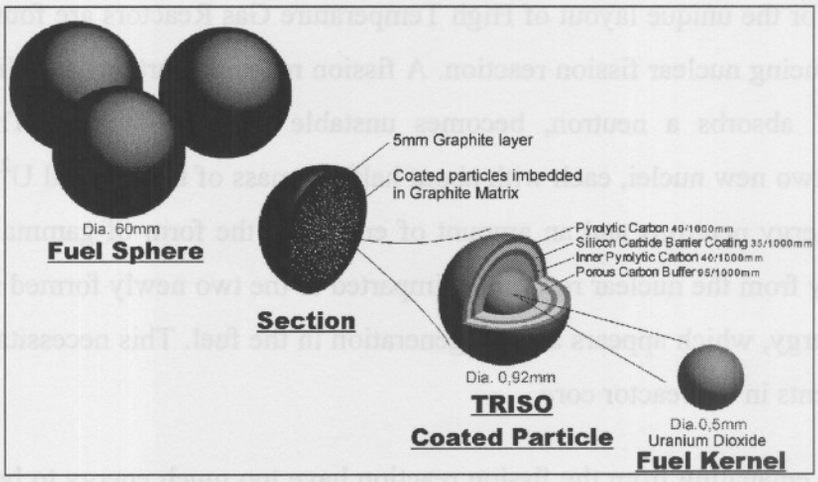


Figure 2.1. Fuel design for the PBMR (Van Staden *et al.* 2002).

A TRISO particle consists of a 0.5mm grain of UO_2 fuel coated with layers of porous graphite, pyrolytic graphite, silicon carbide and then again pyrolytic graphite to create a small sealed container, as shown in Figure 2.1. Coated particle fuel have been developed for use in combination with graphite moderator, due to graphite having good thermal conductivity and high-temperature structural stability. Regarding the efficiency of graphite as moderator, consider the fact that a carbon nucleus is much heavier (12 amu) than that of hydrogen (1 amu). As the mass of a hydrogen nucleus can be considered equal to the mass of a neutron, a neutron transfers much more energy per collision to a hydrogen nucleus than it would transfer to a carbon nucleus. Therefore, many more carbon nuclei than hydrogen nuclei are required to slow down a neutron (Lamarsh and Barratta, 2001). For this reason, graphite-moderated reactor cores

have a large volume and low power density (2 to 6 MW/m^3) compared to water moderated reactors (100 MW/m^3 for a Pressurised Water Reactor such as Koeberg).

For a pebble bed type HTR, thousands of TRISO particles are embedded in a graphite matrix to create a spherical "fuel sphere" as shown in Figure 2.1. In the PBMR, about 400 000 of these spherical graphite fuel elements are packed in an annular cavity to create the reactor core, a heat generating packed bed through which the coolant is circulated (Matzner, 2004).

Low power density makes gas cooling viable, so that in modern HTRs helium is used as coolant. Helium has excellent heat transfer properties, low compressibility and, therefore, high sonic speed as well as being chemically and neutronically inert. Another advantage is that gas cooling makes a direct thermal power conversion cycle possible. Design and safety calculations of a HTR are also much simpler than for a water-cooled reactor because there is no possibility for two-phase flow in the core.

2.4 Reactor layout

The reactor vessel and core internals have to accommodate the pebble bed in critical configuration and provide adequate coolant flow, while being safe at all times, i.e. not releasing fission products. The critical parameter here is the maximum fuel temperature.

At sustained fuel temperatures above 1600°C, the diffusion of certain radioactive fission products out of the TRISO particles is increased. The mechanism of this selective diffusive transport through silicon carbide is not yet understood well enough to find a workaround, but it has been quantified sufficiently to design a nuclear power plant to safely use this fuel, as the existence of the PBMR project proves. Therefore, fuel temperature must remain below 1600°C under all possible circumstances (Kugeler *et al.* 2003). The worst circumstance for a pebble bed HTR would be a Depressurised Loss of Forced Cooling (DLOFC) accident, in which the only modes of heat removal from the core would be conduction and radiative heat transfer through the pressure vessel. Therefore, a steel pressure vessel is required (instead of prestressed concrete) and the diameter of the reactor is determined by the radial thermal resistance of the reactor core (Kugeler, *et al.* 2003).

To benefit from economy of scale, the reactor thermal power has to be maximised. In the PBMR this is done by adding a fixed graphite central reflector and increasing the height of the reactor, thus increasing the core volume without increasing the length of the radial heat removal

path. In this way safety is not compromised. This is how the basic geometry of the PBMR was arrived at, as shown in Figure 2.2.

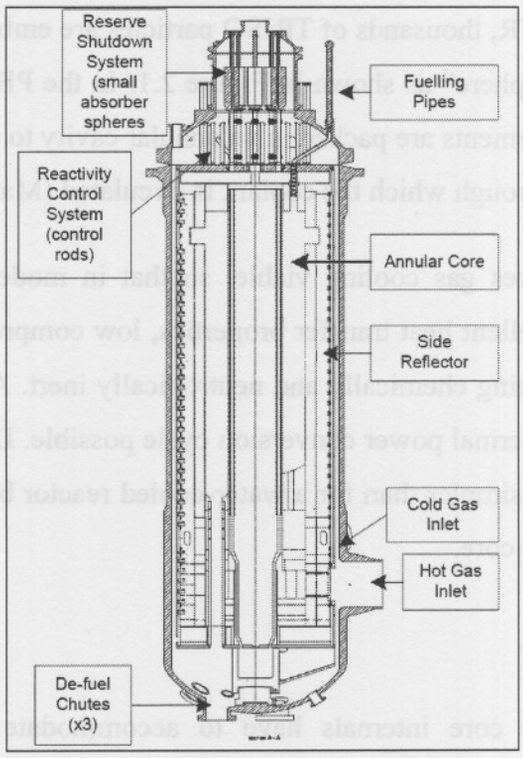


Figure 2.2. The general layout of the PBMR (Matzner, 2004).

However, neutron loss is minimised by using the core geometry nearest to spherical, i.e. with the height to width ratio near 1. This requirement conflicts with the safety requirement, so that the best option to prevent neutron loss is to use a thick graphite reflector. To limit radial heat loss during full power operation, helium upflow channels are placed in the side reflector. The fluid in these channels absorbs radial heat loss from the core before the helium flows into the pebble bed from the top (Matzner, 2004).

To maintain a critical pebble bed configuration, spent fuel is removed while fresh fuel is added, according to the German MEDUL (multiple pass) fuel cycle. In the original German cycle, each fuel sphere passes through the core about 15 times while the PBMR uses only six fuel passes (Stoker and Reitsma, 2004). For this purpose there are fuel loading penetrations at the top of the core, as well as fuel unloading chutes at the bottom of the reactor.

2.5 Detailed heat removal paths from the reactor

From a heat transfer point of view, modelling of a pebble bed HTR is a daunting task because of the complexity of the fuel distribution. The layered fuel particles are randomly distributed in the fuel spheres, while the fuel spheres are randomly packed in the porous bed that makes up the core.

In each fuel particle, heat is generated according to the thermal neutron flux at that point in the reactor. This heat is conducted through the TRISO particle layers into the surrounding graphite, where the combined effect of heat-generating particles sets up a radial temperature gradient in the fuel sphere. Heat is conducted to the sphere surface where it is removed by convection heat transfer to the helium coolant flow. An axial temperature gradient is set up in the pebble bed as the helium heats up. Due to the highly turbulent flow through the space between the spheres, an increased amount of flow mixing occurs in the pebble bed. This effect is called dispersion or braiding. It acts as an increased heat conduction perpendicular to the flow direction.

When there is no coolant flow in the pebble bed as, for example, during an accident situation, other heat transfer mechanisms come into play in the pebble bed. Fuel sphere surfaces exchange heat via radiation, while heat conduction also takes place through the contact points between spheres. Thus, there are internal temperature gradients in the fuel particles, superimposed on the temperature gradients in the fuel spheres, which are, once again, superimposed on the temperature gradient across the pebble bed.

Under full flow conditions, almost all heat is removed by the coolant flow while some heat is still lost by conduction and radiation to the components surrounding the reactor. PBMR tolerates the cost of heat loss during the lifetime of the normal operation of the reactor, due to the cost benefit of not to have active cooling mechanisms for accident scenarios. Under accident conditions, core heat is removed by conduction/radiation from the core to the side reflector, from where it is conducted to the pressure vessel surface. The reactor pressure vessel is cooled mostly by radiation heat transfer to the Reactor Cavity Cooling System (RCCS).

Except for the heating in the fuel spheres, secondary heating effects occur in the central and side reflectors, which are built up from interlocking graphite blocks. The gaps between these blocks create small flow channels that permit coolant to leak from the main flow path (the helium upflow channels in the side reflector) into the core. This causes a measure of cooling that counters the effect of gamma ray heating in the side reflector. Although this is a secondary

heat transfer effect, it has serious consequences for the neutron balance in the reactor, as the control rods are housed in the side reflector and their reactivity contribution is highly temperature dependent.

2.6 Previous pebble bed HTRs

The first operating pebble bed reactor was the 46MW AVR (Arbeitsgemeinschaft Versuchs Reaktor), built during the 1960s at Jülich in Germany (IAEA, 2002). It operated exceptionally well for 21 years and was decommissioned in 1988. It had a steel pressure vessel that housed a helium circulator and steam generator above the pebble bed core, while the steam generator drove a traditional Rankine power generation cycle.

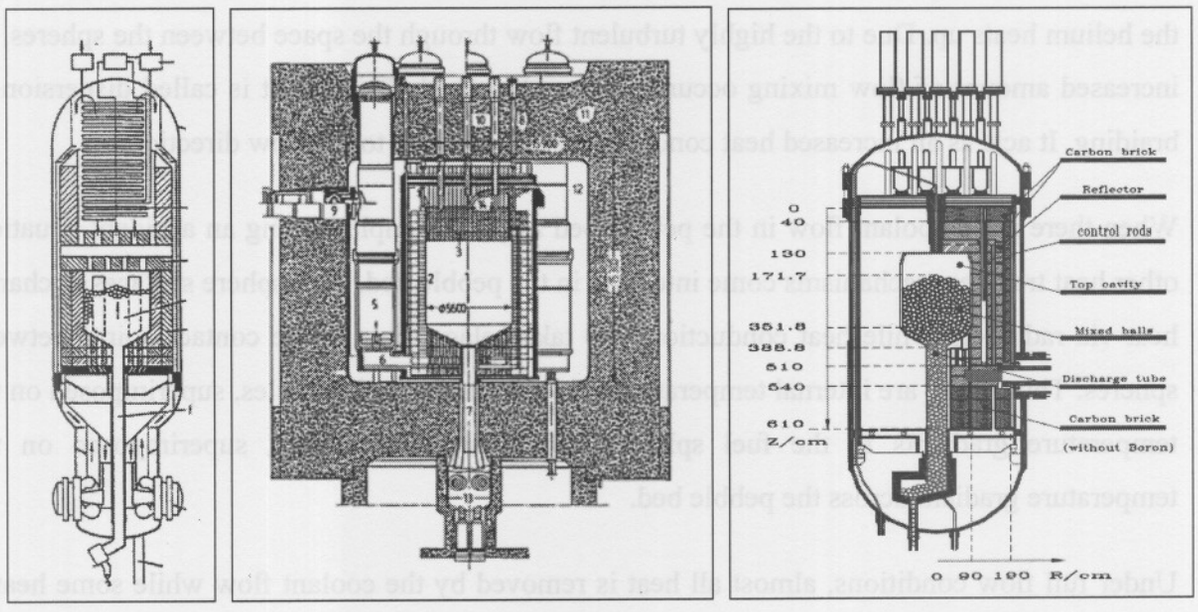


Figure 2.3. Various pebble bed reactors, from left to right: the AVR, the THTR and the HTR-10 (not to scale) (Kugeler *et al.* 2003, IAEA 2006).

The two most important contributions of the AVR are the demonstration of the safety features inherent to the HTR concept, as well as acting as a fuel development platform. Numerous particle fuel designs were tested, from the early BISO particles up to the current state-of-the-art Low Enriched Uranium (LEU) TRISO particles. BISO particles did not have a silicon carbide layer. Various fuels were tested, such as uranium carbide, thorium/uranium combinations, as well as several levels of uranium enrichment.

The next pebble bed HTR was also built in Germany, namely the 750MW(Thermal) Thorium High Temperature Reactor (THTR) at Schmehausen (IAEA, 2002). Its construction started in

1971 and after a series of delays, delivered its first electricity in 1984. It was, however, shut down and dismantled after 1989, due to the political climate changing strongly against nuclear power, following the Chernobyl disaster.

Except for a control rod that was designed to be forced into the pebble bed, the THTR operated flawlessly during its short operational lifetime. It was fuelled with a mixture of Highly Enriched Uranium (HEU) and Thorium, housed in TRISO particles that were dispersed in 60mm graphite spheres. The core, steam generators and helium coolant circulators were all housed in a prestressed concrete vessel. As with the AVR, the primary helium loop provided heat for a secondary water-based Rankine power cycle.

The most recent pebble bed HTR to be operated is the Chinese HTR-10. It is a 10MW reactor intended for research on the general operation of pebble bed HTRs and went critical for the first time in 2000. It is fuelled with LEU TRISO particles in a 60mm graphite sphere – the fuel design standardised in Germany. Since the start of its operation, results from the HTR10 research programme have been widely publicised and provides valuable experimental data for computer code validation.

Prismatic block-type HTRs have also been built and operated, such as Fort St Vrain and Peach Bottom in the United States and the DRAGON test reactor in the UK. At present Japan operates a 30MW block-type research reactor, the High Temperature Test Reactor (HTTR), while a joint Russian-American effort designs the 600MW plutonium-burning GT-MHR.

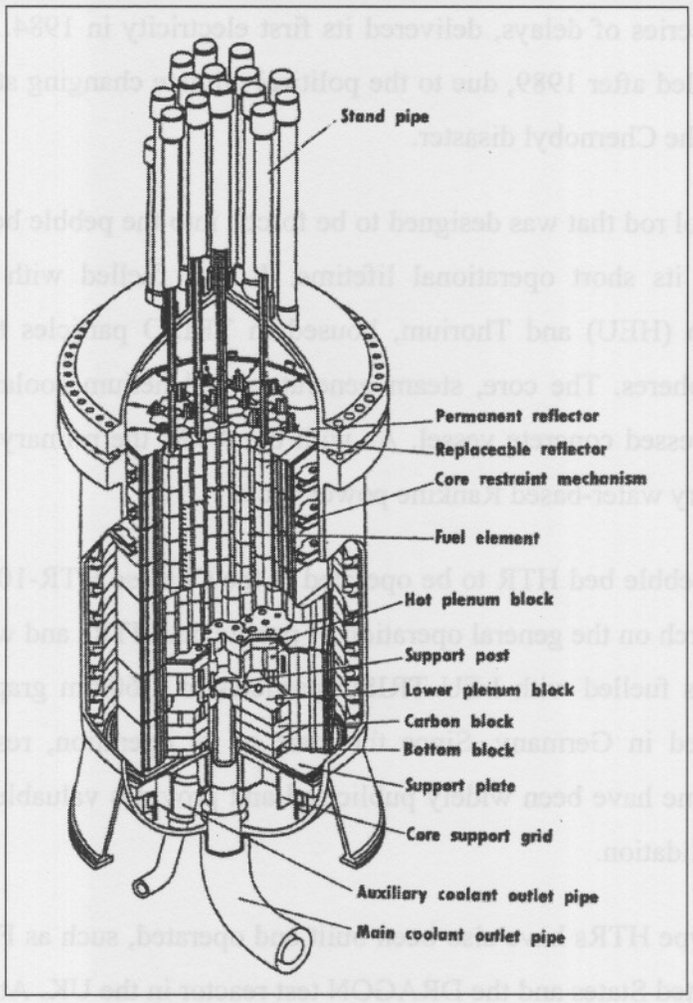


Figure 2.4. A cutaway view of the HTTR.

Pebble bed reactors operating on the multiple-pass fuel cycle appear to have an economic advantage over block-fuelled reactors, as online refuelling makes continuous operation possible. Refuelling of a block-type HTR requires shutdown and opening of the core, leading to downtime, possible release of diffused fission products and increased personnel radiation exposure. All these factors increase the cost of operating a block-type HTR (Slabber, 2004).

For this, as well as historic reasons, the South African utility, Eskom, decided to pursue pebble bed technology.

2.7 Conclusion

This chapter described the design of pebble bed HTRs according to the various requirements and consequences of the nuclear fission reaction. The advantages of coated particle fuel were

pointed out, as well as the design principles for an inherently safe nuclear reactor. Earlier examples of pebble bed HTRs were also discussed.

Chapter 3

Literature study of reactor simulation

3.1 Introduction

This chapter will build on the background the previous chapter has given on the operation of HTRs by focusing on previous work on pebble bed reactor modelling. Its place in systems simulation, as well as the context and necessity of system simulation, is discussed, along with the approaches followed by previous researchers to simulate pebble bed HTRs. The limitations of current reactor models are also pointed out at the end of this chapter.

3.2 Reactor modelling and systems simulation

3.2.1 The scope of detailed calculation codes

As described in the previous chapter, the heat transfer paths inside the reactor are so complex that dedicated calculation codes are developed for pebble bed HTR cores. Such a thermal-fluid code is mandatory in the detailed design of a reactor as the neutronic properties are inextricably linked to the temperature field in the reactor. Dedicated reactor design codes also take into account many other phenomena such as fuel burnup, intermixing of old and fresh fuel in the core, as well as the effect of fast fluence on graphite reflectors. An example of such a code suite is VSOP, which is described in more detail later on in this chapter.

Similar to detailed reactor design codes, Computational Fluid Dynamics (CFD) codes also focus on detail flow and temperature patterns inside components and attempt to include as many phenomena as possible. The treatment of many detailed phenomena comes at an overhead cost in terms of calculation time, which renders CFD unsuitable for determining the interactions between numerous components. Within the engineering design process, dedicated reactor design codes and CFD are thus limited to the detail component design level.

However, all components are part of larger systems in which components interact with each other. This interaction is taken into account at a higher level of the engineering design process, namely system level. At system level, conceptual design is done, system operation is determined and component operating envelopes can be determined from parametric studies (Blanchard & Fabrycky, 1998).

3.2.2 The necessity of systems simulation

In the context of HTRs, the reactor is always the heat source that forms part of a larger system, which could be an electrical power generation system, a desalination plant or some other type of plant that requires process-heat. Such plants could have components like intermediate heat-exchangers for process-heat application or cogeneration in which a direct Brayton (gas-turbine) cycle and a Rankine (steam) cycle uses the same reactor as heat source to obtain maximum efficiency.

With the PBMR, for example, the closed direct gas cycle creates a strong coupling to the rest of the power conversion system. For steady-state operation, the combination of reactor, heat exchangers and turbomachinery in the main power system must be optimised for best economy, without compromising safety. During transient events like startup, load change or loss-of-coolant-accidents, the close coupling between reactor component temperatures, system flow rates and turbomachinery shaft speed is also essential to take into account in order to establish proper event procedures.

These calculations can only be done with codes that simulate all plant components simultaneously, i.e. system simulation codes. System simulation codes are able to do tasks that are impossible with specialised component codes, such as sensitivity analysis, optimisation and transient operation analyses (Cullimore, 2001).

3.2.3 Brief description of systems simulation

The focus of systems simulation is on gaining an understanding of the behaviour of an integrated system and the interactions between elements of the system.

As described by Greyvenstein (2006), several levels of detail can be distinguished in systems simulation. In first-order cycle analysis, the impact of process conditions and cycle layout on system performance is determined. This is typically used for the first concept calculations of a system.

Second-order analysis has the same goal, but the level of accuracy is improved by taking piping losses, compressor and turbine efficiency and secondary flows such as leak or cooling flows into account.

Third order analysis takes sufficient component detail into account to assess the effect of component design or operating conditions on system performance. In order to take component

detail into account, the simple analytical models used in second-order analysis are replaced with more advanced implicit or explicit models such as lookup tables (for turbomachinery performance maps) and one-dimensional discretised pipe and heat exchanger models. Third order analysis can also be transient simulations.

A limitation of third order analysis is that the behaviour of components can only be calculated for the ranges covered by the characteristic charts. A system such as a heat exchanger, a boiler or a reactor has complex flow and heat transfer relations that cannot be quantified by a characteristic chart but would rather require a specialised tool such as a 3-D Computational Fluid Dynamics code. CFD codes are, however, slow and not well suited for optimisation studies, or transient simulations of a complete power plant, for example.

An extension of third order systems simulation models overcomes this limitation by embedding accurate multi-dimensional CFD models of selected components into the systems simulation solver. The CFD component models in the simulation codes are usually "tailor made" for the specific component, thereby avoiding the overhead of linking a general CFD code with a systems simulation code. The implicit coupling between the systems code and the CFD model improves ease of use and reduces solution time. This approach is referred to as the network or Systems CFD (SCFD) approach.

With SCFD codes, both system and component performance can be calculated for various or transient operating conditions. It has a wide range of applications, such as component sizing, system optimisation, sensitivity analysis, control system parameter estimation or simulating plant behaviour in a training simulator (Greyvenstein, 2006).

3.2.4 Reactor modelling in systems simulation

In contrast to other components in systems simulation, a HTR has flow paths and heat generation that is completely dispersed throughout the thermal mass of the core. The heat flow paths are also highly dependent on the operation state of the reactor. To illustrate this point, consider full-flow full-power operation of the PBMR. Helium enters the core assembly at 500°C at the bottom inlet plenum, flows up through the side reflector in the riser channels and then downwards through the core to exit at 900°C. For this case, most of the heat conducted radially outward through the side reflector is taken up by the inflowing helium. During a loss-of-flow condition, the decay heat from the core is conducted radially outward through the side

reflector, core barrel, reactor pressure vessel and eventually taken up by the reactor cavity cooling system (Kugeler *et al.* 2003).

It is clearly impossible to characterise such diverse heat transfer behaviour with simple correlations or lumped models as is the case with other thermal system components. The only adequate way to treat a reactor is to use a discretised (i.e. a CFD) reactor model that takes sufficient detail into account. Extensive work on the simulation of these phenomena has been done since the 1970s, even though it mostly treats the reactor in isolation.

3.3 Previous HTR reactor models

In the German HTR research programme, the computer codes VSOP and TINTE have been developed at the Forschungszentrum Jülich for design and simulation of pebble bed HTRs. VSOP (Very Superior Old Programs) is an assembly of many specialised reactor codes, each calculating a specific aspect of the reactor. Included in the VSOP suite is a code that solves the 4-group neutron diffusion equations, while in TINTE the 2-group neutron diffusion equations are solved. A module in VSOP also keeps track of the burnup and power level of representative "packets" of spheres in the various pebble flow paths of the reactor core. This is due to the fact that VSOP was created as a design tool for pebble bed reactors while TINTE was intended as a transient simulation tool. In VSOP, THERMIX-DIREKT does the thermal-fluid calculations while the thermal-fluid model is integrated into TINTE.

Both THERMIX and TINTE are assumed to use a pseudo-homogeneous approach for modelling the pebble bed as it is described as the state-of-the-art approach in a leading German technical journal, the VDI-Wärmeatlas (Tsotsas, 2002). In the pseudo-homogeneous approach, a single local representative temperature for the pebble bed and the interstitial fluid is assumed. Special separate methods then have to be developed to treat the sphere internal temperature gradient and convection heat transfer between the fluid and the solid.

3.3.1 TINTE

TINTE (**TI**me-dependent **N**eutronics and **T**emperatures) is a partly modular computer code for calculating transient events in the primary loop of HTRs. The time-dependent equations describing the prompt and delayed neutron fields, the temperature fields for fuel elements, components and cooling gas, as well as the fluid flow, are discretised in two-dimensional axi-

symmetric geometry. TINTE can also calculate air-ingress-corrosion with graphite as found in HTRs.

Temperatures are calculated for heterogeneous (fuel elements) and homogeneous (reflectors etc.) structures. Besides conduction and convection heat transfer, radiative heat transfer in cavities is also calculated. Forced convection, as well as natural convection flow, is calculated. Time-dependent diffusive mixing of different types of gases, evaporation and condensation as well as graphite corrosion due to the accidental ingress of oxidizing gases, can also be calculated.

The solution is divided into four separate models, namely the gas flow model, the gas, solid and fuel surface element temperature model, the fuel element internal model and the chemical model (gas mixing and corrosion). Due to the nonlinear coupled nature of the problem, these algorithms are solved in an iterative manner until convergence.

The pebble bed pressure drop, as well as convection heat transfer calculation, is based on experimental correlations. Additional one-dimensional elements have been added to TINTE in order to simulate components like safety valves or bursting discs.

Fuel sphere internal temperatures are either calculated to a high degree of accuracy with a finite difference solution or with a simple analytic model. The finite difference solution requires much more computer storage and takes more time to solve than the analytic model. The fuel sphere properties can be traced along several different paths through the reactor to take flux profile, fast neutron irradiation and temperature history into account.

TINTE can calculate radiation heat transfer in cavities as well. This is important, due to the high temperatures at which HTRs operate. In TINTE, the zones adjacent to a cavity have to be very thin for the solid temperature to approximate the cavity surface temperature as all solid temperatures are calculated at cell centres. The solid and fluid temperatures are solved simultaneously with a coupled block solver (Gerwin and Scherer, 2001).

The strength of TINTE lies in its ability to solve two-group space-time kinetic neutronics, which is necessary to calculate, for example, a control rod withdrawal. For such calculations, solution of the elliptic equations describing neutronic behaviour is the limiting factor, not solution of the thermal-fluid equations.

3.3.2 THERMIX

The THERMIX code was developed within the Institute for Reactor Development (ISR today) based on the work of Banaschek (1993) and Petersen (1983). The code is employed for steady-state and quasi steady-state thermal-fluid calculations of pebble bed reactor cores (Schürenkrämer, 1984; Cleveland and Greene, 1986). It uses the finite volume discretisation on an axi-symmetric two-dimensional geometry.

It calculates sphere internal conduction and heat generation, effective heat transfer between fuel spheres, as well as convection heat transfer from the pebble bed to a fixed coolant temperature (Verfondern, 1983). THERMIX does not have detailed neutronic or flow capabilities and thus has to be used in conjunction with a neutronics code such as PANTHER (steady-state neutronics) or KINEX (point-kinetic neutronics). For accurately calculating the gas flow field, THERMIX is used in conjunction with a code such as DIREKT or KONVEK. To obtain a solution, the heat transfer between the solids and fluid is solved iteratively.

For each control volume an appropriate material composition can be defined, if necessary, with an effective porosity when part of the control volume is occupied by a fluid. Typically for the finite volume discretisation, one local temperature characterises the solid temperature of a control volume. Similar to TINTE, THERMIX uses a library of materials that can be linked to software that keeps track of the fast neutron irradiation and temperature history of a group of spheres.

The DIREKT code has been developed in order to solve the time-dependent equations for convective (flow) heat transport and to establish the gas temperature distribution for the reactor. As such, it can be seen as the complementary calculation of THERMIX, that is, it describes the fluid part of a mesh volume. The heat convection calculation allows cross element heat transfer, in order to describe the circulation and eddying of the gas in the pebble-bed in transient cases with no forced cooling.

The first step towards obtaining the gas temperature distribution is taken by combining the continuity and momentum equations, which yield the pressure and mass flow rate distribution over the reactor at fluid temperatures of the previous iteration.

The second step consists of solving the energy equation with new pressure and mass flow rate distribution as input, together with the solid temperature distribution from THERMIX to determine the new gas temperature distribution. These two steps are iterated until convergence.

When the new gas temperature distribution is known, the convective heat transfer needed in THERMIX is calculated from Newton's law of cooling.

3.3.3 Conclusion on TINTE and THERMIX

It appears that solution techniques for assembled systems had not yet matured when these codes were created. This remark is based on the observation that the modelling of different phenomena in TINTE and THERMIX is still segregated in different algorithms, while in most current system simulation codes, the solid and fluid energy equations are solved as one single system. Solving all energy equations simultaneously provides vast improvements in terms of convergence and solution speed. Computer and programming constraints at the time of these codes' development, enforced certain simplifications and limitations onto these codes. These hurdles are also overcome by present computer and programming technology. With a well-formalised, robust and adaptable solution method, more attention can be paid to accurate discretisation methods and taking more phenomena into account.

3.4 Detailed reactor model/systems code coupling

One option to include reactor performance in a system simulation, is to link either a CFD or a detailed reactor model to a systems simulation code, such as the work by Verkerk (2000) and Kikstra (2001).

Verkerk (2000) linked a detailed reactor model in PANTHER/THERMIX/DIREKT to the thermal-fluid simulation code RELAP5 for simulating a complete pebble bed nuclear power plant. His research focused on the dynamic behaviour of a pebble bed reactor when coupled to a direct Brayton power cycle. He simulated the proposed Dutch ACACIA plant. He did, however, report very long solution times due to, firstly, slow data exchange between the linked codes, and secondly, difficult solution due to the segregation of the problem into separate solvers.

Kikstra (2001) used Aspen Custom Modeler to perform a similar analysis, but focused on the dynamic characteristics of the power conversion equipment (turbomachinery and heat exchangers). He used a very simplified model of the reactor to establish general trends in the system performance.

But even if a very simplified CFD model is coupled to a system simulation code, there are still two separate solvers running simultaneously on parts of the same problem, so that information has to be exchanged either with an explicit or a semi-implicit interface (so-called shallow or

deep coupling). This requires considerable programming effort to maintain consistency between the two codes. An explicit interface, furthermore, limits the timestep length in transient simulations (Aumiller *et a.l*, 2001).

3.5 Integrated systems simulation reactor models

Another approach that can only be followed in fundamentally oriented system simulation codes, is to assemble a geometrically discretised reactor model from the basic calculation elements already available in the code, such as flow resistances, convection and conduction heat transfer elements. Such a model was created by Stempniewicz (2002) in the thermal-fluid simulation code SPECTRA. (**S**ophisticated **P**lant **E**valuation **C**ode for **T**hermal-hydraulic **R**esponse **A**ssessment). It consists of a large library of physical models with which a simulation model of a complete fossil-fuelled or nuclear power plant (including the containment) can be assembled.

A similar approach appears to be followed in RELAP5-3D, the system simulation code developed by the Idaho National Energy and Environmental Laboratory (INEEL, 2004) for simulating water-cooled nuclear reactors. RELAP5-3D is capable of simulating complex two-phase flow phenomena in one-dimensional flow elements and three-dimensional flow fields, as well as performing detailed neutronics calculations in the reactor subnetwork.

Du Toit *et al.* (2003) also created a reactor model by using the calculation elements available in *Flownex* (Swift, 2006), the code used for the PBMR plant simulation. The abovementioned methods discretised the reactor into control volumes or nodes, and control volume faces or elements. In essence, the subnetwork that resulted from this discretisation was a rudimentary CFD model within the framework of a system simulation code, i.e. a Systems CFD (SCFD) model. Figure 3.1 gives a schematic representation of the reactor discretisation in *Flownex*.

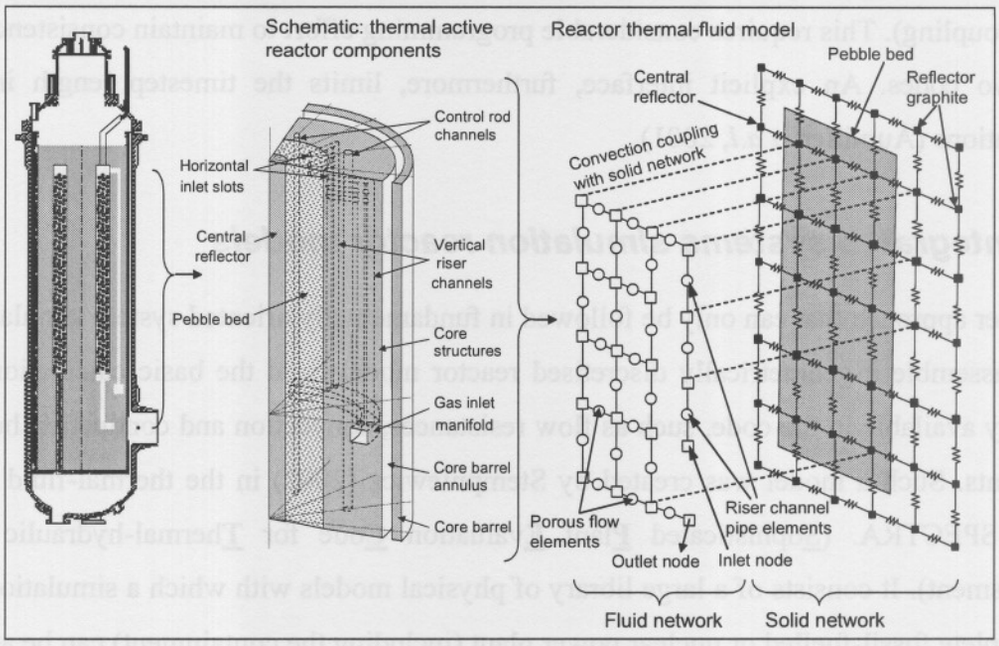


Figure 3.1. A network discretisation of the PBMR reactor.

Another contribution of Du Toit *et al.* (2003) was the introduction of a consistent pseudo-heterogeneous approach to model the pebble bed, i.e. there are separate fluid and solid temperatures at all positions in the pebble bed. With this approach, the temperature distribution inside pebbles, effective pebble bed conduction, convection heat transfer, as well as fluid energy conservation are solved as a single system, together with all other components of the power plant. The fact that there is a fully implicit coupling between all components in the simulation is the most important advantage of this approach, as it gives the shortest possible solution time.

3.6 Limitations in current approaches

The reactor models of Stempniewicz and Du Toit can be regarded as pioneer systems simulation models that work well and give useful results. But as the main objective of these developments were simply to get working reactor calculation models, many coarse approximations were made and simplified calculation elements were used. As an example, cartesian elements were used for all conduction elements, including the sphere discretisation (Swift, 2006). Such simple elements require considerable grid refinement to reach grid independence, thereby generating large numbers of nodes which slows down the simulation.

The model by Stempniewicz was also limited by the capabilities of SPECTRA, specifically in modelling the heterogeneity of the pebble bed. He had to use radiation heat transfer links between various zones of the pebble bed to model effective conduction (Stempniewicz, 2006).

Therefore, the discretisation methods used for these reactor models are not yet well investigated or optimised. Many questions on the modelling approaches for some phenomena, like detailed radiation heat transfer or conjugate heat transfer across holed solids still remain unanswered. The use of a pseudo-heterogeneous pebble bed model also means entering uncharted terrain, as the old, pseudo-homogeneous pebble bed/wall heat transfer correlations do not apply and there is not yet concensus on the ideal network topology at the pebble bed wall. It has also been found that the main reason for pebble bed solid temperature grid dependence is the first-order convection heat transfer scheme used in the core. These traits still limit the application of these reactor models.

Therefore, there is a twofold opportunity with regard to these reactor models: firstly, to improve grid independence by improving the discretisation methods and secondly, to investigate the importance and implementation of other phenomena into a systems simulation reactor model.

3.7 Conclusions

In this chapter, the unique requirements to reactor models in system simulation codes was discussed and descriptions were given of some historical codes as well as state-of-the-art HTR thermal-fluid calculation codes. It was observed that, despite huge advances in recent times, present systems-simulation reactor models still have certain limitations due to their discretisation methods. It was also found that the relation of discretisation method to the calculation speed of system simulation reactor models has not been studied closely. As an introduction to such a study, the next chapter describes the theoretical basis of a systems-simulation reactor model.

Chapter 4

Background theory

4.1 Introduction

This chapter starts with a description of the network approach for discretising a thermal-fluid system. From this follows the development of rudimentary reactor models that preceded the work of Du Toit *et al.* (2003). The fundamental equations of their reactor model are described, followed by a critical review of their discretisation of the conservation equations. With this in mind, some areas are pointed out in which current schemes have room for improvement, after which alternative discretisation approaches are described. This study will investigate some of these alternative discretisation methods and how they can be used to create a new reactor model.

4.2 The network or system CFD approach

4.2.1 General network approach

In general, the network or Systems CFD approach is a method of creating a consistent numerical discretisation of a complex thermal-fluid system. The numerical discretisation can then be solved, using standard matrix solution techniques.

The basic building block of the network approach is the control volume, or node, which represents a certain volume of fluid or solid in which single scalar values are assumed to be representative of average conditions in the control volume as a whole. Mass and energy conservation is applied to determine the change in thermal properties of the fluid within the control volume. To illustrate this, consider the energy conservation equation (Eq.(4.1)) for the stationary incompressible fluid control volume in Figure 4.1.

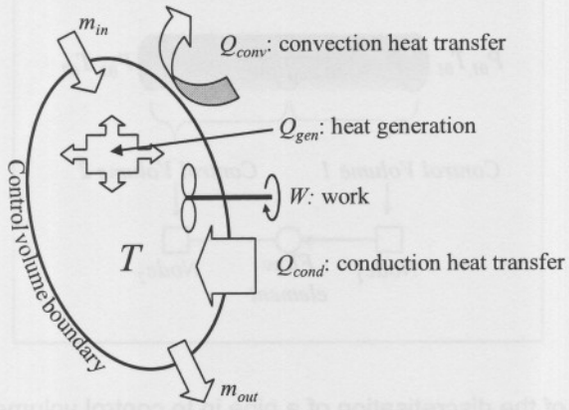


Figure 4.1. Various heat transfer paths to and from a control volume.

$$\frac{d\left(\rho \forall c_p T\right)}{dt} = Q_{cond} + Q_{cond} + Q_{gen} + W + \sum \dot{m}_{in} c_p T_{in} - \sum \dot{m}_{out} c_p T_{out} \tag{4.1}$$

The representative temperature T in the control volume will increase when there is heat generation (Q_{gen}) inside, work (W) done on the control volume or conduction or convection heat transfer from across the control volume boundary (Q_{cond} and Q_{conv}). There may be several mass flow streams into and out of the control volume, each representing a certain loss or gain in enthalpy for the control volume ($\sum \dot{m}_{in} c_p T_{in}$ and $\sum \dot{m}_{out} c_p T_{out}$).

These control volumes are linked by flow elements, which could be mass flow or heat flow elements. The heat flow elements in Eq.(4.1) could be convection and conduction elements, described by Eqs.(4.2) and (4.3).

$$Q_{conv} = hA\left(T_{conv} - T\right) \tag{4.2}$$

$$Q_{cond} = \frac{kA}{L}(T_{cond} - T) \tag{4.3}$$

T_{conv} and T_{cond} are the temperatures of adjacent control volumes with which heat is exchanged by convection and conduction respectively.

On the mass flow elements, momentum conservation is solved to create a balance between the control volume pressures and element massflows. Each type of flow element has a massflow/pressure drop characteristic determined by the type of flow element and its geometry.

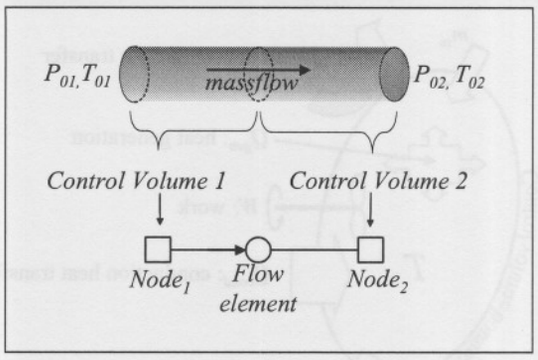


Figure 4.2. Illustration of the discretisation of a pipe in to control volumes, showing the network representation as well.

By dividing a thermal-fluid system into appropriate control volumes and linking the control volumes with appropriate flow elements, a network can be set up that represents a whole thermal-fluid system, for example the simple pumping system shown in Figure 4.3.

The discretised network gives rise to a set of simultaneous non-linear equations that have to be solved in the most efficient way. Flownex solves compressible and incompressible momentum and mass conservation with an adaptation of the SIMPLE algorithm, namely the Implicit Pressure Correction Method (IPCM) developed by Greyvenstein and Laurie (1994), while energy conservation is solved separately from the flow equation in one single matrix, i.e. solid and fluid node enthalphies together. Extensive detail on the development of the solution algorithms for the network method is available in Van Ravenswaay (1998) and Botha (2003), but as the solution method in Flownex is formally unconditionally stable and well-optimised, this study will not go into further detail on solution methods.

4.2.2 The use of correlations

Unlike CFD, the network approach models components at a high level as its interest lies in overall system behaviour and fast simulation times. Therefore, often the most efficient way to represent component characteristics is with correlations. For example, pressure drop in turbulent pipe flow is calculated with the Darcy-Weisbach correlation (Shames, 1992), while pipe bends, entry and exit losses are modelled with loss coefficients. As seen in Figure 4.3, pressure rise over a pump is calculated from the pump head/flow chart instead of solving the detail of the pump rotor velocity triangles, while convection heat transfer coefficients are calculated with Nusselt number correlations instead of solving the flow field. Other high-level examples include the use of heat exchanger performance charts and turbomachine performance charts.

However, correlations are only applicable where properties of a component can be lumped, as is frequently the case during steady-states. When properties cannot be lumped, as is frequently the case during transients, the domain has to be discretised as described in the next paragraph.

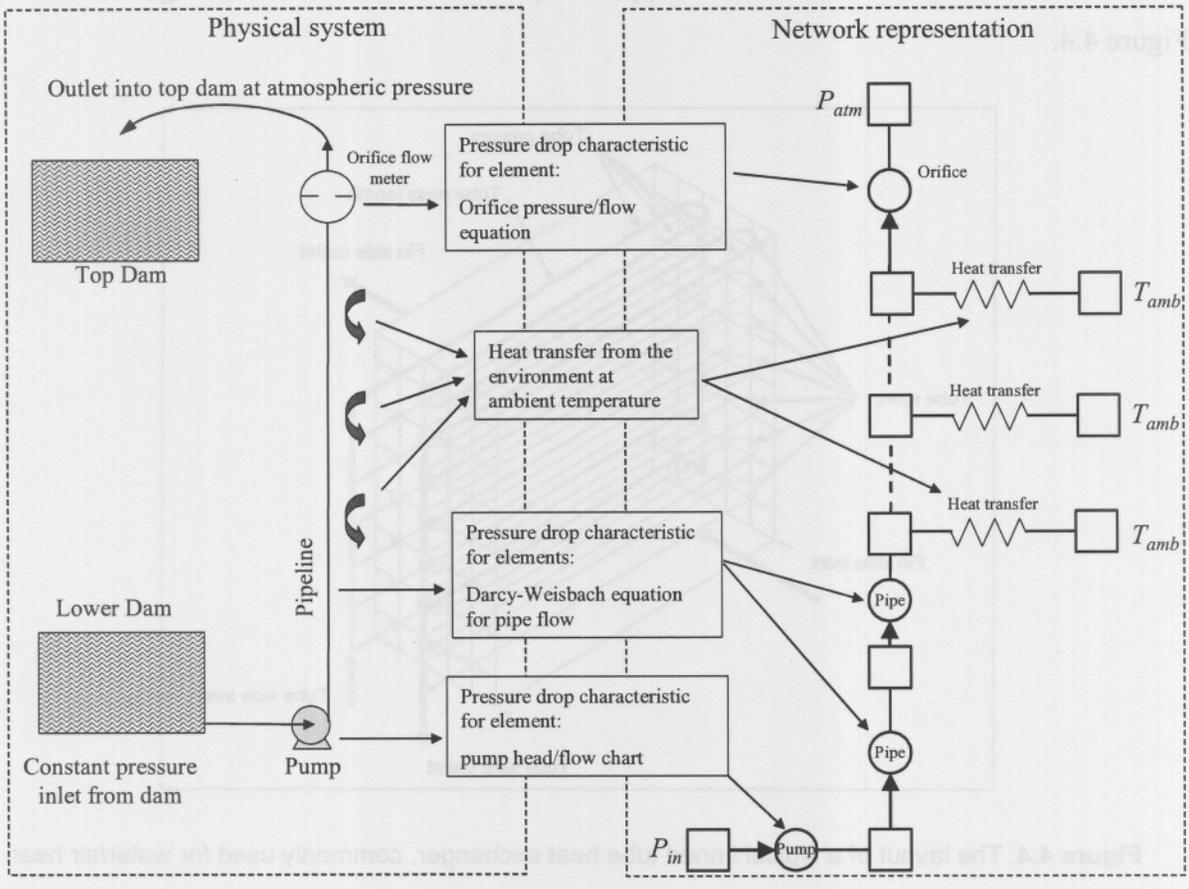


Figure 4.3. A setup with two dams, a pump, a pipeline and a orifice flow meter represented with the network approach on the right. Heat transfer is also treated efficiently.

4.2.3 Discretised components in the network approach

For most heat exchangers, steady-state performance can be calculated with simple correlations such as those of the effectiveness NTU method (Incropera and DeWitt, 1996). This method relates massflow, heat capacity, inlet and outlet temperatures to heat transfer in a very simple way. Therefore, the NTU method is very well-suited for conceptual design calculations at a plant`s intended operating point. But since it does not take thermal mass into account, or the fact that the heat exchanger thermal mass is dispersed throughout the fluid in the heat-exchanger, the NTU method cannot be used for transient analysis.

When there are no overall correlations available for a certain geometry of heat exchanger or when the dispersed thermal mass has to be taken into account, the heat exchanger can be

discretised by dividing it into a number of small sections. The topology of the network connections is chosen to represent the topology of the actual flow and heat transfer paths. Consider, for example, a finned-tube air/water heat exchanger with water flowing on the tube side and air flowing on the fin side. A typical layout for such a heat exchanger is shown in Figure 4.4.

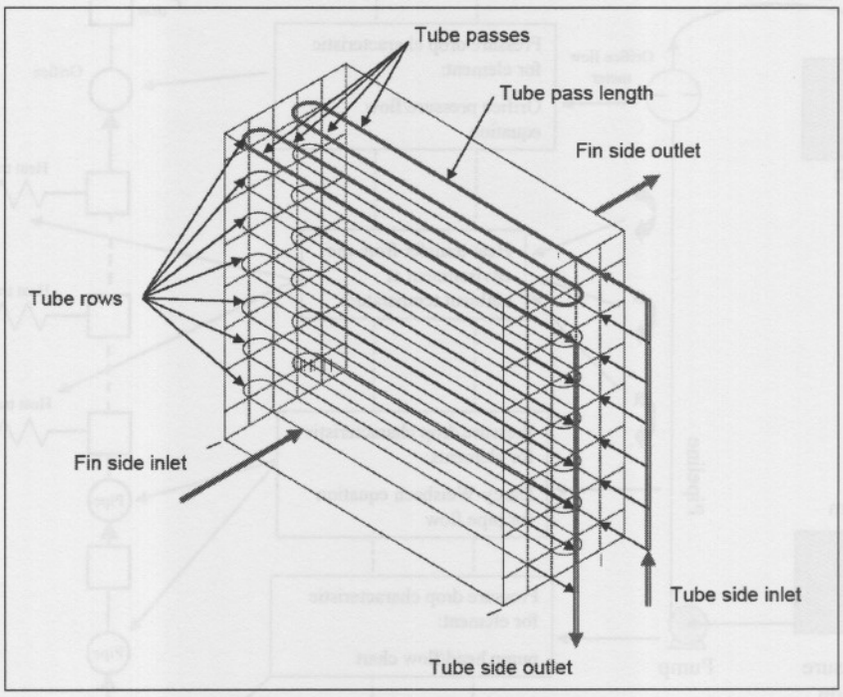


Figure 4.4. The layout of a typical finned tube heat exchanger, commonly used for water/air heat exchange.

The flow paths of the above heat exchanger are shown on the righthand side of Figure 4.5, with the network representation of a portion of the heat exchanger core shown on the left of Figure 4.5.

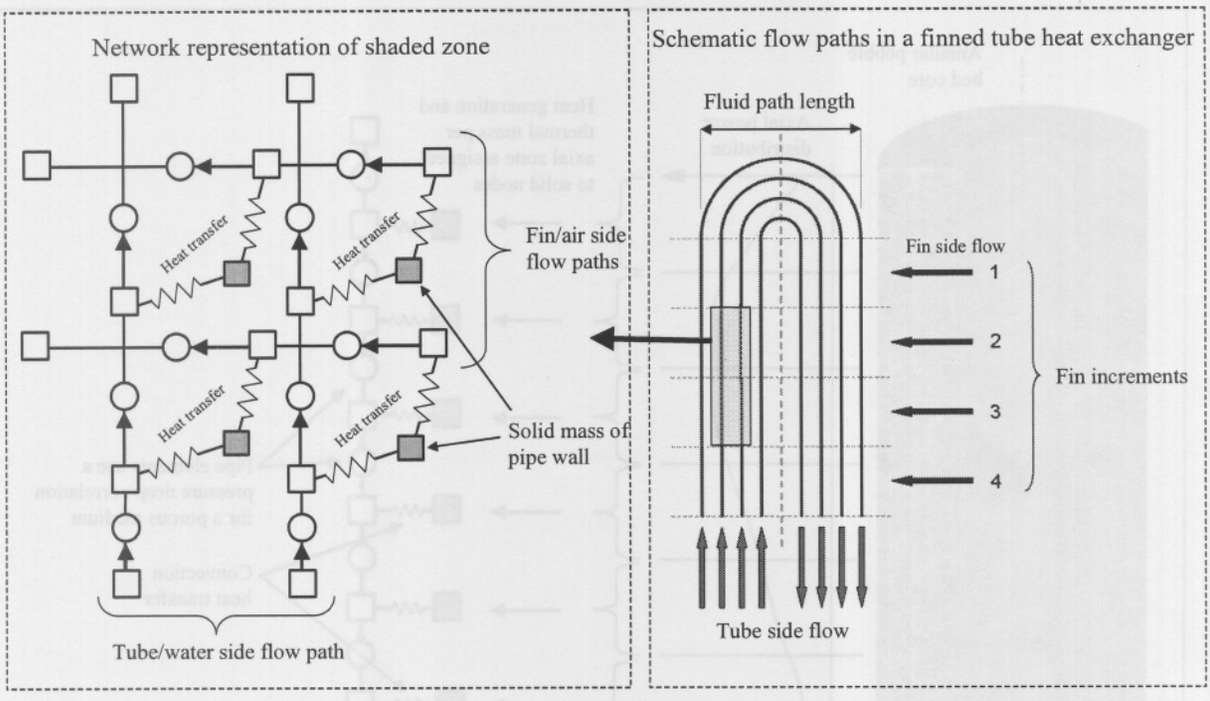


Figure 4.5. The flow paths of a typical finned tube heat exchanger on the right, with the network representation of the shaded part on the left (Swift, 2006).

For the flow and heat transfer elements in the above figure, the appropriate pressure drop and heat transfer correlations for pipe flow are implemented for each pipe section. In this way, all fundamental phenomena that affect the heat exchanger's transient response is captured.

4.3 Development of reactor models with the network approach

4.3.1 First generation reactor models

A nuclear reactor has thermal mass and heat generation dispersed throughout the core, similar to a heat exchanger. The simplest method to take the reactor thermal mass into account is with a one-dimensional reactor model, assuming a uniform flow profile throughout the pebble bed. All the thermal mass in an axial zone can be lumped in order to get a first-order approximation for the gas temperature transient response. Such a reactor model created with the network approach is shown in Figure 4.6.

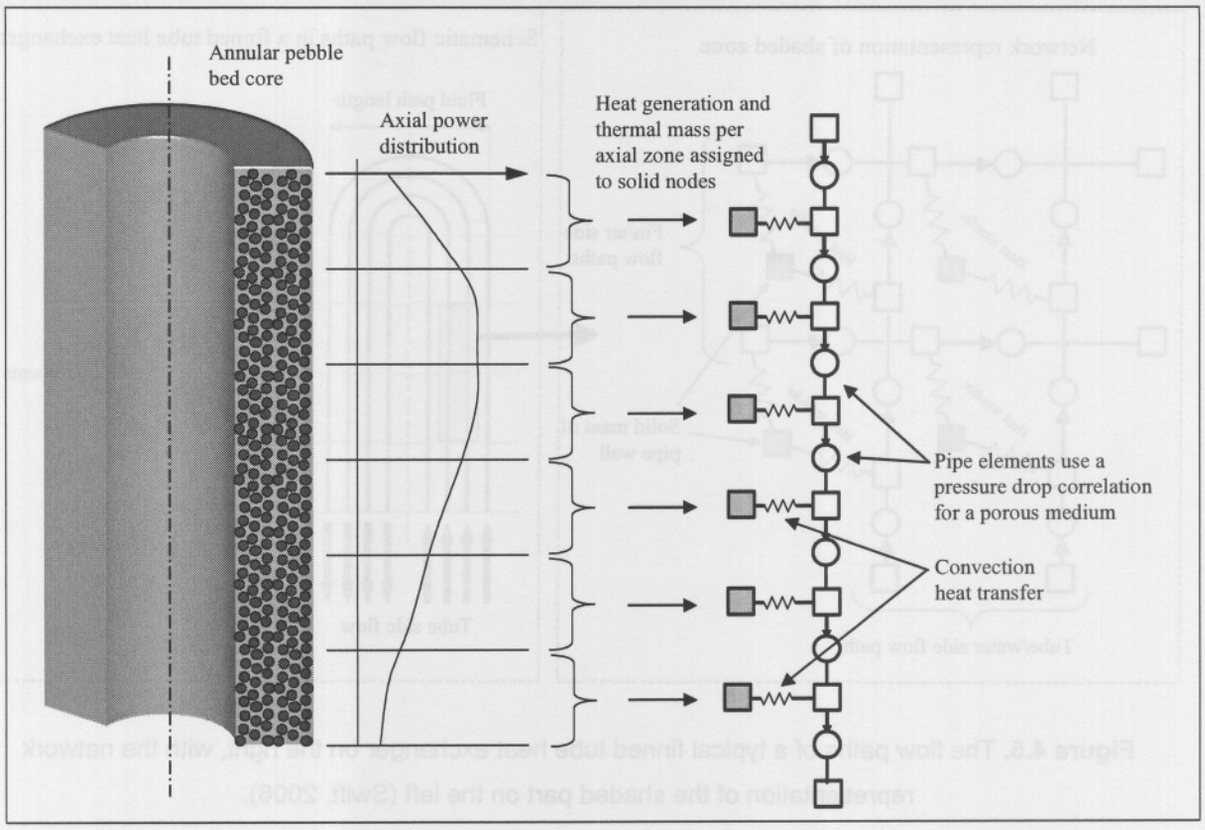


Figure 4.6. A first-generation pebble bed reactor model for systems simulation.

4.3.2 Second generation reactor models

The first generation reactor model described in the previous chapter is only first-order accurate, while the network approach gives the opportunity to create more accurate models which will yield additional information. Thus, with the aim of accurately calculating the plant response over a wide power and mass flow rate range (between 110 percent and 30 percent of nominal values), the Generation II *Flownex* reactor model (Swift, 2006) was developed. The reactor model also had to provide for radial variations in fluid velocity while porosity was constant and heat generation was assumed volumetrically constant in the radial direction.

The radial detail was resolved by discretising the bed into several parallel flow paths, while for each pebble bed zone the temperature profile inside a representative fuel sphere was also calculated. This was done by discretising the sphere into spherical shells, each represented by a solid node. The network discretisation of this reactor model is shown in Figure 4.7, as presented in the *Flownex* Manual. Effectively, the Generation II reactor model is equivalent to an axially symmetrical two-dimensional CFD model.

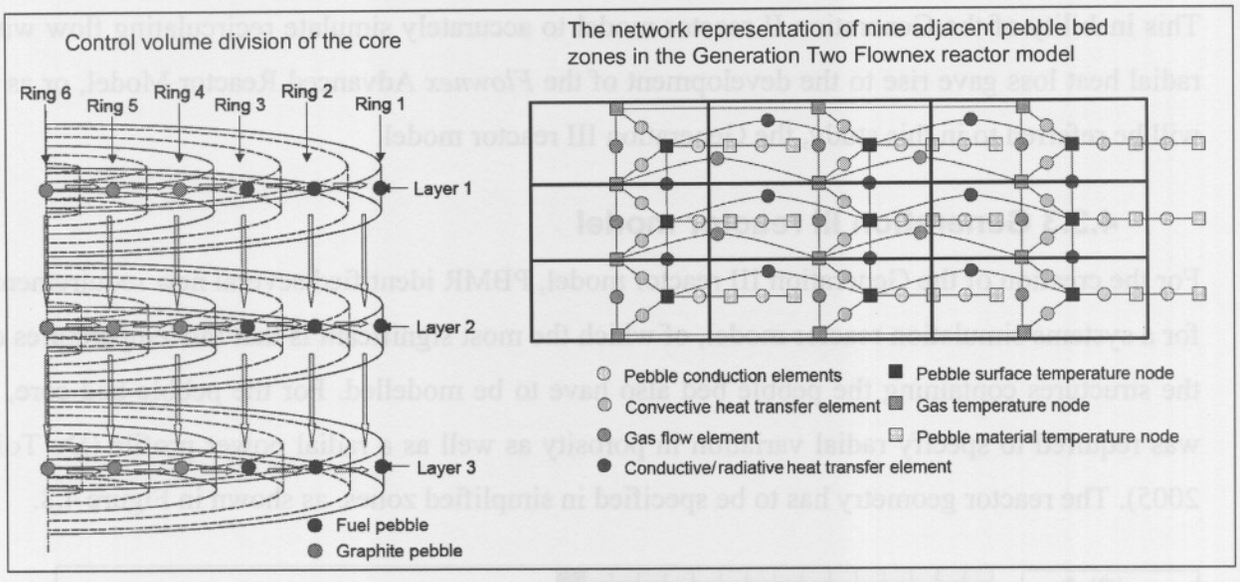


Figure 4.7. The network discretisation in the Generation II Flownex reactor model.

The inclusion of a sphere model enables the Generation II reactor model to be linked to a point-kinetic neutronics model, as the average fuel and moderator temperatures are available from the discrete sphere model. The sphere discretisation model also gives an approximation for the value and location of the maximum fuel temperature.

Note that the convection heat transfer element couplings in Figure 4.7 are different from that in Figure 4.6. The topology in Figure 4.7 is superior to that shown in Figure 4.6, as it calculates the heat transfer between the solid and the control volume average fluid temperature, not between the solid and the control volume exit temperature. It was found that, due to this discretisation, the transient response of the Generation II reactor model reached grid independence with much fewer increments than the discretisation in Figure 4.6 (Van der Merwe and Van Antwerpen, 2006).

It must be noted that the convection discretisation only has an accuracy advantage above a certain mass flow rate, of which the details are described in Paragraph 6.3 in Chapter six. Another limitation of the convection discretisation is that it is not accurate when the flow angle deviates significantly from the axial direction, as typically occurs during shutdown or Loss Of Forced Cooling events when a recirculation flow pattern develops in the reactor.

This, however, is not an issue for the Generation II reactor model as it was only required to be applicable at high mass flow rates. Therefore, no side reflectors or radial heat loss from the pebble bed was taken into account.

This inability of the Generation II reactor model to accurately simulate recirculating flow with radial heat loss gave rise to the development of the *Flownex* Advanced Reactor Model, or as it will be referred to in this study, the Generation III reactor model.

4.3.3 Generation III reactor model

For the creation of the Generation III reactor model, PBMR identified several new requirements for a systems simulation reactor model, of which the most significant is that the temperatures of the structures containing the pebble bed also have to be modelled. For the pebble bed core, it was required to specify radial variation in porosity as well as a radial power profile (Du Toit, 2005). The reactor geometry has to be specified in simplified zones, as shown in Figure 4.8.

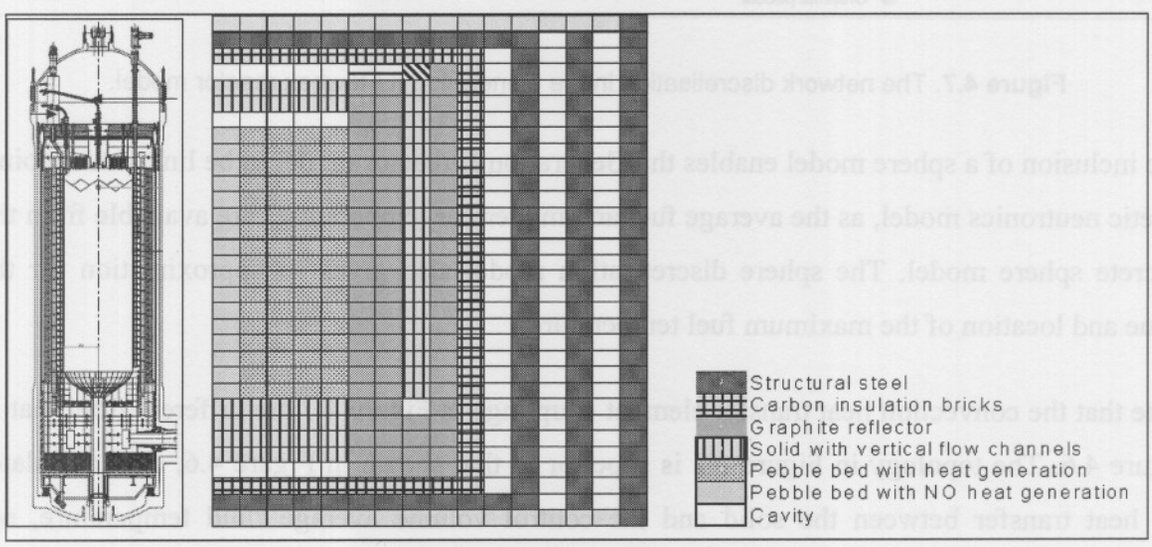


Figure 4.8. The 268MW PBMR and its geometrical zones input for a reactor thermal-fluid model.

Calculating the temperatures in the core structures entails the modelling of all flow paths in the reactor, two-dimensional conduction in all the solids containing the pebble bed core, as well as convection heat transfer between the flow paths and the solids. For accurate core structure temperature calculation, it is also necessary to take radiation heat transfer across cavities, two-dimensional heat conduction, as well as heat generation in these structures into account.

To accomplish this, Du Toit *et al.* (2003) revised the theoretical basis of the reactor model by deriving a consistent mathematical model of the complete reactor model. This consists of mass, momentum and energy conservation equations for the fluid, energy conservation for a spherical solid, energy conservation for the solid structures surrounding the core, as well as a conservation equation that describes the effective conductivity for the pebble bed. The various

energy conservation equations are linked by means of boundary terms, such as convection heat transfer or contact conduction resistances.

A major contribution of Du Toit *et al.* (2003) was the creation of a pseudo-heterogeneous model for the pebble bed, which refers to the use of separate energy equations for the fluid and the solid in the pebble bed. Previous pebble bed models assumed a pseudo-homogeneous model for the pebble bed as described by Tsotsas (2002).

The following section describes the conservation equations that form the theoretical basis for the Generation III reactor model.

4.4 Generation III Reactor model conservation equations

The reactor model investigated in this study is also based on the conservation equations derived by Du Toit (2005). These equations are presented in the following paragraphs, followed by a critical evaluation of the discretisation techniques used in the Generation III *Flownex* reactor model.

4.4.1 Fluid equations

From an order-of-magnitude analysis for porous flow and inclusion of certain thermodynamic relationships, the compressible conservation equations in axial-symmetric cylindrical coordinates are simplified to the following relations:

Radial momentum conservation:

$$\varepsilon\rho\frac{\partial u_r}{\partial t} = -\varepsilon\frac{\rho V^2}{2T_o}\frac{\partial T_o}{\partial r} - \varepsilon\frac{p}{p_o}\frac{\partial p_o}{\partial r} - \varepsilon\rho g\frac{\partial y}{\partial r} - B_r \tag{4.4}$$

Axial momentum conservation:

$$\varepsilon\rho\frac{\partial u_z}{\partial t} = -\varepsilon\frac{\rho V^2}{2T_o}\frac{\partial T_o}{\partial z} - \varepsilon\frac{p}{p_o}\frac{\partial p_o}{\partial z} - \varepsilon\rho g\frac{\partial y}{\partial z} - B_z \tag{4.5}$$

with B being the flow resistance force, g acceleration and p pressure. T is temperature, u_r and u_z is velocity components while V is absolute velocity, i.e. vectorial sum of u_r and u_z. ε is porosity and ρ is density. The subscript 0 refers to stagnation conditions. The energy equation for the fluid is given by:

$$\frac{\partial}{\partial t}(\varepsilon\rho e_0)+\frac{1}{r}\frac{\partial}{\partial r}(\varepsilon r\rho e_0 u_r)+\frac{\partial}{\partial z}(\varepsilon\rho e_0 u_z)=\varepsilon\frac{\partial p}{\partial t}$$
$$+\frac{1}{r}\frac{\partial}{\partial r}\left(\varepsilon r k_{feff}\frac{\partial T}{\partial r}\right)+\frac{\partial}{\partial z}\left(\varepsilon k_{feff}\frac{\partial T}{\partial z}\right)+\varepsilon\rho\left(g_r u_r+g_z u_z\right)+q_{sf} \quad (4.6)$$

where e is enthalpy and q'''_{sf} is the heat per unit volume transferred from the porous block to a fluid. k_{feff} is the fluid effective conductivity of which the calculation is discussed in Section 5.7.

4.4.2 Equations for solids

The energy conservation equation for porous materials is given by

$$\frac{\partial}{\partial t}\left[(1-\varepsilon)\rho_s e\right]=\frac{1}{r}\frac{\partial}{\partial r}\left\{(1-\varepsilon)r\left[k_s\frac{\partial T}{\partial r}\right]\right\}$$
$$+\frac{\partial}{\partial z}\left\{(1-\varepsilon)\left[k_s\frac{\partial T}{\partial z}\right]\right\}+(1-\varepsilon)\left(q'''_{fs}+q'''_s\right) \quad (4.7)$$

where e is the specific internal energy of the material, while the subscript s refers to "solid". k is conductivity, q'''_s is the heat generation per unit volume and q'''_{fs} heat per unit volume transferred from fluid to the porous material.

For the internal mass of a fuel sphere, energy conservation in one-dimensional spherical coordinates is given by the equation

$$\frac{\partial}{\partial t}\left[\rho_p e\right]=\frac{1}{r^2}\left[\frac{\partial}{\partial r}\left(k_p r^2\frac{\partial T}{\partial r}\right)\right]+q'''_p \quad (4.8).$$

As all pebble bed mass is associated with the sphere internal energy equation, the pebble bed surface energy equation is given by

$$\frac{1}{r}\frac{\partial}{\partial r}\left[r k_{eff}\frac{\partial T}{\partial r}\right]+\frac{\partial}{\partial z}\left[k_{eff}\frac{\partial T}{\partial z}\right]=0 \quad (4.9)$$

in which k_{eff} refers to an effective conductivity in the pebble bed. The effective conductivity includes the effect of radiation, conduction and interstitial convection in the porous bed.

4.5 Generation III Reactor model discretisation

In this section, the fundamental properties of the flow discretisation in Flownex are explained, followed by a description of the network topology of the Generation III reactor model.

4.5.1 Basic properties of the flow discretisation

Du Toit (2005) demonstrated that the network discretisation of the conservation equations (4.4) to (4.7) and (4.9) is equivalent to the well-known staggered grid CFD discretisation. This implies that the network discretisation has similar solution properties to the staggered grid approach. This equivalence between the network discretisation and the staggered grid discretisation is shown in Figure 4.9.

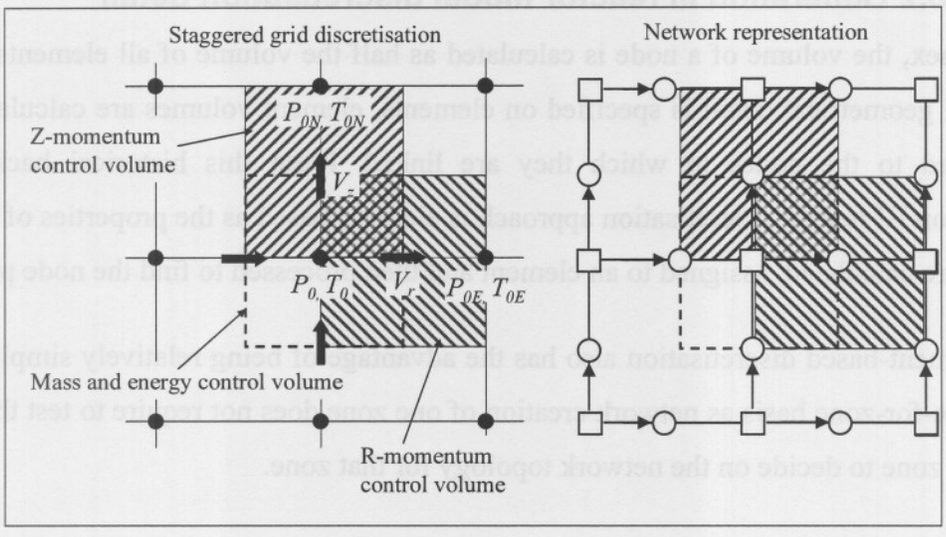


Figure 4.9. The staggered grid discretisation in CFD, showing the primary conservation variables of total pressure and total temperature on the nodes and velocity (for momentum) on staggered control volumes between nodes. The network representation is on the right-hand side.

The only additional requirement to the Flownex elements used in the pebble bed core, is that *z*- and *r*-direction velocities have to be stored on the nodes as well, in order to calculate the absolute velocity for the packed bed Reynolds number. This will be treated in greater detail in Section 5.6.

The fact that the conservation equations are expressed in terms of total pressure and total enthalphy (or total temperature) is used to great advantage on the staggered grid discretisation, as no interpolation is necessary for solution of the primary variables. The staggered grid provides excellent coupling between the pressure and velocity fields as well.

The staggered grid arrangement is, however, limited to orthogonal grids so that in current commercial CFD codes, it is replaced by the co-located grid scheme that can handle irregular cell shapes in complex geometry. For co-located grids, special techniques are necessary to

prevent the so-called "checkerboard effect" which results from pressure/velocity field decoupling. This phenomenon is described in textbooks on CFD, e.g. Ferziger and Peric (1999).

Thus, Du Toit *et al.* (2003) showed that the conservation equations for the pebble bed core can efficiently be discretised into system simulation elements. The following section will describe the detail of how the elements were linked in the Generation III reactor model.

4.5.2 Generation III reactor model discretisation detail

In Flownex, the volume of a node is calculated as half the volume of all elements linked to it. Thus, all geometrical detail is specified on elements, element volumes are calculated and then distributed to the nodes to which they are linked. From this historical background, the Generation III reactor discretisation approach is element-based as the properties of a zone in the reactor are calculated, assigned to an element and then processed to find the node properties.

This element-based discretisation also has the advantage of being relatively simple to program on a zone-for-zone basis as network creation of one zone does not require to test the type of the adjacent zone to decide on the network topology for that zone.

Any discretisation has to take into account that material properties, flow resistance properties, and heat transfer characteristics differ from zone to zone, i.e. the properties used for flux elements have to be somehow averaged. In the element-based approach, this is done by placing elements on both sides of a control volume boundary, i.e. each element has constant properties, while the change in material properties is managed by using two parallel elements, as illustrated for solid nodes and conduction elements as shown in Figure 4.10.

The fact that two elements are used between one node does not increase the time to solve the energy or flow matrices, as the number of equations are determined by the number of nodes (Van Antwerpen and Greyvenstein, 2006). The use of two parallel elements only increases the calculation overhead cost in terms of updating between solution iterations.

In the element-based discretisation, the method used to calculate node volume was inherited from systems-simulation elements. As illustrated in Figure 4.11, this entails calculating the volume and mass of each element and then dividing the mass between the two adjacent nodes. If Cartesian elements (i.e. trapezoidal volumes) are used, the total volume is grid-dependent, but in the Generation III Reactor model, the total volume is accurately calculated according to the cylindrical coordinate system.

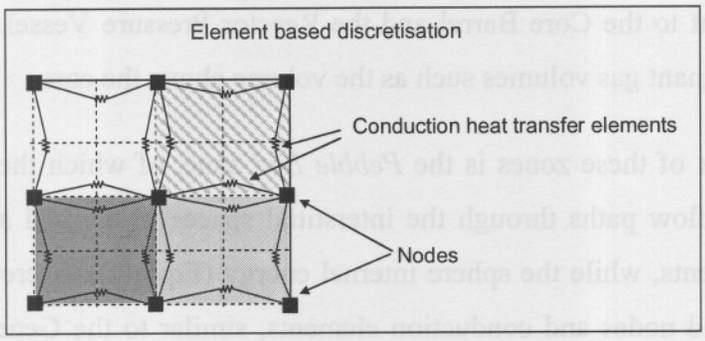


Figure 4.10. Methods of dealing with change in material properties across control volumes, using the discretisation of a solid zone as example (Swift, 2006). Each coloured zone represents a different material type. Node mass calculation is explained in greater detail in Figure 4.11.

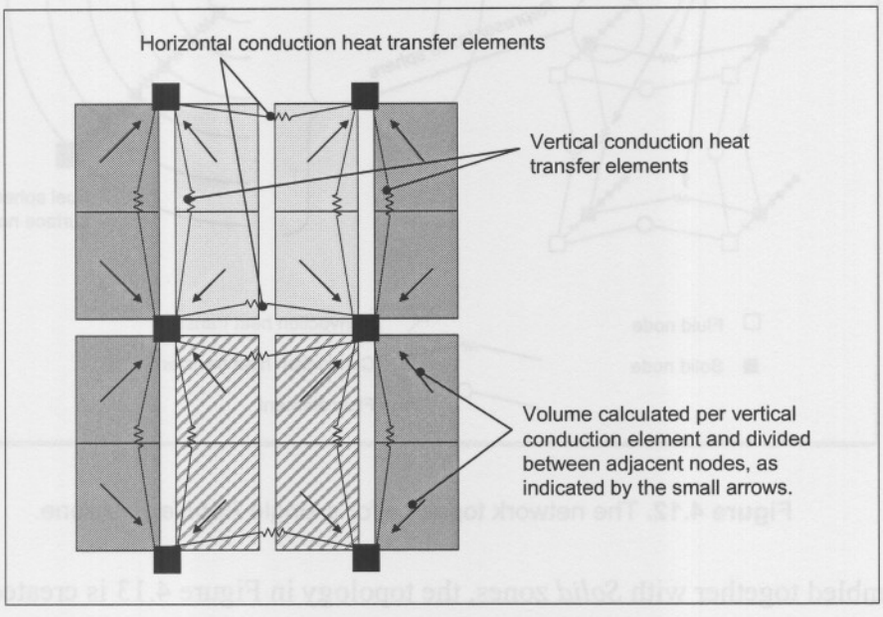


Figure 4.11 The method by which node mass is calculated from the elements. Note that volume is assigned only to the vertical conduction elements and then divided between nodes. Each coloured zone represents a different material type.

In principle, there are six zone types available in the Generation III Reactor model, namely *Solid with 1-D Flow, Solid with 2-D Mixed Flow, Solid, Horizontal* or *Vertical Cavity, Single Cavity* and *Pebble Bed.*

The *Solid with 1-D Flow* zone is typically used to model the part of the side reflector through which the helium riser channels pass. *Solid with 2-D Mixed Flow* zone is used where there are branching flow channels inside a solid, such as at the outlet plenum, where various flow paths join. The *Solid* zone models only conducting solids while the *Vertical Cavity* is used to model

the spaces adjacent to the Core Barrel and the Reactor Pressure Vessel. The *Single Cavity* is used to model stagnant gas volumes such as the volume above the core.

The most complex of these zones is the *Pebble Bed* zone, of which the network is shown in Figure 4.12. The flow paths through the interstitial spaces in the bed are represented by the porous flow elements, while the sphere internal energy (Eq.(4.8)) discretisation is represented by a series of solid nodes and conduction elements, similar to the Generation II reactor. The solids and fluid are linked by convection elements.

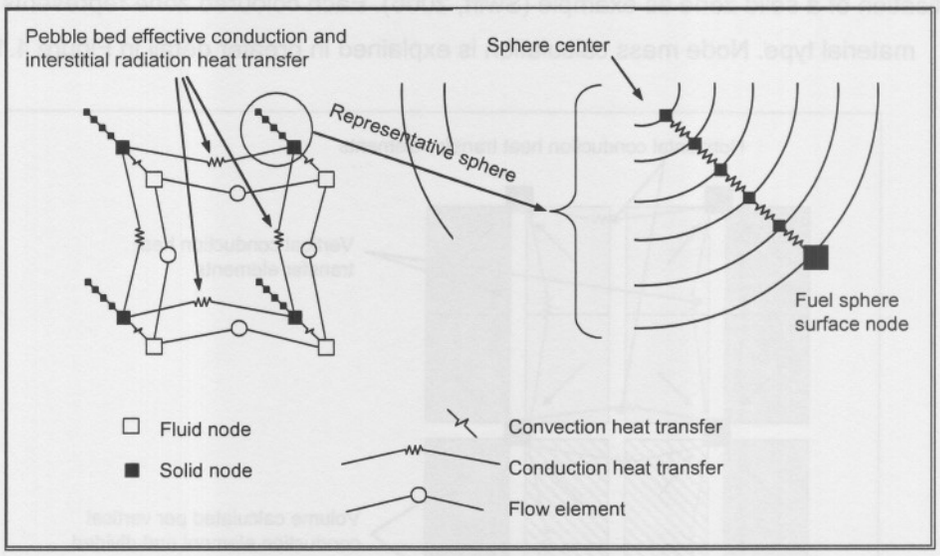


Figure 4.12. The network topology for a single *Pebble Bed* zone.

When assembled together with *Solid* zones, the topology in Figure 4.13 is created.

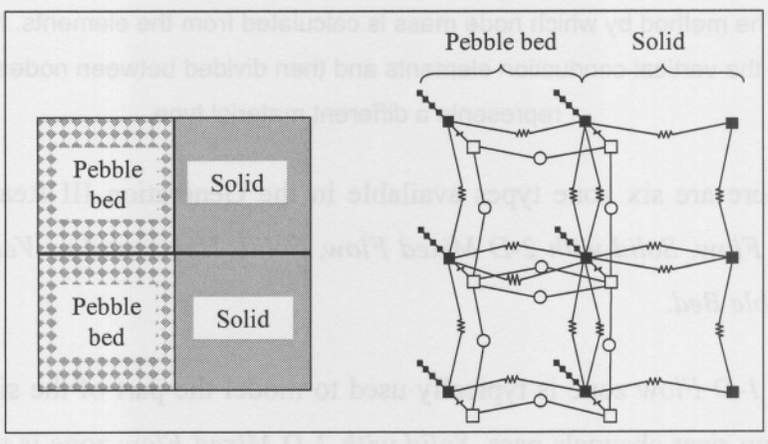


Figure 4.13. The network topology of assembled *Pebble Bed* and *Solid* zones, as it occur at the pebble bed/side reflector interface.

The *Single cavity* zone, *Solid* zone, *Solid with 1-D Vertical Flow* zone, as well as the *Horizontal cavity* network topology are shown in Figure 4.14. Radiation elements are placed across open cavities such as the *Horizontal cavity* and the *Single cavity* while the convection heat transfer coefficient is calculated with the Dittus-Boelter equation for turbulent flow or with a fixed heat transfer coefficient. The pressure drop in the *Horizontal cavity*, as well as in the *Solid with 1-D* Flow zones is calculated with the Darcy-Weisbach friction factor.

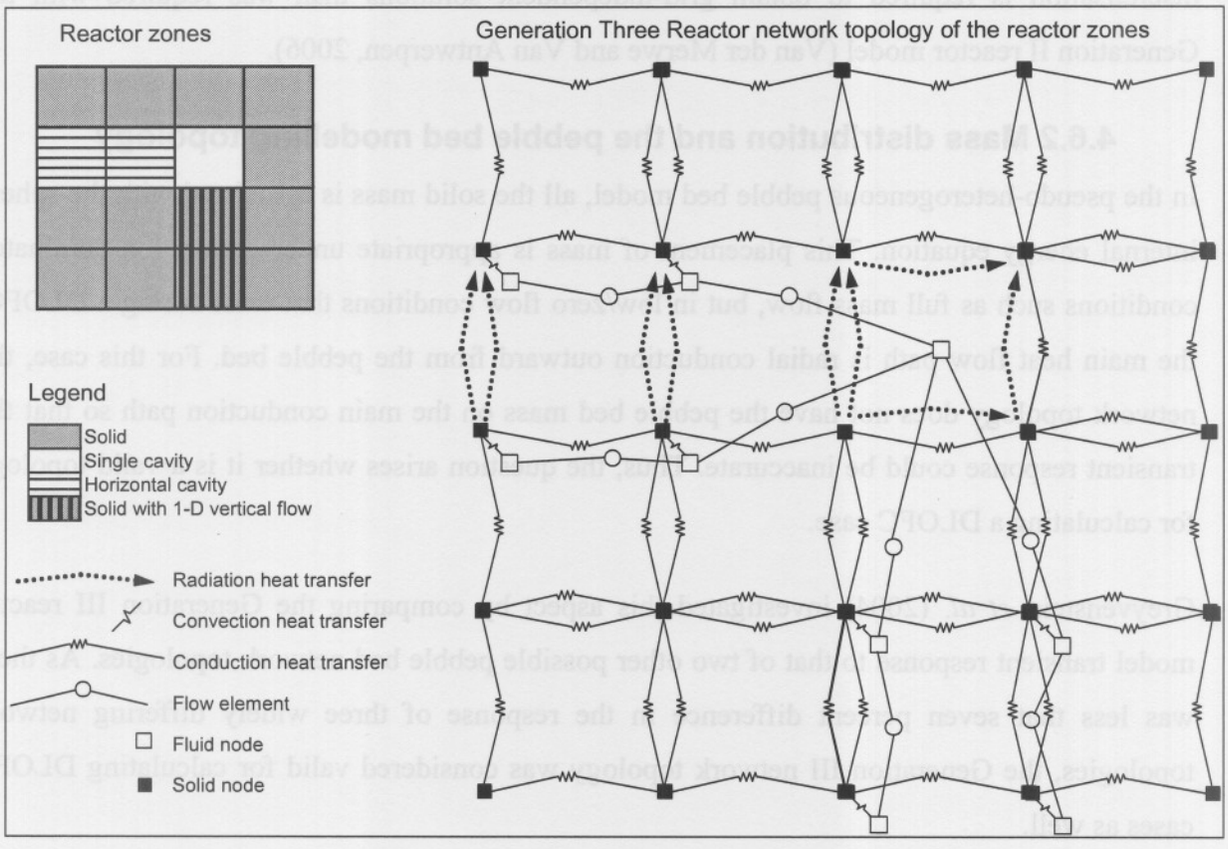


Figure 4.14. A typical combination of zones encountered in the solids around a pebble bed reactor core, with the Generation III network layout.

4.6 Properties of the Generation III Reactor model discretisation

Some of the capabilities of the Generation III reactor model came at the expense of accuracy in another area, as is the case with the convection discretisation. In other areas, such as the pseudo-heterogeneous pebble bed network topology, there had been some uncertainty with regard to the appropriateness of the approach. All these issues follow directly from the network topology chosen to represent the reactor.

4.6.1 Convection discretisation

As the Generation III reactor model was required to calculate full mass flow conditions (unidirectional flow in the pebble bed) as well as natural circulation that occurs during low/zero mass flow (multidirectional flow in the pebble bed), it could not use the same directionally-biased convection discretisation scheme used in the Generation II reactor model (described in Section 4.3.2). With the Generation III reactor model it was found that a finer pebble bed discretisation is required to obtain grid-independent solutions than was required with the Generation II reactor model (Van der Merwe and Van Antwerpen, 2006).

4.6.2 Mass distribution and the pebble bed modelling topology

In the pseudo-heterogeneous pebble bed model, all the solid mass is associated with the sphere internal energy equation. This placement of mass is appropriate under convection-dominated conditions such as full mass flow, but in low/zero flow conditions that exist during a DLOFC, the main heat flow path is radial conduction outward from the pebble bed. For this case, the network topology does not have the pebble bed mass on the main conduction path so that the transient response could be inaccurate. Thus, the question arises whether it is a valid topology for calculating a DLOFC case.

Greyvenstein *et al.* (2004) investigated this aspect by comparing the Generation III reactor model transient response to that of two other possible pebble bed network topologies. As there was less that seven percent difference in the response of three widely differing network topologies, the Generation III network topology was considered valid for calculating DLOFC cases as well.

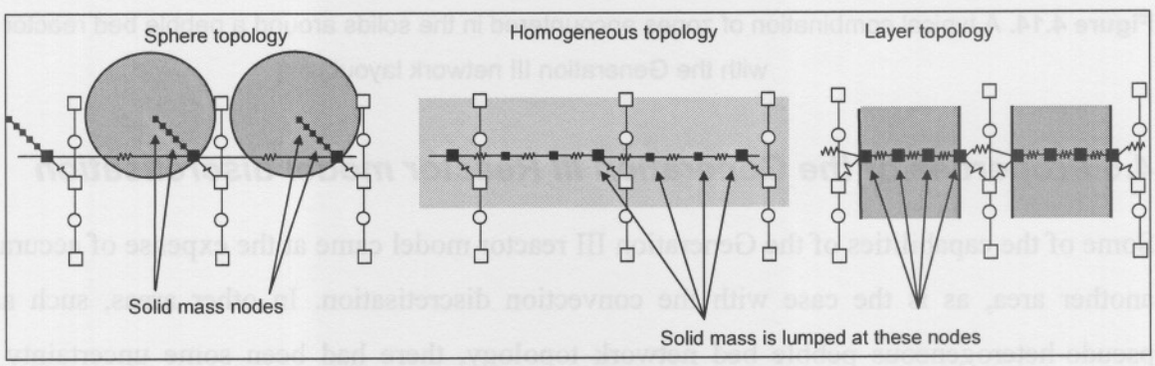


Figure 4.15. Pebble bed topologies that were used to test the transient response validity, as calculated with the Generation III network topology, referred to as the "sphere topology" in this figure.

It must also be kept in mind that an actual DLOFC transient happens over a much longer time than the step temperature change with which transient response of numerical methods is typically tested. Details of the work by Greyvenstein *et al.* (2004) can be found in Appendix B.

4.6.3 Artifical natural circulation paths

As shown in Figure 4.14 and Figure 4.16, a *Solid with 1-D Flow* zone creates two flow elements as the nodes are created at the zone edges. But as these paths are connected to one node at a single cavity, a vertical channel such as the flow riser channels in the side reflector, or the control rod holes will be represented by two parallel flow paths.

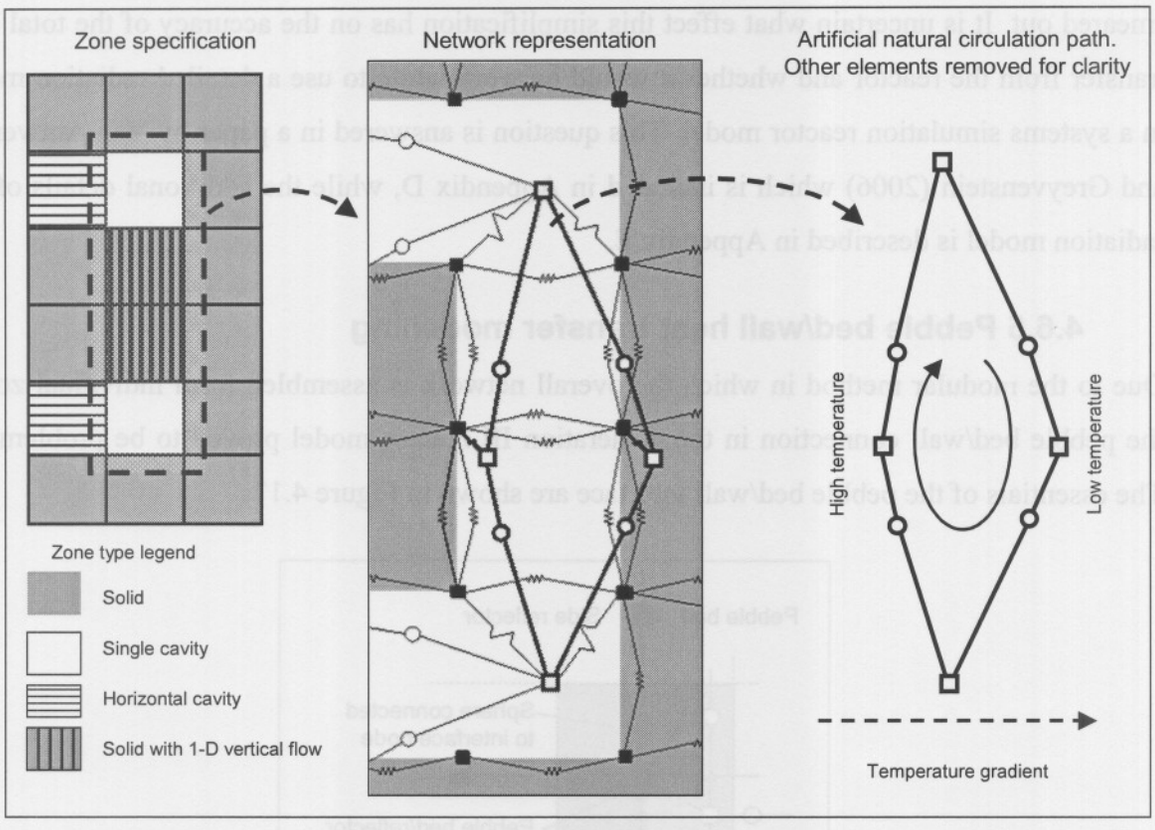


Figure 4.16. An illustration of the creation of artificial natural circulation paths in the Generation III reactor model topology for *Solid with 1-D Flow*.

This causes no problems at full mass flow, but during low/zero mass flow, there is a temperature gradient across these zones so that a density-driven natural circulation cell develops. These natural circulation cells can be very difficult to solve as the flow rate and heat transfer are interdependent and sometimes inherently oscillatory. This means that natural convection can cause great convergence problems, thereby severely slowing down a simulation.

This has to be avoided at all cost, especially if the circulation cell is artificially created as is the case with the *Solid with 1-D Flow* zone.

4.6.4 Radiation heat transfer modelling

As illustrated in Figure 4.14, only radiation heat transfer between directly opposing surfaces is modelled. Due to the geometry being axi-symmetrical and the fact that opposing surfaces frequently have the same area, the view factor is fixed at unity.

This method of modelling radiation heat transfer would transfer the temperature profile on one side of a cavity directy to the other side of a cavity, while in reality, the temperature profile is smeared out. It is uncertain what effect this simplification has on the accuracy of the total heat transfer from the reactor and whether it would be worthwhile to use a detailed radiation model in a systems simulation reactor model. This question is answered in a paper by Van Antwerpen and Greyvenstein (2006) which is included in Appendix D, while the additional details of the radiation model is described in Appendix E.

4.6.5 Pebble bed/wall heat transfer modelling

Due to the modular method in which the overall network is assembled from individual zones, the pebble bed/wall connection in the Generation III reactor model proved to be problematic. The essentials of the pebble bed/wall interface are shown in Figure 4.17.

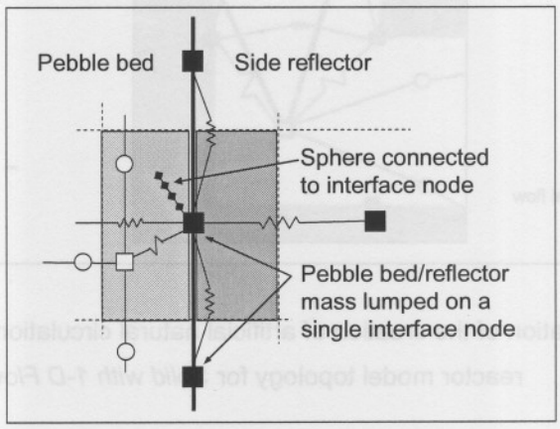


Figure 4.17. The Generation III network topology at the pebble bed/wall interface.

The solid node placed at the bed/wall interface gets half its volume from the reflector and the other half of its volume from the pebble bed. This negates the fact that there is a distinct thermal resistance between the pebble bed and the wall, as observed by many researchers (IAEA, 2000).

The possibility to specify a bed/wall "effective contact resistance" heat transfer coefficient, as well as a fluid/wall heat transfer coefficient, should be provided. With the present topology, great effort has to be made to match calculation results with experimental results as demonstrated by Van der Merwe (2005), as well as Van der Merwe and Van Antwerpen (2006).

4.6.6 Sphere discretisation

In the Generation III reactor, the representative fuel spheres are modelled with conduction elements that assume linear area variation along the radius, while the actual area variation is quadratic. This leads to a mass distribution between nodes that was found to require about ten sphere subdivisions to get a grid-independent average temperature transient response. As the number of nodes per sphere is multiplied by the number of pebble bed zones in the reactor, the sphere model is the greatest single contributor to the number of nodes in the reactor.

Therefore, any accuracy increase in the modelling of the fuel spheres will result in less nodes per sphere that will in turn have a significant impact on the total number of nodes in the reactor model. As solution speed is directly proportional to the number of nodes in the reactor, an increase in sphere accuracy will directly result in faster simulations. Therefore, this area of research is expected to yield the greatest improvement in solution speed.

4.7 Alternative network topologies

As shown in the preceding paragraphs, the most important properties of the Generation III reactor model follow from the element-based approach, used to assemble the calculation network.

An alternative to the "element-based" network discretisation of the Generation III reactor model is the so-called "control-volume based" approach in which a node is placed in the center of each control volume. Node volumes are directly calculated analytically and heat and fluid flow elements are inserted afterwards, according to the local situation. Du Toit *et al.* (2003) demonstrated that, for a two-dimensional porous flow domain, the "control-volume based" approach is equivalent to the staggered-grid approach in CFD. As shown in Figure 4.9, flow elements represent convective fluxes across control volume boundaries and for energy conservation, the elements represent heat fluxes (i.e. conduction or convection) across control volume boundaries.

With the element-based approach, the domain had half control volumes at edges, while the control-volume based approach resulted in full control volumes at edges, as shown in Figure 4.18.

In order to accurately specify or calculate boundary temperatures in the control-volume based discretisation, it is necessary to have nodes at the domain edges. In many simulation codes, all nodes are assumed to have mass, as the solution methods in explicit time discretisation require all nodes to have nonzero mass.

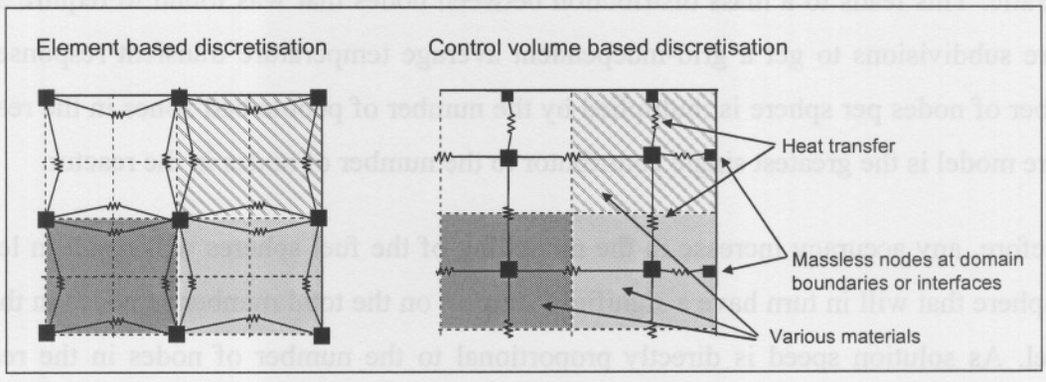


Figure 4.18. Methods of dealing with change in material properties across control volumes, using the discretisation of a solid zone as example.

However, this is not the case in *Flownex*, which uses a fully implicit time discretisation scheme. Therefore, it is possible to use massless nodes for boundary temperature specification or to find the temperature at an interface as illustrated in Figure 4.18. This capability is a particular advantage in modelling the pebble bed/wall interface and radiation heat transfer in cavities. It was, however, not used in the Generation III reactor model as nodes were placed at the control volume boundaries.

As shown in Figure 4.18, the control-volume based scheme requires composite flow elements to deal with changes in zone properties. While this issue is resolved in CFD by simply refining the grid near interfaces, it is not desirable in a system simulation code as grid refinement slows down the simulation. These composite heat flow elements for the control-volume based approach are discussed in the following section, together with the radiation heat transfer elements.

The control-volume based approach and its composite elements form part of a new discretisation approach which has been developed for this study. The new reactor model based on this approach is referred to as the Generation IV reactor model.

The motivation for deriving this approach was to gain insight into the effect of discretisation method on calculation result and to determine whether the control-volume based approach was more useful than the element-based approach. The rationale is that one will be able to distinguish the effects of discretisation method from physical fundamentals when the same case is calculated with both the element-based approach and the control-volume based approach.

Anticipated benefits of the control-volume based approach are expected to be a slight increase in calculation speed, as well as avoiding artificial natural circulation paths as described in Paragraph 4.6.3. The increase in calculation speed is expected from the fact that composite elements halve the number of elements necessary to handle material property discontinuities and, therefore, also the bookkeeping. The control-volume based Generation IV reactor model will also be useful as a benchmark for the Generation III reactor model.

4.8 Fluid and heat flow elements for control-volume based discretisation

4.8.1 Composite flow element

The first requirement to implement the control-volume based discretisation is to have a composite flow element to deal with changes in zone type. It is called a composite element as its flow characteristic are a combination of the pressure drop characteristics of the two types of zones it connects. As shown in Figure 4.19, a composite element is necessary to connect nodes across a change in zone type, such as a transition from a solid with flow channels to a porous medium, or from a cavity to a pipe bundle. This was no issue with the element-based discretisation, as nodes were placed at the interfaces and elements never crossed interfaces.

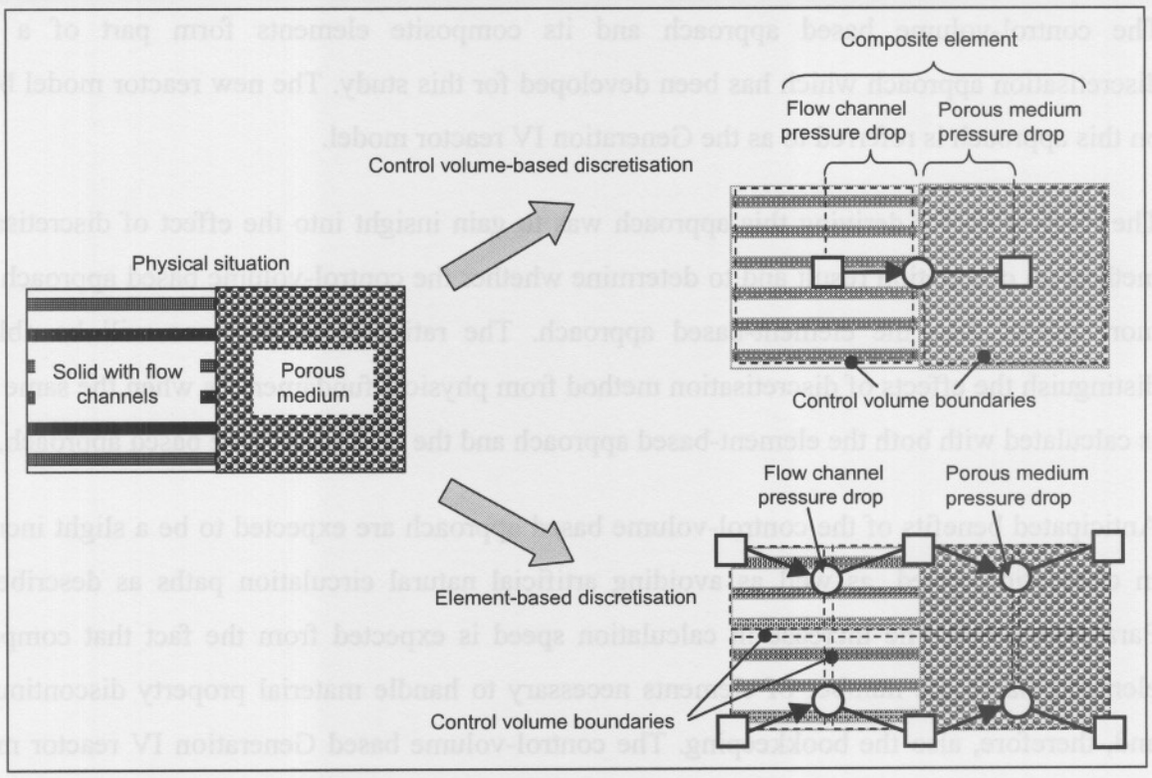


Figure 4.19. Discretisation of the flow path at an interface, according to the control-volume based and the element-based approaches.

In the composite flow element, the pressure drop coefficient is built up from two parts to deal with the possible discontinuity across two control volumes. The discretised momentum conservation equation is the same for the radial and axial direction, while the radial geometry is taken into account by the different inlet and outlet areas of the element, as shown in Figure 4.20.

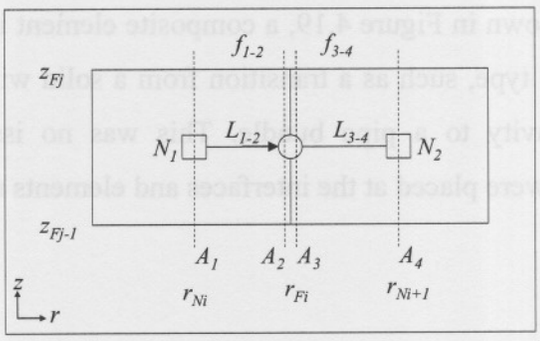


Figure 4.20. Graphic description of some composite flow element inputs in axially symmetric coordinates.

With some of the symbols illustrated in Figure 4.20, the various areas are calculated with Eq.(4.10).

$$
\begin{aligned}
A_1 &= \varepsilon_1 2\pi r_{Ni}\left(z_{Fj} - z_{Fj-1}\right) \\
A_2 &= \varepsilon_1 2\pi r_{Fi}\left(z_{Fj} - z_{Fj-1}\right) \\
A_3 &= \varepsilon_2 2\pi r_{Fi}\left(z_{Fj} - z_{Fj-1}\right) \\
A_4 &= \varepsilon_2 2\pi r_{Ni+1}\left(z_{Fj} - z_{Fj-1}\right)
\end{aligned}
\tag{4.10}
$$

The subscripts N and F refer to node and face respectively, while ϵ denotes the porosity or permeability of the control volume and i is the radial control volume index.

The flow resistance force B in Eqs.(4.4) and (4.5) for this element is given by

$$
\begin{aligned}
B = \frac{1}{2}\rho_{1-2}\left(\frac{f_{1-2}\left(\left|\bar{V}_{N1}\right|\right)\forall_{1-2}}{D_{h1-2}}\right)\left|u_{1-2}\right|u_{1-2}\varepsilon_{1-2} \quad &+\frac{1}{2}\rho_{3-4}\frac{f_{3-4}\left(\left|\bar{V}_{N2}\right|\right)\forall_{3-4}}{D_{h3-4}}\left|u_{3-4}\right|u_{3-4}\varepsilon_{3-4} \\
+\frac{1}{2}K_1\rho_1\left|u_1\right|u_1\varepsilon_1 A_1 \quad &+\frac{1}{2}K_{23}\rho_2\left|u_2\right|u_2\varepsilon_2 A_2 \quad +\frac{1}{2}K_4\rho_4\left|u_4\right|u_4\varepsilon_4 A_4
\end{aligned}
\tag{4.11}
$$

with f representing the friction factor. D_h and $\forall$ are the hydraulic diameter and the volume of a flow element section respectively, denoted by subscripts *1-2* or *3-4*. K_1 and K_4 are the loss coefficients at the inlet and outlet of the flow element, while K_{23} pertains to possible area change loss at the interface between sections 1 and 2. For reverse, as well as forward flow, this loss coefficient is based on the velocity at A_2, referring to Figure 4.20.

It is important to note that the friction factor f in Eq.(4.11) is a function of Reynolds number and that the magnitude of the absolute velocity $\left|\bar{V}\right|$ must be used when calculating f. The value of $\left|\bar{V}\right|$ is evaluated at the nearest node, which is either node 1 or node 2 in Figure 4.20. For porous flow, the expressions in Eq.(4.11) are simplified and will be discussed in greater detail in Section 5.5.

The vector-valued absolute velocity $\bar{V}$ on nodes is calculated from all the flow elements connected to a node. On each pebble bed flow element, the average of adjacent node velocities is used to calculate the Reynolds number. The approximation of using such compounded averaging is considered adequate, as the Reynolds number only has a second-order effect on the flow resistance calculation accuracy.

4.8.2 Composite solid conduction element

For implementing the control-volume based discretisation, conduction heat transfer also requires a composite heat transfer element to deal with material type changes at interfaces, as shown in Figure 4.21.

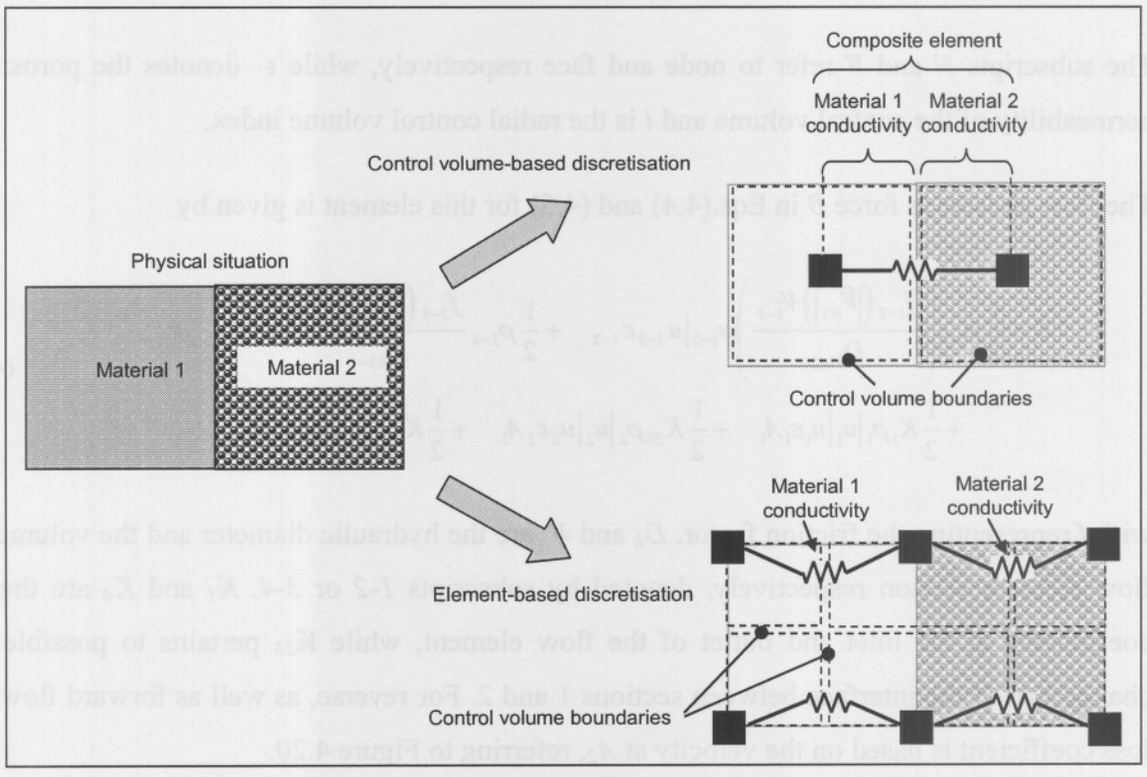


Figure 4.21. Discretisation of the heat flow path at an interface, according to the control-volume based and the element-based approaches.

The heat resistance of a composite conduction element is thus assembled from the material properties of the control volumes it connects. This is accomplished by calculating the conductivity k and conduction shape factor F for each of the element parts separately as shown in Figure 4.22.

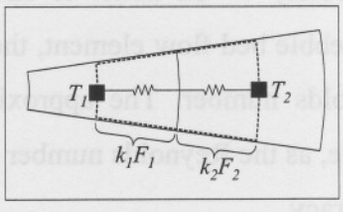


Figure 4.22. Illustration of the symbols for heat flux calculation between two control volumes.

The thermal resistance for the heat path between nodes 1 and 2 will then be given by

$$R_{tot} = \frac{1}{k_1 F_1} + \frac{1}{k_2 F_2} \tag{4.12}.$$

It was found that Eq.(4.12) is not necessarily the most accurate way to calculate the heat resistance across an interface. For an investigation into methods of calculating the heat resistance, the average conductivity k_{ave} is defined so that R_{tot} is given by

$$\frac{1}{R_{tot}} = \frac{k_{ave}}{\frac{1}{F_1} + \frac{1}{F_2}} \tag{4.13}.$$

A first method to be investigated is calculating k_{ave} at the average temperature of the two control volumes, as shown in Figure 4.23.

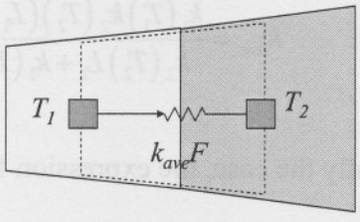


Figure 4.23. Conduction heat transfer topology for using conductivity at average temperature.

$$k_{ave} = k\left(\frac{T_1 + T_2}{2}\right) \tag{4.14}$$

This first method will be referred to as the "one-block" scheme for conductivity, denoted by *1B*. Another method will be referred to as the "two-block" scheme for conductivity (denoted by *2B*) because the conduction element is divided into two geometrical regions, each associated with the conductivity of its control volume, as shown in Figure 4.24. For this method the total heat resistance is given by Eq.(4.15)

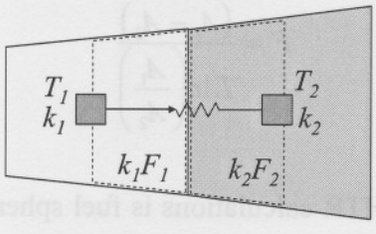


Figure 4.24. Conduction heat transfer topology for using conduction resistances in series.

Error! Objects cannot be created from editing field codes. (4.15)

The third method for variable conductivity presented in Patankar (1980), does take geometry into account by means of length-weighted averaging. The implementation is similar to the one-block scheme for conductivity, but with the average conductivity given by Eq.(4.16), as shown in Figure 4.25.

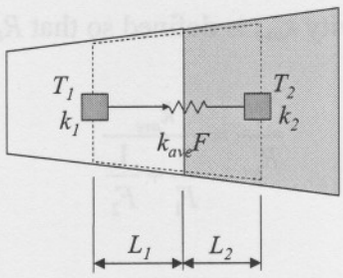


Figure 4.25. Conduction topology for using the weighted average for conductivity.

$$k_{ave} = \frac{k_1(T_1)k_2(T_2)(L_1+L_2)}{k_2(T_2)L_1 + k_1(T_1)L_2} \tag{4.16}$$

If $L_1 \approx L_2 = L$, which is frequently the case, the expression for k_{ave} simplifies to:

$$k_{ave} = \frac{2k(T_1)k(T_2)}{k(T_2)+k(T_1)} \tag{4.17}$$

This method for conductivity is referred to in this document as the weighted method, denoted by *w*.

In order to assess the grid dependence of these methods, heat flow is simulated through a trapezoidal conducting body made of the same material as the PBMR fuel spheres. In order to isolate the effect of the conductivity scheme, an analytical form factor is used. It can be shown that the form factor for a trapezoid with face areas A_1 and A_2 and length L is given by

$$F = \frac{(A_1 - A_2)}{L\ln\left(\frac{A_1}{A_2}\right)} \tag{4.18}.$$

A representative material for HTR calculations is fuel sphere graphite, for which the following material conductivity polynomial was used, as found in Van Rensburg (2003):

$$k(T) = (-8.9452e-10)T^3 + (5.5014e-6)T^2 + (-1.4127e-2)T + 30.018 \quad [W/mK] \tag{4.19}$$

with temperature in Kelvin. The temperature range for the conductivity test is 500°C to 1400°C, i.e. ΔT= 900K. The direction of the temperature gradient was switched to test for anisotropy, i.e. whether the combination A_1(500°C)/A_2(1400°C) gave the same heat flux as A_1(1400°C)/A_2(500°C). The geometry and grid divisions shown in Figure 4.26 were used for the grid-dependence study. Even though the discretisation in Figure 4.26 has half control volumes at the ends, it applies to the question of conduction discretisation at hand. The elements connecting the control volumes still have to take varying conductivity and area into account.

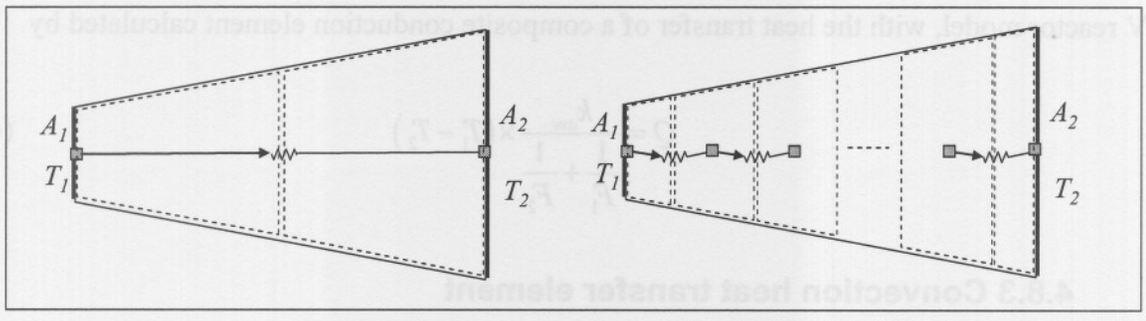


Figure 4.26. Geometry used for studying the contribution of varying conductivity to grid dependence. The grid on the left has one subdivision and the one the right shows the general subdivision scheme.

The grid-dependence study results of the various methods are shown in Figure 4.27.

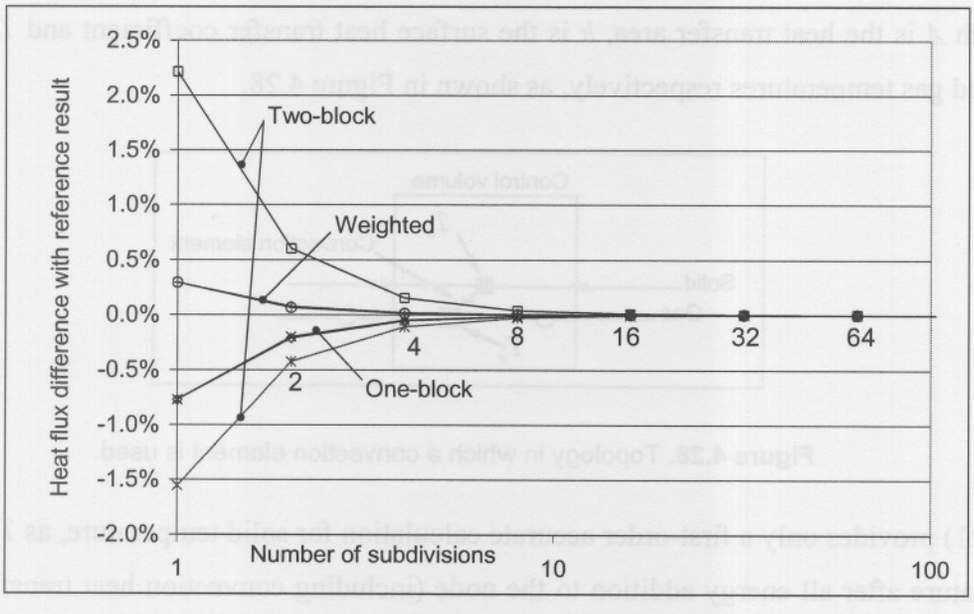


Figure 4.27. Grid dependence attributed to temperature dependent conductivity. The grid-independent result of all cases are equal and are used as reference.

The most striking feature of the grid-dependence test is that the two-block scheme is anisotropic when a coarse grid is used, i.e. the heat flow for the combination A_1(500°C)/A_2(1400°C) is not equal to the heat flow for the combination A_1(1400°C)/A_2(500°C). Overall, it is seen that the error introduced by discretisation of temperature-dependent conductivity is reasonably small, less than 2.5 percent for the two-block method.

The one-block scheme is isotropic, but still displays more grid dependence than the weighted method. The weighted method for conductivity is isotropic and requires the least grid refinement to reach a certain accuracy. This method will, therefore, be used for the Generation IV reactor model, with the heat transfer of a composite conduction element calculated by

$$Q = \frac{k_{ave}}{\frac{1}{F_1} + \frac{1}{F_2}} \times \left(T_1 - T_2\right) \tag{4.20}$$

4.8.3 Convection heat transfer element

Heat transfer between solids and fluid in a control volume is managed by the convection heat transfer element, as described by

$$Q = hA\left(T_s - T_g\right) \tag{4.21}$$

in which A is the heat transfer area, h is the surface heat transfer coefficient and T_s and T_g are solid and gas temperatures respectively, as shown in Figure 4.28.

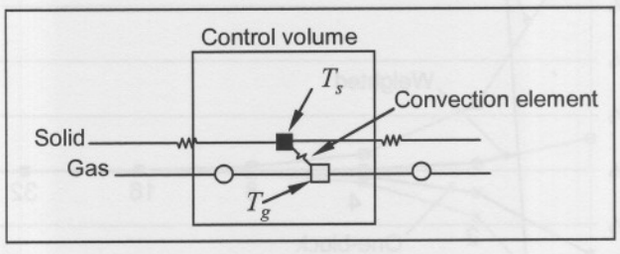


Figure 4.28. Topology in which a convection element is used.

Eq.(4.21) provides only a first-order accurate calculation for solid temperature, as T_g is the node temperature after all energy addition to the node (including convection heat transfer) has been taken into account. The refinement of this element is described in Section 6.3.

The heat transfer coefficient is found from correlations for the dimensionless temperature gradient or Nusselt number. The Nusselt number is usually a function of Reynolds number,

hydraulic diameter and fluid properties, which are found from the gas node as described for the composite flow element in Section 4.8.1.

The Nusselt number correlation is determined by the geometry of the flow path, such as round flow channels or a porous medium. For round flow channels through a solid, the Dittus-Boelter correlation for the turbulent flow is used, while the Kugeler-Schulten correlation (described in Section 5.6) is used for calculating the heat transfer coefficient in the pebble bed.

4.8.4 Radiation elements

Radiation heat transfer is an important mode of heat transfer in HTRs due to the high operating temperatures, as well as the fact that during a Loss Of Forced Cooling event, heat is radiated from the graphite reflector to the core barrel and from there again to the Reactor Pressure Vessel.

For calculating radiation heat transfer in the reactor, diffuse radiation, grey surfaces and a non-participating gas are assumed. Gas interaction with radiation heat transfer can be neglected in HTRs due to the helium working fluid. For a gas molecule to interact with electromagnetic radiation, it has to have an electrostatic charge distribution as is the case with polar molecules such as CO_2 or H_2O. As this is not the case with non-polar molecules such as N_2 or monatomic molecules such as helium, they do not interact with radiation heat transfer.

Note that radiation heat transfer across interstitial spaces in the pebble bed is not treated explicitly, but is included in the Zehner-Schlünder correlation for pebble bed effective conductivity which is described in Section 5.8.1. Rather, radiation is calculated only across cavity zones.

The standard method to calculate radiation heat exchange between multiple surfaces, namely the "electrical resistance network method", is efficiently implemented in *Flownex* by the placement of massless nodes on control-volume surfaces around cavities, as illustrated in Figure 4.29.

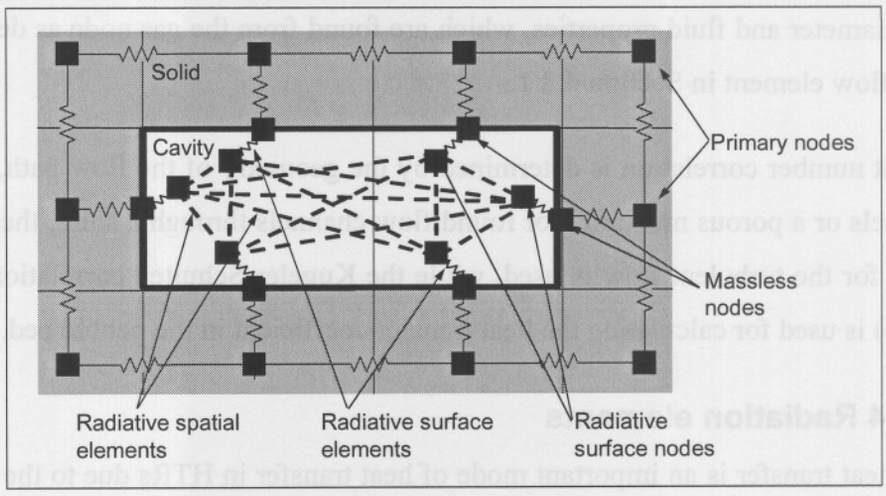


Figure 4.29. Topology of the radiation and conduction network around a cavity.

An additional node is placed on each surface to represent the effective spatial temperature T_{sp} (Incropera and DeWitt, 1996). This would be the temperature at which the environment perceives the surface to be, while the actual temperature T is different, depending on emissivity ε and the area A. The relation between actual temperature T and perceived or spatial temperature T_{sp} is described by the equation

$$Q = \frac{\sigma \varepsilon A}{1-\varepsilon}\left(T^4 - T_{sp}^4\right) \tag{4.22}$$

where Q is heat transfer. In Figure 4.29, the connections between the radiative surface nodes are the radiative spatial elements, of which the heat transfer is calculated by Eq.(4.23)

$$Q_{sp,ij} = A_i F_{ij} \sigma \left(T_{sp,i}^4 - T_{sp,j}^4\right) \tag{4.23}$$

The view factor F_{ij} is defined as the fraction of radiation leaving surface i that is intercepted by surface j. It can also be described as the fraction surface j occupies of the total view from surface i. The mathematical definition is given by the following integral (Incropera and DeWitt, 1996):

$$F_{12} = \int_{A_1}\int_{A_2} \frac{\cos\theta_1 \cos\theta_2}{\pi r_{12}^2} dA_2 dA_1 \tag{4.24}$$

with r_{12} being the distance between dA_1 and dA_2 and θ_1 and θ_2 being the angles between r_{12} and normal vectors on the surfaces of dA_1 and dA_2. All the variables are shown in Figure 4.30.

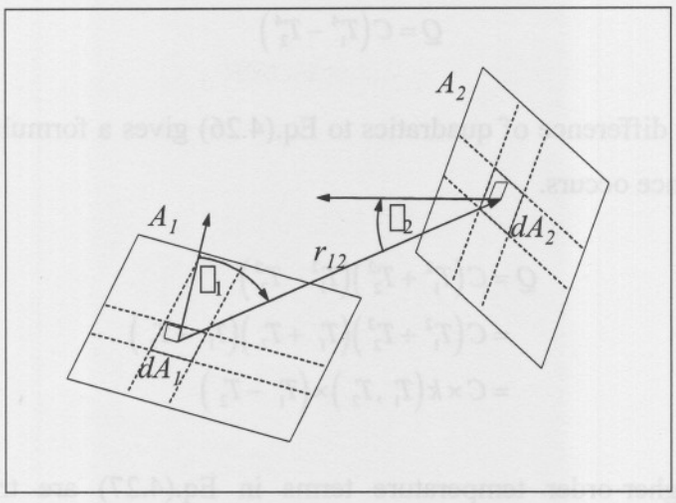


Figure 4.30. Illustration of the view factor integral variables.

Despite the difficulty of analytically evaluating the integral in Eq.(4.24), many view factors have been evaluated and were compiled by Howell (2001) into a numbered view factor catalogue that is available on the Internet. The view factors for axi-symmetric cylindrical geometry used in this study are derived from a paper by Brockmann (1994) and are described in detail in Appendix D.

When there are only two surfaces in an enclosure, all heat leaving one surface is taken up by the other, so that Eqs(4.22) and (4.23) can be combined to obtain the following well-known expression (Incropera and DeWitt, 1996):

$$Q_{12} = \frac{\sigma\left(T_1^4 - T_2^4\right)}{\frac{1-\varepsilon_1}{\varepsilon_1 A_1} + \frac{1}{A_1 F_{12}} + \frac{1-\varepsilon_2}{\varepsilon_2 A_2}} \tag{4.25}$$

For multiple surfaces exchanging radiation, summation of the heat flows to and from temperature points results in a system of equations that has to be solved simultaneously with all the other nodes and elements in the reactor model.

Directly solving in terms of temperatures raised to the fourth power is not possible as matrix solution methods require linear relationships. Therefore the radiation spatial and radiation surface element equations ((4.22) and (4.23)) are linearised by using the characteristic that the general form of the radiation heat transfer equations consists of some constant C, multiplied by the difference of temperatures raised to the fourth power.

$$Q = C\left(T_1^4 - T_2^4\right) \tag{4.26}$$

Twice applying the difference of quadratics to Eq.(4.26) gives a formula in which a first-order temperature difference occurs.

$$\begin{aligned} Q &= C\left(T_1^2 + T_2^2\right)\left(T_1^2 - T_2^2\right) \\ &= C\left(T_1^2 + T_2^2\right)\left(T_1 + T_2\right)\left(T_1 - T_2\right) \\ &= C \times k\left(T_1, T_2\right) \times \left(T_1 - T_2\right) \end{aligned} \tag{4.27}$$

The remaining higher-order temperature terms in Eq.(4.27) are treated as temperature-dependent conductivity $k\left(T_1, T_2\right) = \left(T_1^2 + T_2^2\right)\left(T_1 + T_2\right)$, while the complex spatial radiation network is treated as a conduction network. This approach is used in *Flownex* and TINTE (Gerwin and Scherer, 2001).

4.9 Network topologies for control-volume types

The use of abovementioned elements at control volume-level is now illustrated with some examples. The same six basic zone types that are used in the Generation III reactor model are used for the reactor model in this study, namely: Solid, Solid with one-dimensional flow, Solid with two-dimensional mixed flow, Horizontal or vertical flow cavity, Single cavity and Pebble bed.

4.9.1 Solid

This zone is the most common in the pebble bed reactor model. It consists simply of a solid node connected with composite conductive elements to adjacent solid nodes.

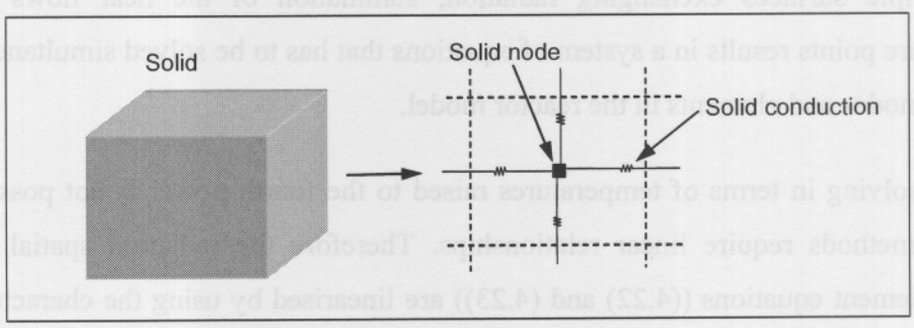


Figure 4.31. Network representation of a solid type control volume.

4.9.2 Solid with one-dimensional flow

A control-volume type that illustrates the network approach very well is "solid with one-dimensional flow". Solid material, with flow passages passing through it, is typically encountered at the coolant riser channels in the side reflector or at control rod channels. Because of the pipe geometry of the flow channels, the Darcy-Weisbach correlation is used for calculating pressure drop, while the Dittus-Boelter correlation or a fixed heat transfer coefficient is used in the convection heat transfer between solid and fluid nodes. For the solid conduction along the flow channel direction, the area is reduced with a permeability factor, while a conduction form factor is used to account for the reduced conduction area in the transverse direction due to the presence of the flow channel. In this way, geometrical detail is taken into account without adding complexity to the solution. The network topology for this control-volume type is as shown in Figure 4.32.

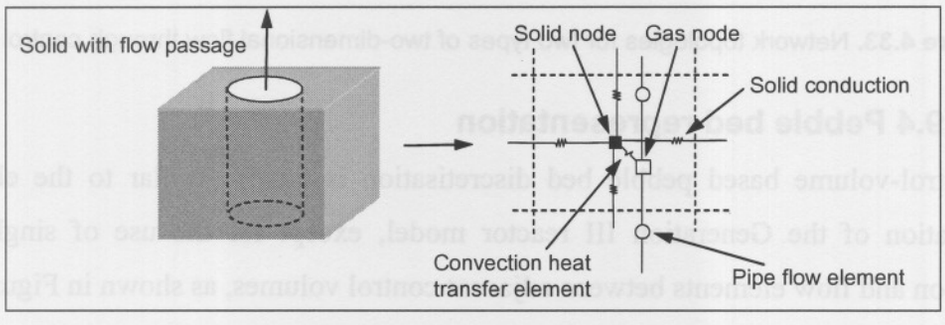


Figure 4.32. Nodes and elements used to represent a solid with one-dimensional flow through it.

4.9.3 Solid with two-dimensional mixed flow

Two situations arise, namely mixed flow and unmixed flow. A mixed flow zone is useful to create bends and channel junctions in the computer-generated discretisation of the reactor.

Unmixed two-dimensional flow is encountered where the control rods channels pass between the horizontal flow channels, connecting the pebble bed cavity and the vertical coolant flow channels. The network topologies are shown in Figure 4.33.

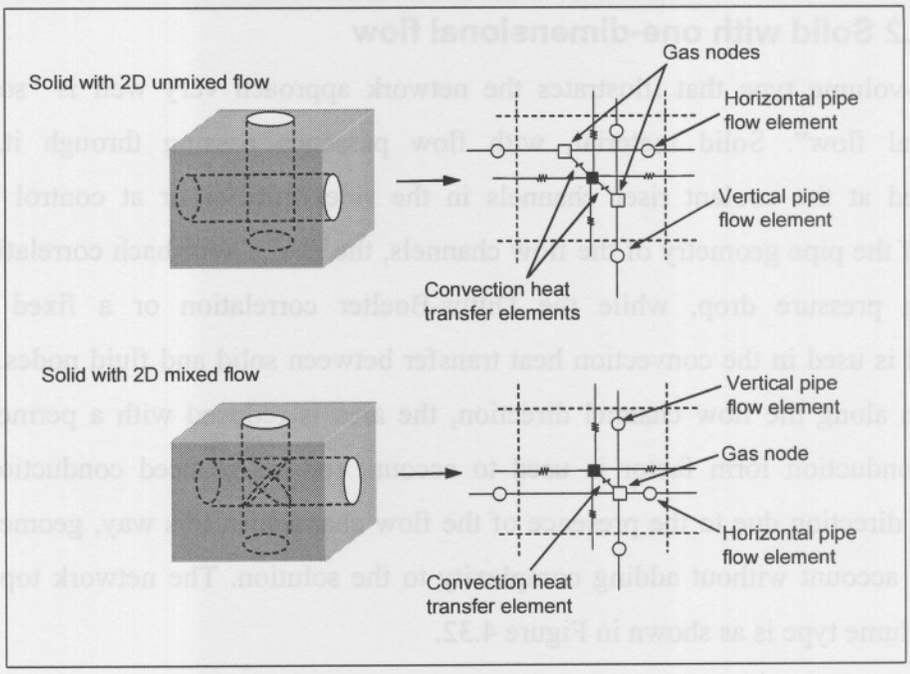


Figure 4.33. Network topologies for two types of two-dimensional flow through control volumes.

4.9.4 Pebble bed representation

The control-volume based pebble bed discretisation is nearly similar to the element-based discretisation of the Generation III reactor model, except for the use of single composite conduction and flow elements between adjacent control volumes, as shown in Figure 4.34.

The analysis of Greyvenstein *et al.* (2004) of the validity of the bed-discretisation also holds for the control-volume based pebble bed discretisation, as discussed in Section 4.6.2.

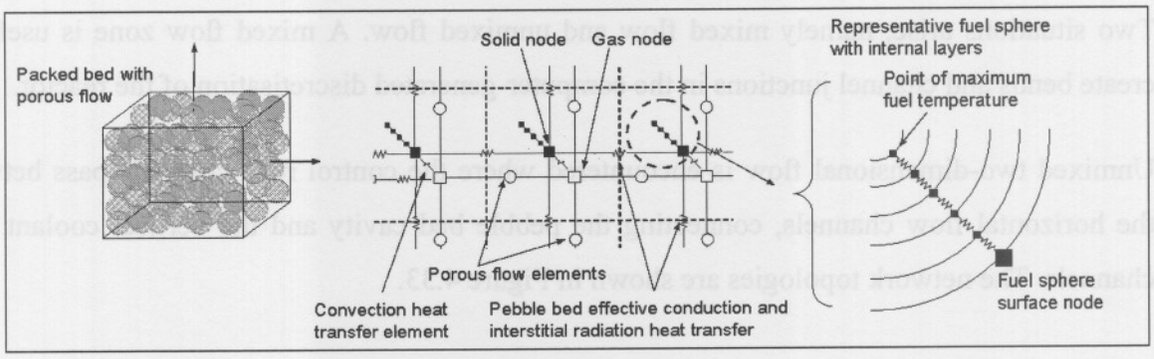


Figure 4.34 Assembly of nodes and elements representing a pebble bed zone.

4.9.5 Pebble bed/wall interface

In the pseudo-homogeneous pebble bed models as described in the VDI Wärmeatlas (Tsotsas, 2002), the solid and gas in the pebble bed were represented by a single energy equation which

used a wall heat transfer coefficient from a correlation such as the one by Martin and Nilles (1993). In contrast, the pseudo-heterogeneous pebble bed model created by Du Toit *et al.* (2003) requires separate pebble bed/wall and fluid/wall correlations. On this point, the following paragraphs will point out that the pseudo-heterogeneous pebble bed model has not been consistently implemented in the Generation III reactor model.

The pseudo-heterogeneous mathematical model for the solid part of the pebble bed assumes it to be a microscopically homogeneous solid, i.e. it is homogeneous and porous right up to the reflector wall, so that the thermal resistance between the pebble bed and the wall is described by a contact-resistance heat transfer coefficient. Similarly, the pebble bed fluid exchanges heat with the wall through a heat transfer coefficient.

Therefore, the most obvious improvement to the current Generation III reactor model would be to separate the pebble bed and reflector nodes and add appropriate elements to obtain the topology in Figure 4.35.

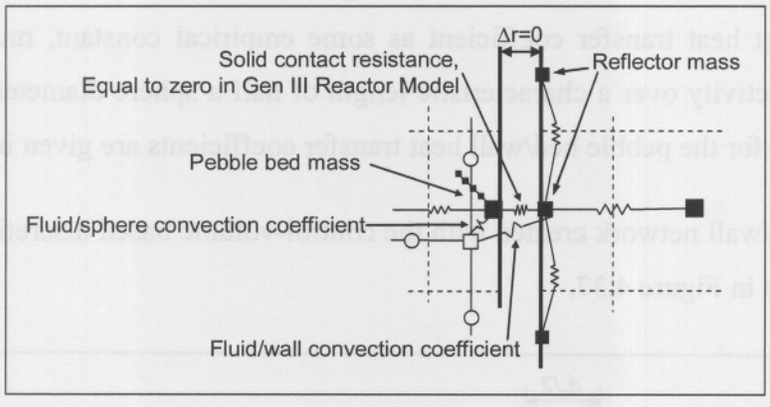


Figure 4.35. A first alternative pebble bed/wall topology for the Generation III reactor model.

In terms of the above discussion, the pebble bed/wall topology for the control-volume based discretisation should be as shown in Figure 4.36.

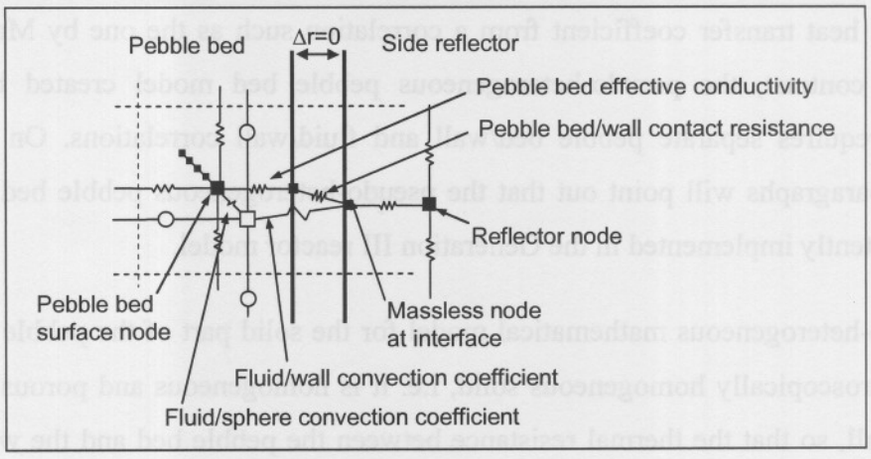


Figure 4.36. The pebble bed/wall topology for the control-volume based discretisation, assuming a homogeneous porous solid up to the wall.

However, the assumption of a homogeneous porous solid breaks down within one half sphere diameter from the wall. Therefore, it makes physical sense for the control volume at the wall to have a dimension of one sphere diameter, so that its sphere surface node is located at half a sphere diameter from the wall. For this configuration it is convenient to define the pebble bed/wall contact heat transfer coefficient as some empirical constant, multiplied by the bed effective conductivity over a characteristic length of half a sphere diameter. Further details on the correlations for the pebble bed/wall heat transfer coefficients are given in Section 6.4.

The pebble bed/wall network created with the control-volume based discretisation thus have the topology shown in Figure 4.37.

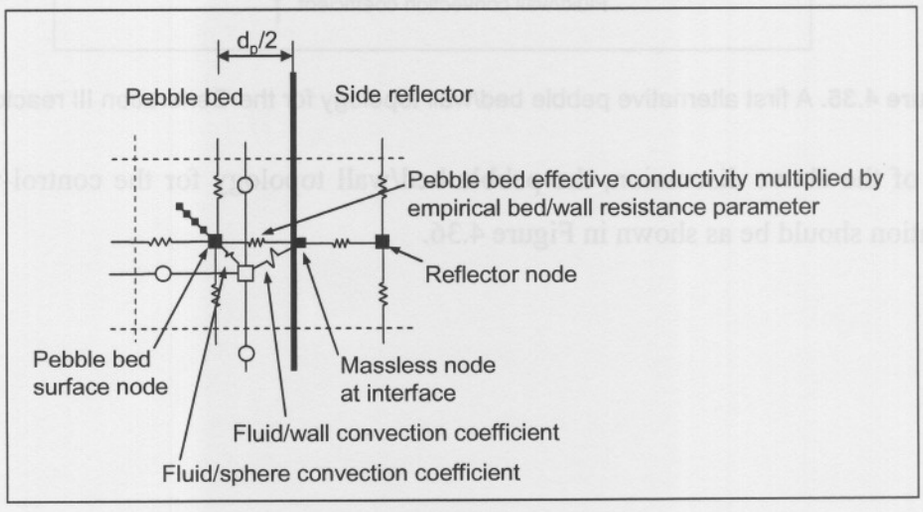


Figure 4.37. The pebble bed/wall topology for the control-volume based discretisation.

4.9.6 Cavities

Two types of cavities are used to model void spaces in the reactor geometry, namely single cavities and flow cavities which could either be horizontal or vertical. For single cavities, stagnant flow is assumed, so that only inlet and outlet flow pressure losses occur in such cavities. Because of the stagnant flow assumption, the whole gas volume is lumped into a single node, as shown in Figure 4.38.

Horizontal and vertical cavities assume throughflow and, therefore, hydraulic diameter, pressure drop and heat transfer correlations can be specified. The typical layout of the calculation network at the top of a pebble bed is shown in Figure 4.38.

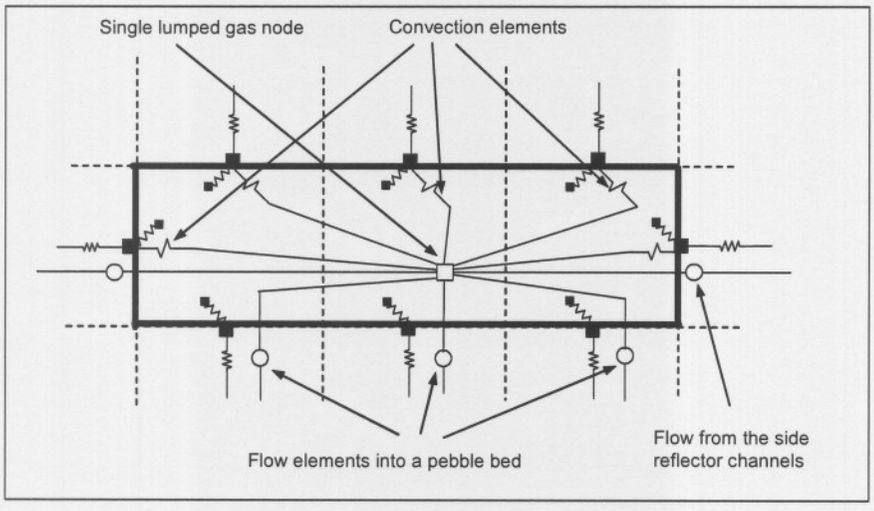


Figure 4.38. Network topology used to represent a single cavity, radiation spatial elements omitted.

The horizontal and vertical cavity network layouts will be similar to that shown in Figure 4.38, except that there is a gas node for every control volume.

Keep in mind that all cavity walls are also connected to each other with a radiation heat exchange network as shown in Figure 4.29. Radiation networks use so many elements that figures of cavity zones could become cluttered (Figure 4.39), therefore, they are omitted in Figure 4.38.

4.10 Assembly of reactor zones

Figure 4.39 illustrates how a reactor like the PBMR is discretised with the control-volume based approach. The geometry is represented with control-volume types, from which the

simulation network is generated automatically, according to the topological rules described in the preceding paragraphs.

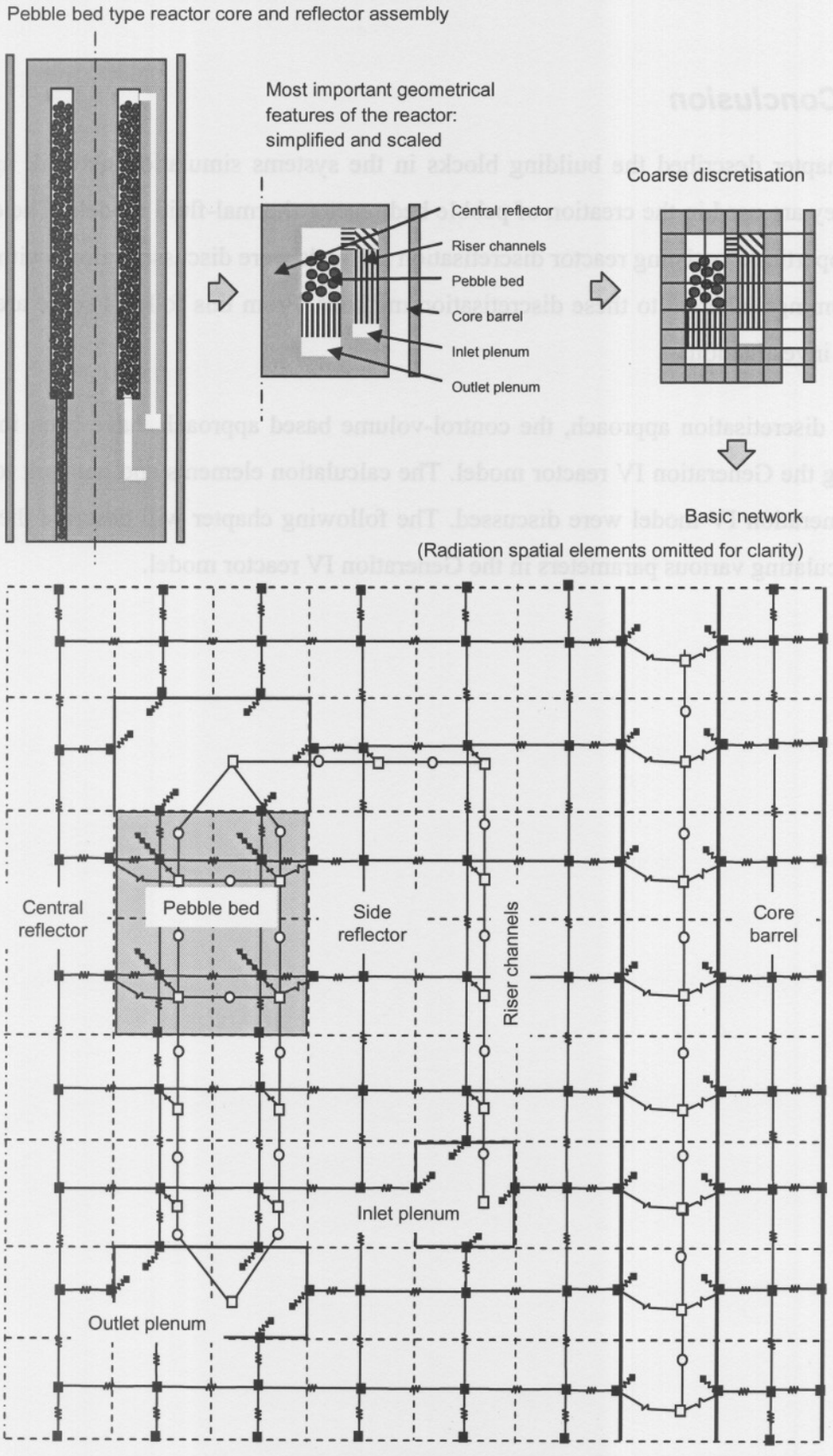


Figure 4.39. The discretisation process for a pebble bed type reactor with a central column.

4.11 Conclusion

This chapter described the building blocks in the systems simulation network approach and how they are used in the creation of pebble bed reactor thermal-fluid models. The development and properties of existing reactor discretisation methods were discussed, along with some of the shortcomings inherent to these discretisation methods. From this follows some areas that need further investigation.

A new discretisation approach, the control-volume based approach, have been introduced for creating the Generation IV reactor model. The calculation elements and network topologies for the Generation IV model were discussed. The following chapter will describe the correlations for calculating various parameters in the Generation IV reactor model.

Chapter 5

Correlations

5.1 Introduction

The previous chapter described the numerical framework of the Generation IV reactor model. This numerical framework requires a considerable number of correlations to describe mechanisms or phenomena such as convection heat transfer or pressure drop in a porous medium. For calculating the various mechanisms and phenomena in a pebble bed high-temperature reactor, this chapter presents standardised correlations that were tried and tested by previous researchers.

5.2 Overview of heat transfer mechanisms in a pebble bed reactor

The two most important steady-state conditions for a pebble bed reactor are full-power operation and Loss Of Forced Cooling. In both cases, heat is generated in the spheres but the rest of the heat removal path differs greatly between the two steady-states. For full power operation, the coolant removes heat from the core, while during a Loss Of Forced Cooling event, the core decay heat is removed by means of conduction radially outward from the core and radiation across the reflector/core barrel/pressure vessel cavities.

When simulating these mechanisms, the characteristics of the physical process, as well as the properties of the numerical simulation technique, have to be taken into account. As shown in Figure 5.1, the maximum fuel temperature is physically determined by the neutron reaction, while it is numerically influenced by the transient response, resistance distribution and sphere discretisation. In Figure 5.1 the mechanisms along the heat transfer paths to the eventual heat sinks are indicated for both normal reactor operation as well as Loss Of Forced Cooling accidents. Thus, Figure 5.1 provides an overview of heat-removal mechanisms from a pebble bed HTR.

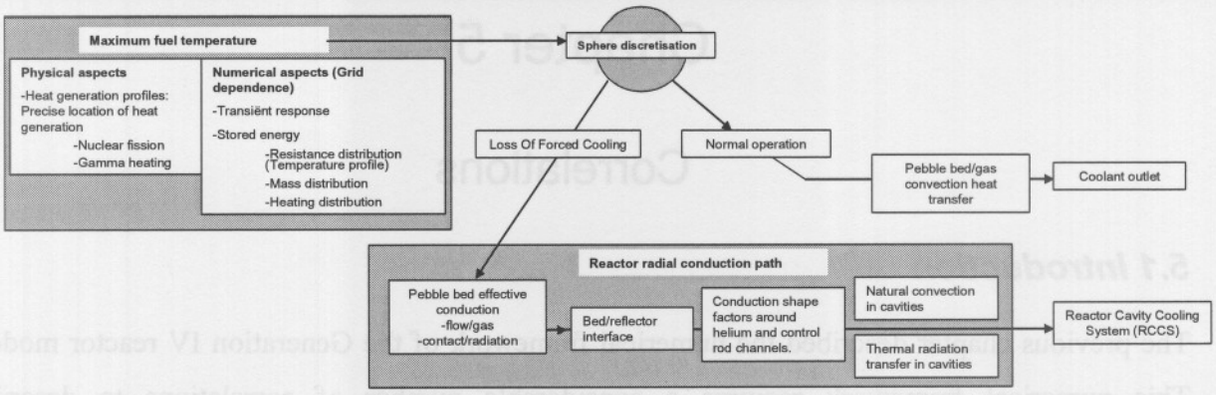


Figure 5.1 Flow diagram of reactor heat removal paths.

5.3 Heat generation in a pebble bed reactor

5.3.1 Large-scale

In a nuclear reactor, the local heat generation is proportional to the product of the neutron flux and the local effective cross-section. The effective cross-section in turn is highly temperature dependent. Thus, heat generation is calculated by the neutronics model, while the thermal-fluids code calculates the temperature field, given the heat generation.

As this study focuses on thermal-fluid reactor modelling, the total power is fixed for steady-state conditions and multiplied with a normalised power distribution to find the local heat generation. The heat distribution is either specified with a power distribution chart or with polynomials, of which the details are given in Appendix A.

Similar to the Generation II reactor model in Flownex, the point-kinetic neutronic model is used to find the total power during transient simulations (Swift, 2006). It must be kept in mind that the point-kinetic model is only accurate when the spatial and temporal variables are separable, i.e. the power level can change without change in the normalised shape of the neutron flux profile (p 144, Stacey, 2001). This is required, as the point-kinetic model characterises the behaviour of the reactor as a whole with a few constants, while these constants actually represent the integrated feedback effects from zones all-over the reactor. The feedback effect of a zone is determined by the local neutron flux shape.

Therefore, a neutron diffusion code like VSOP is used to calculate the point-kinetic parameters for some general reactor operating conditions, such as full mass flow and power, 40 percent mass flow and power, as well as accident conditions with or without SCRAM. For each of these

cases, the temperature distribution, the control rod setting and therefore the neutron flux profile is different.

When the reactor geometry (including control rod position) undergoes only small changes or if the change is over the whole reactor (such as a flow temperature change or xenon transient), the point-kinetic model gives good results.

Regarding the location of heat generation, gamma ray heating of the reflectors is of considerable importance as the neutron scattering and absorption cross-sections of the control rods and reflectors are temperature-dependent. The exact value of this heating is difficult to establish accurately. Equally difficult to calculate is the cooling effect of leak flows. Therefore, it is considered a conservative approach to neglect side reflector heating, as well as the leak flow cooling effect. To enable the investigation of gamma ray heating, heat generation can be specified for three zones, namely the central reflector, the pebble bed and the outer reflector.

5.3.2 Fuel element- or sphere-scale

With approximately 90 percent of heat production in the fuel kernels and 10 percent in the moderator and reflector (Lamarsh and Barratta, 2001), it will be simpler and conservative to assume no heat generation in the fuel sphere shell. Heat generation placed in the center part of the sphere will result in higher temperatures than heat generation placed at the sphere surface shell.

5.3.3 Transient behaviour: point-kinetic neutronics

Heat generation in a nuclear reactor is composed of two components, namely the instantaneous fission heat release and the delayed heat release from the decay of fission products. Both heat generation mechanisms are modelled with the point-kinetic neutronics model. The instantaneous normalised power level $\tilde{P}_n$ is calculated from the reactivity, reactor constants and the relative concentration of six groups of neutron precursor isotopes, while the decay heat is calculated from the relative concentration of three groups of decay heat producing isotopes. These equations for point-kinetic neutronics are described in many textbooks on reactor analysis, such as Stacey (2001). The instantaneous normalised power level is given by:

$$\frac{d\tilde{P}_n}{dt} = \frac{\rho - \beta}{\Lambda}\tilde{P}_n + \sum_{i=1}^{6}\lambda_i \tilde{C}_i \qquad (5.1)$$

where ρ is reactivity, β is the delayed neutron fraction, Λ the average neutron lifetime and λ_i the decay constant of neutron precursor group i that has a normalised concentration of $\tilde{C}_i$ (all normalised parameters are indicated with a "~" sign). The rate of change in relative concentration of the six neutron precursor isotope groups is given by Eq.(5.2)

$$\frac{d\tilde{C}_i}{dt} = \frac{\beta_i}{\Lambda}\tilde{P}_n - \lambda_i \tilde{C}_i \quad for \;\; i = 1\ldots 6 \tag{5.2}$$

where β_i is the production constant of isotope group i.

The rate of change in normalised concentration $\tilde{D}_k$ for decay-heat producing isotope group k is given by:

$$\frac{d\tilde{D}_k}{dt} = \beta_k \tilde{P}_n - \lambda_k \tilde{D}_k \quad \text{for } k = 1\ldots 3 \tag{5.3}$$

with β_k the dimensionless production constant for decay group k, λ_k the decay constant for the group in [s^{-1}]. For this equation to be consistent, the unit of $\tilde{D}_k$ has to be [s]. This is not a problem as the absolute value of $\tilde{D}_k$ makes no difference to the results, as long as its value relative to β_k and λ_k is calculated correctly.

In steady-state full-power reactor operation (i.e. $\tilde{P}_n$ =1), decay heat producing isotopes reache an equilibrium state at which production equals decay (i.e. $\frac{d\tilde{D}_k}{dt} = 0$), so that the steady-state concentration is given by:

$$\tilde{D}_k = \frac{\beta_k}{\lambda_k} \tag{5.4}$$

At any time, the normalised heat production from the decay-heat isotopes is given by Eq.(5.5):

$$\tilde{P}_{dec} = \sum_{k=1}^{3} \lambda_k \tilde{D}_k \tag{5.5}$$

so that steady-state normalised decay heat production is given by Eq.(5.6):

$$\begin{aligned}\tilde{P}_{dec} &= \sum_{k=1}^{3} \lambda_k \frac{\beta_k}{\lambda_k} \\ &= \sum_{k=1}^{3} \beta_k\end{aligned} \tag{5.6}$$

Under steady-state conditions, the (otherwise time-dependent) total reactor power P_{tot} equals the nominal power of the reactor $P_{tot} = P_{nom}$, while in a transient state, the total power equals the nominal power multiplied by a fraction x. Therefore

$$P_{tot} = xP_{nom} \tag{5.7}$$

For steady-state conditions, x obviously equals one. But x should also equal the sum of normalised instantaneous power $\tilde{P}_n$ and normalised decay heat $\tilde{P}_{dec}$, which is larger than one in a steady-state:

$$\left(\tilde{P}_n + \tilde{P}_{dec}\right)_{SS} = \left(1 + \sum_{k=1}^{3} \beta_k\right)_{SS} > 1 \tag{5.8}$$

Therefore, x has to be normalised by the sum of steady-state normalised power values, so that it follows that

$$x = \frac{\tilde{P}_n + \tilde{P}_{dec}}{\left(\tilde{P}_n + \tilde{P}_{dec}\right)_{SS}} \tag{5.9}$$

When the steady-state values of $\tilde{P}_n$ and $\tilde{P}_{dec}$ are substituted, one obtains the following:

$$x = \frac{\tilde{P}_n + \tilde{P}_{dec}}{\left(1 + \sum_{k=1}^{3} \beta_k\right)} \tag{5.10}$$

so that one can write:

$$P_{tot} = P_{nom} \frac{\tilde{P}_n + \tilde{P}_{dec}}{\left(1 + \sum_{k=1}^{3} \beta_k\right)} \tag{5.11}$$

$$\text{or} \quad P_{tot} = P_{nom} \frac{\tilde{P}_n}{\left(1 + \sum_{k=1}^{3} \beta_k\right)} + P_{nom} \frac{\tilde{P}_{dec}}{\left(1 + \sum_{k=1}^{3} \beta_k\right)}$$

The implication of Eq.(5.11) is that the actual value of decay heat would be described by Eq.(5.12).

$$\text{Decay heat}[\text{MW}] = P_{nom}[\text{MW}]\frac{\tilde{P}_{dec}[-]}{\left(1+\sum_{k=1}^{3}\beta_k\right)} \tag{5.12}$$

The modelling constants for the point-kinetic neutronics model are reactor-specific, as well as operating condition-specific and are only specified per case study.

5.4 Pebble bed porosity

The fuel spheres in the pebble bed are heated internally by nuclear fission and cooled on the outside by helium flowing through the packed bed. The temperature level of the spheres depends on the thermal resistances inside the spheres, as well as the helium flow rate. Both the sphere surface heat transfer coefficient and the pressure drop (i.e. coolant flow rate) are highly sensitive to the porosity of the pebble bed. Therefore, any temperature-field calculation of a pebble bed reactor core has to take porosity variations into account.

Near the wall of a packed bed, the porosity varies greatly, due to the wall enforcing a certain ordering on the spheres. Directly next to the wall, the porosity has a maximum value of 1. As the pressure drop decreases with increasing porosity, a higher flow velocity is expected at the wall.

Careful study of the near-wall porosity revealed it to have a damped oscillatory pattern that smooths out after about five sphere diameters from the wall (Du Toit, 2004). If, however, the porosity is calculated for increments of one sphere diameter, a smooth, nearly exponential variation up to the bulk porosity is found, as shown in Figure 5.2.

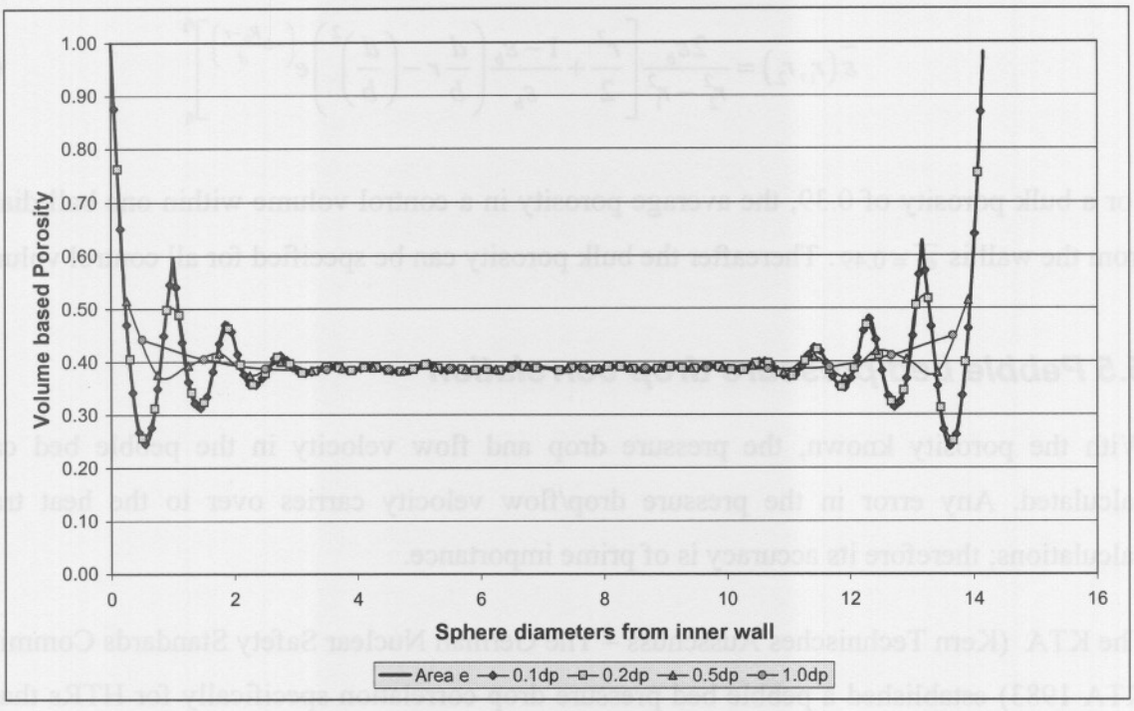


Figure 5.2. Volume-based radial variation in porosity for various peel thicknesses for an annular packed bed. The annular height is 14 sphere diameters. (Du Toit, 2004).

Specifically when using the Reynolds-Averaged Navier-Stokes (RANS) equations to model the flow in the porous bed, it will be advantageous if the porosity variation can be described by an exponential variation instead of an oscillatory variation. This is due to the fact that an oscillatory variation requires many more control volumes than an exponential variation to resolve the variation in porosity.

Du Toit (2004) investigated several exponential variations and found the correlation by Hunt and Tien (1990) to be the most accurate. Their correlation is given by:

$$\varepsilon(r) = \varepsilon_b \left[1 + \frac{1-\varepsilon_b}{\varepsilon_b} \exp\left(-b \frac{R_0 - r}{d} \right) \right] \tag{5.13}$$

where ε_b is the bulk porosity and b approximates the change in porosity. For spherical particles, a value of 6 is recommended for b. R_0 is the wall radius, r is the radial position and d is the particle diameter.

To determine the average porosity for a region between r_1 and r_2, Eq.(5.13) is multiplied by the area and integrated by parts to obtain the void volume of the region. Division by the region volume gives the average porosity for a region:

$$\bar{\varepsilon}(r_1,r_2)=\frac{2\varepsilon_b}{r_2^2-r_1^2}\left[\frac{r^2}{2}+\frac{1-\varepsilon_b}{\varepsilon_b}\left(\frac{d}{b}r-\left(\frac{d}{b}\right)^2\right)e^{\left(-b\frac{R_0-r}{d}\right)}\right]_{r_1}^{r_2} \tag{5.14}$$

For a bulk porosity of 0.39, the average porosity in a control volume within one ball diameter from the wall is $\overline{\varepsilon_d}=0.49$. Thereafter the bulk porosity can be specified for all control volumes.

5.5 Pebble bed pressure drop correlation

With the porosity known, the pressure drop and flow velocity in the pebble bed can be calculated. Any error in the pressure drop/flow velocity carries over to the heat transfer calculations; therefore its accuracy is of prime importance.

The KTA (Kern Technisches Ausschuss – The German Nuclear Safety Standards Commission, KTA 1983) established a pebble bed pressure drop correlation specifically for HTRs that uses 60mm diameter fuel spheres. This equation is given by

$$\begin{aligned}\Delta p &= \psi\frac{1-\varepsilon}{\varepsilon^3}\frac{H}{d_p}\frac{1}{2}\rho V_0^{\,2}\\ \psi &= \frac{320}{\left(\frac{\mathrm{Re}}{1-\varepsilon}\right)}+\frac{6}{\left(\frac{\mathrm{Re}}{1-\varepsilon}\right)^{0.1}}\\ \mathrm{Re} &= \frac{\rho V_0 d}{\mu}\end{aligned} \tag{5.15}$$

where d is the pebble bed particle diameter and V_0 the superficial velocity. This equation is valid for a particle based Reynolds number range of $1\le \mathrm{Re}/(1-\varepsilon)\le 10^5$ and a porosity range of $0.36\le\varepsilon\le 0.42$.

Eq.(5.15) can be rewritten in vector form as follows

$$-\vec{\nabla}p=\left[\frac{160\nu}{d^2}\cdot\frac{(1-\varepsilon)^2}{\varepsilon^3}+\frac{3\left|\vec{V}_0\right|}{d}\cdot\frac{(1-\varepsilon)^{1.1}}{\varepsilon^3}\cdot\left(\frac{\mu}{\rho\left|\vec{V}_0\right|d}\right)^{0.1}\right]\rho\vec{V}_0 \tag{5.16}$$

Note that the bracketed part of Eq.(5.16) contains the absolute value of velocity $\left|\vec{V}_0\right|$. The reason for this is that the flow condition in the bed is characterised by the Reynolds number, which is a function of the absolute velocity.

As mentioned in Section 4.8.1, the flow nodes and elements in the network-discretisation of the pebble bed have some special features that enable this two-dimensional effect to be taken into account.

5.6 Convection heat transfer correlation

The KTA (1983) recommends the correlation by Kugeler and Schulten for calculating convection heat transfer between helium coolant and 60mm diameter fuel spheres. It is given as

$$h_{KS} = \frac{k_g}{d}\left[\frac{1.27}{\varepsilon^{1.18}}\mathrm{Re}^{0.36}\,\mathrm{Pr}^{0.33} + \frac{0.033}{\varepsilon^{1.07}}\mathrm{Re}^{0.86}\,\mathrm{Pr}^{0.5}\right] \tag{5.17}$$

where k_g is the gas molecular conductivity, d the fuel sphere diameter and Pr the fluid Prandtl number, defined by

$$\mathrm{Pr} = \frac{c_p \mu}{k_g} \tag{5.18}$$

where μ is the gas viscosity and c_p the gas specific heat. The Reynolds number is defined by

$$\mathrm{Re} = \frac{\rho V_0 d}{\mu} \tag{5.19}$$

where V_0 is the local superficial velocity, ρ is the gas density. This correlation is valid for $100 \le \mathrm{Re} \le 10^5$, $0.36 \le \varepsilon \le 0.42$, $H/d \ge 4$ and $D_{ch}/d \ge 20$, where H is the height of the reactor and D_{ch} the hydraulic diameter of the reactor (outer diameter minus inner diameter in the case of an annulus). The Kugeler & Schulten correlation is based on the global superficial velocity, but because it was tested for beds with a large D_{ch}/d ratio, it is assumed to be applicable when using the local superficial velocity of a discrete control volume.

For very low Reynolds numbers, Vortmeyer and Le Mong (1976) presented the following correlation:

$$h = \frac{k_g}{d} 1.04\,\mathrm{Re}^{0.6} \tag{5.20}$$

This correlation is valid for Reynolds numbers between 10 and 200 and for a ratio of bed effective to gas conductivity ratio of 25, i.e. $k_{eff}/k_{gas} = 25$.

5.7 Dispersion heat transfer

5.7.1 Convective and diffusive heat transfer

Not to be confused with convection heat transfer, convective heat transport is the transfer of heat by means of fluid movement. When examining the relation of convective heat transfer with other mechanisms in a pebble bed, consider the fluid energy conservation equation

$$\begin{aligned}&\frac{\partial}{\partial t}\left(\varepsilon\rho e_0\right)+\frac{1}{r}\frac{\partial}{\partial r}\left(\varepsilon r\rho e_0 u_r\right)+\frac{\partial}{\partial z}\left(\varepsilon\rho e_0 u_z\right)=\varepsilon\frac{\partial p}{\partial t}\\&+\frac{1}{r}\frac{\partial}{\partial r}\left(\varepsilon r k_{feff}\frac{\partial T}{\partial r}\right)+\frac{\partial}{\partial z}\left(\varepsilon k_{feff}\frac{\partial T}{\partial z}\right)+\varepsilon\rho\left(g_r u_r+g_z u_z\right)+q_{sf}\end{aligned} \tag{4.6}$$

where k_{feff} is the fluid effective conductivity, e_0 the total enthalpy and q_{sf} the heat transfer from the fuel spheres to the fluid. The convective terms are $\frac{1}{r}\frac{\partial}{\partial r}\left(\varepsilon r\rho e_0 u_r\right)$ and $\frac{\partial}{\partial z}\left(\varepsilon\rho e_0 u_z\right)$ while the diffusive (conductive) terms are $\frac{1}{r}\frac{\partial}{\partial r}\left(\varepsilon r k_{feff}\frac{\partial T}{\partial r}\right)$ and $\frac{\partial}{\partial z}\left(\varepsilon k_{feff}\frac{\partial T}{\partial z}\right)$. Note that the absolute velocities u_r and u_z are used instead of the superficial velocities u_{0r} and u_{0z}. Superficial velocity equals absolute velocity times the porosity, i.e. $u_0 = \varepsilon u$.

In most engineering flow problems, fluid convective heat transport is several orders of magnitude larger than fluid diffusive or conductive heat transport. In such cases, the diffusive terms in the fluid energy equation Eq.(4.6) can be neglected without losing accuracy, but to properly establish when fluid conduction can be neglected, a quantitative analysis has to be done.

To quantify the relation between convective and conductive heat transfer, consider a case where fluid at a certain temperature T_1 flows at a rate of $\dot{m}$ into a control volume that is at a temperature T_2. That represents a heat addition of Q_{conv} into that control volume, given by

$$Q_{conv} = \dot{m}\left(e_2 - e_1\right) \tag{5.21}.$$

For this problem, the length scale for the temperature gradient $T_2 - T_1$ is taken as the hydraulic diameter D_h. For helium in particular, it is an accurate approximation to say that $e_2 - e_1 \approx c_p\left(T_2 - T_1\right)$ and as $\dot{m} = \rho u_0 A$, it holds that

$$Q_{conv} = \rho u_0 A c_p \left(T_2 - T_1\right) \tag{5.22}$$

where u_0 is the superficial fluid velocity, ρ is fluid density and A the area through which the stream passes. Conduction heat transfer Q_{cond} over the same distance is given by

$$Q_{cond} = \frac{k_g A}{D_h}\left(T_2 - T_1\right) \tag{5.23}$$

where k_g is the fluid molecular conductivity.

The ratio between convective and conductive transport is defined as the Peclet number Pe, which, for this case is given by

$$\begin{aligned} \mathrm{Pe} &= \frac{Q_{conv}}{Q_{cond}} = \frac{\rho u_0 A c_p \left(T_2 - T_1\right)}{\frac{k_g A}{D_h}\left(T_2 - T_1\right)} \\ \therefore \mathrm{Pe} &= \frac{\rho c_p u_0 D_h}{k_g} \end{aligned} \tag{5.24}$$

Thus, for Peclet numbers much higher than one, convective heat transport dominates and fluid conductive heat transfer may be neglected, while in cases with very small Peclet numbers conduction heat transfer dominates. It is interesting to note that $\mathrm{Pe} = \mathrm{Re}\,\mathrm{Pr}$ where Re is the Reynolds number and Pr is the Prandtl number defined in Eq.(5.18) , i.e.

$$\mathrm{Pe} = \mathrm{Re}\,\mathrm{Pr} = \frac{\rho u_0 D_h}{\mu} \cdot \frac{c_p \mu}{k_g} \tag{5.25}.$$

5.7.2 Dispersion heat transfer modelling

Usually, the bulk flow direction is used to calculate convective heat transfer. However, due to turbulence, there are transverse velocity variations which cause mixing. While the transverse flow variations are small in fluid streams in a pipe, the highly irregular flow paths in a pebble bed causes orders of magnitude higher transverse velocity variation. This transverse flow variation causes a phenomenon referred to as "braiding" or dispersion. Dispersion is the

transport of mass relative to the bulk flow direction, due to transverse velocity variations. It appears as enhanced mixing between parallel flow streams or as greatly enhanced fluid conduction heat transfer.

Thus, dispersion is a convective heat transfer mechanism that appears as enhanced diffusive heat transfer in all directions. Therefore, dispersion heat transfer is taken into account by increasing the fluid effective conductivity k_{feff}. As diffusive heat transfer is already solved as part of the fluid energy equation in *Flownex*, only a correlation for k_{feff} is necessary.

It is useful to define a Peclet number Pe_{feff} based on the fluid effective conductivity k_{feff} and with hydraulic diameter equal to one sphere diameter d, so that Pe_{feff} is given by

$$\mathrm{Pe}_{feff} = \frac{\rho c_p u_0 d}{k_{feff}} \tag{5.26}.$$

As quoted by Tsotsas (2002) in the VDI Wärmeatlas, Bauer (1977) found that Pe_{feff} for a pebble bed is given by

$$\mathrm{Pe}_{feff} = 8\left(2-\left(1-2\frac{d}{D_{ch}}\right)^2\right) \tag{5.27}$$

where D_{ch} is the pebble bed core hydraulic diameter, which, for an annular bed equals the difference between core outer and inner diameter while d is the sphere diameter. In the above formula, the coefficient of the bracketed term is the dispersion shape factor, which equals eight for a sphere-pebble bed. The dispersion shape factor quantifies the particle shape influence on the ratio of convective to fluid effective conductive heat transfer. The bracketed term in Eq.(5.27) is the ratio between the pebble bed average superficial velocity and the core superficial velocity (Kuerten *et al.* 2004), i.e. the bracketed term account for wall effects.

However, as the reactor model, considered in this study, solves a control-volume discretisation of the pebble bed, the wall effects are explicitly accounted for in the calculated velocity profile. Therefore, an infinitely large bed $(D_{ch} \to \infty)$ can be assumed on each control volume so that Eq.(5.27) simplifies to

$$\mathrm{Pe}_{feff} = 8 \tag{5.28}.$$

The fluid effective conductivity can thus be rewritten as

$$k_{feff} = \frac{\rho c_g u_o d}{\mathrm{Pe}_{feff}} \tag{5.29}$$

where d is the hydraulic diameter of the pebble bed, namely the sphere diameter.

When isotropic dispersion is assumed, the fluid effective conductivity is uniformly enhanced in all directions. As described by Tsotsas (2002) in the VDI Wärmeatlas, more advanced dispersion models assume anisotropic dispersion and employ different fluid-effective Peclet numbers parallel to the flow direction and perpendicular to the flow direction. For isotropic dispersion, the magnitude of the absolute velocity $|\overline{u}_0|$ is used for u_0 in Eq.(5.29).

The accuracy of calculating dispersion in the bulk flow direction is severely compromised by numerical diffusion and in the bulk flow direction, dispersion is overshadowed by convective heat transport. Therefore, the error is negligible when dispersion is only taken into account perpendicular to the bulk flow direction, as is done in the Generation IV reactor model.

The pebble bed wall prevents transverse velocity variations so that k_{feff} approaches zero in the vicinity of the wall. However, it is not necessary to treat this explicitly in the Generation IV reactor model, as other considerations dictate that the flow element nearest to the wall is at a distance of half a sphere diameter, as shown in Figure 4.37. At this distance the flow field is dominated by the presence of spheres instead of the wall.

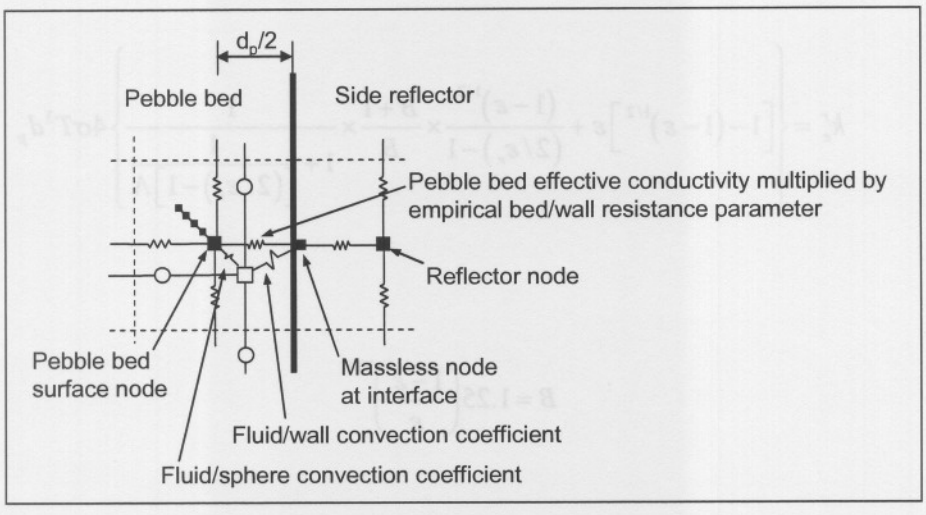


Figure 4.37. The pebble bed/wall topology for the control-volume based discretisation.

5.8 Pebble bed conduction

The pebble bed is treated as a homogeneous solid of which the conductivity can be calculated with the well-known method of Zehner and Schlunder, as presented by Du Toit (2005). This method captures the complex heat transfer phenomena in the bed, namely the combined effect of conduction between spheres, contact resistance, interstitial radiation heat transfer, as well as conduction through stagnant interstitial gas. In this study, the correlation modified by Breitbach and Bartels (as quoted by Niessen and Stöcker, 1997) is used. This form of the correlation was used to model the SANA experiment and it has the advantage of taking the contact pressure between spheres into account elegantly, as shown in Eq.(5.35). Breitbach and Bartels used the particle conductivity as reference for some correlated ratios, while the original version by Zehner and Schlunder used the fluid conductivity as reference.

The correlation for bed effective conductivity k_{eff} consists of three parts, namely equivalent conductivities for radiation k_e^r (Eq.(5.31)), gas conduction k_e^g (Eq. (5.34)) and solid conduction k_e^c (Eq. (5.35)) which adds up as follows:

$$k_{eff} = k_e^r + k_e^g + k_e^c \tag{5.30}$$

These components are now discussed separately.

5.8.1 Radiation and solid conduction

The correlation for k_e^r is given by (Niessen and Stöcker, 1997)

$$k_e^r = \left\{ \left[1-\left(1-\varepsilon\right)^{1/2}\right]\varepsilon + \frac{\left(1-\varepsilon\right)^{1/2}}{\left(2/\varepsilon_r\right)-1} \times \frac{B+1}{B} \times \frac{1}{1+\dfrac{1}{\left[\left(2/\varepsilon_r\right)-1\right]\Lambda}} \right\} 4\sigma T^3 d_p \tag{5.31}$$

where

$$B = 1.25\left(\frac{1-\varepsilon}{\varepsilon}\right)^{10/9} \tag{5.32}$$

and

$$\Lambda = \frac{k_p}{4\sigma T^3 d_p} \tag{5.33}.$$

In the above two equations, the Stephan-Boltzmann constant $\sigma = 5.67 \times 10^{-8} \left[\mathrm{W/m^2K^4} \right]$, d_p is the particle diameter, ε being the bed void fraction and ε_r the particle surface emissivity. Radiation is represented by the first term in the brackets and is the dominating term at high temperatures. Λ is the Planck number, or ratio between conductive and radiative heat transfer.

5.8.2 Gas Conduction and Solid Conduction

This part of the effective conductivity takes the stagnant thermal conductivity, due to the interstitial fluid in the pebble bed, into account. Based on a one-dimensional heat flow model for conduction through a packed bed of spherical particles, Zehner and Schlünder proposed a correlation for the stagnant thermal conductivity. This correlation was tested by Prasad *et al.* (as quoted by Niessen & Stöcker, 1997) and is given by

$$\frac{k_e^g}{k_{mol}} = 1 - \sqrt{1-\varepsilon} + \frac{2\sqrt{1-\varepsilon}}{1-\lambda_{fp}B} \times \left[\frac{\left(1-\lambda_{fp}\right)B}{\left(1-\lambda_{fp}B\right)^2} \ln\left(\frac{1}{\lambda_{fp}B}\right) - \frac{B+1}{2} - \frac{B-1}{1-\lambda_{fp}B} \right] \tag{5.34}$$

with λ_{fp} being the ratio between the fluid conductivity (also referred to as molecular conductivity) and the particle conductivity, i.e. $\lambda_{fp} = k_{mol}/k_p$.

5.8.3 Contact conduction and solid conduction

The last part of the effective conductivity deals with the prediction of the contact area conduction for a pebble bed where the pebbles are subjected to a compressive load such as the weight of the pebbles. Hertzian elastic deformation (Niessen & Stöcker, 1997) is used to determine the radius of the contact area between two spheres. The conductive heat flux was analysed by Chen & Tien (as quoted by Niessen & Stöcker, 1997) for the three close-pack cubic arrangements to determine the contact resistance. The conductivity is given as:

$$\frac{k_e^c}{k_p} = \left[\frac{3\left(1-\mu_p^2\right)}{4E_p} f d_p \right]^{1/3} \frac{1}{0.531S} \left(\frac{N_A}{N_L} \right) \tag{5.35}$$

where

$$f = p\frac{S_F}{N_A} \tag{5.36}$$

N_A is the number of spheres per unit area and N_L the number of spheres per unit length. For the simple cubic packing we have $S=1$, $S_F=1$, $N_A=1/d_p^2$ and $N_L=1/d_p$. Further μ_p is the Poisson ratio for the spheres and E_p the Young's modulus (modulus of elasticity) for the spheres. The external pressure p is estimated by taking the weight of the spheres in the pebble bed.

5.8.4 Total effective conductivity

For some cases or first approximations, implementation of the bed conductivity can be eased considerably with the simple relation in Eq.(5.37). The coefficients *a* and *b* are fitted to results from the Zehner-Schlunder model in Eq.(5.30), capturing only the temperature-dependence.

$$k_{eff}(T) = aT^b \tag{5.37}$$

5.9 Conclusion

The discretisation framework discussed in Chapter 4 requires various pressure drop and heat transfer correlations for the pebble bed core. This chapter described correlations and methods for calculating heat generation, pebble bed porosity, pressure drop relations, convection heat transfer, dispersion heat transfer as well as pebble bed conduction. The methods in this chapter were validated by previous researchers, while the next chapter describes flow and heat transfer models that were investigated in this study.

Chapter 6

Extensions and refinements

6.1 Introduction

In the previous chapter many well-established correlations used in a pebble bed numerical discretisation were discussed. Room for improvement was found in the convection heat transfer discretisation, the sphere discretisation, in modelling techniques for the bed/wall interface and in conduction heat transfer across the holed reflector blocks. This chapter describes the refinements that were made on these modelling methods.

6.2 Sphere discretisation

6.2.1 Background

Since the discretised fuel sphere model is duplicated in each pebble bed control volume, it adds a large number of nodes and elements to the model. Therefore, the most efficient reduction in the number of elements (and, therefore, increase of simulation speed) is to use the coarsest sphere discretisation that is still accurate.

The parameters which the fuel sphere model must calculate accurately are maximum fuel temperature, mass-averaged temperature and temperature transient response. The sphere transient response determines how the reactor behaviour is predicted for estimating control system parameters. The mass-averaged temperature is also of great significance because it is the only thermal-fluid input to the reactivity calculation in the point-kinetic neutronics model.

6.2.2 New discretisation methods

With these requirements in mind, two new sphere discretisation methods were derived during this study. The first method, referred to as the "Staggered Volume" method, increases the accuracy of the steady-state volume-average temperature by using different grids for allocating heat generation and thermal mass to nodes. This method is valid for a minimum grid size of three nodes in the heat generating zone of the sphere and it can be incremented to increase transient response accuracy.

The other sphere discretisation developed during this study is referred to as the "Analytical Sphere" method, due to being derived from the steady-state analytical temperature solution for

a sphere with constant volumetric heat generation. With this method, a complete fuel sphere can be represented with only four nodes, as shown in Figure 6.1.

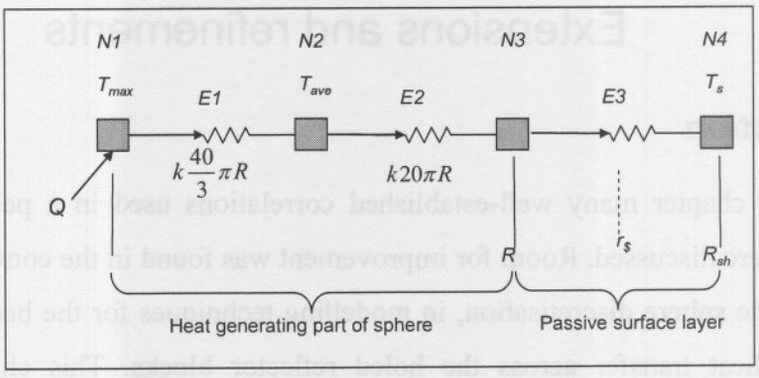


Figure 6.1. Network layout for the "Analytical Sphere" discretisation.

In the "Analytical Sphere" method, all the sphere mass is lumped at a single node for which the average temperature is calculated accurately (N2 in Figure 6.1), while all heat generation is assigned to another node that calculates the steady-state maximum temperature accurately (N1 in Figure 6.1).

For use with both the "Staggered Volume" and the "Analytical Sphere" methods, a procedure was developed to accurately calculate the average temperature of a passive graphite layer, as represented by N3 and N4 in Figure 6.1.

The volumes of the nodes in the "Analytical Sphere" scheme in Figure 6.1 are given by

$$\begin{aligned} V_1 &= 0 \\ V_2 &= \frac{4}{3}\pi R^3 \\ V_3 &= \frac{4}{3}\pi\left(r_s^3 - R^3\right) \\ V_4 &= \frac{4}{3}\pi\left(R_{sh}^3 - r_s^3\right) \end{aligned} \tag{6.1}$$

with r_s given by

$$r_s^3 = R^3 + \frac{3}{2}\left(R_{sh} + R\right)R_{sh}R - \frac{R\left(R_{sh}^3 - R^3\right)}{R_{sh} - R} \tag{6.2}$$

so that the volume-averaged temperature of the surface layer is grid-independent. The conduction shape factors for the elements are given by

$$F_1 = \frac{40}{3}\pi R \tag{6.3},$$

$$F_2 = 20\pi R \tag{6.4},$$

and

$$F_3 = \frac{4\pi}{\frac{1}{R} - \frac{1}{R_{sh}}} \tag{6.5}.$$

6.2.3 Results and recommendation

The only error introduced in the "Analytical Sphere" scheme is the discrete handling of conductivity, i.e. for constant conductivity, steady-state temperatures are calculated analytically correct. The temperature-dependence of fuel sphere graphite conductivity was found to introduce a negligible difference with a grid-independent model.

The downside to the "Analytical Sphere" discretisation is that, due to the zero mass of the sphere centre node (N1 in Figure 6.1), the maximum fuel temperature response to a step increase in power overshoots that of a grid-independent, conventionally discretised sphere by about 30 percent. Still, the largest difference in average temperature between this discretisation and a grid independent sphere solution (transients included) was less than 1.5 percent. In contrast, the "Staggered Volume" requires the same number of increments than existing discretisation methods to give a grid-independent transient response.

As the maximum fuel temperature error created by the "Analytical Sphere" model is well known and its occurrence is limited to short time periods, it can be dealt with by careful interpretation of maximum fuel temperature results. On account of the "Analytical Sphere" scheme requiring the least number of nodes for accurate transient response, it is considered the most useful of the two discretisation methods developed in this study.

Tests of the maximum and average temperature grid dependence, transient response of some existing discretisations, as well as derivation of two new schemes, are presented in Appendix F.

6.3 Convection heat transfer discretisation

In the spatial discretisation of the pebble bed, each control volume contains both solid material and gas. The same situation also arises in the spatial discretisation of heat exchangers. In these cases, the energy conservation for the solid is coupled to fluid energy conservation by means of convection heat transfer. Some unexpected challenges emerged when investigating the accuracy of convection heat transfer calculation on such a discretised domain. This is now illustrated with a one-dimensional problem.

6.3.1 One-dimensional case

Consider a fluid heater in which fluid flows through an electrically heated pipe that is insulated on the outside. To calculate the surface temperature of the heated wall, one would need the heat transfer coefficient, as well as the boundary values namely, electrical heat input, fluid inlet temperature and the flow rate. This problem can be accurately calculated in one dimension.

A one-dimensional finite volume discretisation yields control volumes, each with a single average solid wall temperature and a single average fluid temperature, as shown in Figure 6.2.

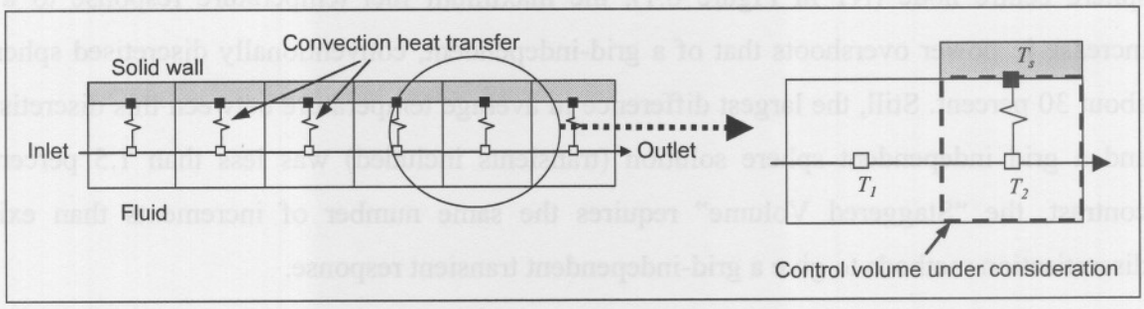


Figure 6.2. A one-dimensional discretisation of fluid passing through a heated solid with the domain discretisation on the left and the control-volume detail on the right.

In Figure 6.2 and in Eq.(6.6), T_1 is the inlet temperature of the control volume under consideration, i.e. the outlet temperature of the upstream control volume. As the heat generation per control volume is fixed, the temperature rises (i.e. the control-volume exit temperature T_2) can be found from conservation of energy:

$$Q = mc_p\left(T_2 - T_1\right) \tag{6.6}$$

As the heat is transferred to the fluid by means of convection, it can be said that

$$Q = hA(T_s - T_2) \tag{6.7}$$

with h the control volume heat transfer coefficient and T_s the solid temperature. Equating Eq.(6.6) and Eq.(6.7) and solving for T_s it is found that

$$T_s = \frac{mc_p(T_2 - T_1)}{hA} + T_2 \tag{6.8}$$

The situation in the control volume is illustrated in Figure 6.3.

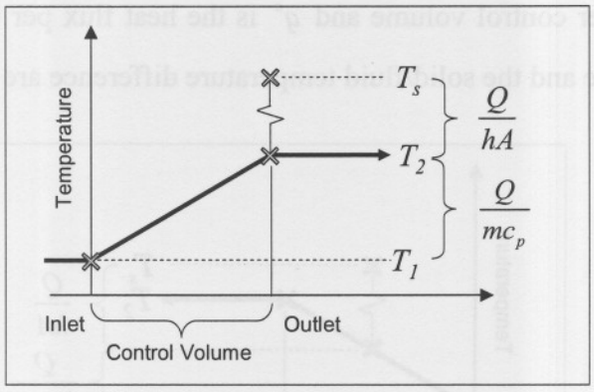


Figure 6.3. Temperature rise in a control volume, as well as solid/fluid temperature difference when Eq.(6.8) is used for calculating solid temperature.

The solution of T_s from Eq.(6.8) is only first-order accurate as Q in (6.6) is the heat addition between points 1 and 2 in Figure 6.2, while Q in Eq.(6.7) is the convection heat transfer across the boundary of the control volume to T_2. A more accurate discretisation will be as shown in Figure 6.4.

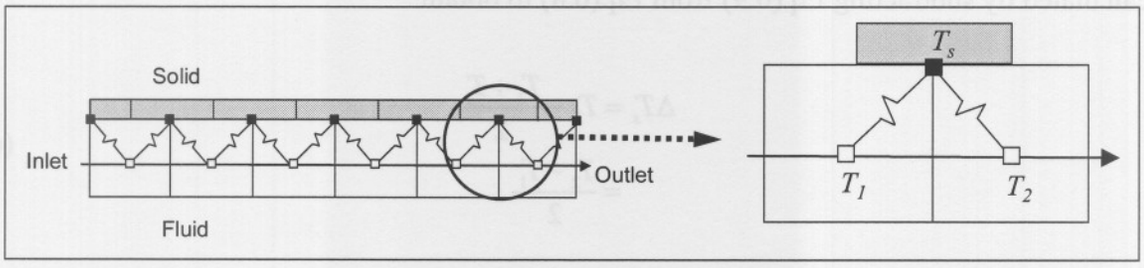


Figure 6.4. A convection heat transfer scheme that is second-order accurate.

For the discretisation in Figure 6.4, it follows from energy conservation that

$$Q = hA\left(T_s - \frac{T_1 + T_2}{2}\right) = mc_p\left(T_2 - T_1\right)$$
$$\Rightarrow T_s = \frac{mc_p\left(T_2 - T_1\right)}{hA} + \frac{T_1 + T_2}{2} \quad (6.9).$$

It can be shown that T_s is also given by

$$T_s = T_1 + \frac{q''A}{2mc_p} + \frac{q''A}{hA} \quad (6.10)$$

where A is the area per control volume and q'' is the heat flux per unit area. The temperature rise per control volume and the solid/fluid temperature difference are shown in Figure 6.5.

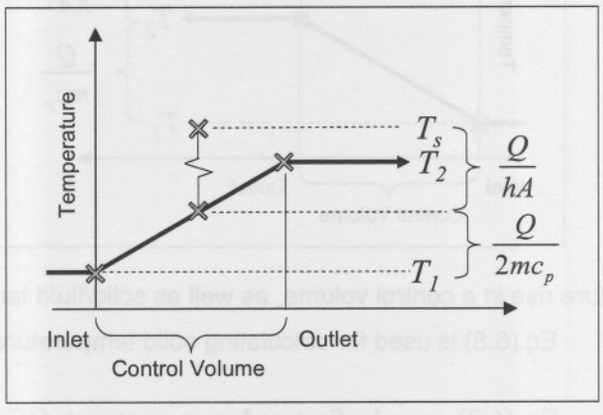


Figure 6.5. Temperature rise and solid/fluid temperature difference when the fluid average temperature is used.

The solid temperature difference between the two discretisation schemes ΔT_s can easily be calculated by subtracting Eq.(6.9) from Eq.(6.8) to obtain

$$\Delta T_s = T_2 - \frac{T_2 + T_1}{2} = \frac{T_2 - T_1}{2} \quad (6.11).$$

Eq.(6.11) states that the error in the first-order scheme (meant as its difference from the second-order scheme) is proportional to the temperature rise ($T_2 - T_1$) per control volume. But as the temperature rise ($T_2 - T_1$) equals Q/mc_p and Q equals the heat flux multiplied by area A, it follows that

$$\Delta T_s = \frac{q''A}{2\dot{m}c_p} \qquad (6.12).$$

From Eq.(6.12) it can be seen that for fixed heat flux and constant specific heat c_p, the error is proportional to the area per control volume A and inversely proportional to the mass flow m, which implies that solid temperature accuracy increases with increasing mass flow and decreasing grid size.

The fact that the second scheme (Eq.(6.9), convection to average temperature) is second-order accurate implies that it will require much less increments to give a grid-independent solid temperature than the first scheme (Eq.(6.8), convection to control volume outlet temperature). This was demonstrated by Olivier (2005) in his research on the network discretisation of heat exchangers.

However, convection heat transfer to the average fluid temperature is complicated by a boundedness issue. Referring to Figure 6.6, the fluid exit temperature can exceed the solid temperature when $1/(hA)$ becomes smaller than $1/(2\dot{m}c_p)$.

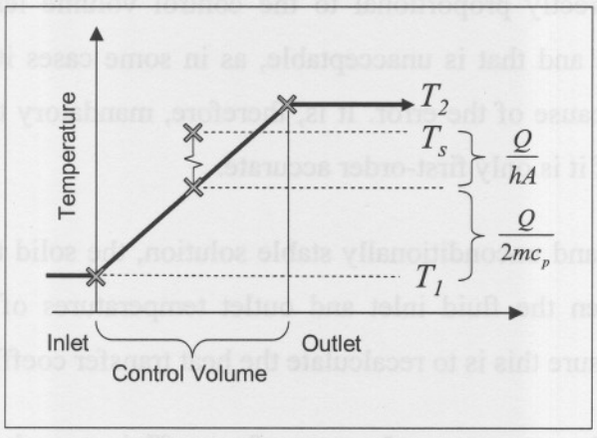


Figure 6.6. When solid temperature is coupled to fluid average fluid temperature, the fluid exit temperature is larger than solid temperature when $1/(hA) < 1/(2\dot{m}c_p)$.

Interestingly, $hA/\dot{m}c_p$ is the Stanton number, commonly used to characterise heat exchangers.

The condition $\frac{1}{hA} < \frac{1}{2\dot{m}c_p}$, can thus be rearranged to obtain

$$\frac{hA}{\dot{m}c_p} > 2 \text{ or } \mathrm{St} > 2 \qquad (6.13).$$

Thus, the outlet temperature T_2 will exceed the solid temperature T_s when the Stanton number is larger than two. Suppose this situation arises in a constant wall-temperature heat exchanger (such as a condenser), then the numerical solution for the heated fluid temperature will oscillate unrealistically as shown in Figure 6.7.

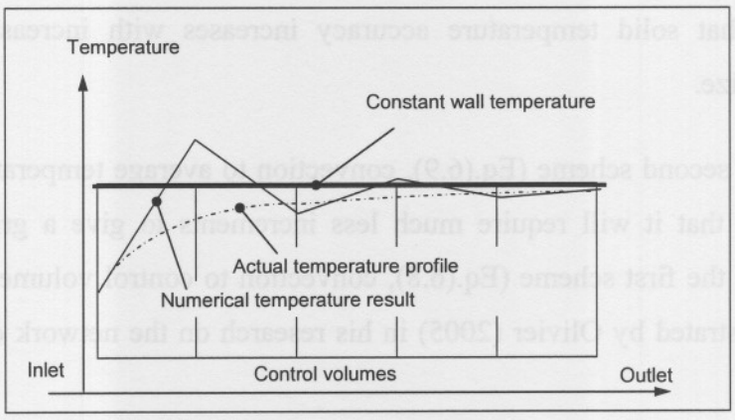


Figure 6.7. Temperature oscillations in a constant wall temperature heat exchanger due to the unboundedness of solid/average fluid temperature coupling.

The oscillations in Figure 6.7 can be overcome by grid refinement, as the area per control volume (in hA) is directly proportional to the control volume length. Still, the method is essentially unbounded and that is unacceptable, as in some cases it can prevent convergence and thereby hide the cause of the error. It is, therefore, mandatory to have an unconditionally stable solution, even if it is only first-order accurate.

To ensure a bounded and unconditionally stable solution, the solid temperature must never be in the interval between the fluid inlet and outlet temperatures of the control volume. The simplest method to ensure this is to recalculate the heat transfer coefficient.

In the solution algorithm, a new area/heat transfer coefficient product $(hA)^*$ can be calculated when T_s equals T_2. By setting $(hA)^*$ equal to $2\dot{m}c_p$, the Stanton number is equal to two and the solution will be bounded and stable, with the temperature relations as shown in Figure 6.8.

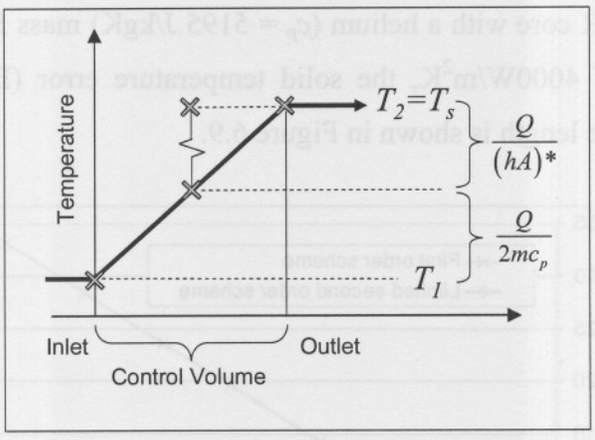


Figure 6.8. Temperature relations for a bounded solution by modifying the convection heat transfer resistance.

Mathematically it means replacing hA in Eq.(6.9) with $2mc_p$ to obtain

$$T_s = \frac{mc_p(T_2 - T_1)}{2mc_p} + \frac{T_1 + T_2}{2}$$
$$T_s = \frac{T_2 - T_1}{2} + \frac{T_1 + T_2}{2} \tag{6.14}$$
$$\therefore T_s = T_2$$

which proves that T_s will be limited. The error $\Delta T_{s,2nd}$ caused by this limiting method is found by subtracting T_s from T_2, with T_s calculated with Eq.(6.10) and T_2 replaced by $T_1 + q''A/mc_p$ as follows

$$\Delta T_{s,2nd} = T_2 - T_s$$
$$= T_1 + \frac{q''A}{mc_p} - \left(T_1 + \frac{q''A}{2mc_p} + \frac{q''A}{hA} \right) \tag{6.15}$$
$$\therefore \Delta T_{s,2nd} = \frac{q''A}{2mc_p} - \frac{q''}{h}$$

The above equation states that the limiting method also causes an error proportional to control volume area A, thus to control volume size. Still, the error is only present when hA is larger than $2mc_p$ and it is smaller than the error of the first-order method (Eq.(6.12)) by q''/h.

For the 400MW PBMR core with a helium (c_p = 5195 J/kgK) mass flow of 185kg/s and a heat transfer coefficient of 4000W/m^{2}K, the solid temperature error (Eqs.(6.12) and (6.15)) for varying control volume length is shown in Figure 6.9.

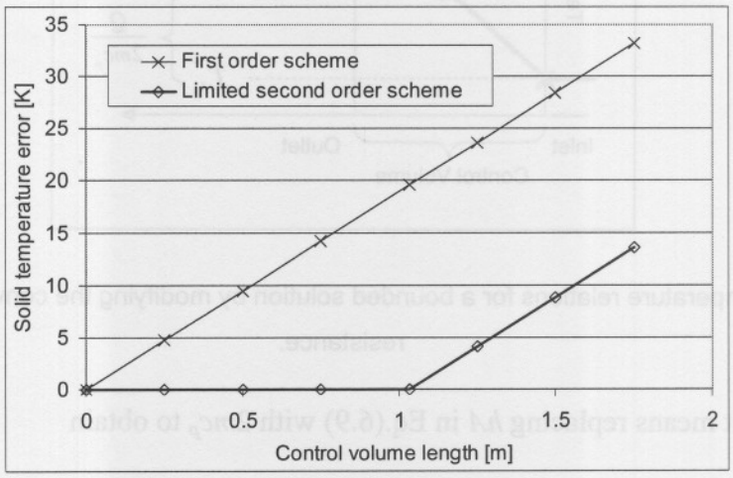


Figure 6.9. Error (per control volume) as calculated with Eqs.(6.12) and (6.15), as a function of increment size for the PBMR pebble bed core at full power and mass flow. $hA/2mc_p$ equals one at an increment length of 1.033m.

As the number of increments are inversely proportional to the grid size, Figure 6.9 is redrawn to represent a typical grid-dependence study in Figure 6.10, showing the number of axial increments required for the PBMR reactor core at full power and full mass flow.

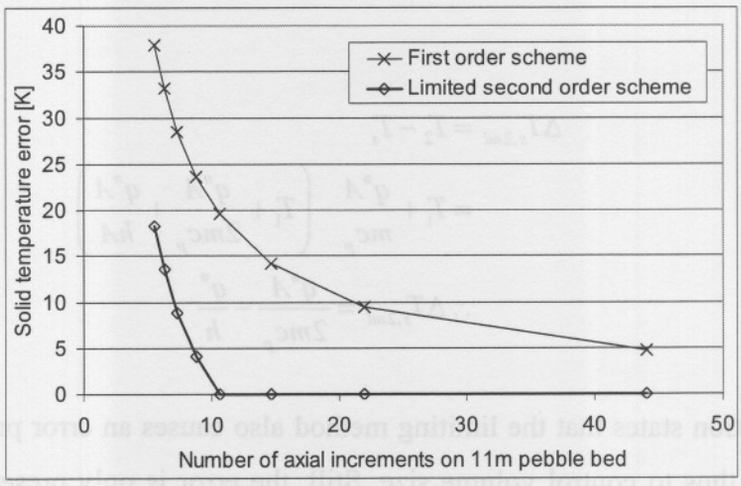


Figure 6.10. Data from Figure 6.9, in the form of a typical grid dependence test.

As solution time is proportional to the number of increments, it will be insightful to compare the number of increments for the two schemes to give the same error. For that purpose, the x and y axes in Figure 6.10 are switched to give Figure 6.11.

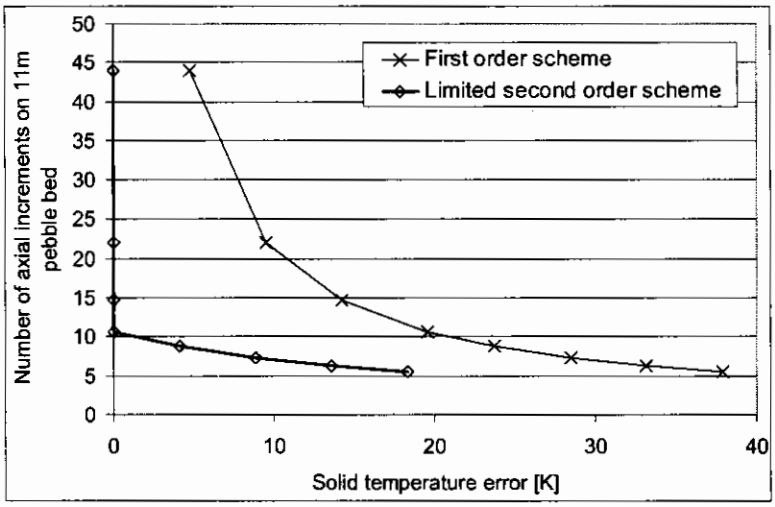


Figure 6.11. Number of axial increments for the PBMR core (400 MW, full mass flow) as a function of the desired error. In general, solution time is proportional to the number of increments.

Figure 6.11 shows that the first-order scheme can be expected to take much longer to solve to the same level of accuracy than the second-order scheme.

6.3.2 Two-dimensional case

For the one-dimensional case described above, the inlet and outlet temperatures are well-defined, as there is only one inlet and one outlet to a control volume. For the two-dimensional case in a porous medium such as the pebble bed, there are multiple inlets and outlets to a control volume. The outlet temperature of a node is well-defined and it will be the same at every outlet. The inlet temperature is not well-defined and differs, together with mass flow, from inlet to inlet.

To consider the implementation of convection heat transfer in two dimensions, consider the control volume in Figure 6.12, which will be used as a case study. It is discretised into solid and fluid nodes that are coupled by convection heat transfer.

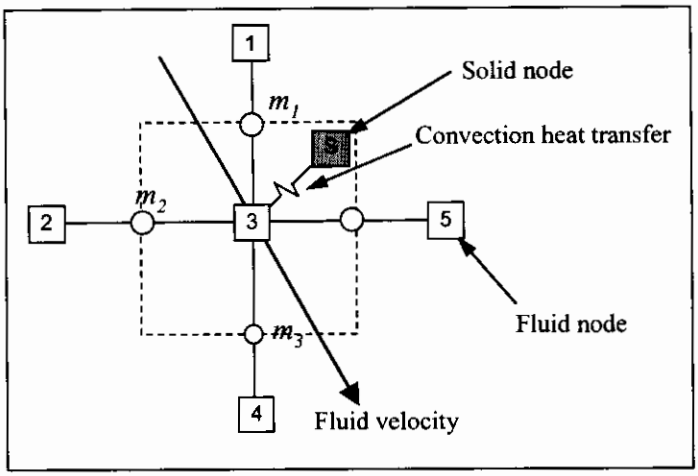


Figure 6.12. Nodes for explaining the treatment of convection heat transfer in two dimensions.

6.3.3 First-order accurate convection heat transfer in two dimensions

The simplest convection discretisation is first-order accurate and it is applied to the case study in Figure 6.12 by calculating convection heat transfer with the equation

$$Q = hA\left(T_s - T_3\right) \tag{6.16}$$

For incompressible flow, the energy equations for nodes 3 and s are then given by

$$\begin{aligned} \frac{de_3}{dt} &= hA\left(T_s - T_3\right) + \dot{m}_1 e_1 + \dot{m}_2 e_2 - \dot{m}_4 e_3 - \dot{m}_5 e_3 \\ m_s c \frac{dT_s}{dt} &= \dot{Q} - hA\left(T_s - T_3\right) \end{aligned} \tag{6.17}$$

where e is enthalpy, c the solid node specific heat, $\dot{Q}$ the heat generation in the solid node, m_s the solid node mass and m_3 the fluid node mass, assuming constant fluid density. $\dot{m}_4$ and $\dot{m}_5$ are outflows from node 3 and are, therefore, associated with the node enthalpy e_3. The symbol e is used for enthalpy as h is used for heat transfer coefficient.

To enable the simultaneous solution of temperature and enthalpy, define a reference temperature T_{ref} so that enthalpy e is approximated by

$$e = c_p\left(T - T_{ref}\right) \tag{6.18}.$$

As the reference temperature is fixed, its derivative with respect to time is zero. Substituting Eq.(6.18) into Eq.(6.17) gives the following for a steady-state:

$$\begin{aligned} 0 &= hA(T_s - T_3) + \dot{m}_1 c_p T_1 + \dot{m}_2 c_p T_2 - \dot{m}_4 c_p T_3 - \dot{m}_5 c_p T_3 + (+\dot{m}_1 + \dot{m}_2 - \dot{m}_4 - \dot{m}_5) c_p T_{ref} \\ 0 &= \dot{Q} - hA(T_s - T_3) \end{aligned} \quad (6.19).$$

For steady-state and incompressible flow, the reference temperature term in the above equation is zero due to mass conservation, so that Eq.(6.19) can be rearranged as follows

$$\begin{aligned} hAT_s \quad -(hA + \dot{m}_4 c_p + \dot{m}_5 c_p) T_3 &= -(\dot{m}_1 c_p T_1 + \dot{m}_2 c_p T_2) \\ -hAT_s \quad +hAT_3 &= -\dot{Q} \end{aligned} \quad (6.20).$$

T_1 and T_2 are considered boundary values so that T_s and T_3 can be solved from the above set of equations. T_s is calculated with first-order accuracy by Eq.(6.20).

6.3.4 Implicit method for second-order convection heat transfer in two dimensions

For second-order accurate convection discretisation, the convection heat transfer has to be divided between the flow streams connected to a node and between upstream and downstream node per fluid stream as shown in Figure 6.13.

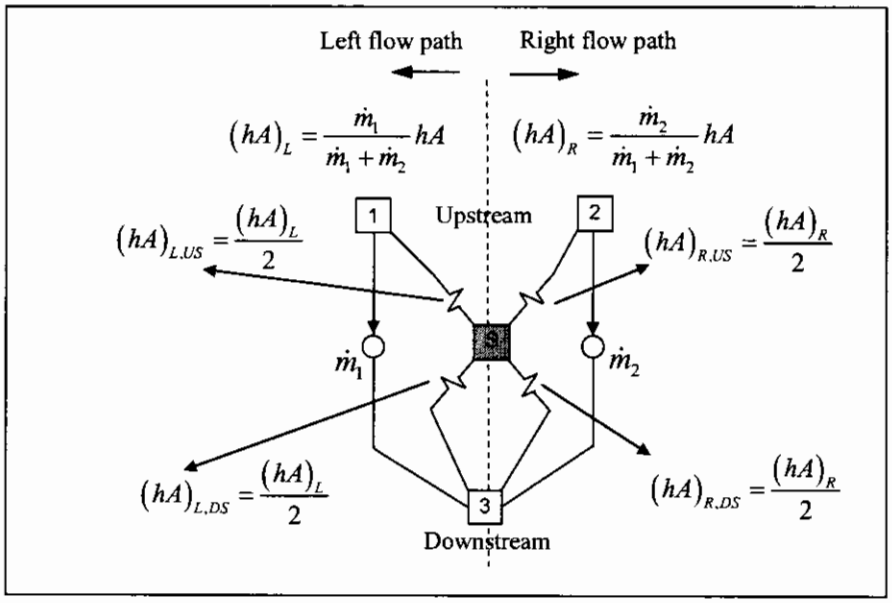


Figure 6.13. Division of the convection heat transfer between two flow streams according to mass flow. Left and Right are used for ease of explanation, but the method of division holds for any number of inlet flow streams to node 3.

With the division of hA as done in Figure 6.13, the energy equations of the applicable nodes are given by

$$
\begin{aligned}
m_s c\frac{dT_s}{dt} &= \dot{Q} - \frac{hA}{2}\left(T_s - T_3\right) - \frac{hA}{2}\frac{\dot{m}_1}{\dot{m}_1+\dot{m}_2}\left(T_s - T_1\right) - \frac{hA}{2}\frac{\dot{m}_2}{\dot{m}_1+\dot{m}_2}\left(T_s - T_2\right) \\
m_1\frac{de_1}{dt} &= \frac{hA}{2}\frac{\dot{m}_1}{\dot{m}_1+\dot{m}_2}\left(T_s - T_1\right) - \dot{m}_1 e_1 + \dot{m}_A e_A \\
m_2\frac{de_2}{dt} &= \frac{hA}{2}\frac{\dot{m}_2}{\dot{m}_1+\dot{m}_2}\left(T_s - T_2\right) - \dot{m}_2 e_2 + \dot{m}_B e_B \\
m_3\frac{de_3}{dt} &= \frac{hA}{2}\left(T_s - T_3\right) + \dot{m}_1 e_1 + \dot{m}_2 e_2 - \dot{m}_4 e_3 - \dot{m}_5 e_3
\end{aligned}
\qquad (6.21).
$$

with $\dot{m}_A e_A$ and $\dot{m}_B e_B$ being the inlet boundary flows into nodes 1 and 2.

Replacing enthalpy with Eq.(6.18), Eq.(6.21) can be rearranged for steady-state conditions as

$$
\begin{aligned}
0 &= \dot{Q} - \left(\frac{hA}{2} + \frac{hA}{2}\frac{\dot{m}_1}{\dot{m}_1+\dot{m}_2} + \frac{hA}{2}\frac{\dot{m}_2}{\dot{m}_1+\dot{m}_2}\right)T_s + \left(\frac{hA}{2}\right)T_3 + \frac{hA}{2}\frac{\dot{m}_1}{\dot{m}_1+\dot{m}_2}T_1 + \frac{hA}{2}\frac{\dot{m}_2}{\dot{m}_1+\dot{m}_2}T_2 \\
0 &= \frac{hA}{2}\frac{\dot{m}_1}{\dot{m}_1+\dot{m}_2}T_s - \left(\frac{hA}{2}\frac{\dot{m}_1}{\dot{m}_1+\dot{m}_2} + \dot{m}_1 c_p\right)T_1 + \dot{m}_A c_p T_A \\
0 &= \frac{hA}{2}\frac{\dot{m}_2}{\dot{m}_1+\dot{m}_2}T_s - \left(\frac{hA}{2}\frac{\dot{m}_2}{\dot{m}_1+\dot{m}_2} + \dot{m}_2 c_p\right)T_2 + \dot{m}_B c_p T_B \\
0 &= \frac{hA}{2}T_s + \dot{m}_1 c_p T_1 + \dot{m}_2 c_p T_2 - \left(\dot{m}_4 c_p + \dot{m}_5 c_p + \frac{hA}{2}\right)T_3
\end{aligned}
\qquad (6.22).
$$

The above equation set can be rearranged in matrix formulation as

$$
\begin{bmatrix}
-\left(\frac{hA}{2}\frac{\dot{m}_1}{\dot{m}_1+\dot{m}_2} + \dot{m}_1 c_p\right) & 0 & 0 & \frac{hA}{2}\frac{\dot{m}_1}{\dot{m}_1+\dot{m}_2} \\
0 & -\left(\frac{hA}{2}\frac{\dot{m}_2}{\dot{m}_1+\dot{m}_2} + \dot{m}_2 c_p\right) & 0 & \frac{hA}{2}\frac{\dot{m}_2}{\dot{m}_1+\dot{m}_2} \\
\dot{m}_1 c_p & \dot{m}_2 c_p & -\left(\dot{m}_4 c_p + \dot{m}_5 c_p + \frac{hA}{2}\right) & \frac{hA}{2} \\
\frac{hA}{2}\frac{\dot{m}_1}{\dot{m}_1+\dot{m}_2} & \frac{hA}{2}\frac{\dot{m}_2}{\dot{m}_1+\dot{m}_2} & \frac{hA}{2} & -\left(\frac{hA}{2} + \frac{hA}{2}\frac{\dot{m}_1}{\dot{m}_1+\dot{m}_2} + \frac{hA}{2}\frac{\dot{m}_2}{\dot{m}_1+\dot{m}_2}\right)
\end{bmatrix}
\begin{bmatrix} T_1 \\ T_2 \\ T_3 \\ T_s \end{bmatrix}
=
\begin{bmatrix} -\dot{m}_A c_p T_A \\ -\dot{m}_B c_p T_B \\ 0 \\ -\dot{Q} \end{bmatrix}
\qquad (6.23)
$$

where T_A , T_B and $\dot{Q}$ are boundary values so that the system of equations can be solved for node temperatures T_1,T_2,T_3 and T_s. Solid temperature T_s can be solved with second-order accuracy. The above set of equations can be referred to as the implicit implementation of second-order convection heat transfer in two dimensions because all node temperatures can be solved directly.

Remember that in Figure 6.13, the solid node connects to node 1 and node 2 because of the flow direction in the case study of Figure 6.12. If the flow direction changes, other nodes will be connected to the solid node. Also note in Eq.(6.23) that the energy equations for node 1 and node 2 contain mass flow terms from elements that are not connected to them, which is not desirable, as it requires considerable bookkeeping in the solution algorithm. This bookkeeping is complicated further by the fact that the flow direction determines which element mass flows are used. Figure 6.14 presents the network representation of this second-order convection discretisation, as described by Eq.(6.23).

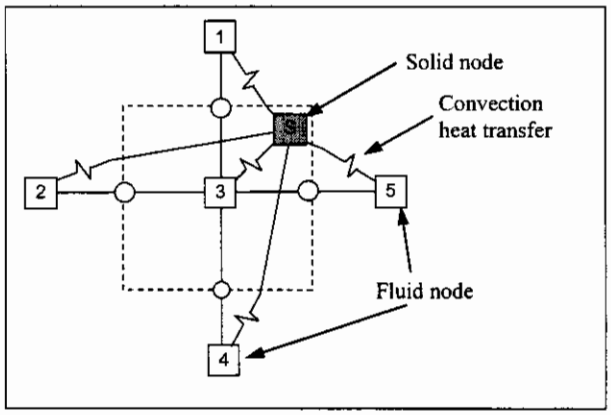


Figure 6.14. The network topology for an implicit implementation of second-order accurate convection heat transfer in two dimensions. Note that when a convection heat transfer element links the solid node to an outflow node, its convection heat transfer coefficient is set to zero.

It is concluded that the implicit implementation of second-order accuracy convection heat transfer in two dimensions (Eq.(6.23) and Figure 6.14) is impractical due to the difficult bookkeeping it requires.

6.3.5 Explicit method for second-order convection heat transfer in two dimensions

An alternative method to implement second-order accurate convection heat transfer in two dimensions is to explicitly calculate a representative inlet temperature to a fluid node.

To calculate a representative inlet temperature, consider the control volume in Figure 6.12 where there is inflow to node 3 from nodes 1 and 2 and outflow to nodes 4 and 5. Therefore, the heat Q transferred from the solid to the fluid stream into node 3 is described by

$$\begin{aligned} Q &= m_2 c_p \left(T_3 - T_2\right) + m_1 c_p \left(T_3 - T_1\right) \\ &= m_2 c_p T_3 - m_2 c_p T_2 + m_1 c_p T_3 - m_1 c_p T_1 \\ &= c_p \left(\left(m_2 + m_1\right) T_3 - \left(m_2 T_2 + m_1 T_1\right)\right) \\ &= \left(m_2 + m_1\right) c_p \left(T_3 - \frac{m_2 T_2 + m_1 T_1}{m_2 + m_1}\right) \end{aligned} \tag{6.24}.$$

Define the total mass flow m_T as the sum of inflows, i.e. $\left(m_2 + m_1\right)$ and the representative inflow temperature T_{in} as the following massflow-averaged value

$$T_{in} = \frac{\sum_{\text{inflow}} m_i T_i}{\sum_{\text{inflow}} m_i} = \frac{m_2 T_2 + m_1 T_1}{m_2 + m_1} \tag{6.25}.$$

Eq.(6.24) then simplifies to

$$Q = m_T c_p \left(T_3 - T_{in}\right) \tag{6.26}$$

As for the one-dimensional case, a first-order accurate equation for convection heat transfer is

$$Q = hA\left(T_s - T_3\right) \tag{6.27}.$$

The second-order accurate approximation for convection heat transfer is then given by

$$Q = hA\left(T_s - \frac{T_3 + T_{in}}{2}\right) \tag{6.28}$$

To explain the implementation of the above second-order accurate equation, the convection heat transfer terms in Eq.(6.17) are replaced with Eq.(6.28) to obtain

$$\begin{aligned} m_s c \frac{dT_s}{dt} &= \dot{Q} - hA\left(T_s - \frac{T_3}{2} - \frac{T_{in}}{2}\right) \\ m_3 \frac{de_3}{dt} &= hA\left(T_s - \frac{T_3}{2} - \frac{T_{in}}{2}\right) + \dot{m}_1 e_1 + \dot{m}_2 e_2 - \dot{m}_4 e_3 - \dot{m}_5 e_3 \end{aligned} \tag{6.29}.$$

where e is fluid enthalpy, and c is the solid specific heat.

Rewriting Eq.(6.29) for steady-state after substituting all enthalpy terms with Eq.(6.18) results in

$$\begin{aligned} -hAT_s \quad & +\frac{hA}{2}T_3 \quad = \quad -\dot{Q}-\frac{hA}{2}T_{in} \\ hAT_s \quad & -\left(\frac{hA}{2}+\dot{m}_4c_p+\dot{m}_5c_p\right)T_3 \quad = \quad -\left(\dot{m}_1c_pT_1+\dot{m}_2c_pT_2\right)-\frac{hA}{2}T_{in} \end{aligned} \tag{6.30}$$

which can be rewritten in matrix form as

$$\begin{bmatrix} -\left(\frac{hA}{2}+\dot{m}_4c_p+\dot{m}_5c_p\right) & hA \\ \frac{hA}{2} & -hA \end{bmatrix} \begin{bmatrix} T_3 \\ T_s \end{bmatrix} = \begin{bmatrix} -\left(\dot{m}_1c_pT_1+\dot{m}_2c_pT_2\right)-\frac{hA}{2}T_{in} \\ -\dot{Q}-\frac{hA}{2}T_{in} \end{bmatrix} \tag{6.31}.$$

T_1 and T_2 can be considered boundary values for this system, so that T_{in} can be calculated directly with Eq.(6.25). T_s and T_3 can then be solved from the above equation with T_s calculated second-order accurate. In practice, however, it is necessary to explicitly calculate the representative inlet temperature T_{in} between each solution iteration. This explicit method presents a simple and practical way to implement second-order accurate convection heat transfer in two dimensions.

The boundedness issue described in Section 6.3.3 applies to two dimensions as well and it is treated in the same way, namely by ensuring that the Stanton number St is smaller that two. In two-dimensional flow, the Stanton number is based on the total mass flow $\dot{m}_T$ as follows

$$\mathrm{St}=\frac{hA}{\dot{m}_Tc_p} \tag{6.32}.$$

Unboundedness is prevented by setting hA equal to $2\dot{m}_Tc_p$ whenever

$$\frac{hA}{\dot{m}_Tc_p}>2 \text{ or } \mathrm{St}>2 \tag{6.33}.$$

A general form of Eq.(6.31) and the limiting methods of Eqs.(6.32) and (6.33) were implemented in the Flownex Generation IV reactor model and tested. No difference in solution time was noticed when compared with the simpler first-order accuracy convection heat transfer scheme.

From the limiting equation $hA = 2\dot{m}c_p$, a maximum increment size can be calculated for which the second-order accurate convection discretisation is grid independent.

To find the relation between increment length and heat transfer, the ratio of heat transfer area A (i.e. sphere surface area A_{sph}) to pebble bed volume V_{bed} is given by

$$\begin{aligned} \frac{A_{sph}}{V_{bed}} &= \frac{A_{sph}}{V_{sph}} \frac{V_{sph}}{V_{bed}} \\ \frac{A_{sph}}{V_{bed}} &= \frac{4\pi r^2}{\frac{4}{3}\pi r^3}(1-\varepsilon) \\ \therefore A &= \frac{3}{r}(1-\varepsilon)V_{bed} \end{aligned} \tag{6.34}$$

where r is the fuel sphere diameter and ε is the control volume porosity. As the size of the control volume is the product of control volume face area (or superficial flow area) A_{face} and increment length Δx, it can be said that

$$A = \frac{6}{d}(1-\varepsilon)\Delta x A_{face} \tag{6.35}$$

with d being the fuel sphere diameter. Replace the heat transfer area in the limiting equation $hA = 2\dot{m}c_p$ with Eq.(6.35) and rearrange to obtain

$$\Delta x = \frac{\dot{m}c_p d}{3(1-\varepsilon)hA_{face}} \tag{6.36}$$

For a helium-cooled pebble bed reactor core in which d is 0.06m, the specific heat for helium c_p is 5195 J/kgK and porosity ε is 0.39, while the heat transfer coefficient h is calculated with the Kugeler-Schulten correlation Eq.(5.17). With Eq.(6.36), the maximum grid size can be calculated for various gas temperatures and mass fluxes (i.e. $\dot{m}/A_{face}$ ratios), as shown in Figure 6.15.

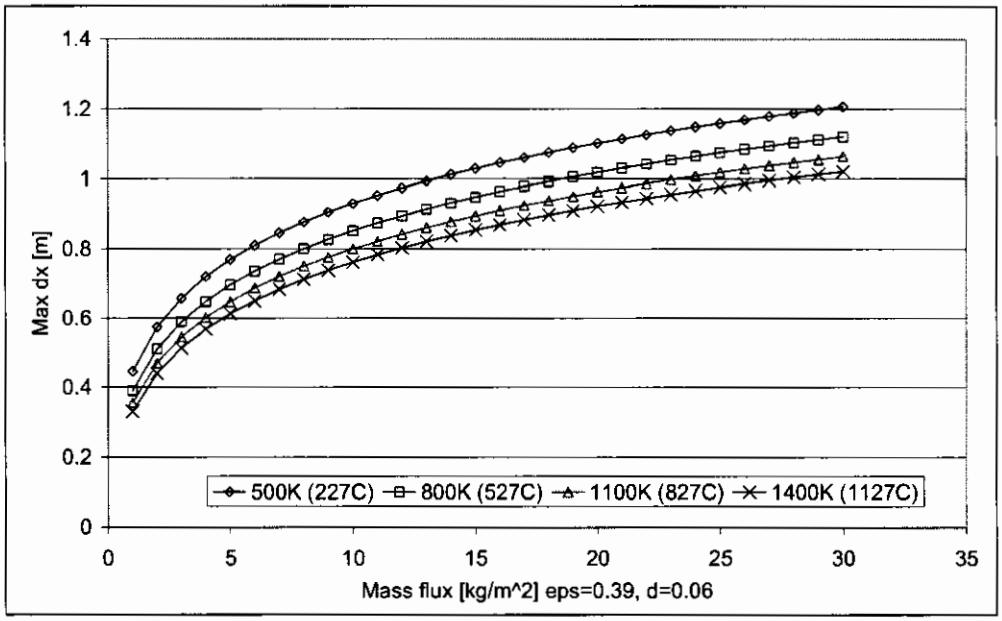


Figure 6.15. Maximum grid length values for which convection heat transfer can be calculated unconditionally stable to second-order accuracy, as a function of superficial mass flux for a helium-cooled pebble bed HTR core at four different fluid temperatures.

The maximum grid length values in Figure 6.15 are a function of temperature, due to the fluid property temperature dependence, as the heat transfer coefficient depends on both fluid density and fluid conductivity.

At full mass flow, the PBMR operates with a mass flux in the order of 24 kg/m^2, requiring a grid size of at least 0.9m to obtain a grid independent solid temperature solution with.

Thus, this section presented a simple method to obtain second-order accuracy for convection heat transfer calculation in two dimensions. It requires much less increments in the flow direction than a first-order scheme to give grid independent solid temperatures. This is a great advantage as the reduction in the number of nodes drastically reduces calculation time.

6.3.6 Flow direction dependency

The convection discretisation methods described in the preceding paragraphs are not influenced by the direction of the flow. This is clear when one considers that for a constant mass flow per unit area and constant heat generation, the average temperature in a control volume is constant, regardless of the direction of the flow. The only temperature phenomenon that is direction-dependent is numerical diffusion, associated with first-order upwind differencing in convective flow discretisations. This phenomenon is well-known and many discretisations schemes have been proposed to increase accuracy, as described in the textbooks by Ferziger and Peric (1999)

or Versteeg and Malalasekera (1995). However, none of these methods are considered applicable to the network-approach for system simulation.

Numerical diffusion is demonstrated in Figure 6.16 on a square cartesian grid with incompressible flows of different temperatures and the same velocities from both directions. The calculated temperature profile is clearly highly grid-dependent.

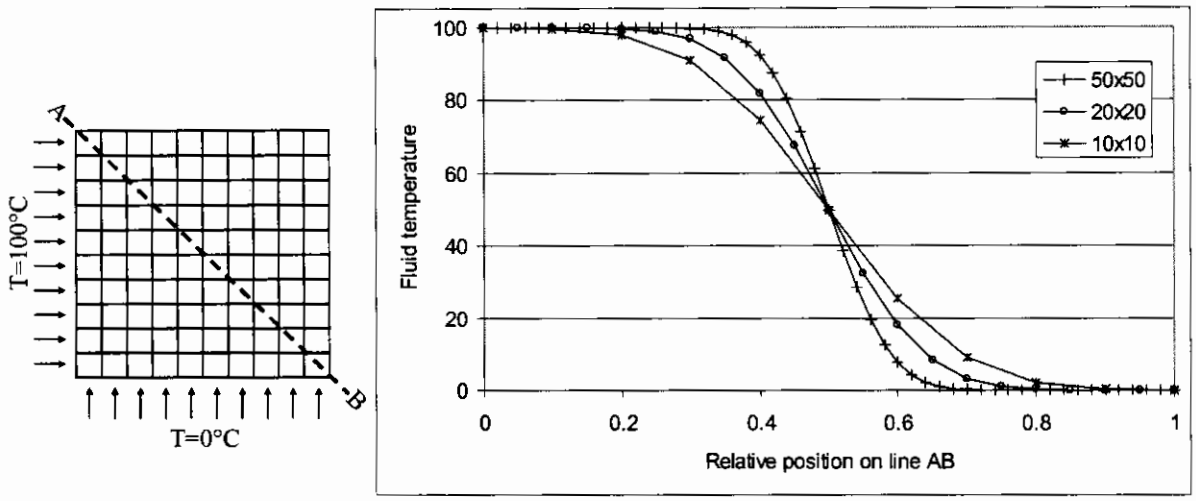


Figure 6.16. A demonstration of the grid dependence of numerical diffusion in a convective heat transport problem. It shows fluid temperature on the diagonal line AB, for three grid refinements.

The diagonal temperature profile across two mixing flow streams (similar to Figure 6.16) was also calculated for a case where there was convection heat transfer from a solid over the whole domain. For this case, the effect of convection discretisation on solid temperature was exactly the same as for one-dimensional or other two-dimensional flows, namely that the second-order scheme gave lower, more accurate solid temperatures.

This steady-state result is valid for any two-dimensional case in which a solid exchanges heat with a passing fluid because the only difference between various cases (i.e. a flat plate, a heat exchanger or a porous medium) is the ratio of flow heat capacity $\left(\dot{m}c_p\right)$ to convection heat transfer capacity $\left(hA\right)$.

6.4 Pebble bed/wall heat transfer correlations

As stated in Section 4.9.5, the pseudo-heterogeneous pebble bed model introduced by Du Toit *et al.* (2003) requires explicit correlations for the pebble bed/wall contact resistance, as well as

the fluid/wall resistance. The network topology created according to the control-volume based scheme for this pseudo-heterogeneous approach is repeated in Figure 4.37 below, for convenience.

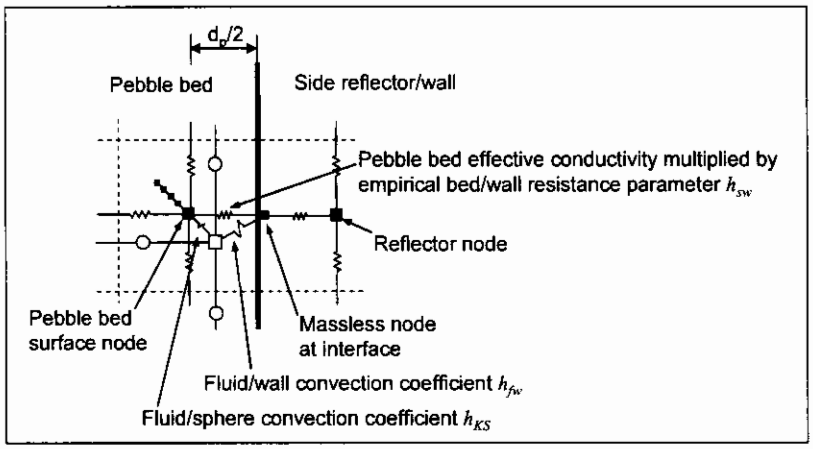


Figure 6.17. The pebble bed/wall topology for the control-volume based discretisation. Mathematical descriptions of h_{sw} and h_{fw} are given in Eqs. (6.37) and (6.38).

As there are presently no correlations available for either the solid contact resistance or the fluid/wall heat transfer coefficient, the PBMR company decided to address this issue by building a test facility to, amongst others, measure these quantities. Results are expected by the end of 2007.

Until the test results become available, one has to rely on the existing knowledge base for correlations. For that purpose, consider the heat transfer mechanisms that come into play between the pebble bed and the wall, as illustrated in Figure 6.18.

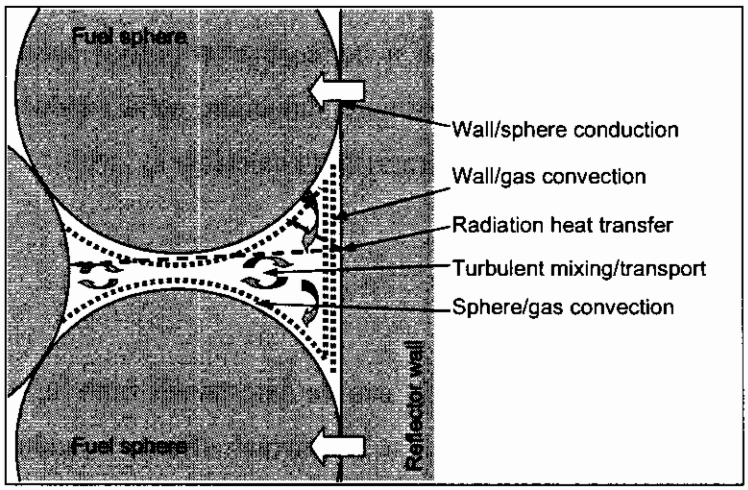


Figure 6.18. Heat transfer phenomena at the pebble bed/wall interface.

The most obvious heat transfer mode from the wall is convection heat transfer to the interstitial fluid, as it has the largest contact surface with the wall. The fluid in contact with the wall is constantly being replaced, due to the convective transport of the fluid through the bed and the associated dispersion resulting from the irregular flow paths in the porous bed. The fluid is also in constant contact with the pebbles in the bed and, therefore, exchanging heat. Conduction heat transfer from the wall to the bed takes place through contact between the wall and the pebbles, while there is also radiation heat transfer between the wall and the sphere surfaces but no radiative interaction with the working fluid, as discussed in Section 4.8.4.

As the mechanisms of heat transfer between the fluid and the wall are dependent on the same variables (porosity, interstitial spaces) as the heat transfer between the fuel spheres and the fluid, it appears plausible to assume the same qualitative relationship between heat transfer coefficient and Reynolds number as in the rest of the pebble bed. Thus, it is assumed that the fluid/wall Nusselt number Nu_{fw} would equal some empirical constant C_{fw} multiplied by the Kugeler-Schulten heat transfer correlation Nu_{KS}, the fluid/sphere Nusselt number correlation, i.e.

$$\mathrm{Nu}_{fw} = C_{fw}\mathrm{Nu}_{KS} \tag{6.37}$$

Similarly, the combined effect of sphere contact resistance, sphere-to-sphere radiation and gas conduction are all treated in the Zehner-Schlunder equation, so that it is assumed the pebble bed/wall contact resistance h_{sw} will equal some empirical constant C_{sw} multiplied by the Zehner-Schlunder correlation k_{ZS}. As mentioned in Section 4.9.5, the characteristic length to calculate the heat transfer coefficient from a conductivity is half a sphere diameter d_p, as that is the distance at which the assumption of a homogeneous porous solid breaks down. As the Zehner-Schlunder correlation takes interstitial conduction, solid conduction and radiation heat transfer into account, it is considered appropriate to calculate h_{sw} with

$$h_{sw} = C_{sw}\frac{k_{ZS}}{0.5d_p} \tag{6.38}$$

with C_{sw} being an empirical constant. C_{sw} can be determined from an experiment such as the SANA experiment (described in Section 7.2.1) in which effective conduction effects dominate, i.e. conduction and radiation heat transfer. From the SANA experiment, C_{sw} was estimated as 0.5. As published in IAEA-TECDOC-1163 (2000), other research groups also found the

bed/wall heat transfer factor C_{sw} to be 0.5 when associated with an effective conduction distance of half a sphere diameter at the wall.

An attempt was made at separate radiation and conduction models for the bed/wall heat transfer but it was considered unsuccessful on account of the grossly underestimation of the pebble bed/wall resistance in the SANA experiment. Therefore, detailed experimental work will be necessary for separating the effects of conduction and radiation. At present, the approach that gives the most accurate results is the modification of the Zehner-Schlunder effective conductivity near the wall, as described here.

To determine the fluid/wall empirical constant C_{fw}, a high mass flow case is required, as effective conduction heat transfer is negligible compared to high mass flow convection heat transfer in an HTR. For this purpose, temperature profile results from the Chinese HTR-10 reactor were used, as given in another IAEA-TECDOC (2006). At 10MW power and 4.32kg/s massflow, with dispersion heat transfer included, C_{fw} was estimated at 0.1. The details of this work are described in Section 7.3.5 and in a paper by Van der Merwe *et al.* (2006).

6.5 Heat transfer through the side reflector

The side reflector is essentially a cylindrical shell, composed of interlocking graphite blocks with vertical holes for the control rods and coolant riser channels as shown in Figure 6.19. It is represented by the network topology shown in Figure 6.20. The solid node in Figure 6.20 represents the average temperature in the control volume, which is also the temperature that exchanges heat with the flow temperature.

In the side reflector, the dominant temperature gradient is in the radial direction for both full-power operation and LOFC conditions.

During full-power operation, the side reflector is heated by gamma ray heating and by contact with the pebble bed, while it is cooled by the inlet helium in the vertical coolant flow channels. The high volume flow rate in the riser channels causes turbulent flow, a corresponding high heat transfer coefficient and a large thermal capacity, effectively fixing the reflector outer temperature and limiting outward heat loss. Under these circumstances, two-dimensional heat conduction and possible radiation across the flow channels are totally dominated by the high convection heat removal. Under LOFC conditions, the average temperature is still accurate, as a

large radial temperature gradient exists across the control volume with negligible convection heat removal.

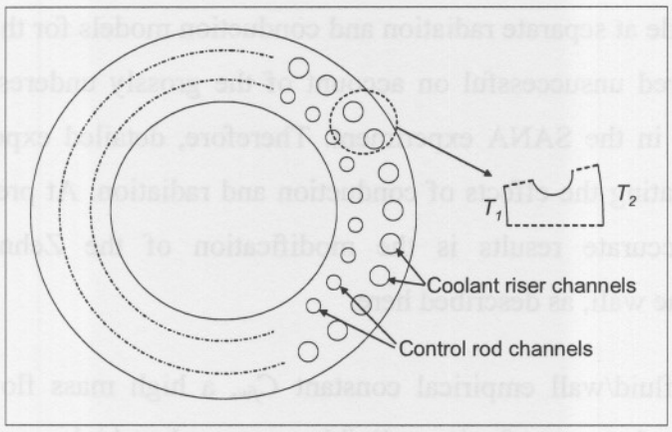


Figure 6.19. Geometry of the side reflector with holes, as well as a piece of simplified geometry.

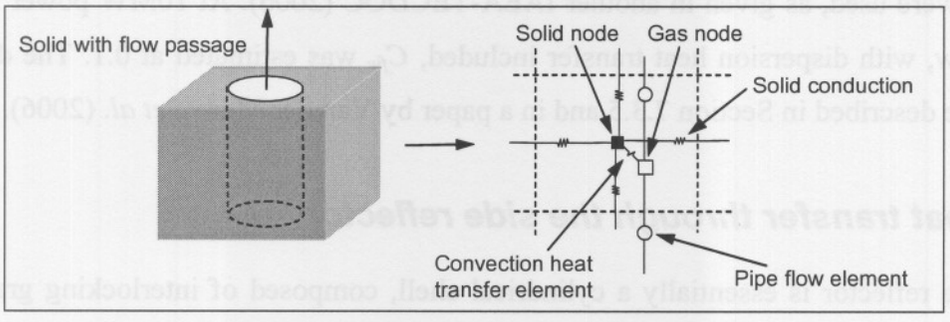


Figure 6.20. Nodes and elements used to represent a solid with one-dimensional flow through it (Figure 4.32 repeated for clarity).

When channels of different temperatures are located at the same radius, this approach will not be accurate, as the assumption of negligible tangential variation will be invalid. This situation could easily arise when control rod channels and coolant channels are located at the same radius.

During a Loss Of Forced Cooling (LOFC) incident, the flow is stagnant in the pebble bed, as well as the riser channels, so that heat radiation and conduction become significant modes of heat transfer. Calculations indicate a temperature difference of about 100°C across the riser channels at a temperature of about 750°C. Under these circumstances, the relative contribution of each phenomenon must be quantified. There could be natural circulation cells in the riser channels, combined with radiation heat transfer while both these phenomena influence the isotherms in the solid around the channels. Still, the systems simulation approach simplifies even this complex situation into a one-dimensional problem. But even though the heat transfer

phenomena have local two-dimensional features, the overall temperature gradient is one-dimensional, so that a one-dimensional approximation should be feasible.

6.5.1 Methods for calculating one-dimensional solid heat conduction

In the Generation III model, a volume-equivalent of the holed solids is used to calculate the radial conduction resistance. The volume-equivalent thermal resistance can be calculated by two methods which will be termed the "one-block" and "three-block" methods in this report.

In the one-block method, the block effective solid fraction (1-ϵ) is multiplied with the conduction shape factor for an annular ring more than two hole diameters thick. In the three-block method (which is current practice in many reactor models) the effective porosity is only calculated for, and applied to the annular ring the thickness of one hole diameter.

The one-dimensional heat transfer q for all these approximations is calculated with Fourier`s law, given by

$$\begin{aligned} q &= -kA\frac{dT}{ds} \\ \int_0^L \frac{q}{A}ds &= -\int_{T_1}^{T_2} kdT \\ q\int_0^L \frac{1}{A}ds &= -\int_{T_1}^{T_2} kdT \end{aligned} \tag{6.39}$$

Define the shape factor F as

$$\frac{1}{F} = \int_0^L \frac{1}{A}ds \tag{6.40}$$

so that

$$\frac{q}{F} = -\int_{T_1}^{T_2} kdT \tag{6.41}$$

For constant conductivity, it then follows that

$$q = -kF\left(T_2 - T_1\right) \tag{6.42}$$

F thus characterises the conduction geometry and has the dimension of length. The analytical shape factor for one-dimensional conduction through an annular solid without holes is given by

$$F = \frac{2\pi\Delta z}{\ln\left(\frac{r_o}{r_i}\right)}, \quad r_o > r_i \tag{6.43}$$

with r_o and r_i being the annulus radii and Δz the axial height of the solid.

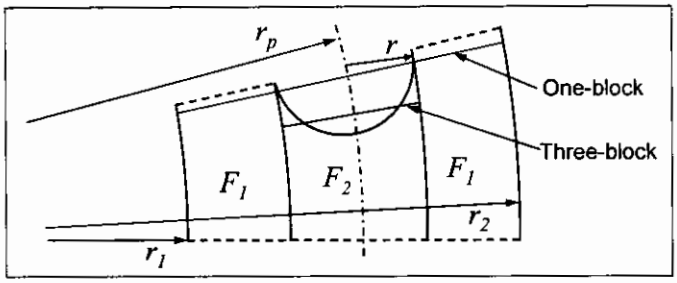


Figure 6.21. Schematic illustration of symbols, as well as the approximations used for the basic geometry of an annular shell with axial holes.

For an annular solid with N axial holes, the one-block approximation is as follows, with the geometry and symbols as shown in Figure 6.21.

$$\begin{aligned} F_{1b} &= (1-\varepsilon)\frac{2\pi\Delta z}{\ln\left(\frac{r_2}{r_1}\right)}, \quad \varepsilon = \frac{V_{hole}}{V_{tot}} \\ &= \left(1-\frac{V_{hole}}{V_{tot}}\right)\frac{2\pi\Delta z}{\ln\left(\frac{r_2}{r_1}\right)} \\ &= \left(1-\frac{N\pi r^2\Delta z}{\pi\left(r_2^2-r_1^2\right)\Delta z}\right)\frac{2\pi\Delta z}{\ln\left(\frac{r_2}{r_1}\right)} \\ &= \left(1-\frac{Nr^2}{\left(r_2^2-r_1^2\right)}\right)\frac{2\pi\Delta z}{\ln\left(\frac{r_2}{r_1}\right)} \end{aligned} \tag{6.44}$$

where r is the hole diameter. The sector between the axes of symmetry in Figure 6.21 spans an arc of only π/N radians. Therefore, F_{1b} in Eq.(6.44) has to be divided by $2N$ to obtain the correct shape factor for the sector with a half-hole in Figure 6.21.

The three-block approximation divides the conducting sector into three radial blocks, as shown in Figure 6.21. This method is used in the Generation III reactor model for treating solids with

holes. For calculating F_2 in Figure 6.21, the three-block approximation applies Eq.(6.44) to the central block containing the hole while F_1 and F_3 are calculated with Eq.(6.43). The overall shape factor is obtained by addition:

$$F_{3b} = \frac{1}{\frac{1}{F_1} + \frac{1}{F_2} + \frac{1}{F_3}} \tag{6.45}$$

When there are many holes around the circumference and the hole radius is small relative to the pitch circle radius, the geometry between the holes is assumed to be roughly approximated by rectangular geometry as shown in Figure 6.22.

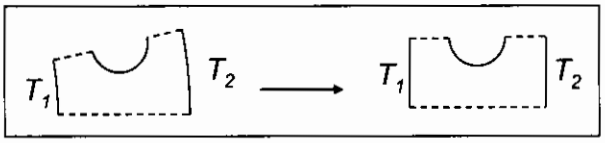


Figure 6.22. Approximation of circular geometry with rectangular geometry.

With rectangular geometry as shown in Figure 6.23, the only non-dimensional parameter necessary to quantify the geometry is the ratio of hole radius r to block width b, i.e. r/b.

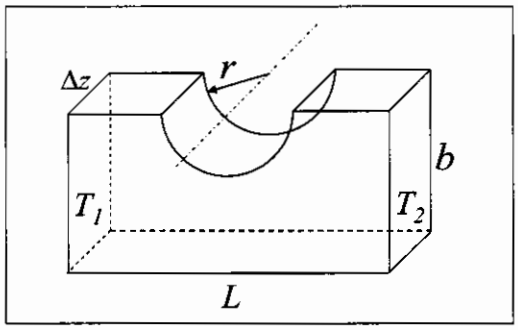


Figure 6.23. Rectangular geometry

For the circular geometry in Figure 6.21, the r/b ratio is given by

$$\frac{r}{b} = \frac{rN}{\pi r_p} \tag{6.46}$$

with r_p being the pitch circle radius. One more parameter is necessary to describe radial geometry in non-dimensional terms, namely the ratio of pitch circle radius to hole radius

$$\frac{r_p}{r} \tag{6.47}$$

The accuracy of the approximations given above was evaluated using CFD models of the rectangular and circular geometries shown in Figure 6.24.

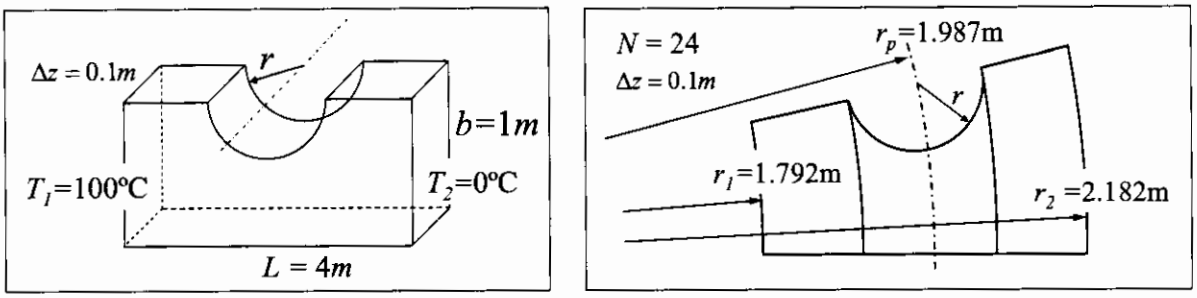


Figure 6.24. Geometries used for parametric studies into the accuracy of the one-block and three-block approximations.

The heat flow through the geometries in Figure 6.24 was calculated with the CFD grids shown in Figure 6.25.

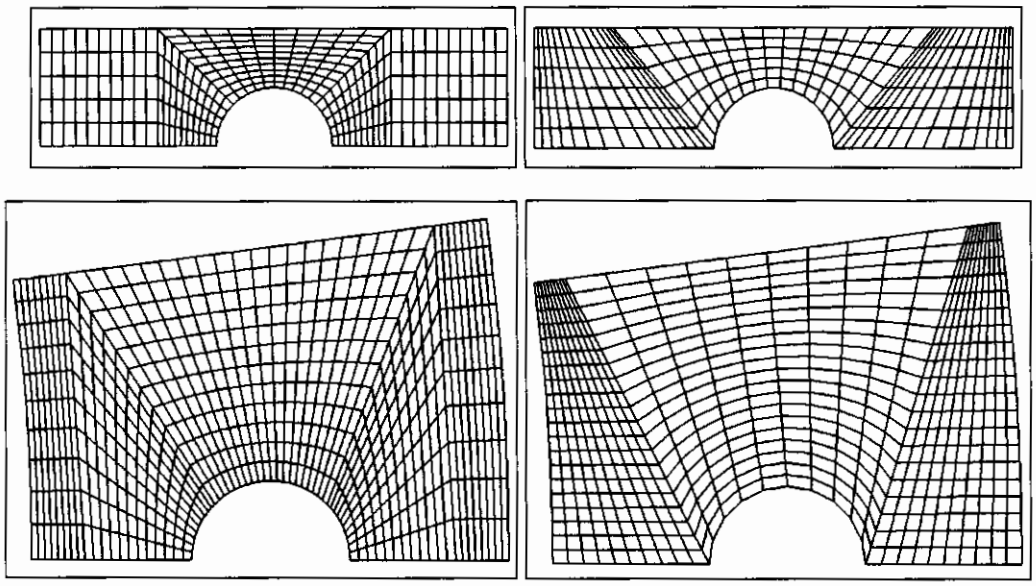


Figure 6.25. CFD grids for evaluating conduction form factors.

The temperature difference was chosen as 100°C and conductivity as 0.01W/mK, so that the numerical value of the heat flow equals the numerical value of the shape factor, i.e. the product $k(T_1-T_2)$ equals one. Heat flow was used as criterion for assessing grid dependence. When the heat flow changed less than one percent upon doubling the number of cells, the solution was considered grid-independent. A typical temperature solution is shown in Figure 6.26.

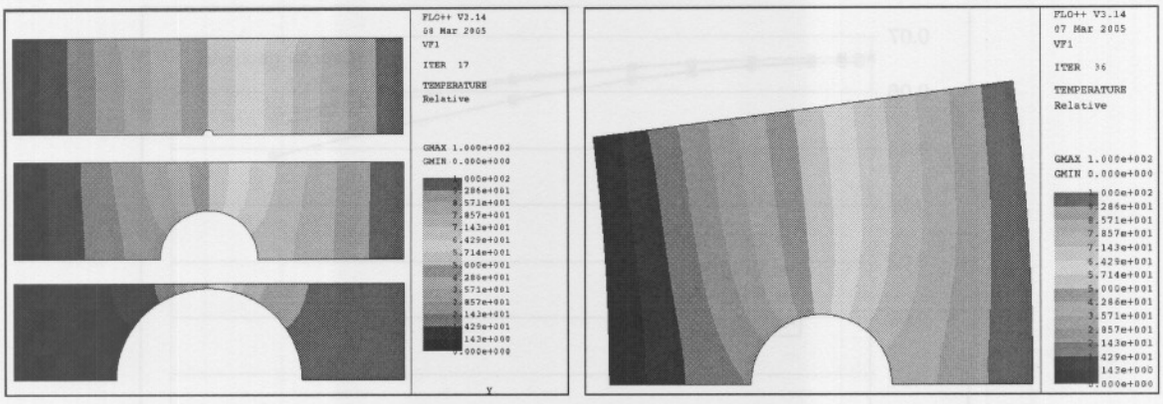


Figure 6.26. Typical temperature distributions across solids with axial holes.

For circular geometry, parametric studies were done for *r/b* ratios of 0.4, as cells in the CFD grid became very distorted at higher *r/b* ratios and that gave rise to convergence problems. For rectangular geometry, it was possible to do calculations up to *r/b* ratios of 0.95. Figure 6.27 and Figure 6.28 present comparisons between CFD results, the one-block and three-block methods for rectangular and circular geometry.

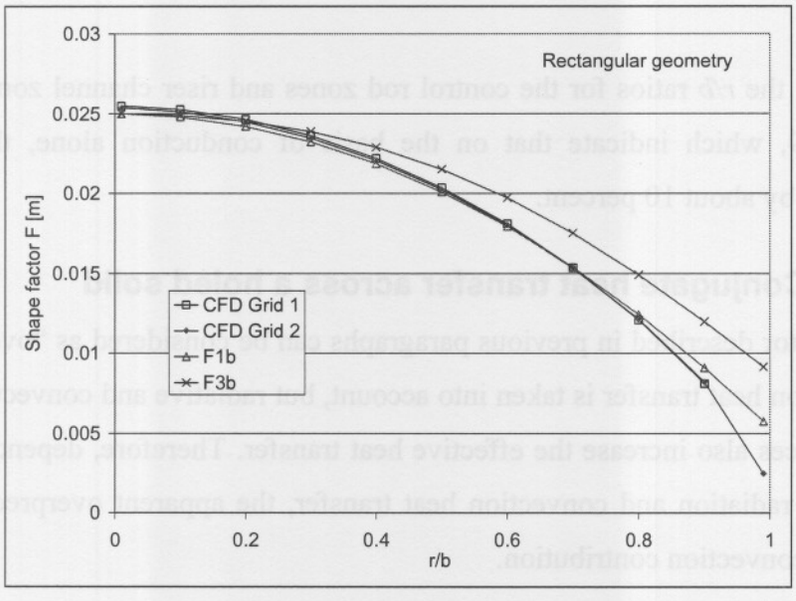


Figure 6.27. Parametric study results for rectangular geometry.

For rectangular geometry, the one-block method is seen to give accurate results up to a *r/b* ratio of 0.8, while the three-block overpredicts the shape factor from *r/b* ratios as low as 0.3.

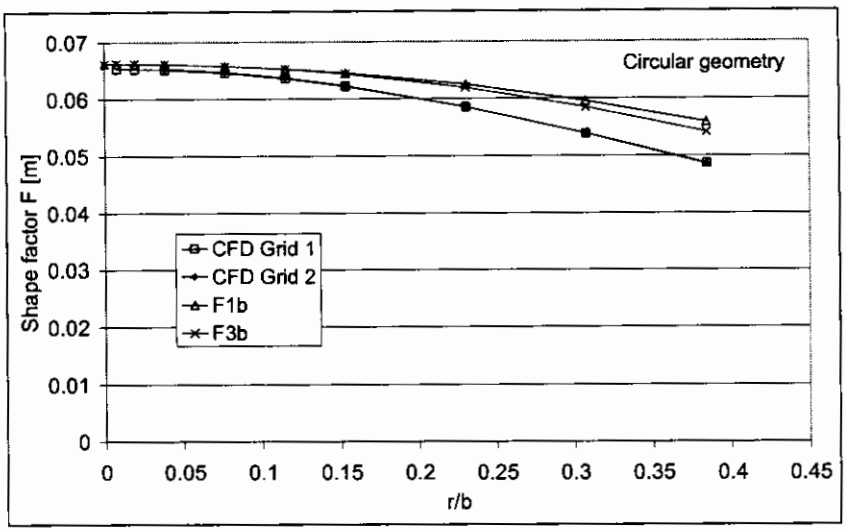


Figure 6.28. Parametric study results for radial geometry with a r_p/r ratio of 30 and r_p 1.987m

As two CFD grids with different topologies give results that differ less than one percent, the numerical results are considered valid. As shown in Figure 6.28, the one-block and the three-block methods overpredict the shape factor for radial geometry by about 10 percent at an *r/b* ratio of 0.3.

In the PBMR, the *r/b* ratios for the control rod zones and riser channel zones are respectively 0.26 and 0.39, which indicate that on the basis of conduction alone, the shape factor is overpredicted by about 10 percent.

6.5.2 Conjugate heat transfer across a holed solid

The shape factor described in previous paragraphs can be considered as "overpredicting" when only conduction heat transfer is taken into account, but radiative and convection heat transfer at the hole surfaces also increase the effective heat transfer. Therefore, depending on the relative magnitude of radiation and convection heat transfer, the apparent overprediction could equal the radiation/convection contribution.

That possibility was explored in Appendix C, where a method was developed to calculate a radiation increase factor g_{rad}, a dimensionless multiplier for the shape factor to take the contribution of radiation heat transfer across a transverse hole into account. The properties for calculation of the radiation increase factor g_{rad} are listed in Table 6-1.

During the investigation for Appendix C, it was found that the average temperature at the hole is the determining parameter for the heat resistance, while temperature difference had a negligible effect on the heat resistance. The conduction past the control rod and helium riser

channels is only of importance during a LOFC condition, as the temperature is convection-dominated during full-power conditions.

Symbol	Description	Risers	Control rods
r_p [m]	Hole pitch radius	2.5	1.9
r [m]	Hole radius	0.085	0.065
N	Number of holes	36	24
b [m]	Half of circumferential distance between holes	0.22	0.25
r/b	Ratio of hole radius to half of circumferential pitch	0.39	0.26
k [W/mK]	Solid conductivity	40	40
ϵ	Emissivity	0.85	0.85
T_{ave}[K]	Average temperature at location during a LOFC	1023 (750°C)	1023 (750°C)
P	Planck number	9.12	11.93
g_{rad}	Radiation increase factor	**1.10**	**1.04**

Table 6-1. Ballpark values for the helium riser channels and control rod channels of the PBMR at LOFC conditions with an average temperature of 750°C.

For the helium riser channels with an r/b ratio of 0.39, the radiation correlation predicts a ten percent increase in heat transfer, due to radiation across the hole (1.10 from Table 6-1) while only a four percent heat transfer increase (1.04 from Table 6-1) is predicted for the control rod channels (r/b = 0.26).

As discussed in the previous section, the three-block method overpredicts the conduction-only shape factors by about ten percent, which means that the apparent overprediction of the three-block method is a good estimate of the increase because of radiation.

Other uncertainties affecting the side reflector conductivity are neutron dose, the effect of natural convection heat transfer in the vertical holes, the effect of leak flow through slits and gaps between blocks, as well as gamma ray heating. Against this background, the existing approach of using the block effective porosity (i.e. the three-block approximation) is considered sufficient for a systems simulation reactor model. Therefore, the Generation IV reactor model will also use the block effective porosity, or the three-block approximation.

6.6 Radiation heat transfer

Due to the geometrical complexity of calculating the view factor, a common approximation in systems simulation codes is to connect only directly opposing surfaces with a view factor of one, as is done in the Flownex Generation III reactor model. To ascertain the validity of this approach, a benchmark calculation of the actual reactor geometry has to be done, using a

detailed radiation model. It is essential that the actual geometry and heating profiles are used for the benchmark, as radiation characteristics are unique for each geometry.

For the purpose of creating such a calculation, a complete radiation heat transfer model was created with the network discretisation described in Section 4.8.4. However, the radiation network described in Section 4.8.4 still required calculation of view factors. Analytical formulae for calculating the basic view factors in right-angular cylindrical geometry were presented by Howell (2001) and Brockmann (1994). However, the basic formulae are only applicable to very simple surfaces while the surfaces in a reactor model are discretised. To calculate the view factors between discretised surfaces, view factor algebra was applied to derive extensions for the basic view factor formulae. The basic view factor formulae from Howell (2001) and Brockmann (1994), as well as the derivation of the auxiliary view factor formulae are presented in Appendix D. Appendix D also presents an investigation into the accuracy of radiation calculation methods.

For evaluating the simple and the detailed radiation heat transfer models, the HTR-10, as well as the 268MW version of the PBMR was used as case studies. Loss-of-Flow events without SCRAM were simulated and the time to recriticality was used as indicator of heat removal effectiveness.

As described in Appendix E, it was found that with the HTR-10, other nonlinear phenomena in the reactor core constrained the solution process. Therefore, the number of radiation elements had no effect on solution time, while with the 268MW PBMR DLOFC (Depressurised Loss Of Forced Cooling), the use of a detailed radiation model increased solution time with 30 percent.

With both the HTR-10 and the PBMR, the radiation model had negligible effect on the total heat resistance from the reactor, as indicated by the change in time that elapsed until recriticality.

For system simulation codes that focus on transient response of a plant, it is not considered worthwhile to use a detailed radiation model, as the gain in accuracy does not justify the increased solution time or the implementation and verification effort.

As the detailed heat transfer model is available in the Generation IV reactor model, it will be used throughout this study.

6.7 Conclusion

This chapter described extensions and refinements to heat transfer calculation and discretisation methods in the reactor model. Investigations were done on the fuel sphere discretisation, the convection heat transfer discretisation in the pebble bed, combined conduction and radiation heat transfer across the holed side reflector, as well as radiation heat transfer modelling in cavities. The studies of sphere and convection discretisation both resulted in the development of new methods that increased calculation speed and accuracy, while the study of combined radiation and conduction and the study of radiation heat transfer concluded that the status quo in modelling methods is adequate and appropriate for systems simulation models.

The next chapter presents results that were obtained with the integrated reactor model.

Chapter 7

Results

7.1 Introduction

This chapter describes the experimental cases that were simulated to ascertain the validity of the integrated reactor model. The SANA experiment, conducted in Germany, was simulated to demonstrate natural convection and effective conduction, while the Chinese HTR-10 reactor was used to demonstrate simulation of a full-scale reactor. Grid dependence studies are also presented to estimate the reduction in calculation time that can be realised from methods presented in this study.

7.2 SANA experiment

The SANA experiment was conducted in the 1980`s at Jülich research center to investigate the self-acting decay heat removal from High Temperature Gas-cooled Reactors in loss-of-flow conditions. It has been widely used as an experimental benchmark for reactor simulation codes (IAEA, 2000). As shown in Figure 7.1, the SANA experimental setup consists of a central graphite heater surrounded by a sphere pebble bed. At the bottom, the pebble bed is supported on insulating bricks and on top it is covered with insulating fibre mat. Thus, there are no flow channels to the pebble bed and, therefore, no forced convection.

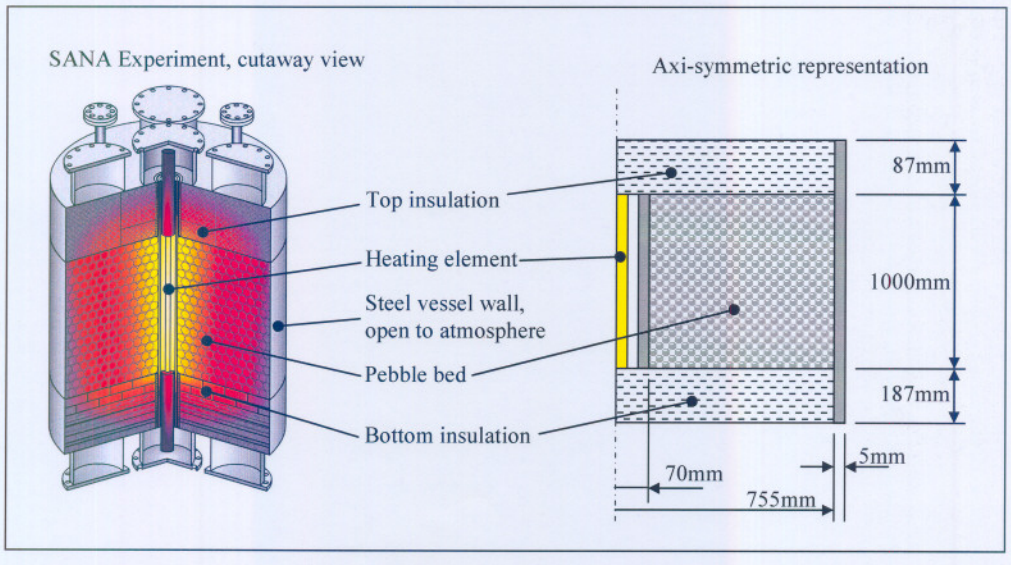


Figure 7.1. Cutaway and axi-symmetric views of the SANA experiment.

For this study, the setup with 60mm graphite spheres, nitrogen gas and only one central heating element was selected. With nitrogen, natural convective heat transport was found to be much more important than with helium. As the presence of natural convection increases the complexity of the situation, any errors in the modelling approach are assumed to show up more clearly.

The three heat transfer mechanisms that play a role in the absence of forced convection are pebble bed/wall heat transfer, pebble bed effective conductivity and dispersion heat transfer. For modelling pebble bed effective conductivity, the existing methods of Zehner and Schlünder were used while the method by Bauer and Schlünder was used to model dispersion (k_{feff} defined in Section 5.7). However, the bed/wall and fluid/wall modelling parameters C_{sw} and C_{fw} (defined in Section 6.4) for pebble bed/wall heat transfer in pseudo-heterogeneous pebble bed models are not yet well established.

The control volume discretisation of the SANA experiment is shown in Figure 7.2, as well as the location of temperature measurement points in the SANA packed bed. Thermocouples were placed in radial rows at several heights in the SANA packed bed, of which the most useful results were obtained from the thermocouple rows at, respectively, 7 cm, 50 cm and 93 cm from the bottom of the packed bed.

It was found from sensitivity studies that modelling the top and bottom insulation had a negligible effect on the temperature results. Therefore, adiabatic top and bottom boundaries were assumed for the results presented here. A grid dependence test was done with three different pebble bed grid sizes namely 7x7, 15x15 and 29x29.

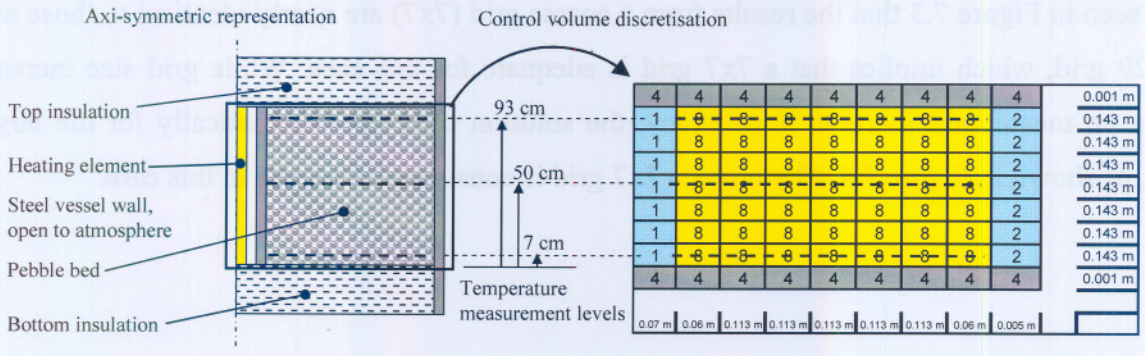


Figure 7.2. The zones and increment sizes for a 7x7 pebble bed simulation of the SANA experiment. Zones:1: Heating element; 2: Outer shell with fixed temperatures; 4: Insulation boundary; 8: Pebble bed.

Table 7-1. Material property polynomial coefficients that were used for the SANA experiment.

	Thermal conductivity W/mK				Density kg/m^3
	A_0	a_1	A_2	a_3	a_0
SANA graphite	310.598	-0.56986	0.000453	-1.28E-07	1669
Insulation	0.1	0	0	0	1669

The material property polynomial have the following general form

$$f(T) = \sum_{i=0}^{n} a_i T^i \tag{7.1}$$

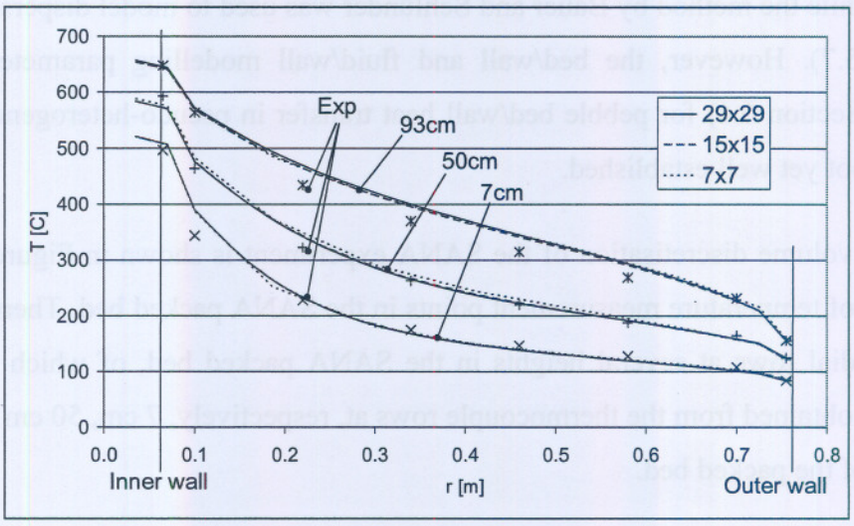


Figure 7.3. Grid dependence calculations with three pebble bed grid sizes. Shown here are radial temperature profiles at three different vertical positions in the SANA experiment, operating at 10kW, using nitrogen and 60mm graphite balls. For this case, a bed/wall parameter C_{sw} of 0.5 was used while the value of C_{fw}=0.1 had negligible effect./

It is seen in Figure 7.3 that the results from a coarse grid (7x7) are nearly identical to those of a 29x29 grid, which implies that a 7x7 grid is adequate for this case. While grid size increase gives no meaningful increase in accuracy, the solution time rises dramatically for the larger grid, as shown in Figure 7.4. Therefore, a 7x7 grid is considered adequate in this case.

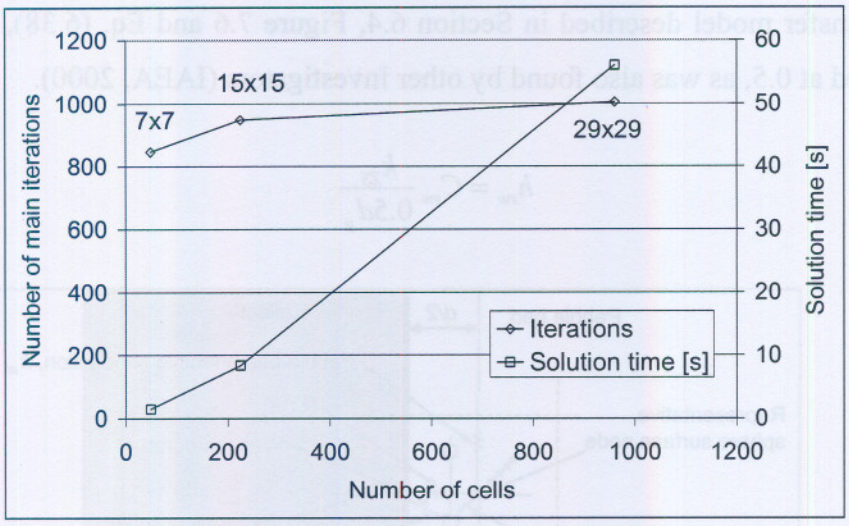


Figure 7.4. Solution time for the various grid sizes.

In general, it was found with the SANA experiment simulations that the natural convection was difficult to solve. Mass flow, pressure and temperature relaxation parameters had to be set very small to obtain convergence. The natural convection velocity field is shown in Figure 7.5.

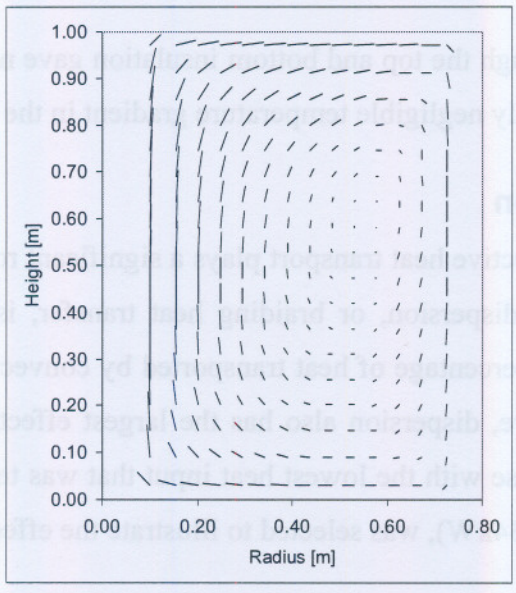


Figure 7.5. Fluid velocity vectors in the SANA experiment, calculated with the Generation IV reactor model.

7.2.1 Pebble bed/wall heat transfer

The porosity profile by Hunt and Tien was used as described in Paragraph 5.4. Due to the dominance of pebble bed effective conduction in the SANA experiment, it is insensitive to the fluid/wall convection heat transfer coefficient so that the bed/wall thermal resistance can be estimated from the sharp temperature rise against the wall which is visible in Figure 7.7. For the

wall heat transfer model described in Section 6.4, Figure 7.6 and Eq. (6.38), the constant C_{sw} was estimated at 0.5, as was also found by other investigators (IAEA, 2000).

$$h_{sw} = C_{sw} \frac{k_{ZS}}{0.5 d_p} \tag{6.38}$$

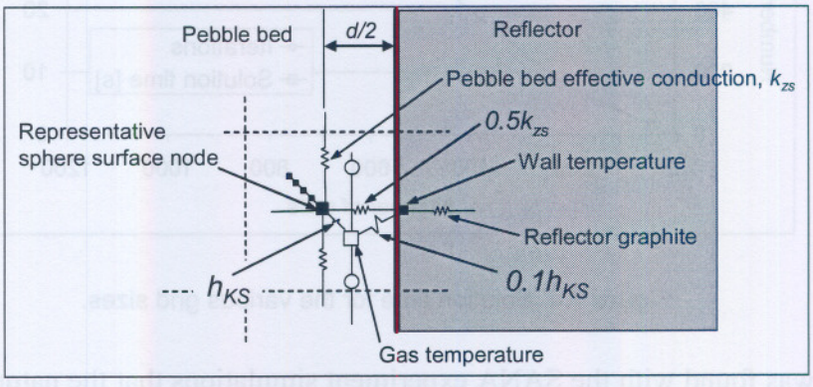


Figure 7.6. The pebble bed/wall heat transfer model used in this study. KS and ZS refer to Kugeler-Schulten and Zehner-Schlunder respectively, while the factor 0.5 for solid conduction was estimated from the SANA simulations.

Modelling heat loss through the top and bottom insulation gave no worthwhile improvement in accuracy, as there was only negligible temperature gradient in the vertical direction.

7.2.2 Dispersion

For cases in which convective heat transport plays a significant role, it was found that accuracy increased greatly when dispersion, or braiding heat transfer, is taken into account. For the SANA experiment, the percentage of heat transported by convection increases with a decrease in input power. Therefore, dispersion also has the largest effect when the power input is the lowest. Therefore, the case with the lowest heat input that was tested, 5kW nominal heat input (the precise value was 4.34kW), was selected to illustrate the effect of dispersion heat transfer.

As seen in Figure 7.7, the numerical results are closer to the experimental results when dispersion heat transfer is taken into account. This is due to an increase in the bed effective conductivity, caused by the dispersion heat transfer as described in Paragraph 5.7. The inclusion of dispersion heat transfer had no significant effect on solution time as it increased solution time in some cases while lowering it in other cases. In all cases the change in solution time was less than 5%.

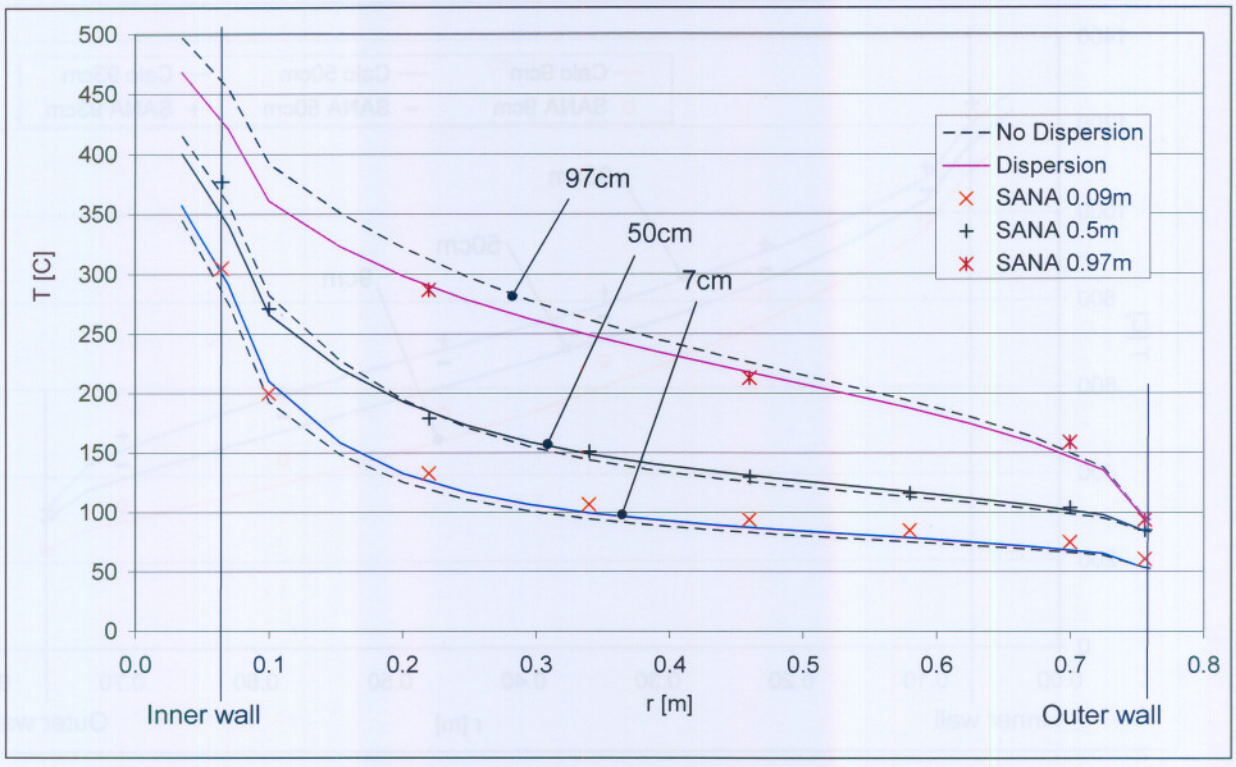


Figure 7.7. The effect of dispersion heat transfer, as shown on this simulation of the SANA experiment with 4.34kW and Nitrogen. Dispersion is more important here than with the 10kW case.

When comparing Figure 7.8 (35 kW) with Figure 7.7 (4.34 kW), it is seen that the temperature variation between the various heights is much less for the 35 kW case than for the 4.34 kW case. This is attributed to the increase in radiation heat transfer, caused by the high temperatures. Convective heat transfer does not increase to the same extent as radiation heat transfer, with the result that there is a much smaller vertical temperature variation in the pebble bed.

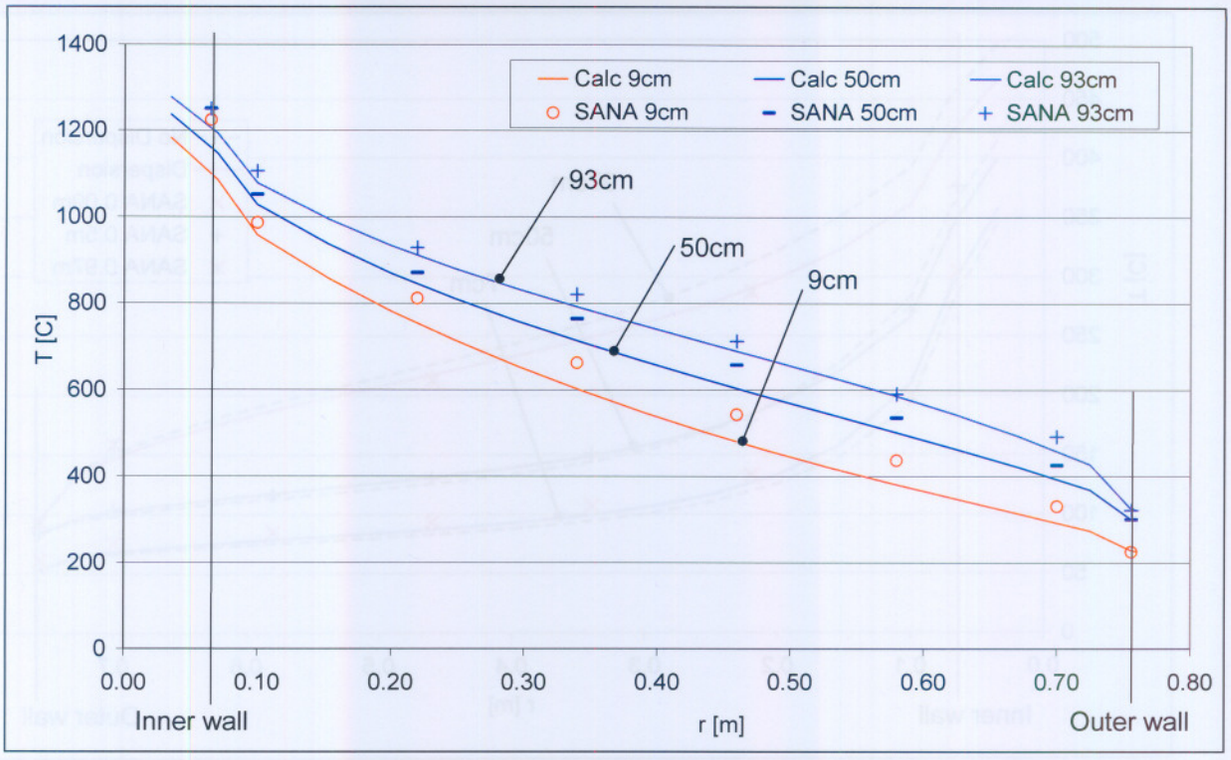


Figure 7.8. SANA results for Nitrogen, 35kW heat input over the full height of the pebble bed.

7.2.3 Comparison with the Generation III Reactor Model

Due to the fact that the Generation III reactor model does not take dispersion heat transport or the solid/wall heat transfer coefficient into account, it is not able to calculate the SANA experiment to the same level of accuracy as the Generation IV reactor model, as shown in Figure 7.9.

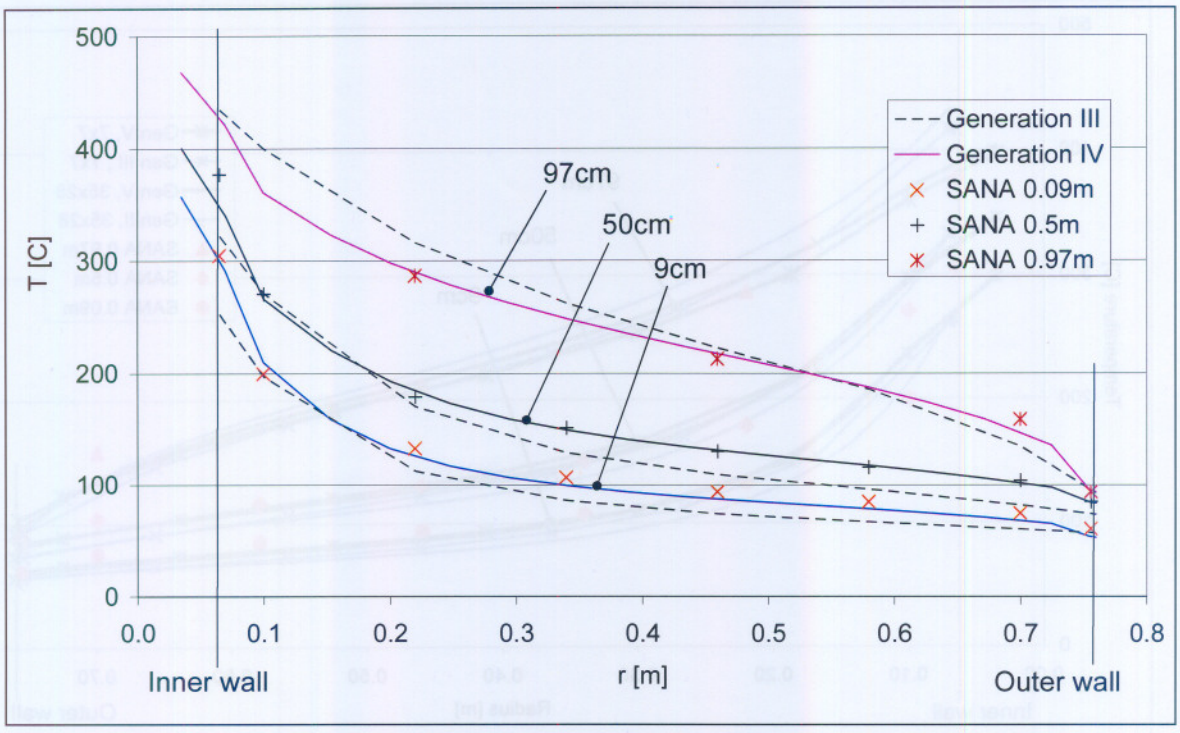


Figure 7.9. Comparison between the Generation IV reactor model and the Generation III reactor model as it is implemented in Flownex. The Generation IV result is for a 15x15 grid while the Generation III result is for a grid with 60 axial increments and 40 radial increments. The SANA experiment with 4.34kW heat addition and nitrogen was simulated.

The Generation III model used for the results in Figure 7.9 has 60 axial and 40 radial increments, while the Generation IV model has only 15 axial and 15 radial increments.

In order to compare the control-volume based discretisation with the element-based discretisation by means of simulating the SANA experiment, the solid/wall heat transfer parameter and dispersion heat transfer have to be disabled. For this case, other differences between the reactor models that could affect the SANA simulation results are the conductivity discretisation, the topology at the pebble bed/wall interface and possibly detail in the implementation of the Zehner-Schlunder equation. The temperature results for the 4.34kW case of the SANA experiment are shown in Figure 7.10.

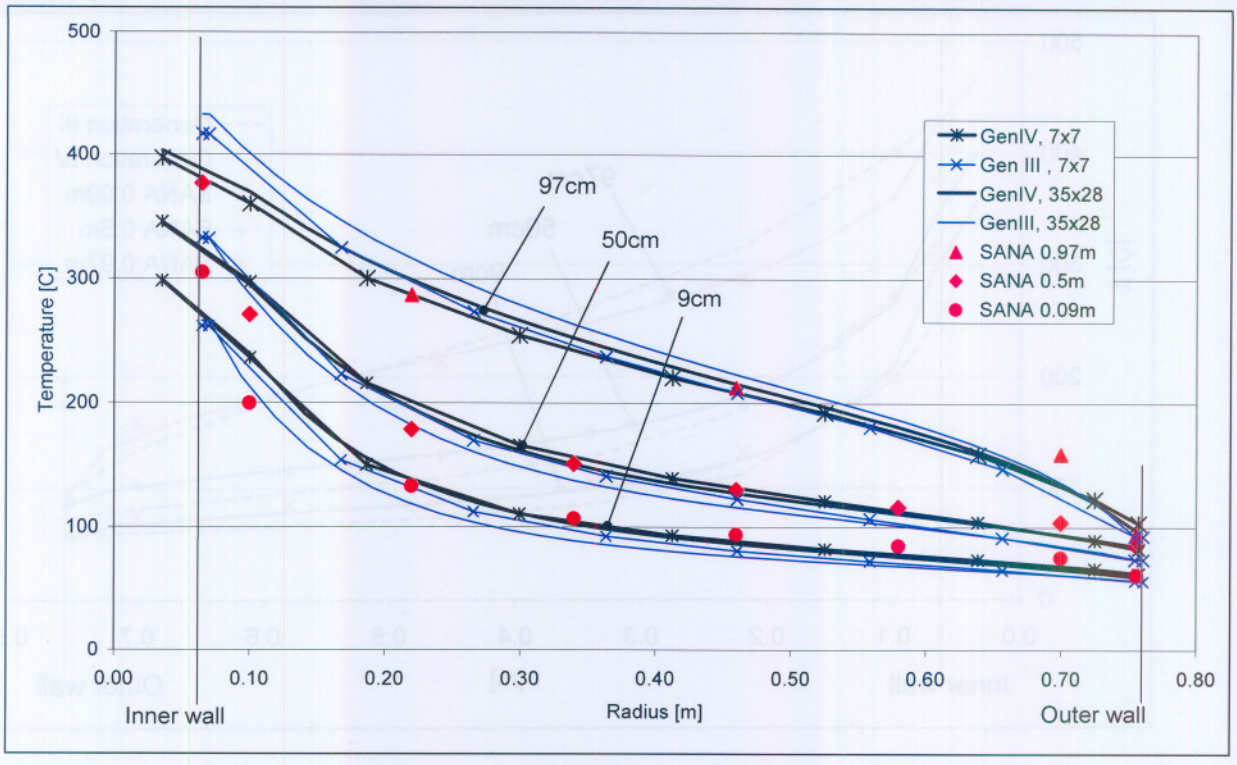


Figure 7.10. Results from the SANA experiment, Generation IV and Generation III reactor models for grid sizes of 7x7 increments and 35x28 increments.

The code in which the Generation IV reactor model was implemented, limited the maximum grid size to 35 axial increments by 28 radial increments, which was the grid size used for generating the results in Figure 7.10.

Figure 7.10 shows that the Generation IV reactor model is less grid dependent than the Generation III reactor model as the differences between the 35x28 and 7x7 grids are less for the Generation IV reactor model than for the Generation III model. However, there are still considerable temperature differences between the Generation IV and Generation III results for the same grid size. These are attributed to the combined effect of the conductivity discretisation, the topology at the pebble bed/wall interface and possible differences in the implementation of the Zehner-Schlünder equation.

It is thus concluded that the effect of different discretisation schemes is smaller than the effect of different mathematical models.

7.2.4 Conclusion on the SANA calculations

The calculations of the SANA experiment show that the newly developed reactor model can calculate the temperature field with considerable accuracy and reach grid independence with a very coarse grid.

Another opportunity for increasing simulation speed became apparent, namely to develop methods for efficiently solving natural convection problems, of which the equations are elliptic and are slow and difficult to solve.

Regarding discretisation schemes, it was found that the mathematical models that are implemented, have a greater effect than the type of discretisation scheme used. The only remaining consideration is which discretisation scheme provides the simplest framework for implementing various mathematical models. Taking into account the properties of the element-based scheme described in Section 4.6, the control-volume based approach is considered more intuitive and flexible.

7.3 HTR-10 Steady state

Methnani (2005) reported on several coordinated research projects (CRPs) by the IAEA for the validation of HTR core design and thermal-fluid simulation codes. Experiments have been done with some existing experimental facilities and dimensions, material properties and results have been published in order to use it as benchmark cases for code validation. An example is the HTR-10 reactor of the Institute for Nuclear Energy Technology (INET) at Tsinghua University in Beijing, China. Steady-state as well as transient test results, obtained with this reactor were published by the IAEA under the auspices of the CRP-5.

This information will be used to demonstrate the accuracy of the reactor model developed in this study.

7.3.1 Geometry

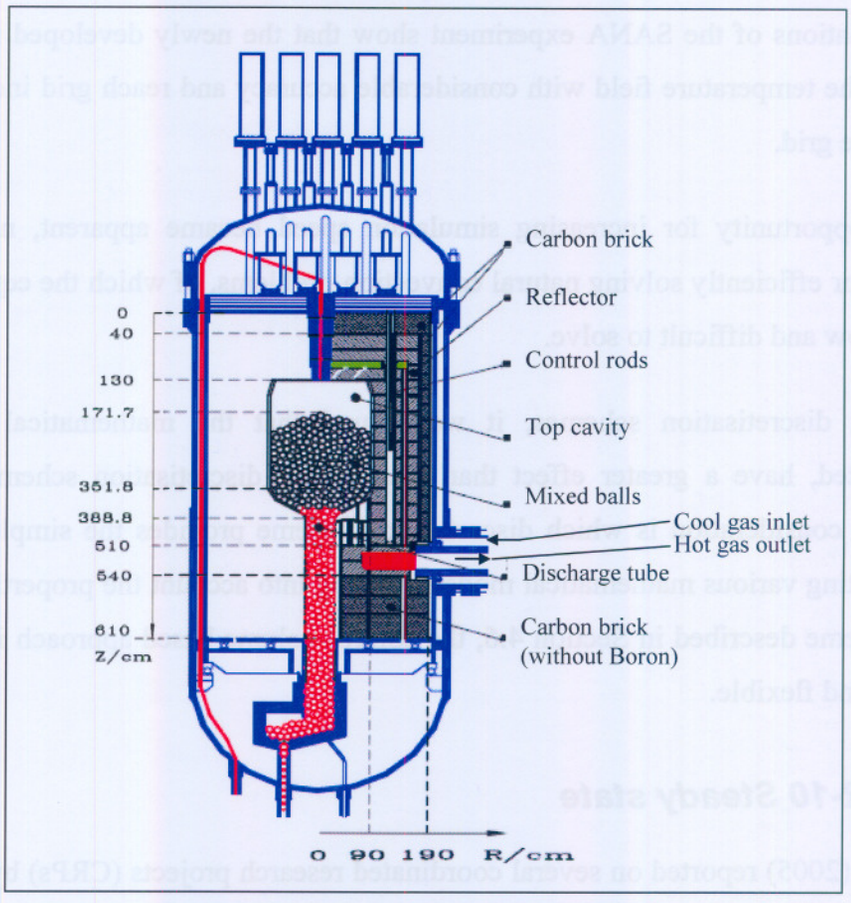


Figure 7.11. Vertical cross-section of the HTR-10. (IAEA, 2006)

Cool (250°C) helium enters the reactor pressure vessel through the annular space between the hot outlet pipe and the outer pressure boundary. It then enters the core assembly through flow channels in the steel bottom support plate and then passes into the helium riser channels in the graphite side reflector. A percentage of the cool inflow gas is passed through the defuelling channel to cool the fuel spheres that are being removed from the reactor core, while a percentage of the flow that has passed into the reflector assembly, leaks to the outlet manifold in the slits between reflector blocks. At the top of the riser channels, more flow is bled off from the main flow stream to cool the control rods and then passes to the outlet manifold. The remaining flow passes through the pebble bed, is heated and exits through the porous bottom reflector and the outlet plenum to the hot outlet pipe. The topology of the leak flow paths is explained schematically in Figure 7.12.

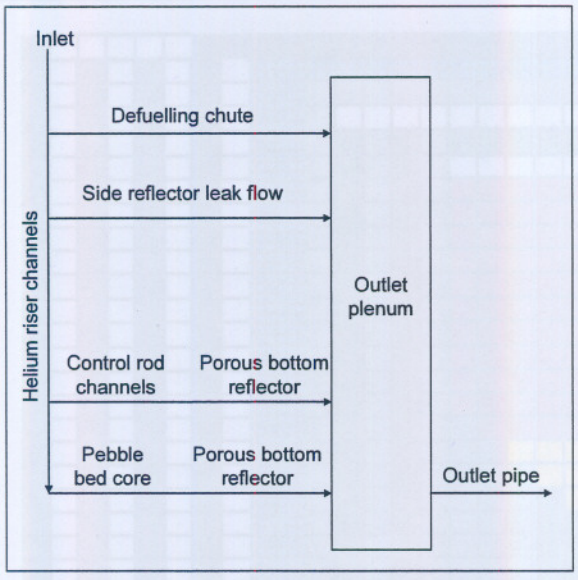


Figure 7.12. Schematic layout of the flow path through the HTR-10 reactor.

The zones that represent the reactor (Figure 7.11), as well as the dimensions for the discretisation, are shown in Figure 7.13.

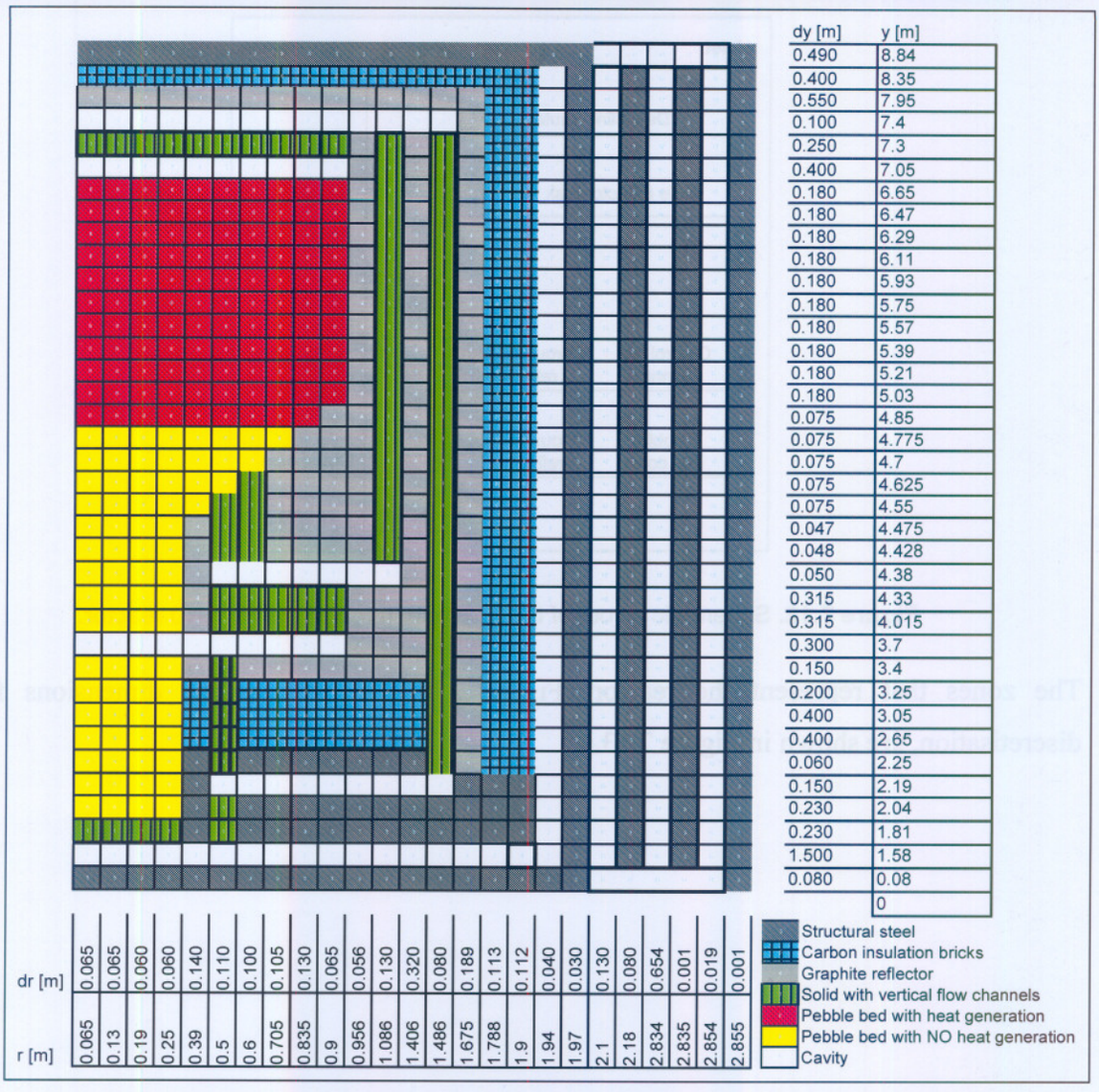


Figure 7.13. Zones and dimensions for describing the reactor geometry and input values.

Other geometrical properties of the reactor include zone permeabilities, hydraulic diameters, hole numbers and diameters, which are shown in Figure 7.14.

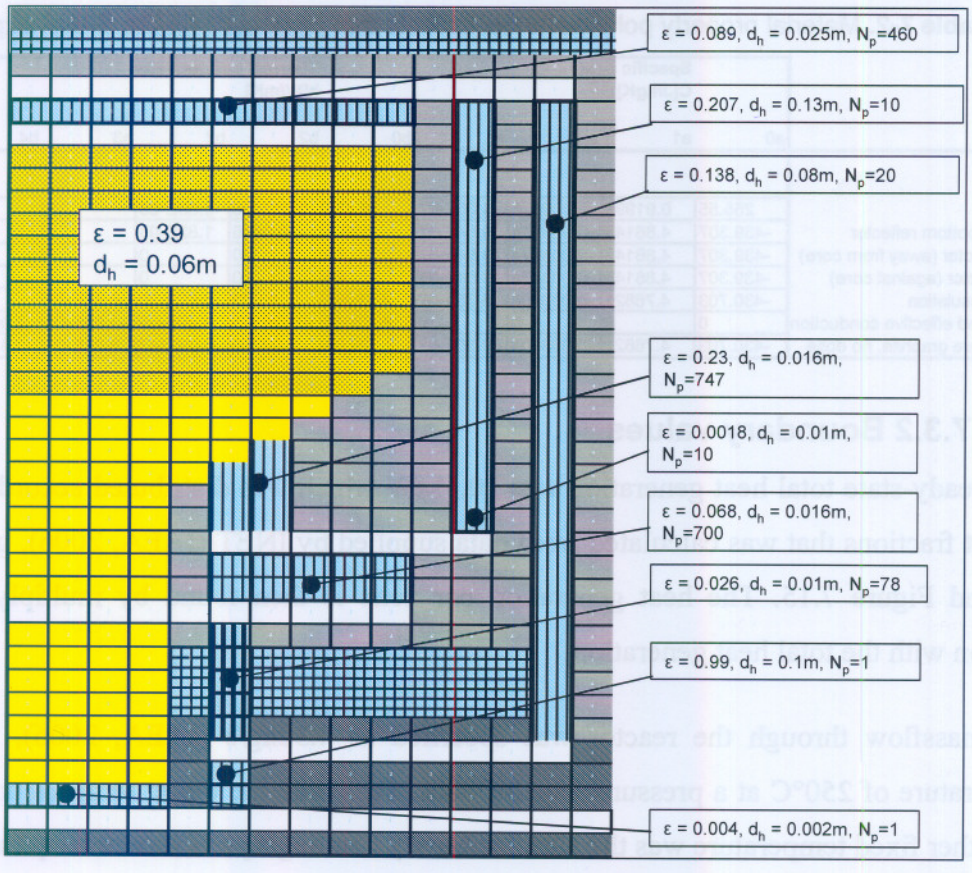


Figure 7.14. Porosity, permeability, hydraulic diameter and number of flow channels for porous flow regions. Some permeabilities and hydraulic diameters were adjusted to obtain the correct flow distribution.

INET stated that the reactor had produced 3000MWh of energy by the time the tests were done. When the corresponding fast neutron fluence values were put into the material property functions supplied by INET, it resulted in a conductivity reduction of only about one to five percent. This effect was offset in some cases when a material property polynomial was correlated to the material data. It was also found that some material property polynomials gave negative values at temperatures lower than 250°C or higher than 1100°C. As temperatures outside this range were frequently calculated during the numerical solution process, the resulting negative material property value causes the temperature solution to diverge. Therefore, material property polynomials were created that are positive for all temperature values, or constant values were used.

Table 7-2. Material property polynomial coefficients that were used for the SANA experiment.

	Specific heat C[J/kgK]				Thermal conductivity k[W/mK]					Density rho[kg/m^3]
	a0	a1	a2	a3	b0	b2	b2	b3	b4	c0
HTR-10										
Steel	255.55	0.91998	-0.000975	4.06E-07	8.433	0.017456	-3.09E-06	0	0	8000
Top and bottom reflector	-439.307	4.86143	-0.003574	9.54E-07	128.5	-0.0846	1.82E-05	0	0	1760
Side reflector (away from core)	-439.307	4.86143	-0.003574	9.54E-07	75	0	0	0	0	1730
Sidereflector (against core)	-439.307	4.86143	-0.003574	9.54E-07	60	0	0	0	0	1760
Carbon insulation	-430.703	4.76621	-0.003504	9.35E-07	4.18055	0.003	-4.62E-20	-8.47E-22	0	1590
Pebble bed effective conduction	0	0	0	0	6.42066	-0.026325	4.49E-05	-2.09E-08	4.06E-12	1
Fuel sphere graphite, no dose	-430.703	4.76621	-0.003504	9.35E-07	25.08	0.09266	-0.000147	8.01E-08	-1.41E-11	1730

7.3.2 Boundary values

The steady-state total heat generation was 10.3MW which was distributed according to a chart of heat fractions that was calculated from data supplied by INET (IAEA, 2006), given in Table 7-3 and Figure 7.15. The heat generation per zone is then found by multiplying the zone fraction with the total heat generation.

The massflow through the reactor was specified as 4.32kg/s (IAEA, 2006), with an inlet temperature of 250°C at a pressure level of 3000kPa, while the outlet temperature was 700°C. The other fixed temperature was the Reactor Cavity Cooling System water loop that was kept at a constant temperature of 50°C. This was treated as a fixed solid surface temperature in the *Flownex* reactor model and coupled to the reactor pressure vessel by means of radiation heat transfer.

The flow rates in the various flow paths are specified in IAEA-TECDOC-TBD (2006) as follows:

Rated Coolant Flow Rate (RCFR):	4.32 kg/s
Fuel discharge tube flow:	1% of Rated Coolant Flow Rate (RCFR)
Control rod channel:	2% of RCFR
Maximum bypass leak flow:	10% of RCFR
Flow through pebble bed:	87% of RCFR

The permeability and hydraulic diameter of the zone at the bottom of the core outlet, the bottom of the control rod channel, as well as the direct leak flow path between inlet and outlet plenums (Figure 7.14), were adjusted to obtain the flow rates given above. These porosity values are not necessarily representative of the actual geometry, but represent a pragmatic approach of dealing with the considerable simplification of these zones. The benchmark definition did not describe details of these flow paths or secondary pressure loss characteristics. When the permeability values given in the benchmark definition were used, it resulted in quite a different flow distribution.

Table 7-3. Heat fractions for the control volumes representing the HTR-10 core, as calculated from data supplied by INET.

	Increment size [m]	0.065	0.065	0.06	0.06	0.14	0.11	0.1	0.105	0.13	0.065
	Radial position [m]	0.065	0.13	0.19	0.25	0.39	0.5	0.6	0.705	0.835	0.9
Increment size [m]	Vertical position [m]										
0.18	6.65	4.14E-04	1.24E-03	1.88E-03	2.57E-03	8.59E-03	9.17E-03	1.01E-02	1.24E-02	1.79E-02	1.02E-02
0.18	6.47	4.91E-04	1.46E-03	2.21E-03	3.01E-03	1.01E-02	1.08E-02	1.17E-02	1.42E-02	2.04E-02	1.17E-02
0.18	6.29	5.69E-04	1.70E-03	2.57E-03	3.49E-03	1.15E-02	1.21E-02	1.31E-02	1.58E-02	2.27E-02	1.29E-02
0.18	6.11	6.04E-04	1.81E-03	2.71E-03	3.70E-03	1.22E-02	1.30E-02	1.40E-02	1.70E-02	2.43E-02	1.37E-02
0.18	5.93	6.43E-04	1.92E-03	2.89E-03	3.93E-03	1.30E-02	1.37E-02	1.48E-02	1.79E-02	2.52E-02	1.42E-02
0.18	5.75	6.57E-04	1.97E-03	2.97E-03	4.03E-03	1.33E-02	1.37E-02	1.48E-02	1.75E-02	2.48E-02	1.40E-02
0.18	5.57	6.16E-04	1.84E-03	2.77E-03	3.76E-03	1.26E-02	1.34E-02	1.43E-02	1.72E-02	2.43E-02	1.37E-02
0.18	5.39	5.76E-04	1.73E-03	2.60E-03	3.53E-03	1.16E-02	1.23E-02	1.32E-02	1.56E-02	2.20E-02	1.24E-02
0.18	5.21	5.46E-04	1.63E-03	2.45E-03	3.33E-03	1.09E-02	1.13E-02	1.22E-02	1.45E-02	2.03E-02	1.12E-02
0.18	5.03	5.39E-04	1.61E-03	2.41E-03	3.25E-03	1.06E-02	1.08E-02	1.16E-02	1.37E-02	1.90E-02	1.03E-02
0.075	4.85	3.34E-04	1.00E-03	1.50E-03	2.02E-03	6.58E-03	6.74E-03	7.23E-03	8.58E-03	1.17E-02	6.01E-03

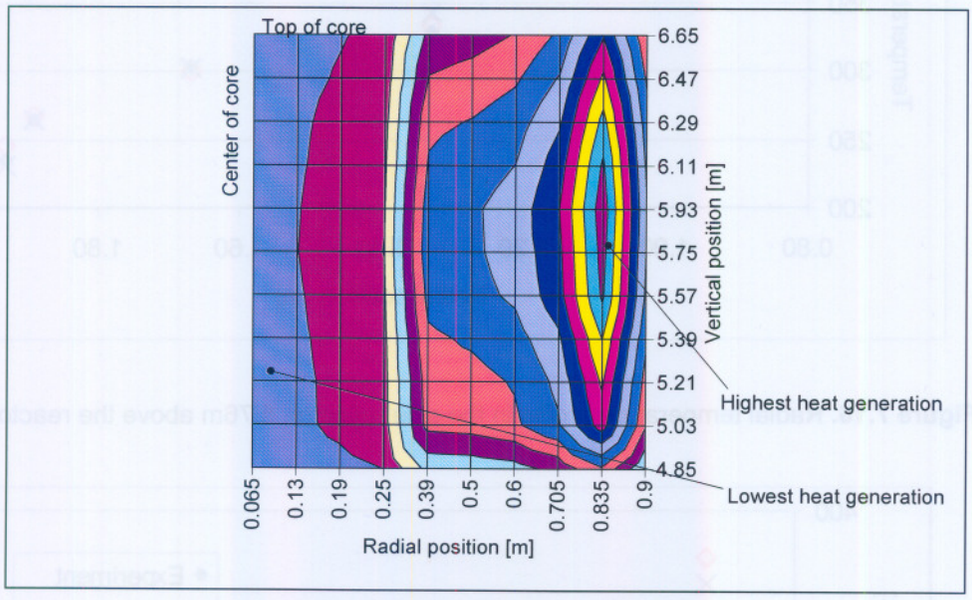


Figure 7.15. HTR-10 core heat distribution. The highest heat generation is near the outer reflector, where the thermal neutron flux is the highest.

7.3.3 Results

The results of the current reactor model developed in this study, along with the values calculated by the Institute of Nuclear Energy Technology (INET) at Tsinghua University, are presented in Figure 7.16 to Figure 7.18. INET used THERMIX to calculate heat conduction and solid temperatures, coupled to the KONVEK code for solving the flow and gas temperature field. Two-dimensional axi-symmetric geometry was assumed.

Figure 7.16 and Figure 7.17 show temperature profiles at two different heights in the side reflector. In both cases, there is good agreement between the calculation and the experiment because C_{fw} was varied to obtain the best agreement between the experiment and the calculation. This case was well suited to determine the fluid/wall heat transfer empirical constant C_{fw}, as the high mass flow through the core dominated "effective conductivity" heat

transfer between the pebble bed and the wall. A value of C_{fw} equal to 0.1 gave the best agreement between experiment and calculation.

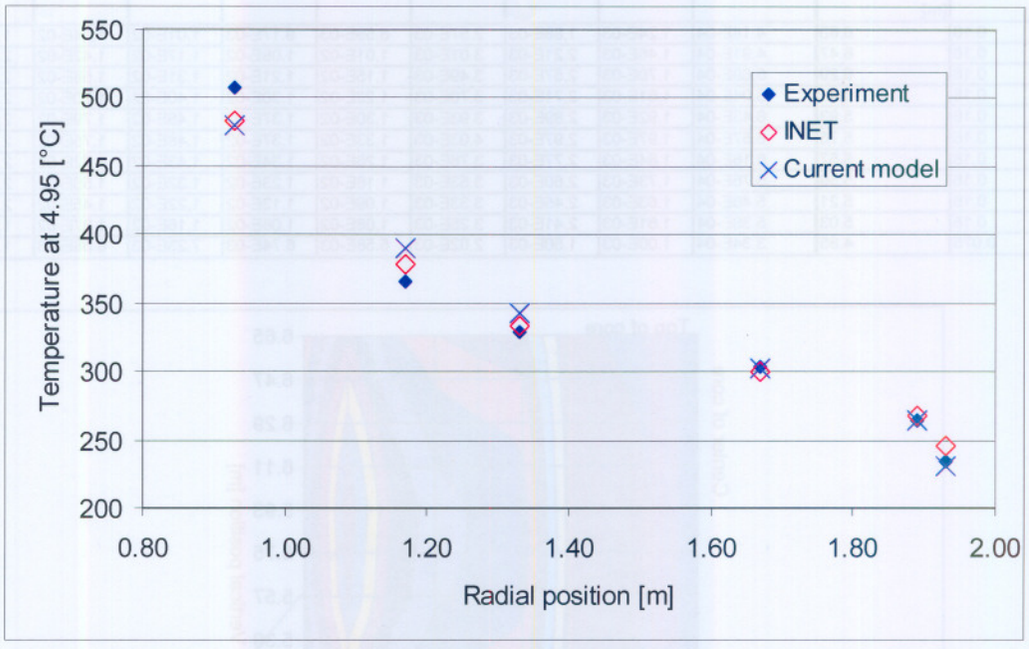


Figure 7.16. Radial temperature profile in the side reflector, 5.76m above the reactor bottom.

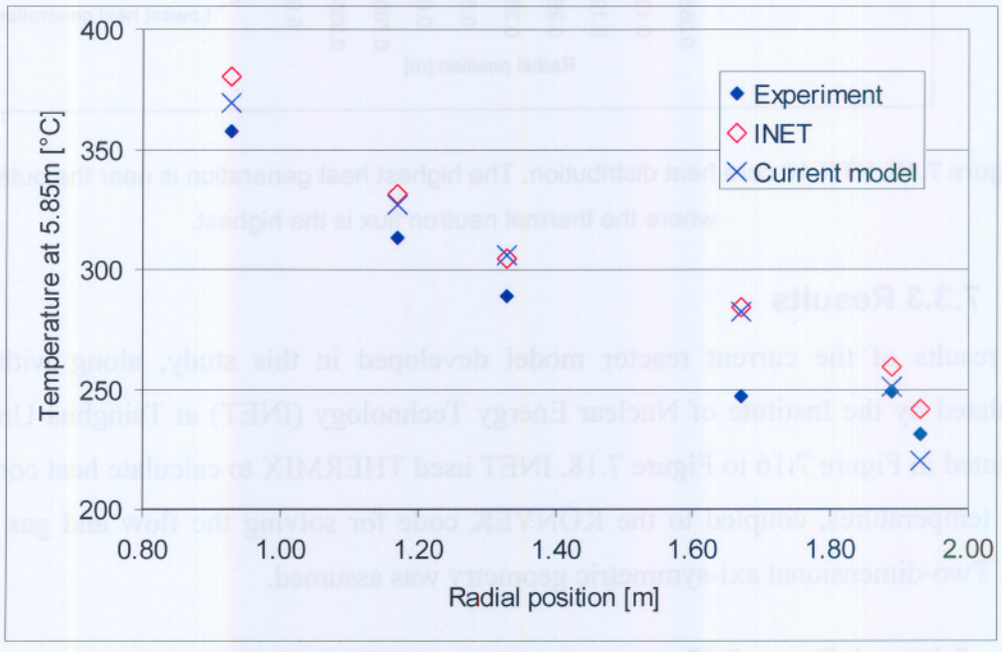


Figure 7.17. Radial temperature profile in the sidereflector, 4.88m above the reactor bottom.

Figure 4.18 shows temperatures at various places along a vertical line from the bottom to the top of the reactor. Radiation heat transfer modelling, had a significant effect on the calculated

temperatures as some of them were at the edges of cavities. Figure 4.18 also shows good agreement between calculation and experimental results.

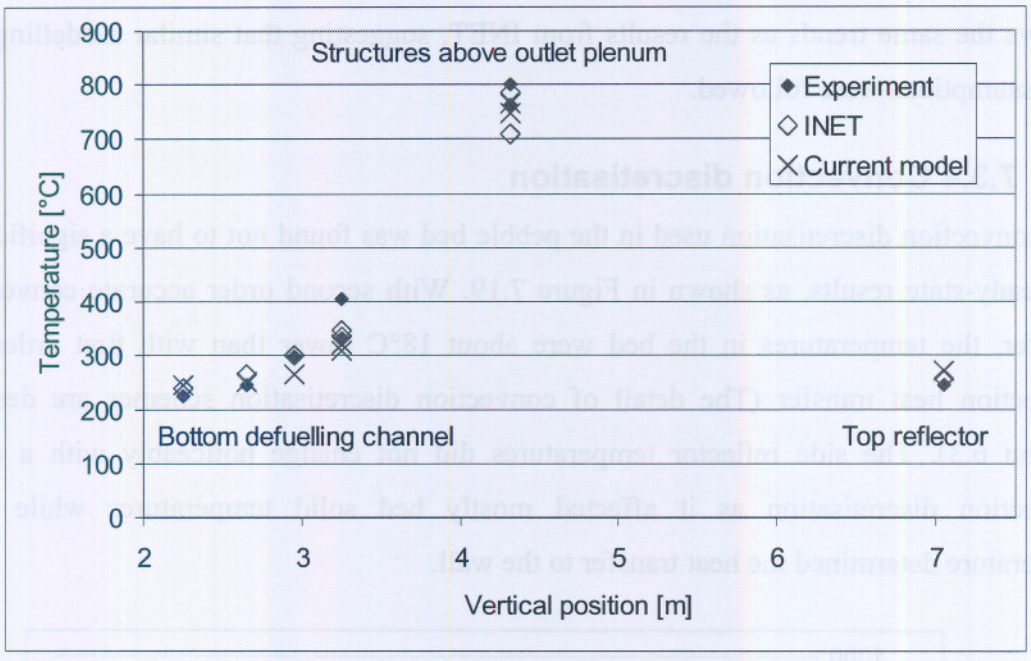


Figure 7.18. Temperatures in core structures, as listed in Table 7-4.

Temperatures were only measured in structures surrounding the core, but nowhere inside the pebble bed core.

Table 7-4. Temperatures in core structures, shown in Figure 7.18

Radius[m]	Height[m]	Experiment	INET	Current model
R [m]	Z [m]	T [C]	T [C]	T [C]
Top reflector				
0.60	7.05	245.6	258.1	272.0
Hot helium plenum				
0.40	4.31	800.2	787.5	767.0
0.60	4.31	763.1	708.8	749.0
Bottom carbon blocks				
0.70	2.25	224.1	239.8	245.0
0.50	2.65	245.7	265.7	252.0
0.50	2.95	296.6	300.0	266.0
0.50	3.25	406.7	346.7	322.0
Defuelling channel				
0.26	3.25	334.2	336.2	311.0
0.26	4.05	881.7	888.3	771.0

The difference in core structure temperatures is not considered to be of great significance, due to the substantial simplifications made in creating the calculation model. The exact temperatures are also highly dependent on the leak flows. It is seen that the current model follows the same trends as the results from INET, suggesting that similar modelling methods and assumptions were followed.

7.3.4 Convection discretisation

The convection discretisation used in the pebble bed was found not to have a significant effect on steady-state results, as shown in Figure 7.19. With second order accurate convection heat transfer, the temperatures in the bed were about 18°C lower than with first order accurate convection heat transfer (The detail of convection discretisation schemes are described in Section 6.3). The side reflector temperatures did not change noticeably with a change in convection discretisation as it affected mostly bed solid temperatures while the fluid temperature determined the heat transfer to the wall.

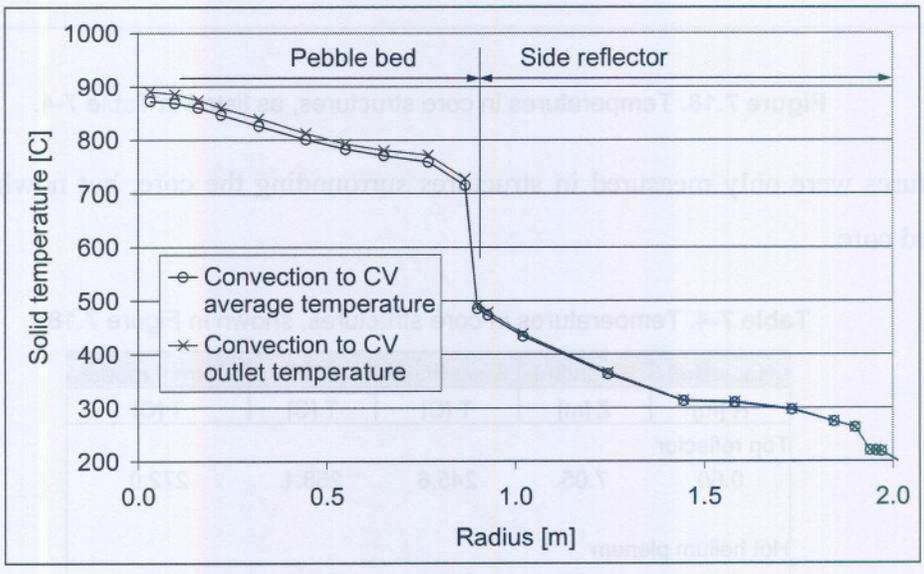


Figure 7.19. The influence of the convection discretisation on the radial solid temperature profile at 4.94m, near the bottom of the pebble bed.

The convection discretisation did not appear to affect the steady-state solution stability or speed.

7.3.5 Wall heat transfer

The bed/wall heat transfer empirical factor C_{sw} was estimated in the simulation of the conduction-dominated SANA experiment. Similarly, the fluid/wall heat transfer empirical

coefficient C_{fw} could be estimated from a simulation of the convection-dominated full massflow, full power HTR-10 simulation. A value of 0.1 for C_{fw} (as used in Eq. (6.37)) was found to give the most accurate heat transfer to the wall, as shown in Figure 7.20 and Figure 7.21.

$$Nu_{fw} = C_{fw} Nu_{KS} \tag{6.37}$$

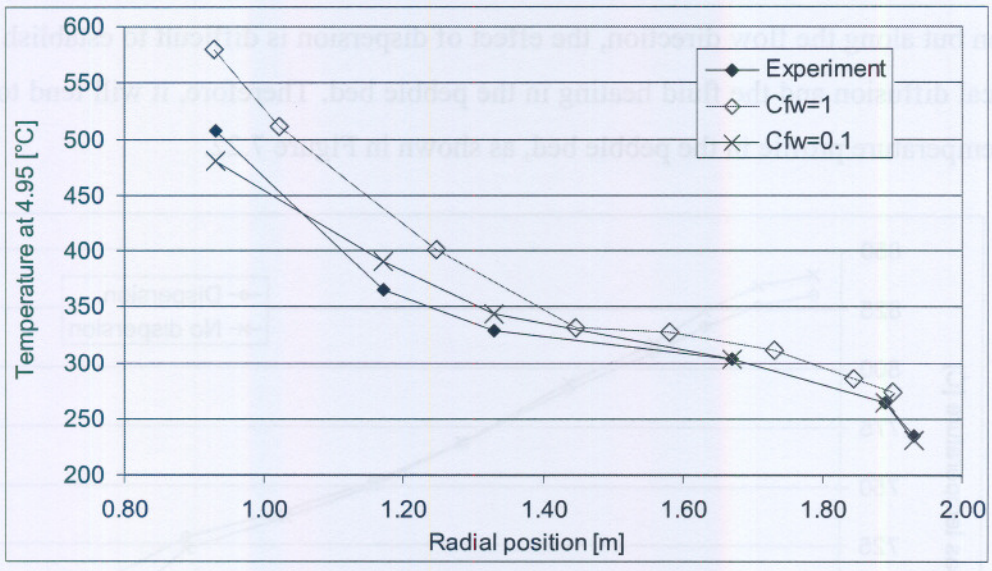


Figure 7.20. Reflector radial temperature profiles at a height of 4.94m (0.8m from the core top) for two values of C_{fw}. When Figure 7.21 is taken into account as well, a value of 0.1 is considered the most accurate.

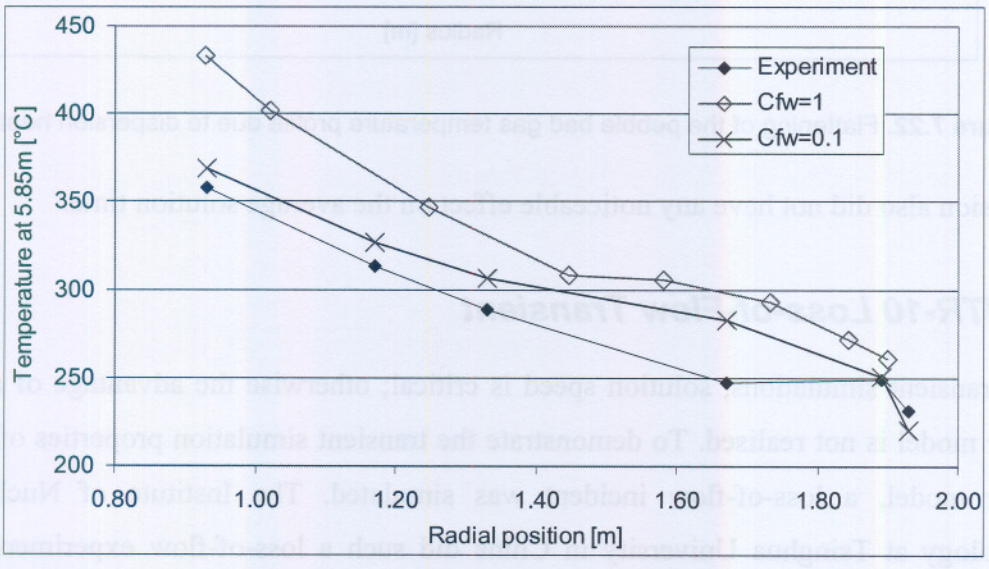


Figure 7.21. Reflector radial temperature profiles at a height of 5.85m (1.7m from the core top) for two values of C_{fw}. Side reflector radial temperature profile at two heights in the reactor, showing the effect of fluid/wall empirical factor C_{fw}.

The Kugeler-Schulten correlation is used for both the heat transfer to the pebble surface and to the wall, with the correction factor applied only to the wall convection area. More accurate values of C_{sw} and C_{fw} are expected to be ascertained with the HTTF experiments.

7.3.6 Dispersion

The effect of dispersion heat transfer is to enhance heat transfer perpendicular to the flow direction but along the flow direction, the effect of dispersion is difficult to establish because of numerical diffusion and the fluid heating in the pebble bed. Therefore, it will tend to flatten the radial temperature profile in the pebble bed, as shown in Figure 7.22.

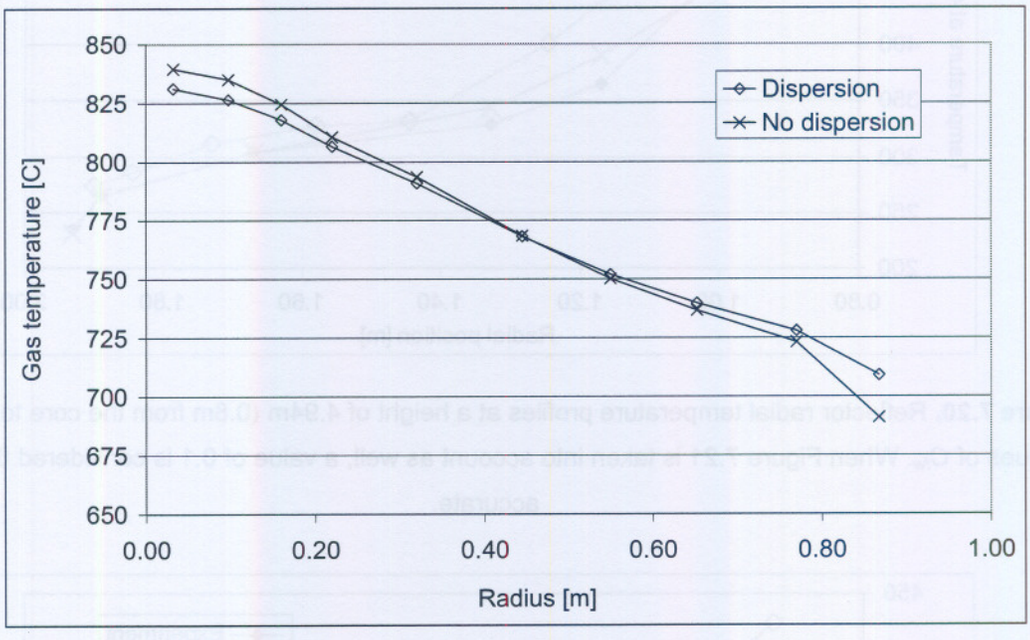


Figure 7.22. Flattening of the pebble bed gas temperature profile due to dispersion heat transfer.

Dispersion also did not have any noticeable effect on the average solution time.

7.4 HTR-10 Loss-of-Flow Transient

With transient simulations, solution speed is critical; otherwise the advantage of a simplified reactor model is not realised. To demonstrate the transient simulation properties of the present reactor model, a loss-of-flow incident was simulated. The Institute of Nuclear Energy Technology at Tsinghua University in China did such a loss-of-flow experiment with their HTR-10 pebble bed reactor. They also made the reactor geometry and experimental results available for the IAEA Coordinated Research Project on reactor simulation software. Therefore, this case was used to demonstrate the capability of the integrated reactor simulation model.

A loss-of-coolant incident is created by shutting down the primary loop helium blower and closing the flow valve to the reactor. After flow to the reactor is stopped, the core temperature increases and the negative fuel temperature reactivity coefficient causes the reactor to shut down. From then on, heat is only removed by the reactor cavity cooling system outside of the reactor pressure vessel. Inside the pressure vessel, conduction, radiation and natural convection are the modes of cooling for the core. Gradually the core cools down sufficiently so that the temperature coefficients cause a recriticality at about 4300 seconds after the flow was stopped.

Provided the information on the reactor heat generation and cooling mechanisms is accurate, this loss-of-flow incident presents a good system-level test for a reactor thermal-fluid model as the heat transfer characteristics of the thermal-fluid model determine the time of recriticality.

The HTR-10 loss-of-flow transient was, however, found to be a difficult case to calculate accurately and the results obtained by many research groups taking part in the IAEA CRP-5 benchmarking effort were unsatisfactory (Van Heerden, 2006). Even if the HTR-10 loss of flow transient is difficult to calculate accurately, its simulation will provide valuable qualitative indications of the important parameters for simulating an actual reactor. Information on the HTR-10 is also much more readily available than for the AVR, the only other pebble bed reactor with which loss-of-flow experiments were done.

7.4.1 Modelling parameters and boundary values

The point kinetic neutronic model described in Chapter 5, was used for calculating the heat generation. Fuel, moderator and reflector temperature reactivity feedback was taken into account while no Xenon reactivity feedback was taken into account. INET (IAEA, 2006) supplied the following reactor kinetic values:

Delayed neutron fraction: $\beta = 0.00726$
Prompt neutron generation lifetime: $\Lambda = 0.00168$

Yield fractions and decay constants for the six neutron precursor groups were taken from a calculation for the PBMR 268MW. The values were assumed applicable to the HTR-10 on account of also being a pebble bed type graphite moderated HTR. The yield fractions were scaled so that their sum equalled the Beta-value as supplied by INET (IAEA, 2006). This approximation is not expected to give significant errors, as the neutronic parameters that have the largest influence on the time of recriticality are the decay heat parameters, the temperature

reactivity feedback coefficients and the total delayed neutron fraction β. To clarify this statement, consider Eq.(5.1).

$$\frac{d\tilde{P}_n}{dt} = \frac{\rho - \beta}{\Lambda}\tilde{P}_n + \sum_{i=1}^{6}\lambda_i \tilde{C}_i \qquad (5.1)$$

Recriticality will occur only when $\frac{d\tilde{P}_n}{dt}$ becomes greater than zero. However, at the time when recriticality typically occurs, the neutron precursor isotopes have already decayed to insignificant levels, so that only the first term in Eq.(5.1) determines recriticality. Therefore, recriticality will occur when ρ becomes larger than β.

INET determined the temperature reactivity coefficients for the fuel to be -2.13 pcm/°C, for graphite moderator -16.2 pcm/°C and for graphite reflector 7.71 pcm/°C, while the delayed neutron precursor group constants are given in Table 7-5.

Table 7-5. Delayed neutron precursor group yield and decay constants

Beta1	0.00028281	Lambda1	3.625200
Beta2	0.00092806	Lambda2	1.406600
Beta3	0.00282808	Lambda3	0.316490
Beta4	0.00136465	Lambda4	0.118300
Beta5	0.00160242	Lambda5	0.031400
Beta6	0.00025398	Lambda6	0.012731

The fuel coefficient pertains to the average temperature over the whole pebble bed, of the inner 50mm diameter part of the fuel spheres. The moderator coefficient pertains to the whole 60mm sphere, i.e. it includes the 5mm surface layer. The reflector temperature coefficient is assumed to pertain to the average temperature of all graphite components surrounding the core.

Decay heat was modelled with three exponential functions of which the coefficients were calculated to match the decay heat profile supplied by INET, shown in Figure 7.23. The production and decay coefficients are given in Table 7-6, while the timestep lengths used in the simulation are given in Table 7-7.

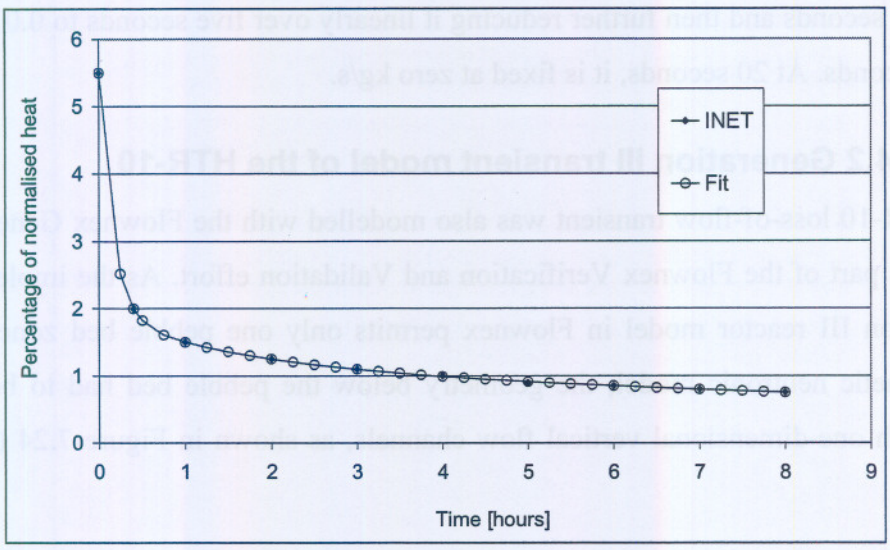


Figure 7.23. Decay heat for the HTR-10, as calculated by INET.

Table 7-6. Production and decay constants for a three-group approximation to the HTR-10 decay heat normalised to nominal power.

β_1	0.036031429
β_2	0.01156977
β_3	0.007398801
λ_1	0.001748196
λ_2	0.000015265
λ_3	0.000172069

Table 7-7. Timestep lengths and the time at which it was applied.

Time[s]	Timestep length[s]
1	0.2
2	0.15
20	0.3
50	0.5
100	1
300	2
500	3
750	4
1275	3
4000	2

Before the loss-of-flow incident, the reactor was at steady-state condition at 2.99MW with an inlet flow temperature of 215°C, an outlet temperature of 650°C and a massflow of 1.2781kg/s. The loss-of-flow incident is simulated by linearly reducing mass flow from 1.2781 kg/s to 1kg/s

over two seconds and then further reducing it linearly over five seconds to 0.01kg/s at a time of seven seconds. At 20 seconds, it is fixed at zero kg/s.

7.4.2 Generation III transient model of the HTR-10

The HTR-10 loss-of-flow transient was also modelled with the Flownex Generation III reactor model as part of the Flownex Verification and Validation effort. As the implementation of the Generation III reactor model in Flownex permits only one pebble bed zone when using the point kinetic neutronic model, the geometry below the pebble bed had to be simplified to a solid with one-dimensional vertical flow channels, as shown in Figure 7.24 (Van Antwerpen, 2006).

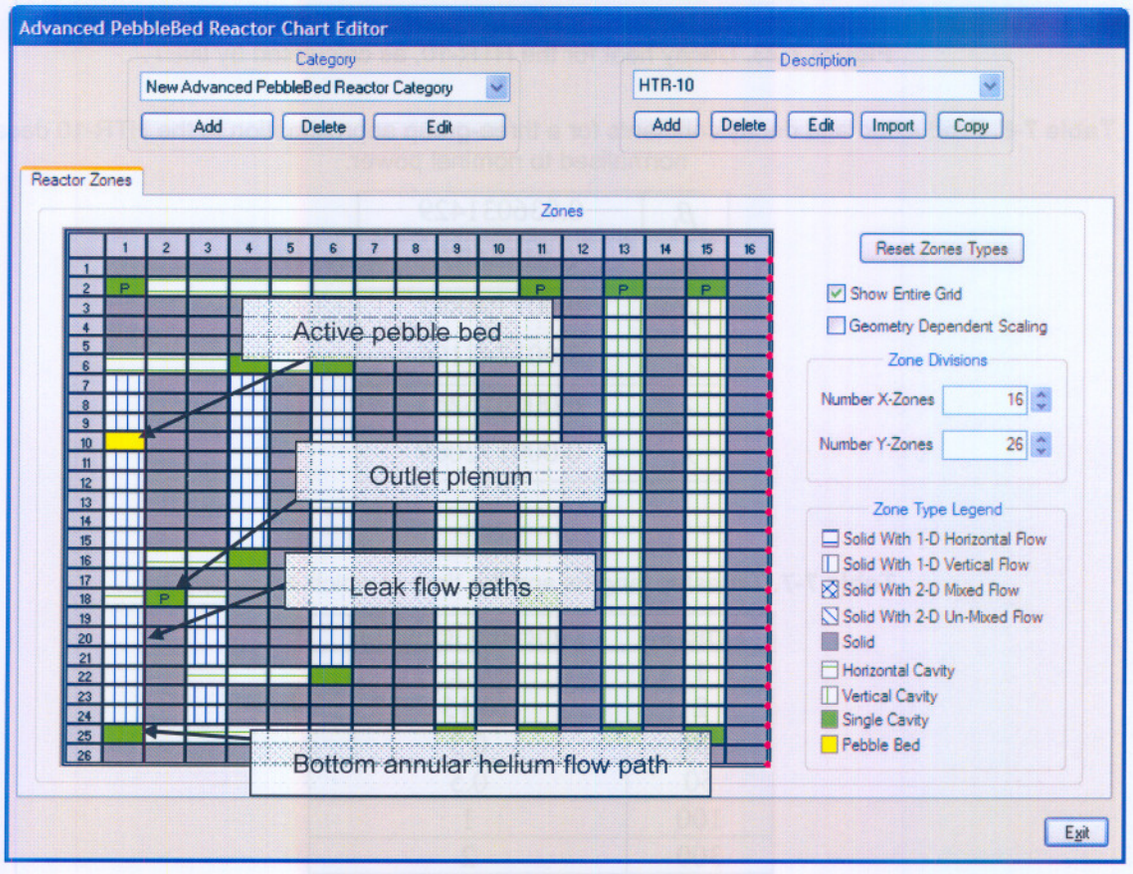


Figure 7.24: Generation III model of the HTR-10 for simulating a transient in Flownex. The grid is not to scale but is equally spaced grid for display purposes (Van Antwerpen, 2006).

7.4.3 Main result

Using the unmodified data provided by INET, the best results obtained with the present reactor model are presented in Figure 7.25 and Figure 7.26. The recriticality result obtained with the Generation III reactor model is shown in Figure 7.26.

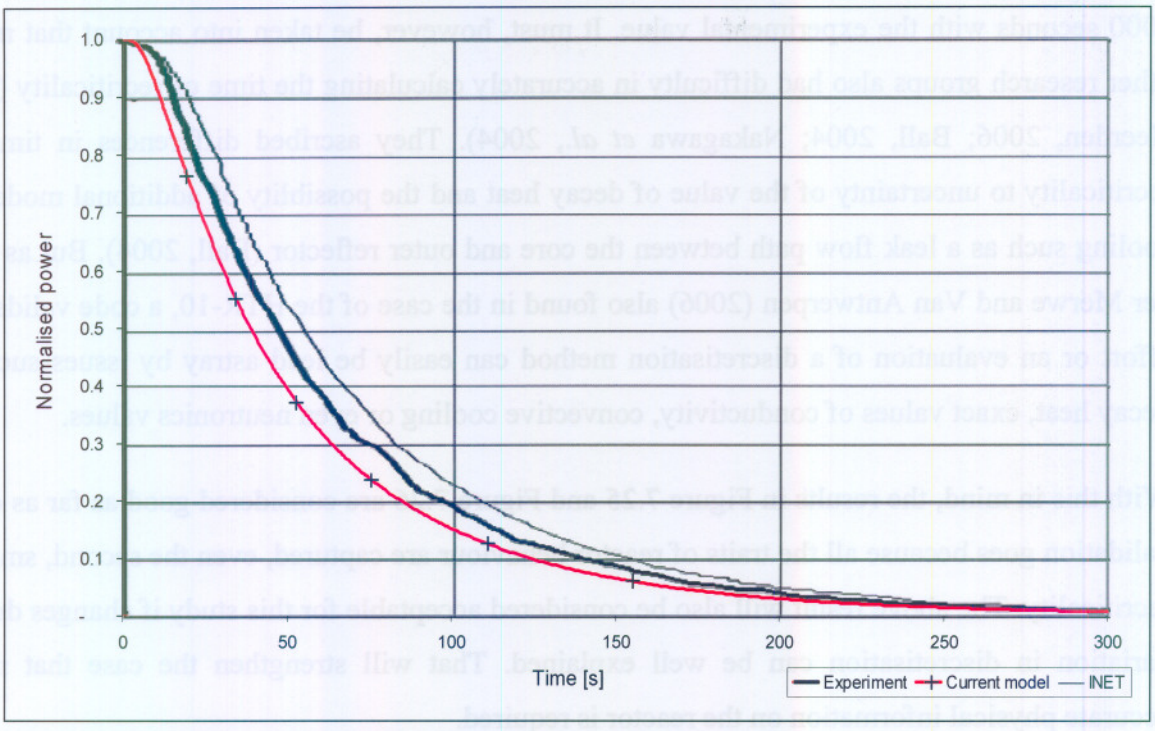


Figure 7.25. Normalised power versus time shortly after stopping coolant flow in the HTR10.

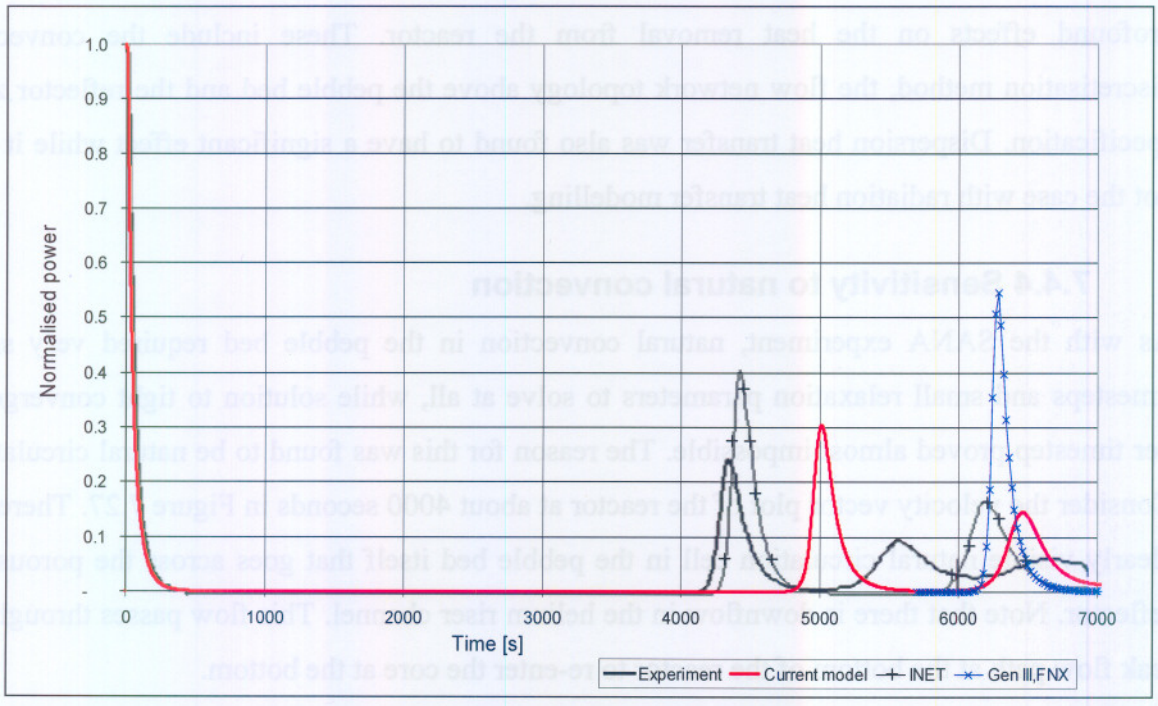


Figure 7.26 Normalised power after stopping coolant flow in the HTR-10, showing recriticality at about 4300 seconds.

The time of recriticality calculated with the *Flownex Research Version* Generation IV reactor model differs by about 700 seconds with the experimental and INET results, which is quite significant, while the result from the Flownex Generation III reactor model differed by about

2000 seconds with the experimental value. It must, however, be taken into account that many other research groups also had difficulty in accurately calculating the time of recriticality (Van Heerden, 2006; Ball, 2004; Nakagawa *et al.*, 2004). They ascribed differences in time of recriticality to uncertainty of the value of decay heat and the possiblity of additional modes of cooling such as a leak flow path between the core and outer reflector (Ball, 2004). But as Van der Merwe and Van Antwerpen (2006) also found in the case of the HTR-10, a code validation effort or an evaluation of a discretisation method can easily be lead astray by issues such as decay heat, exact values of conductivity, convective cooling or even neutronics values.

With this in mind, the results in Figure 7.25 and Figure 7.26 are considered good as far as code validation goes because all the traits of reactor behaviour are captured, even the second, smaller recriticality. The above result will also be considered acceptable for this study if changes due to variation in discretisation can be well explained. That will strengthen the case that more accurate physical information on the reactor is required.

Except for modelling parameter values, the discretisation methods of several mechanisms have profound effects on the heat removal from the reactor. These include the convection discretisation method, the flow network topology above the pebble bed and the reflector zone specification. Dispersion heat transfer was also found to have a significant effect while it was not the case with radiation heat transfer modelling.

7.4.4 Sensitivity to natural convection

As with the SANA experiment, natural convection in the pebble bed required very small timesteps and small relaxation parameters to solve at all, while solution to tight convergence per timestep proved almost impossible. The reason for this was found to be natural circulation. Consider the velocity vector plot of the reactor at about 4000 seconds in Figure 7.27. There is a clearly visible natural circulation cell in the pebble bed itself that goes across the porous top reflector. Note that there is downflow in the helium riser channel. This flow passes through the leak flow path at the bottom of the reactor to re-enter the core at the bottom.

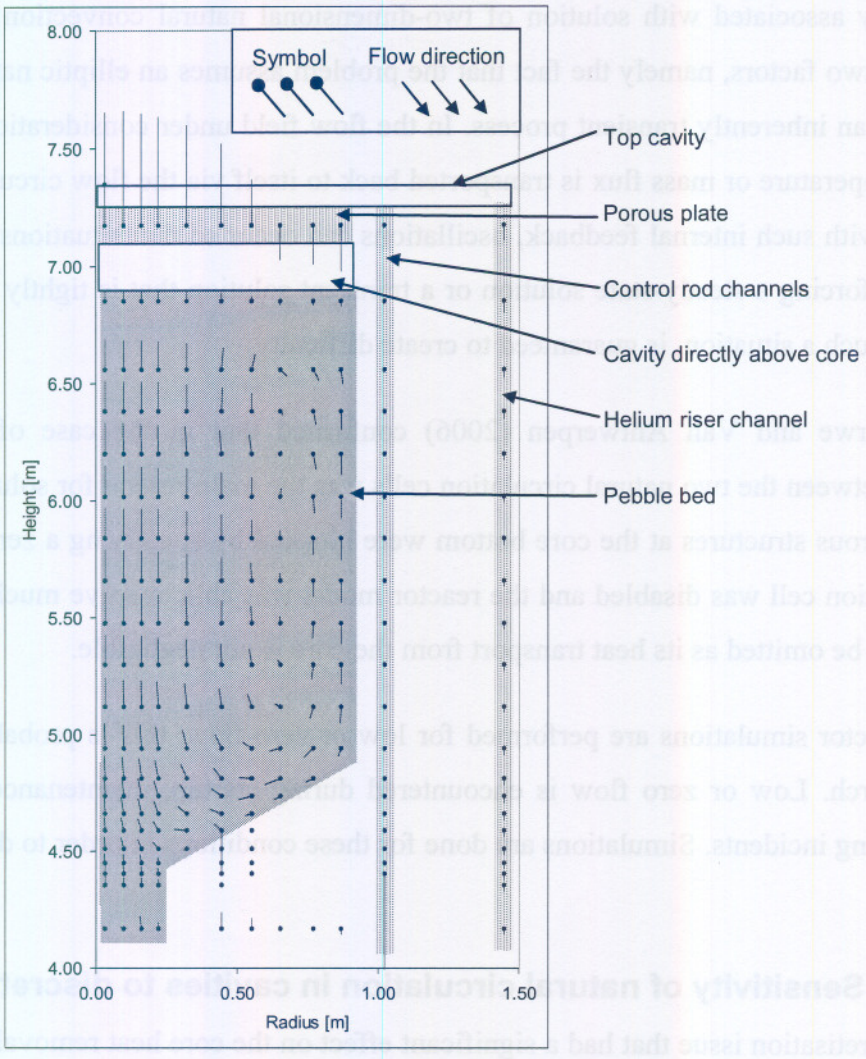


Figure 7.27. Flow vectors in the HTR-10 after a LOFC incident. Note that flow direction is indicated by lines pointing away from the black dots, which indicate node positions.

Thus, the circulation cells that develop can be represented schematically as shown in Figure 7.28.

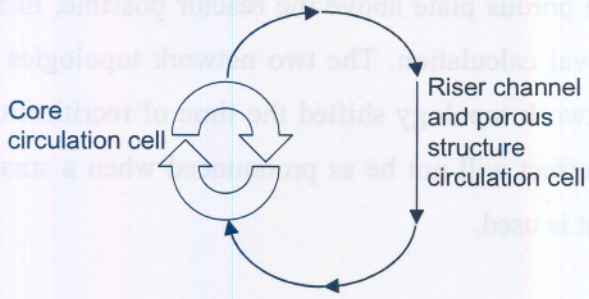


Figure 7.28. Topology of the circulation cells in the HTR10 LOFC case.

The difficulty associated with solution of two-dimensional natural convection flow fields is attributed to two factors, namely the fact that the problem assumes an elliptic nature and that it is frequently an inherently transient process. In the flow field under consideration, any change in a local temperature or mass flux is transported back to itself via the flow circulation. Typical for systems with such internal feedback, oscillations can occur so that situations are inherently unsteady. Enforcing a steady-state solution or a transient solution that is tightly converged per timestep on such a situation, is guaranteed to create difficulty.

Van der Merwe and Van Antwerpen (2006) confirmed that in the case of the HTR-10, interaction between the two natural circulation cells was the main reason for solution difficulty. When the porous structures at the core bottom were blocked by specifying a zero porosity, the outer circulation cell was disabled and the reactor model was able to solve much faster. It can, however, not be omitted as its heat transport from the core is not negligible.

As many reactor simulations are performed for low or zero flow, this is probably an area for further research. Low or zero flow is encountered during startup, maintenance and Loss-of-Forced Cooling incidents. Simulations are done for these conditions in order to design auxiliary systems.

7.4.5 Sensitivity of natural circulation in cavities to discretisation

Another discretisation issue that had a significant effect on the core heat removal under loss-of-flow conditions is the network topology in the cavity above the core. When there is only a single cavity above the core, a single node represents the whole volume. The temperature of this node is the mass-averaged temperature over all the inflows and outflows from the cavity, thereby rendering natural circulation between the top cavity and the cavity above the pebble bed impossible. Splitting the volume into several nodes above the cavity makes natural circulation through the porous plate above the reactor possible, thereby greatly increasing the accuracy of heat removal calculation. The two network topologies are shown in Figure 7.29. This change to the network topology shifted the time of recriticality more than 2000 seconds earlier. Note that this effect will not be as pronounced when a smaller top cavity convections heat transfer coefficient is used.

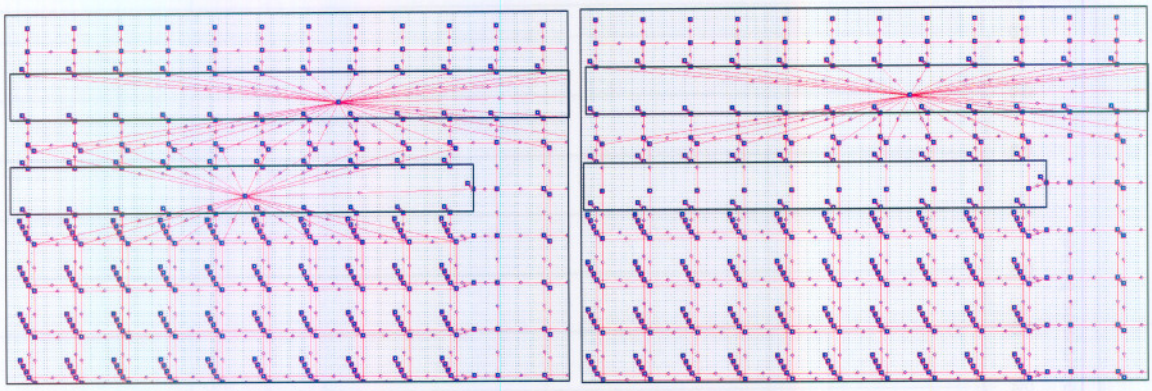


Figure 7.29. The networks for the cavity above the pebble bed as a single cavity (left) or as a series of open vertical flow zones (right).

It must, however, be noted that this effect will be much less pronounced in a tall slender reactor like the PBMR, where the most important heat loss is through the side reflector and pebble bed wall. With the HTR-10, the almost spherical shape of the core makes natural circulation in the top cavities more important than in the case of a tall slender reactor such as the PBMR.

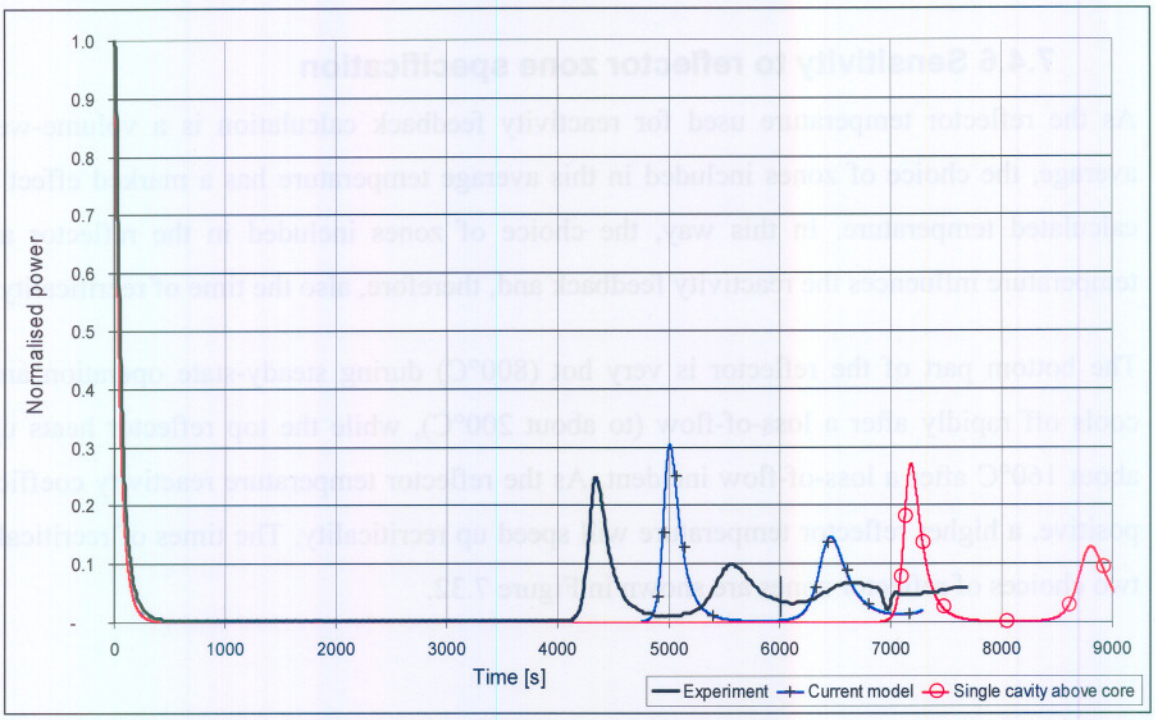


Figure 7.30. Relative power for the two different cavity networks in Figure 7.29.

Two values of convection heat transfer coefficient in the top reflector cavity were tested. Using 15 W/m^2K instead of 30 W/m^2K resulted in retarding recriticality with 600s, as shown in Figure 7.31.

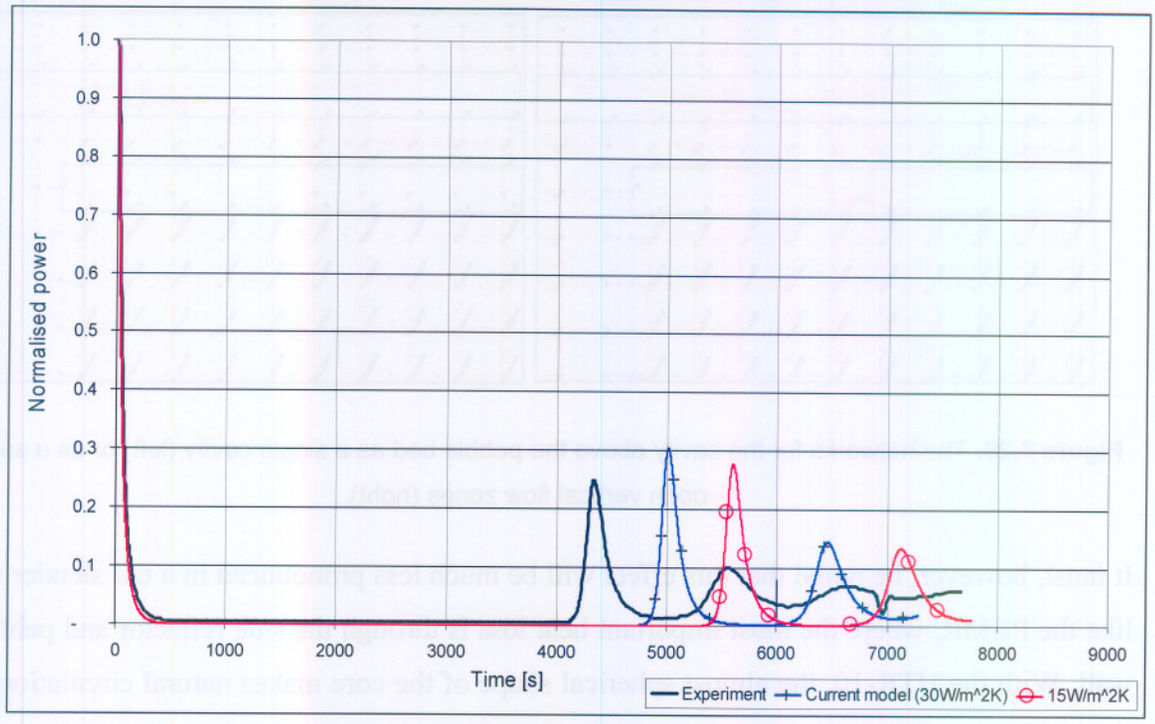


Figure 7.31. The effect of top reflector cavity convection heat transfer coefficient.

7.4.6 Sensitivity to reflector zone specification

As the reflector temperature used for reactivity feedback calculation is a volume-weighted average, the choice of zones included in this average temperature has a marked effect on the calculated temperature. In this way, the choice of zones included in the reflector average temperature influences the reactivity feedback and, therefore, also the time of recriticality.

The bottom part of the reflector is very hot (800°C) during steady-state operation and then cools off rapidly after a loss-of-flow (to about 200°C), while the top reflector heats up with about 160°C after a loss-of-flow incident. As the reflector temperature reactivity coefficient is positive, a higher reflector temperature will speed up recriticality. The times of recriticality for two choices of reflector zones are shown in Figure 7.32.

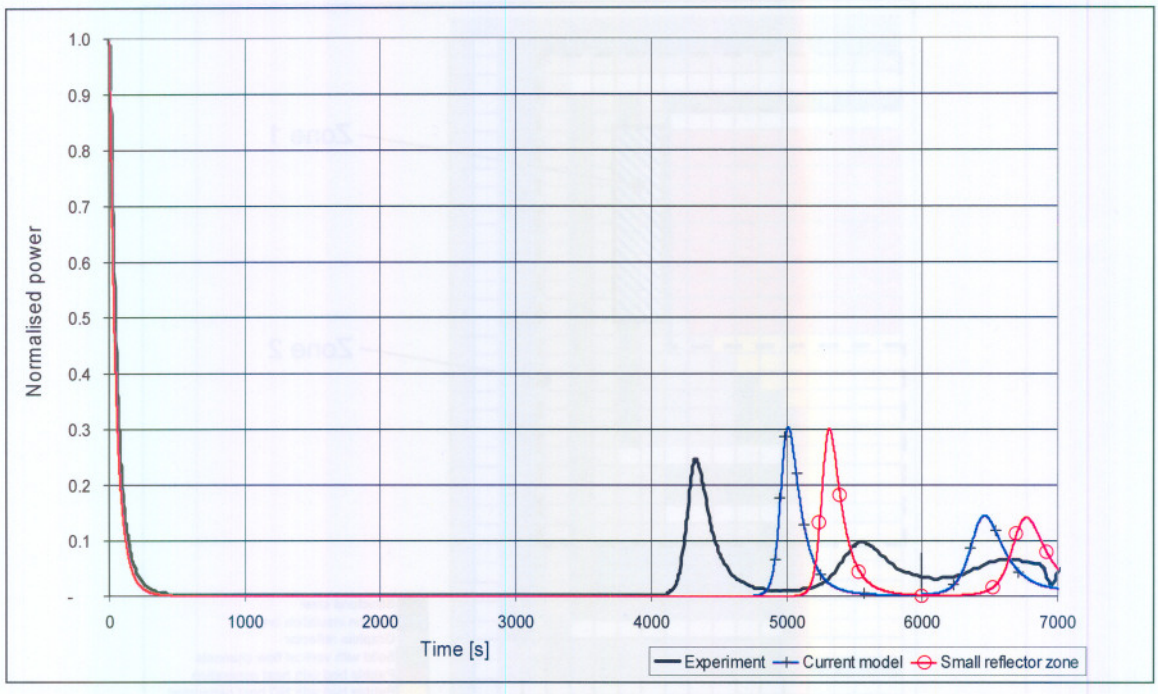


Figure 7.32. Reactivity as a function of time for three different choices of side reflector zones, showing the importance of proper zone specification.

The zones that were used to calculate the reflector average temperature are shown in Figure 7.33. The best agreement with the experimental result is obtained when Zone 2 was used, as is the case with the current model.

7.4.7 Sensitivity to radiation heat transfer

The reactor model described by Du Toit *et al.* (2003) models radiation only by linking directly opposing surfaces with a view factor of one. It is not known how significant the errors caused by the geometrical simplification of this method are. Therefore, to answer this question, a detailed radiation model was developed that takes all possible radiation heat transfer links in a cavity into account, as described in previous chapters and in Appendix D.

As case studies, the HTR-10, as well as the 268MW version of the PBMR, was simulated using both direct radiation couplings and the detailed radiation model. The conclusion of the investigation was that the sophistication of the radiation heat transfer model had a negligible effect on the overall heat removal. That was the case for the HTR-10 reactor, as well as the 268MW PBMR reactor while the PBMR DLOFC case took 30 percent longer to solve when using a detailed radiation model instead of the simplified model. The detail of this investigation is described in a paper presented at the HTR2006 conference, and which is included in this thesis as Appendix D.

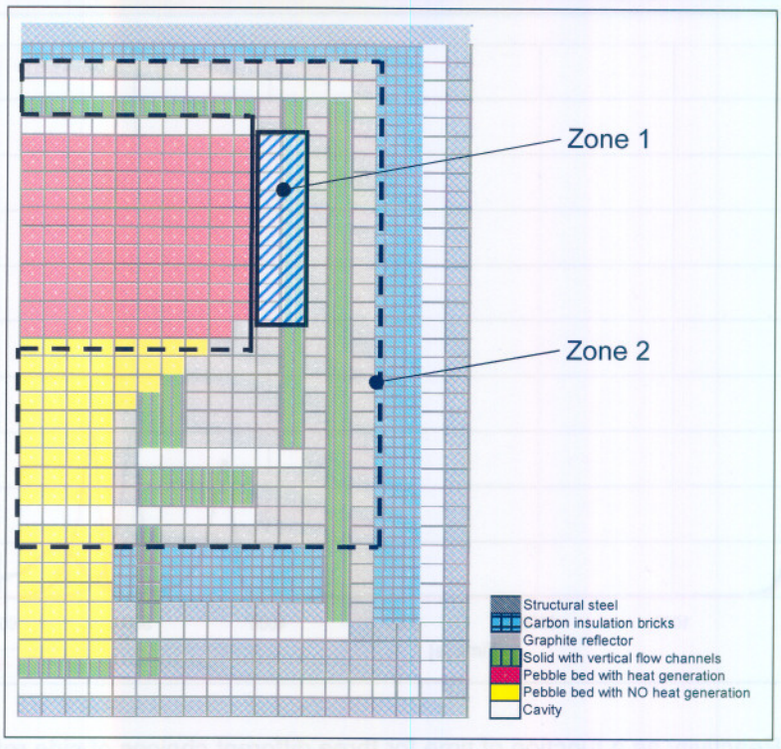


Figure 7.33. Two zone sets that were used to calculate the reflector average temperature for reactivity feedback. Zone 2 gave the best agreement with experimental result. The scale of the reactor grid in the background is distorted to display all cells the same size.

It is also concluded that when overall heat loss from an integrated system is considered, sufficient accuracy can be obtained when linking only directly opposing surfaces with a view factor of 1. However, when local component temperatures are important, as could be the case with metal components above or below the core, a detailed radiation heat transfer model is considered essential, but then, that level of detail falls in the scope of CFD calculations.

For system simulation codes that focus on transient response of a plant, it is not considered worthwhile to use a detailed radiation model, as the gain in accuracy does not justify the increased solution time or the implementation and verification effort.

7.4.8 Sensitivity to convection discretisation

It was seen that the choice of convection discretisation could move the time of recriticality up to 900s (Figure 7.34). Referring to the convection discretisation schemes as described in Paragraph 6.3, the old scheme based on the control volume outlet temperature gave a much earlier recriticality than the new scheme that is based on control volume average temperature. Incidentally, the result from the outlet-based scheme appears to be more accurate than the average control volume temperature convection scheme. Use extreme caution in the

interpration of this result! It is proven in Paragraphs 6.3 and 7.5.1 that the second order convection is more accurate than first order accurate convection discretisation. Therefore, the first order convection scheme can mask other inaccuracies. In this case, it would not show that the heat removal from the reactor is too low.

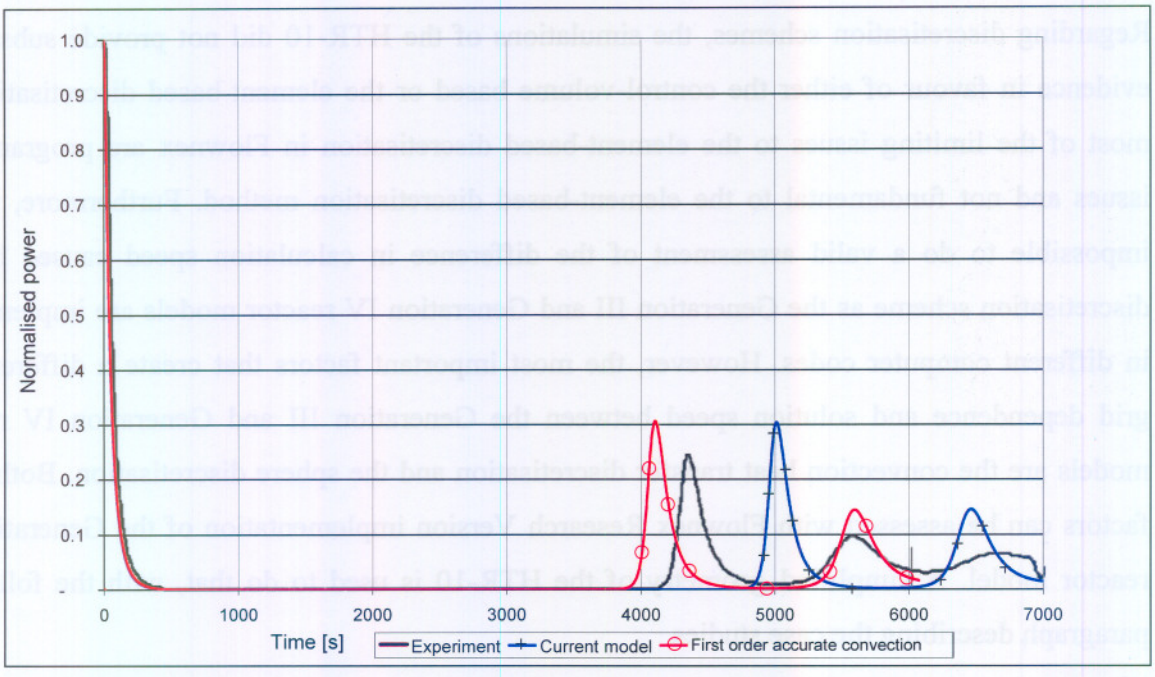


Figure 7.34. Relative power for two different convection discretisation methods.

The reason for the earlier recriticality can be found in the calculated reference temperatures. The second order scheme calculates the steady-state fuel reference temperature as 821°C and the moderator reference temperature as 819°C, while the first order scheme calculates the temperatures as 840°C and 839°C respectively. Higher reference temperatures provide a higher temperature gradient for removing heat from the reactor, thereby requiring less time to recriticality.

The effect of convection discretisation on simulation performance is investigated in more detail and quantified in paragraph 7.5.1.

7.4.9 Conclusion of the HTR-10 Loss-of-Flow Transient

The HTR-10 simulation showed the importance of having reliable input data in terms of material properties, geometry and heat generation boundary values. Additional to those physical parameters, the modelling parameters for heat loss from the reactor also require careful consideration.

The sensitivity of time of recriticality was investigated with regard to the modelling of natural convection, reflector zone specification, convection heat transfer and sphere discretisation. The effect of convection and sphere discretisation will be quantified with a simplified version of the HTR-10 in a following paragraph.

Regarding discretisation schemes, the simulations of the HTR-10 did not provide substantial evidence in favour of either the control-volume based or the element-based discretisation, as most of the limiting issues to the element-based discretisation in Flownex are programming issues and not fundamental to the element-based discretisation method. Furthermore, it was impossible to do a valid assessment of the difference in calculation speed caused by the discretisation scheme as the Generation III and Generation IV reactor models are implemented in different computer codes. However, the most important factors that create a difference in grid dependence and solution speed between the Generation III and Generation IV reactor models are the convection heat transfer discretisation and the sphere discretisation. Both these factors can be assessed with Flownex Research Version implementation of the Generation IV reactor model. A simplified geometry of the HTR-10 is used to do that, with the following paragraph describing the case studies.

7.5 HTR-10 Conceptual geometry to quantify sphere and convection discretisation grid dependence

The purpose of this paragraph is to quantify the difference in performance (accuracy and simulation speed) caused by the most important differences between the Generation III and Generation IV reactor models, namely convection heat transfer discretisation and sphere discretisation. This is done with a loss-of-flow case study of a greatly simplified reactor based on the HTR-10.

The simplifications included assuming adiabatic top and bottom boundaries, simplified inlet and outlet plenum geometry, as well as removing detail from the reactor radial heat removal path. The discretisation of the simplified reactor is shown in Figure 7.35.

All material properties and reactor performance parameters were used as described in paragraph 7.4.1, except that a constant volumetric heat generation was assumed. No dispersion was modelled, the pebble bed effective conductivity was fixed at 20W/mK and the wall heat transfer

parameters C_{sw} and C_{fw} were taken as 1 and 0.1 respectively. Flow inlet temperature was 250°C and the loss of flow event described in paragraph 7.4.1 was simulated.

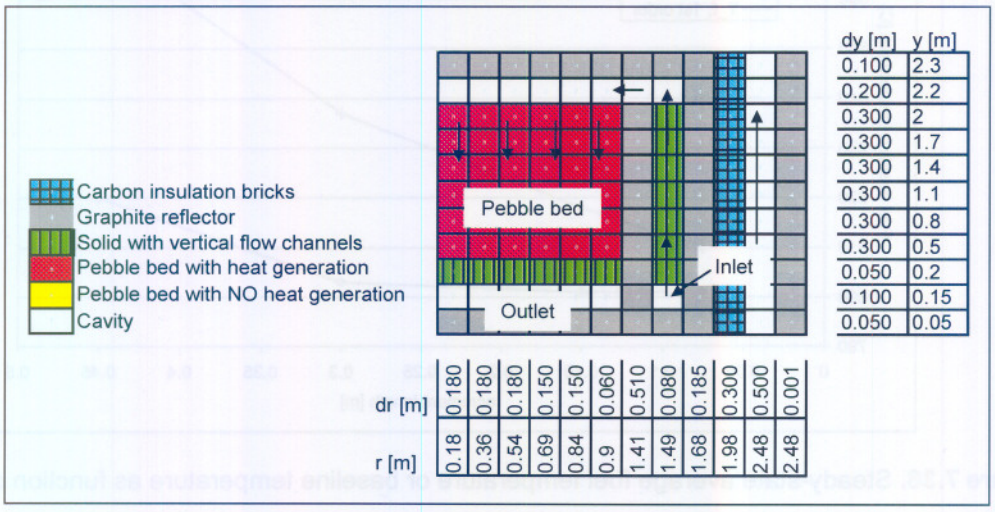


Figure 7.35. Simplified reactor geometry for quantifying the effect of convection and sphere discretisation with six pebble bed axial increments.

7.5.1 Convection discretisation

For determining the effect of convection discretisation, grid sizes of 4, 6, 12 and 24 increments were tested with both first and second order accurate convection heat transfer discretisation. Convection heat transfer discretisation is described in paragraph 6.3. The steady-state average fuel temperature (baseline temperature) and the time of recriticality maximum power was used as measures of grid dependence, while the time required to calculate 100 timesteps was used as performance measure.

In Figure 7.36 the average fuel temperature is shown as a function of increment length, while Figure 7.37 shows it as a function of increment number for the two convection discretisation schemes.

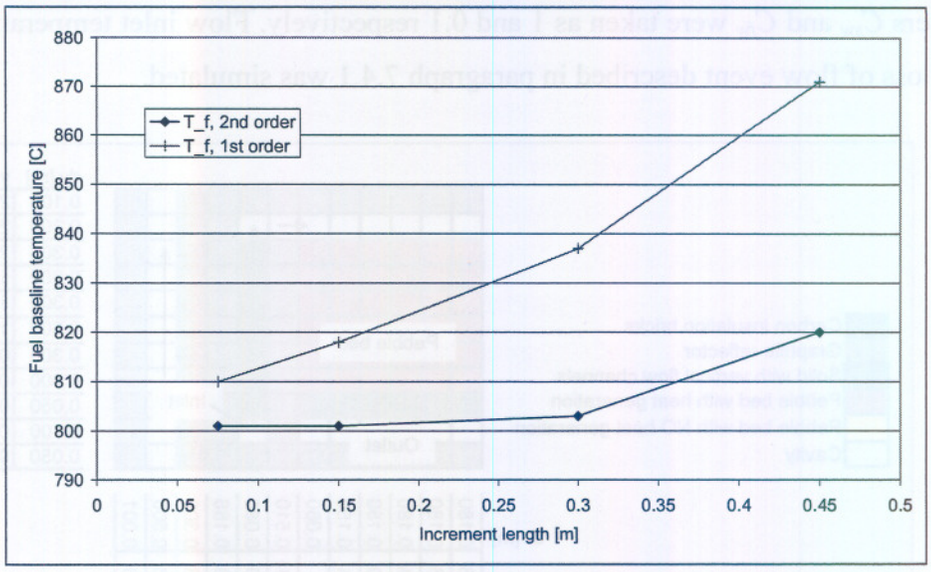


Figure 7.36. Steady-state average fuel temperature or baseline temperature as function of increment length for the modified HTR-10 case in Figure 7.35.

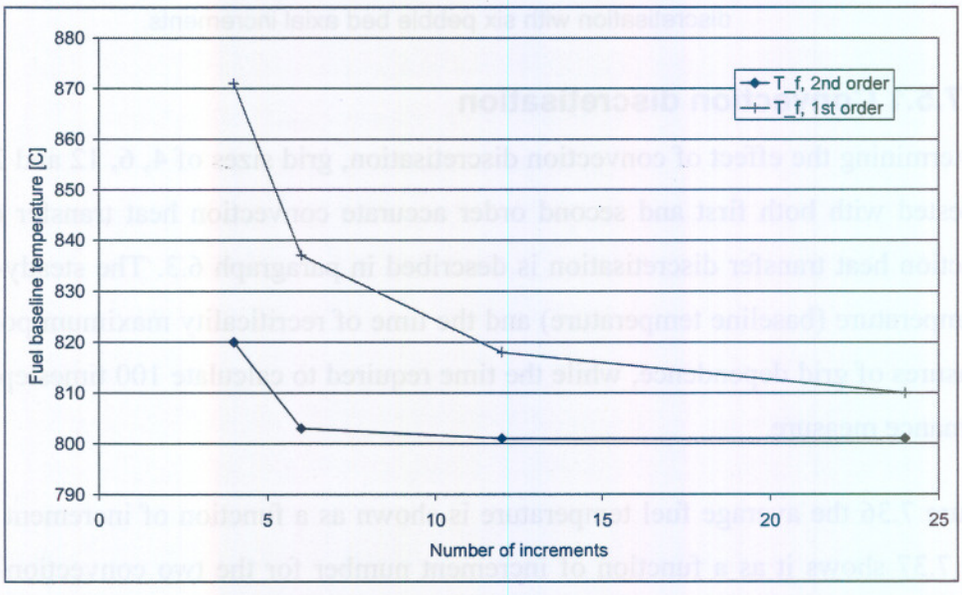


Figure 7.37. Steady-state average fuel temperature or baseline temperature as function of the number of axial increments for first order and second order accuracy convection heat transfer discretisation.

Figure 7.36 and Figure 7.37 show that the second order accurate scheme requires much less axial increments to reach the same level of accuracy than the first order scheme that is currently implemented in the Generation III reactor model. As described in paragraph 7.3.4, the average fuel temperature has a significant effect on the time of recriticality, namely that a higher steady-state average fuel temperature (baseline temperature) causes an earlier recriticality. Therefore, Figure 7.38 shows the time at which recriticality maximum power occurs as function of the number of increments, along with the time required to calculate 100 timesteps in each case.

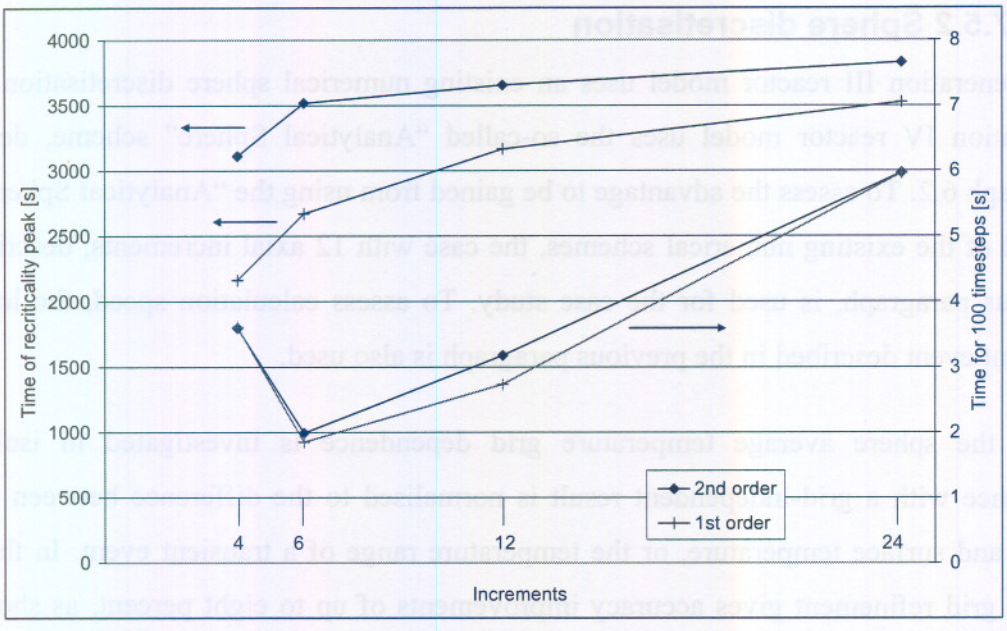


Figure 7.38. Time of recriticality and the time required for simulating 100 timesteps for various grid sizes and both first order and second order convection discretisation.

In Figure 7.38 the calculation time for four increments is so much longer than that of six increments because the control volumes are so large that oscillations occur during solution.

From Figure 7.38 it can be seen that the first order scheme requires 24 axial increments to calculate recriticality to a level of accuracy for which the second order scheme requires only six increments. With 24 increments, calculation of 100 timesteps takes six seconds while it takes only two seconds for six increments, so that the first order scheme takes three times as long to reach the same level of accuracy as the second order convection discretisation.

Thus, by implementing second order accurate convection discretisation in the Generation III reactor model, its calculation speed can be reduced by 60 percent.

If the fuel reference temperature in the point kinetic model is artificially modified to account for the inaccuracy of the convection discretisation, the time of recriticality in case of a loss-of-flow transient could be calculated more accurately. However, that approach will not be valid for simulating the transient response of the reactor while operating, as a full-power neutronic steady-state is only reached when the average fuel temperature equals the reference temperature. An artificially modified reference temperature will cause a large error on the stabilisation power level.

7.5.2 Sphere discretisation

The Generation III reactor model uses an existing numerical sphere discretisation while the Generation IV reactor model uses the so-called "Analytical Sphere" scheme, described in paragraph 6.2. To assess the advantage to be gained from using the "Analytical Sphere" scheme instead of the existing numerical schemes, the case with 12 axial increments, described in the previous paragraph, is used for the case study. To assess calculation speed, the loss-of-flow transient event described in the previous paragraph is also used.

When the sphere average temperature grid dependence is investigated in isolation, the difference with a grid-independent result is normalised to the difference between the sphere center and surface temperature, or the temperature range of a transient event. In this context, sphere grid refinement gives accuracy improvements of up to eight percent, as shown on the righthand axis of Figure 7.39. However, in the context of the integrated reactor model, this improvement in accuracy proved to be negligible. The steady-state average fuel temperature also changed less than one degree Celcius by refining the sphere grid or using the Analytical Sphere scheme, as shown in the lefthand axis in Figure 7.39. Accordingly, the time of recriticality maximum power varied less than 20 seconds between the various sphere discretisations. Thus, it is concluded that the current numerical sphere discretisation used in the Generation III reactor model is appropriate and adequate.

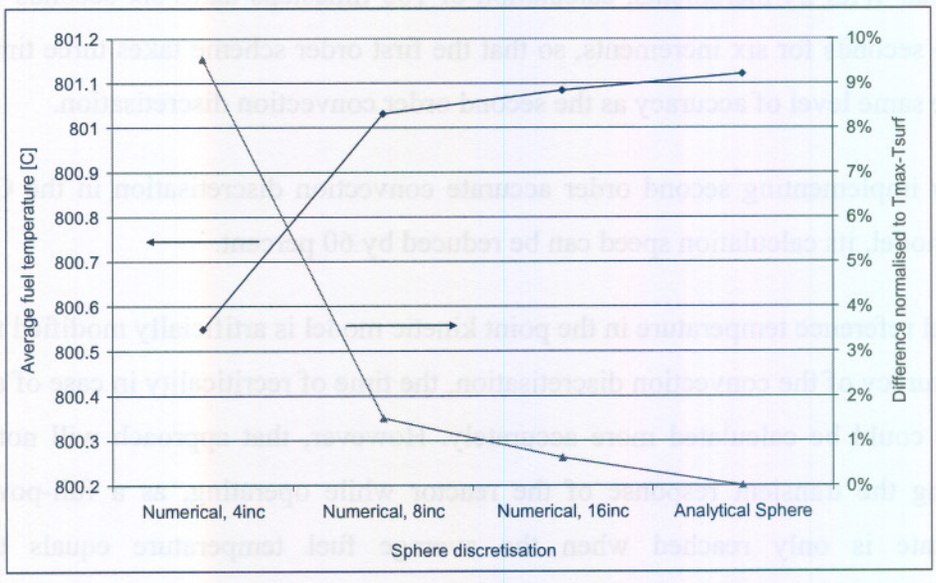


Figure 7.39. Average fuel temperature and normalised difference with the "Analytical Sphere" scheme for various sphere discretisations. The difference between sphere center temperature (T_{max}) and surface temperature (T_{surf}) was six degrees Celcius.

7.6 Conclusion

From the simulations of the SANA experiment, it is seen that the mathematical models that are solved, have a far greater effect on accuracy than the discretisation method with which they are implemented.

The sensitivity studies on the HTR-10 show that its time of recriticality is highly dependent on discretisation, as well as physical values such as the top cavity heat transfer coefficient. For this reason, the HTR-10 has to be simulated in great detail to accurately predict the time of recriticality. Numerical models of the PBMR are much less sensitive to the heat transfer coefficient in the top cavity than the HTR-10, as the PBMR is a tall slender reactor. Due to the PBMR geometry, the top cavity forms a small part of the heat removal path compared to conduction and radiation from the sides of the reactor.

Detail radiation modelling in systems simulation codes is shown not to be necessary, while it is pointed out that the solution difficulties brought about by natural convection have to be dealt with.

As there are also doubts on the HTR-10 material properties and the decay heat, the HTR-10 is not considered a good code validation case. Still, its simulation provides valuable qualitative indications of the importance of various parameters.

The most important improvement to accuracy and calculation speed is to be found from using second order accurate convection discretisation instead of the first order accurate scheme currently used in the Generation III reactor model. Another advantage of the second order convection discretisation scheme developed in this study, is that it applies to both the element-based and control-volume based approaches. It was found to reduce solution time by up to 60 percent for a certain level of accuracy. However, keep in mind that the solution time reduction is also reactor- and condition-dependent.

The advantage of the control-volume based discretisation is not so much accuracy of calculation results, but rather that it provides a simpler, more intuitive framework for implementing mathematical models as described in Sections 4.7 and 4.8.

It was found that when sphere discretisation is investigated in isolation, it promises terrific gains in accuracy, but in the context of an integrated reactor model, the improvement in

accuracy is negligible, so that the existing numerical sphere discretisation in the Generation III reactor model is considered adequate and appropriate.

Chapter 8

Conclusions and recommendations

8.1 Executive summary

This study dealt with the modelling of a pebble bed high-temperature gas-cooled nuclear reactor in a systems simulation code. While some previous reactor models had been developed for systems simulation codes, their discretisation schemes had not been optimised to use the minimum number of grid points. Therefore, this study aimed at increasing the accuracy of the discretisation methods of a reactor model in the *Flownex* systems simulation code, which is used to simulate the PBMR. Increasing the accuracy of a discretisation, makes it less grid-dependent, so that fewer increments are required to obtain an accurate solution. For system simulation codes, the number of grid points are chosen to be appropriate for the specific simulation that is to be performed.

Several aspects of the pebble bed reactor discretisation were investigated and implemented in a *Flownex* reactor model. The comprehensive reactor model was tested by simulating the SANA and HTR-10 steady-state cases, as well as the HTR-10 loss-of-flow experiment published by the IAEA. Several sensitivity studies were performed to assess the effect of some physical, as well as numerical parameters.

The most significant accuracy improvement was gained from developing a second-order accurate convection heat transfer scheme. It used the sum of inflows to a control volume to determine the average fluid temperature for convection heat transfer, resulting in higher accuracy and consequently the attainment of solid temperature grid independence at fewer grid points.

The numerical sphere discretisation method, as well as the crude approximations for radiation heat transfer, that are currently used in many reactor simulation codes, was found to be appropriate and gave adequate accuracy. Two reactor discretisation schemes were also evaluated, namely the control-volume based scheme and the element-based scheme. The control-volume based scheme was found to provide a simpler and more intuitive framework from implementing mathematical models, but not to directly increase accuracy.

8.2 Conclusions

Simulation speed of a thermal-fluid reactor model can be improved by up to sixty percent in some cases if second-order accurate convection heat transfer discretisation is used.

It has been proven that it is not necessary to model detailed radiation heat transfer in a systems simulation code, that it is sufficient to link only directly opposing surfaces with a view factor of one, as is currently done in the *Flownex* Generation III reactor model.

The current numerical sphere discretisation used in the Generation III reactor model has also been found to be appropriate and accurate. From the calculations with the integrated reactor model, it was seen that the mathematical models that are solved has a far greater effect on accuracy than the discretisation method with which they are implemented. Thus, the limitations of the Generation III reactor model are mostly due to programming and implementation issues but not due to its element-based discretisation.

While the control-volume based scheme provides a simpler and more intuitive framework for implementing mathematical models than the element-based discretisation, it does not directly contribute to calculation accuracy.

8.3 Recommendations for future work

8.3.1 Natural convection in pebble beds

This was found to be the most difficult part of the thermal-fluid problem in the reactor. The SANA experiments required very small relaxation parameters to achieve convergence, as did the HTR-10 loss-of-coolant simulations in which natural convection also played an important role. The small relaxation parameters greatly increased simulation time. Therefore, natural convection is the phenomenon limiting reactor simulation speed. Solution speed can probably be improved if methods for elliptic differential equations are researched. There is also scope for developing a sound approach to inherently transient phenomena that do have relatively constant time-average values.

8.3.2 Natural convection in cavities

The observations on the HTR-10 indicated that there is scope for work to firstly, understand the behaviour of natural convection in cavities. Following from this, methods can be developed to create network topologies that accurately represent such cavities by, for instance, accurately

calculating heat transfer coefficients. The PBMR reactor behaviour is not influenced by natural circulation nearly as much as the HTR-10, while the design of some secondary systems may be influenced by the top and bottom reflector temperatures determined by natural convection. Still, determination of these temperatures falls within the scope of CFD, while mostly only phenomena that influence reactor transients are applicable for systems simulation codes.

8.3.3 Pebble bed/wall heat transfer

Modelling of heat transfer between the pebble bed and the reflector wall still requires considerable research. From the experience gained in this study, it appears to be best to decide on a pebble bed/wall network topology with a fixed size and then calibrate the assembled numerical model with a large number of experimental data sets, such as expected from the High Temperature Test Unit and the High Pressure Test Unit. This means that the wall heat transfer correlations will be associated with a specific pebble bed/wall modelling topology.

8.3.4 Space-time neutron kinetics

As the reactor model described in this study is optimised for transient simulation speed, it is appropriate to integrate it with a code that does transient neutronic calculations with the space-time kinetic neutronic model. This would entail a more detailed fuel sphere model in order to separate the uranium dioxide temperature from the fuel coating and graphite temperatures.

8.3.5 Adjusting reference temperature for recriticality calculations

A well-defined relation was found between fuel reference temperature and the time of recriticality. As fuel reference temperature is determined by the convection heat transfer scheme, the error introduced by first order convection discretisation could possibly be compensated for by adjusting the fuel reference temperature.

The limits of applying this method can be researched, as it is expected to be valid only for loss-of-flow cases. For full power transient simulations, this method is not expected to be valid, as a full-power neutronic steady-state is only reached when the average fuel temperature equals the reference temperature. An artificially modified reference temperature will cause a large error on the stabilisation power level.

References

Aumiller, D.L., Tomlinson, E.T., Bauer, R.C. (2001) A coupled RELAP5-3D/CFD Methodology with a Proof-of-Principle Calculation. Nuclear Engineering and Design 205, p83-90

Ball, S. (2004). CRP-5 Benchmark:HTR-10 ATWS Safety Tests. Fifth Research Coordination Meeting of CRP-5 on "Evaluation of High Temperature Gas-Cooled Reactors". Dec. 6-10, 2004, Vienna.

Banaschek, J. (1993) Berechnungsmethoden und Analysen zum dynamischen Verhalten von Kraftwerksanlagen mit Hochtemperaturreaktor, Dissertation, RWTH Aachen, Jül-1841

Bauer, R. (1977) Effektive radiale Wärmeleitfähigkeit gasdurchströmter Schüttungen mit Partikeln unterschiedlicher Form und Größ enverteilung. VDI-H. 582, Düsseldorf, VDI-Verlag.

Blanchard, S.B. Fabrycky, W.J. (1998). Systems engineering and analysis, third edition. Prentice Hall. p176.

Botha, F. (2003) An Explicit Method for the Analysis of Transient Compressible Flow in Pipe Networks. Masters Dissertation. Potchefstroom University for Christian Higher Education (Renamed to Northwest University in 2003).

Brockmann, H. (1994) Analytic angle factors for the radiant interchange among the surface elements of two concentric cylinders. *Int. J. Heat Mass Transfer.* Vol.37, No. 7. pp1095-1100.

Cleveland, J.C., Greene, R.S. (1986) Application of the THERMIX-KONVEK Code to Accident Analyses of Modular Pebble Bed High Temperature Reactors, Oak Ridge National Laboratory, ORNL/TM-9905, August 1986

Cullimore, B.A. (2001) Beyond Point Design Evaluation. Keynote paper. ASME Fluids Engineering Division Summer 2001 Meeting.http://www.crtech.com/docs/papers/NewOsummary.pdf

Du Toit, C.G. (2005) Flownex Theory Manual –Advanced Pebble Bed Reactor (Generation 3). MTech Industrial Document number: FNXTH-0038. Mtech Industrial, (Pty) Ltd. http://www.mtechindustrial.com/.

Du Toit, C.G., Greyvenstein, G.P., Rousseau, P.G. (2003) A Comprehensive reactor model for the integrated network simulation of the PBMR power plant. Proceedings of the 2003 International Congress on Advances in Nuclear Power Plants (ICAPP'03). Cordoba, Spain, 4-7 May 2003

Du Toit. C.G. (2004) Numerical Analysis of the Porosity of Annular Packed Beds. Technical Report PBMR-0077.2. Mtech Industrial, Potchefstoom.

Du Toit. C.G. (2005) Flownex Theory Manual – Advanced Pebble Bed Reactor (Generation 3). Technical Report PBMR-0038. Mtech Industrial, Potchefstoom.

Ferziger, J.H., Peric, M. (1999) Computational Methods for Fluid Dynamics. Second edition. Springer Verlag Berlin Heidelberg New York.

GA (1999) THE GAS TURBINE - MODULAR HELIUM REACTOR. General Atomics. Website at http://gt-mhr.ga.com/R_GTMHR_Project_all.html . Accessed July 2005.

Gerwin, H., Scherer, W. (2001) The Two-Dimensional Reactor Dynamics Programme TINTE. Part 3: Programme Architecture and User`s Manual. Institut für Sicherheitsforschung und Reaktortechnik, Forschunszentrum Jülich.

Greyvenstein, G.P. (2006) The application of systems CFD to the design and optimisation of high-temperature gas-cooled nuclear power plants. ASME POWER 2006 Conference. May 2-4, 2006, Atlanta, Georgia

Greyvenstein, G.P., Laurie, D.P. (1994) A Segregated CFD Approach to Pipe Network Analysis. International Journal for Numerical Methods in Engineering. Vol.37, pp3685-3705

Greyvenstein, G.P., Van Antwerpen, H.J., Rousseau P.G. (2004) The system CFD approach applied to a pebble bed reactor core. International Journal of Nuclear Energy Science and Technology. Inaugural Issue, 2004.

Howell, J. R. (2001). A Catalog of Radiation Heat Transfer Configuration Factors, 2nd edition. Department Of Mechanical Engineering, The University Of Texas At Austin. Available online at http://www.me.utexas.edu/~howell/

Hunt, M.L., Tien, C.L. (1990). Non-Darcian flow, heat and mass transfer in catalytic packed-bed reactors. *Chemical Engineering Science*, 45, pp55-63.

IAEA (2000) IAEA-TECDOC-1163. Heat Transport and Afterheat Removal for Gas Cooled Reactors Under Accident Conditions. The Sana-1 Experiments for Self-Acting Removal of the Afterheat from a Pebble Bed. pp269-332

IAEA (2001) Hydrogen as an energy carrier and its production by nuclear power, IAEA-TECDOC-1085, 2001. Available online at: http://www.iaea.org/inis/aws/htgr/abstracts/abst_30027279.html. Accessed July 2005.

IAEA (2002) IAEA-TECDOC--1198: Current status and future development of modular high temperature gas cooled reactor technology, Chapter 2: HTGR Development and General Features. International Atomic Energy Agency, Vienna (Austria). http://www.iaea.org/inis/aws/htgr/fulltext/gcr_review_02.pdf

IAEA (2006) IAEA-TECDOC-TBD: CRP-5 on HTGR Performance Evaluation (10/1997-12/2007). Draft document as on 1/3/2006. More information at http://www.iaea.org/OurWork/ST/NE/NENP/NPTDS/Projects/HTGR/crps.html

INEEL (Idaho National Energy and Environmental Laboratory) (2004) RELAP5-3D, a description. Available at http://www.inel.gov/relap5/relap5-3.htm

Incropera, F.P., DeWitt, D.P. (1996) Fundamentals of Heat and Mass Transfer. 4thed. John Wiley & Sons.

Ion, S., Nicholls, D., Matzie, R., Matzner, D. (2003) Pebble Bed Modular Reactor: The First Generation IV Reactor To Be Constructed. World Nuclear Association Annual Symposium 3-5 September 2003, London.

Kikstra, J.F. (2001) Modelling, Design and Control of a Cogenerating Nuclear Gas Turbine Plant. Nuclear Research and Consultancy Group (NRG), Petten, The Netherlands. Ph.D. thesis Delft University of Technology.

Koster, A., Matzner, H.D., D.R. Nichols, D.R. (2003) PBMR design for the future. Nuclear Engineering and Design 2800 (2003) pp1–15.

KTA (Kern Technisches Ausschuss) (1983) KTA 3102.2. Reactor Core Design of High-Temperature Gas-Cooled Reactors. Part 2: Heat Transfer in Spherical Fuel Elements. (June 1983)

KTA (Kern Technishes Ausschuss) (1981) KTA 3102.3. Reactor Core Design of High-Temperature Gas-Cooled Reactors. Part 3: Loss of Pressure through Friction in Pebble Bed Cores. (March 1981).

Kuerten, U., Van Sint Annaland, M., Kuipers, J.A.M. (2004) Oxygen Distribution in Packed Bed Membrane Reactors For Partial Oxidation Systems and its Effect On Product Selectivity. International Journal of Chemical Reactor Engineering. Volume 2. Article A24

Kugeler, K., Alkan, Z., Pöppe, N. (2003) High Temperature Reactor Technology. Course Notes Potchefstroomse Universiteit, Faculty of Engineering, 7-11 April 2003.

Lamarsh, J.R., Barratta, A.J. (2001) Introduction to Nuclear Engineering. Third Edition. Prentice Hall.

Lovelock, J. (2004) Nuclear power is the only green solution. The Independent, 24 May 2004. Available online at: http://www.climateark.org/articles/reader.asp?linkid=31936 . Accessed: July 2005.

Marcus, G.H. (2003) Nuclear's Next Generation. Available online at: http://www.memagazine.org/supparch/mepower03/nextgen/nextgen.html . Accessed July 2005.

Martin, H., Nilles, M. (1993) Radiale Wärmeleitung in durchströmten Schüttungsrohren, *Chem. –Ing. –Techn.* 65, pp1468-1477

Matzner, D. (2004) PBMR Project Status And The Way Ahead. 2nd International Topical Meeting on High Temperature Reactor Technology (HTR2004). Beijing, China, September 22-24, 2004. Available online at http://www.iaea.org/inis/aws/htgr/fulltext/htr2004_a04.pdf. Accessed July 2005.

Methnani, M. (2005) Highlights Of Recent IAEA Research Activities On High- Temperature Gas-Cooled Reactors. Proceedings of ICAPP '05, Seoul, KOREA, May 15-19, 2005. Paper 5677.

Moore, P. (2005). Statement to the Congressional Subcommittee on Energy & Resources. 28 April 2005. Available online at: http://www.nei.org/documents/Testimony_Moore_04-28-05.pdf . Accessed July 2005.

Nakagawa, S., Takamatsu, K., Kunitomi, K. (2004) JAERI Calculation of HTR-10 Benchmark Problem. Presentation to the Fifth Research Coordination Meeting of CRP-5 on "Evaluation of High Temperature Gas-Cooled Reactors". Dec. 6-10, 2004, Vienna.

Niessen, H-F., Stöcker, B. (1997). *Data sets of SANA experiment: 1994-1996*, Document JUEL-3409, Forschungszentrum, Jülich.

Olivier, J.C. (2005) Network Modelling Of Transient Heat Exchanger Performance. Masters Thesis. North-west University.

Patankar, S.V. (1980). Numerical Heat Transfer and Fluid Flow. McGraw-Hill, New York.

Petersen, K. (1983) Zur Sicherheitskonzeption des Hochtemperaturreaktors mit natürlicher Wärmeableitung aus dem Kern im Störfall, Jül-1872, KFA.

Rousseau, P., Van Staden, M. (2006) Introduction to the PBMR Heat Transfer Test Facility. Proceedings HTR2006: 3rd International Topical Meeting on High Temperature Reactor Technology. October 1-4, 2006, Johannesburg, South Africa.

Ritch, J. (2005) The Key to Our Energy Future. The Washington Post, 25 April 2005. Available online at: http://www.world-nuclear.org/John_Ritch_speeches/John_Ritch_wp260405.html. Accessed April 2007.

Schürenkrämer, M. (1984) Theoretische und experimentelle Untersuchungen der Naturkonvektion im Kern des Kugelhaufen-Hochtemperaturreaktors, Kernforschungsanlage Jülich GmbH, Jül-1912, April 1984

Shames, I.H. (1992) Mechanics of Fluids, McGraw-Hill, New York.

Slabber, J. (2004) Pebble Fuel Advantages. 2nd International Topical Meeting on High Temperature Reactor Technology. Beijing, CHINA, September 22-24, 2004.

Stacey, W.M. (2001) Nuclear Reactor Physics. John Wiley & Sons, Inc.

Stempniewicz, M.M. (2002) Steady-state and Accident Analyses of PBMR with the Computer Code SPECTRA. Transactions 1st International Topical Meeting on High Temperature Reactor Technology (HTR2002), Petten, Netherlands.

Stempniewicz, M.M. (2006) Personal communication on 3 October 2006, Johannesburg, South Africa.

Stoker, C.C., Reitsma, F. (2004) PBMR Fuel Sphere Source Terms. 2nd International Topical Meeting on High Temperature Reactor Technology (HTR2004). Beijing, China, September 22-24, 2004. Available online at http://www.iaea.org/inis/aws/htgr/fulltext/htr2004_c15.pdf. Accessed July 2005.

Swift, W.J. (2006) *Flownex* Version 7 User Manual, M-Tech Industrial, Potchefstroom, South Africa. http://www.flownex.com/, http://www.mtechindustrial.com/

Tsotsas, E. (2002) VDI Wärmeatlas. 9.Auflage 2002.

Van Antwerpen, H.J. (2006) Flownex Validation Manual: Advanced Pebble Bed Reactor Model (Generation 3) – HTR-10, Document number FNXVV-0038.9. M-Tech Industrial, Potchefstroom, December 2006.

Van Antwerpen, H.J., Greyvenstein, G.P. (2006) Calculation Aspects Of Detailed Radiation Heat Transfer. Proceedings HTR2006: 3rd International Topical Meeting on High Temperature Reactor Technology. October 1-4, 2006, Johannesburg, South Africa

Van der Merwe, J. (2005) Flownex Validation Manual: Advanced Pebble Bed Reactor Model (Generation 3) –SANA Steady-State. Document number FNXVV-0038.7. Mtech Industrial, Potchefstroom, South Africa.

Van der Merwe, J., Van Antwerpen, H.J. (2006) Flownex Validation Manual: Advanced Pebble Bed Reactor Model (Generation 3) – HTR-10. Document FNXVV-0038.9. M-Tech Industrial, Potchefstroom, South Africa

Van der Merwe, J., Van Antwerpen, H.J. (2006) Technical Memo to the PBMR Thermal Hydraulic Analysis Group (THAG) on transient response differences between the Generation Two Reactor model and the Advanced Pebble Bed Reactor Model.

Van der Merwe, J., Van Antwerpen, H.J., Mulder, E.J. (2006) Heat Transfer Correlation Limitations At The Pebble Bed-Reflector Interface. Proceedings HTR2006: 3rd International Topical Meeting on High Temperature Reactor Technology. October 1-4, 2006, Johannesburg, South Africa.

Van Heerden, G. (2006) Personal communication with author. Mr. Van Heerden is a chief analyst at PBMR (Pty Ltd.) and also represented PBMR at the IAEA CRP5 benchmarking effort.

Van Ravenswaay, J.P. (1998) An Implicit Method for Transient Pipe Network Analysis. Masters Dissertation. Potchefstroom University for Christian Higher Education (Renamed to Northwest University in 2003). 1998.

Van Rensburg, P.A.J. (2003) Flownet Uncertainty Analysis for a DLOFC. PBMR document: MR000-018726-3180.

Van Staden, M., Van Rensburg, C.J., Viljoen, C. (2002) CFD Simulation Of Helium Gas Cooled Pebble Bed Reactor. Proceedings of HEFAT2002: 1st International Conference on Heat Transfer, Fluid Mechanics, and Thermodynamics, 8-10 April 2002, Kruger Park, South Africa

Verfondern, K. (1983) Numerische Untersuchung der 3-dimensionalen stationären Temperatur- und Strömunsverteilung im Core eines Kugelhaufen-Hochtemperaturreaktors, Jül-1826, Institut für Reaktorentwicklung, Kernforschungsanlage Jülich GmbH.

Verkerk, E.C. (2000) Dynamics of the pebble-bed nuclear reactor in the direct brayton cycle. Nuclear Research Consultancy Group (NRG), Petten, The Netherlands. Ph.D. thesis Delft University of Technology.

Versteeg, H.K., Malalasekera, W. (1995) An Introduction to Computational Fluid Dynamics, The Finite Volume Method. Longman.

Vortmeyer, D., Le Mong, S. (1976) Ein Verfahren zur Messung von Wärmeübergangszahlen in durchströmten Schüttungen bei Reynolds-Zahlen Re < 200. Verfahrenstechnik 10 Nr.10, 650-

654. As quoted in Achenbach, E. (Date unknown) Helium Cooled Systems. HTR-Pebble Designs. Chapter 5 Part 2.

Appendix A:

Heat generation distribution

A separate radial power distribution is specified for each of the zones, while they all use the same axial power distribution as shown in Figure A.8.1.

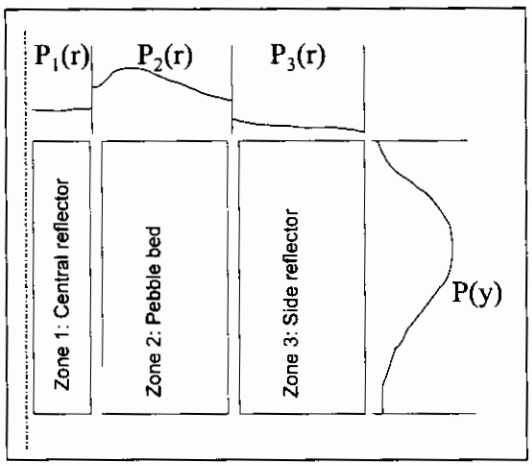


Figure A.8.1. Power distribution zones for the reactor model presented in this document.

Each of the zones in Figure A.8.1 is subdivided into control volumes (CVs) to which heat generation is assigned according to power factors calculated from a non-dimensional power distribution.

The non-dimensional power distribution is typically obtained from detailed neutronic analysis codes in the form a polynomial. Suppose the fourth-order polynomial in Eq.(A.1) describes the power distribution:

$$p_s(r) = a_0 + a_1 r + a_2 r^2 + a_3 r^3 + a_4 r^4 \tag{A.1}$$

With this continuous equation, the heat distribution factors are calculated for discrete control volumes with the integral formula in Eq.(A.2):

$$PF_i = \frac{\int_{r_{i-1}}^{r_i} p_s(r)\,dr}{\int_{r_0}^{R} p_s(r)\,dr} \tag{A.2}$$

with PF_i being the power fraction for CV number i, bounded by r_{i-1} and r_i, as illustrated in Figure A.8.2. R and r_0 bounds the domain that is divided into rows of power-generating CVs.

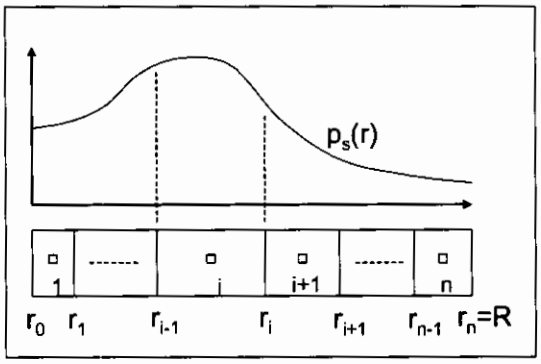


Figure A.8.2. A radial power distribution with indication of the control volume locations.

With $p_s(r)$ given by Eq.(A.1), PF_i is calculated as follows in Eq.(A.3):

$$PF_i = \frac{a_0(r_i - r_{i-1}) + \frac{a_1}{2}(r_i^2 - r_{i-1}^2) + \frac{a_2}{3}(r_i^3 - r_{i-1}^3) + \frac{a_3}{4}(r_i^4 - r_{i-1}^4) + \frac{a_4}{5}(r_i^5 - r_{i-1}^5)}{a_0(R - r_0) + \frac{a_1}{2}(R^2 - r_0^2) + \frac{a_2}{3}(R^3 - r_0^3) + \frac{a_3}{4}(R^4 - r_0^4) + \frac{a_4}{5}(R^5 - r_0^5)} \tag{A.3}$$

The normalising calculation in Eq.(A.2) is used so that the power distribution process conserves energy. Mathematically, this is expressed by Eq.(A.4), which states that the sum of power factors in a certain domain always equal unity, i.e:

$$\sum_{i=1}^{n} PF_i = 1 \tag{A.4}$$

This approach has several advantages, such as that the sum of node values would be unity by definition of the distribution formula, irrespective of the absolute value of the coefficients. Another advantage is that irregular cell sizes can be used.

The power generation P_{ij} in the CV at grid location i,j will then be given by Eq.(A.5):

$$P_{ij} = P_{tot} \times PFz \times PF_i \times PF_j \tag{A.5}$$

with PFz being the zone power fraction and PF_i the radial and PF_j the axial power fractions, calculated with Eq.(A.3) and the appropriate distribution polynomials. The zone power fraction distributes the power generation between the pebble bed and the two reflector zones.

At each pebble bed CV in the two-dimensional reactor discretisation, there are fuel sphere internal nodes, among which P_{ij} is distributed according to spherical volume fractions, determined in the sphere discretisation.

Appendix B:
The system CFD approach applied to a pebble bed reactor core

G.P. Greyvenstein, H.J. van Antwerpen, P.G. Rousseau
School of Mechanical and Materials Engineering, Potchefstroom University for CHE, Private bag X6001, Potchefstroom 2520, South Africa. Tel: +27 18 299 0326, Fax: +27 18 299 0318, Email: mailto:mgigpg@puk.ac.za

Nomenclature

β_{max}	Surface node maximum length fraction
B_i	Biot number
h	transfer coefficient
k	conductivity
L	characteristic length
R_i	pebble bed inner radius
R_o	pebble bed outer radius
T	temperature

Abstract

The system CFD code Flownex is used to simulate the transient behaviour of complete thermal-fluid systems such as the Pebble Bed Modular Reactor. In the context of this system simulation, the complexities in modelling the reactor heat transfer is discussed, as well as appropriate methods of dealing with it. The versatility of the system CFD approach is illustrated with three possible topologies for the pebble bed reactor core model. It is shown that the current pebble bed network topology compares very well to other possible network topologies, while having the advantage of predicting the maximum fuel temperature.

Keywords

Thermal-fluid, system CFD, PBMR, Flownex, thermal conduction network, topology, gas cooled reactor, core modelling.

Introduction

The Pebble Bed Modular Reactor (PBMR) is a high temperature gas cooled nuclear power plant currently being developed by the South African utility ESKOM. It features a direct, three-shaft Brayton cycle with helium as working fluid. The cycle-layout is shown schematically in Figure 1. The complete power cycle, including the

reactor is modelled with the dynamic system Computational Fluid Dynamics (CFD) code Flownex to do integrated design and optimisation [1]. The system CFD representation of the cycle is shown in Figure 2.

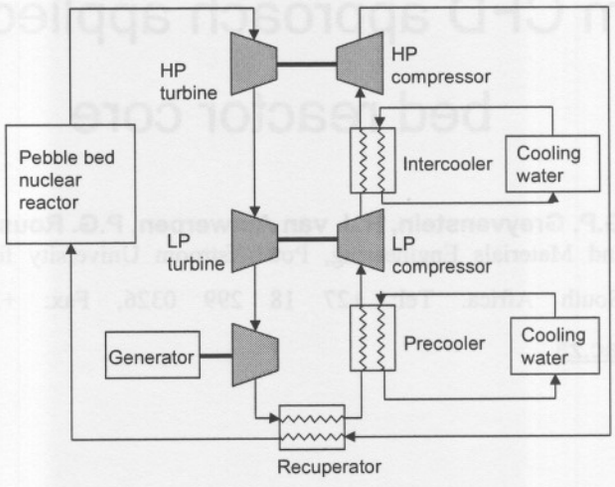


Figure 1: Schematic layout of the three-shaft recuperated Brayton cycle as used in the PBMR system.

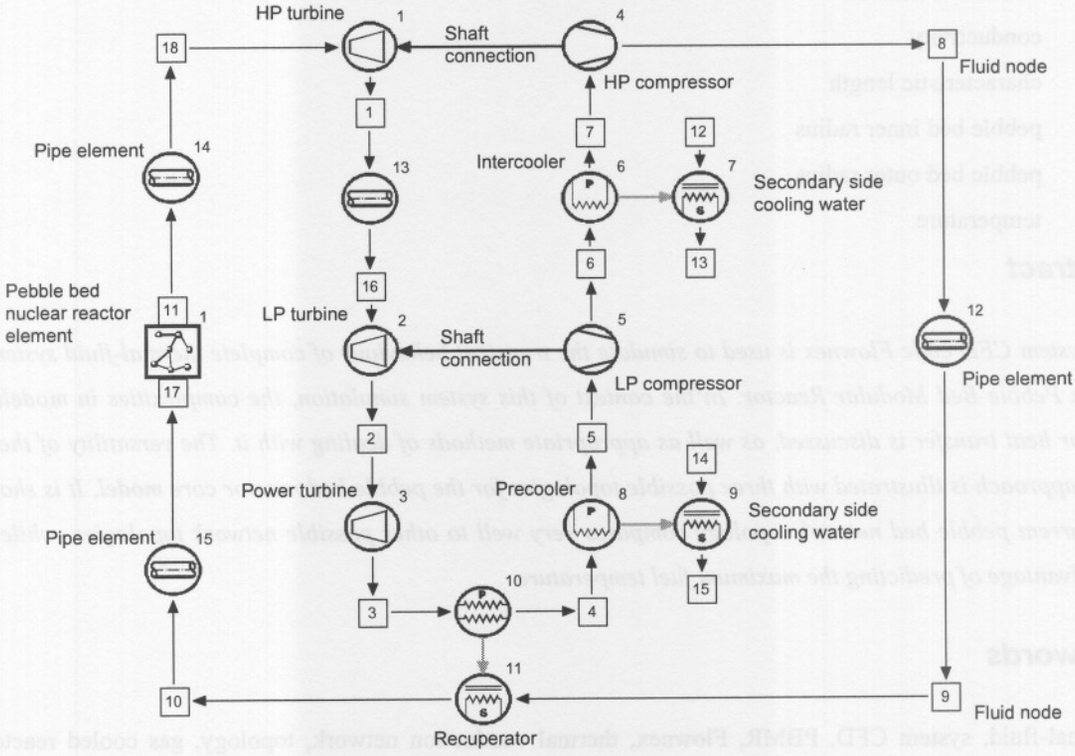


Figure 2: The system CFD representation of the PBMR power cycle in Flownex.

In the system CFD approach used in Flownex, components are modelled as one-dimensional flow and heat transfer elements for high calculation speed, while retaining adequate detail to determine their respective effects on the system. "Adequate detail" is a particularly challenging issue in the case of the nuclear reactor thermal-fluid (TF) model, as the reactor operation is very complex in itself and is profoundly affected by changes in the rest of the

system. Also considering that the reactor is the energy source, it is clearly the most important component in the system.

From a safety point of view, the reactor is also the most critical part of the PBMR system, as it contains the fuel spheres that enclose the nuclear fission products. To prevent fission product release by diffusion, the maximum fuel temperature must under no circumstances rise above 1300°C. Therefore, a thermal-fluid (TF) system simulation model of the reactor must be able to calculate the maximum fuel temperature for all operating conditions. The importance of an accurate reactor TF model is underlined by the fact that fission heat generation is highly dependent on the fuel temperature and transient history.

Developing an accurate heat transfer model of the reactor is not a simple task because of the complexity of the phenomena involved. In the pebble bed, heat is generated in kernels inside the fuel spheres. The heat is then conducted to the sphere surface where it is transferred to the helium by means of convection. In the bed itself, heat is transferred by means of conduction and interstitial radiation in the radial and axial directions.

Several approaches have been used to model such a pebble bed reactor. Verfondern [2] assumed a homogeneous bed, thereby using only three gas conservation equations. Becker and Laurien [3] used a heterogeneous model with three gas conservation equations and one energy conservation equation for the solids. Du Toit *et.al.* [1] implemented a heterogeneous model into Flownex with three gas conservation equations and two energy conservation equations for the solids: one equation accounting for conduction and radiation heat exchange between regions in the pebble bed and another for calculating the temperature distribution inside the fuel spheres. This paper investigates the validity of the approach taken by Du Toit *et. al.* [1] in the context of the system CFD methodology.

Qualitative discussion of different heat transfer mechanisms

Before contemplating reactor modelling approaches, the physics of pebble bed heat transfer is reviewed. As shown in Figure 3, the PBMR fuel consists of coated fissile material kernels, embedded in the graphite matrix of a fuel sphere.

The annular reactor core volume is filled with several thousand such spheres. In the fuel kernels, nuclear fission produces heat that is first conducted through the coatings to the graphite matrix, then to the surface of the fuel sphere. At the fuel sphere surface, gas is heated by convection, while radiation exchanges heat with adjacent spheres. If a temperature gradient exists across the pebble bed, heat transport takes place by means of conduction through the fuel spheres in the bed and with additional interstitial radiation transfer.

It is essential to model these phenomena during system transients as the reactor thermal mass is linked by, and distributed between these different phenomena.

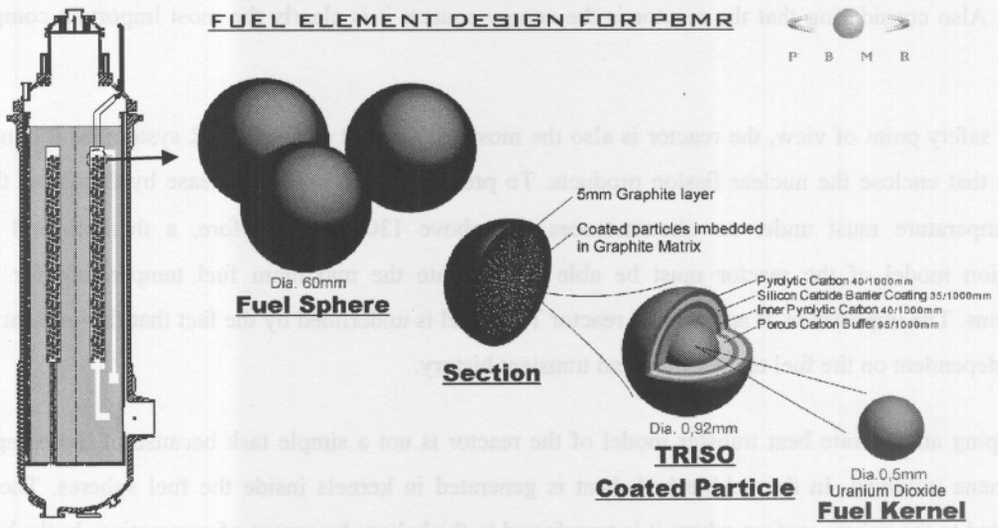


Figure 3: Composition of the PBMR fuel spheres.

Classical CFD

One approach of modelling the thermal behaviour of the pebble bed reactor is to use a three-dimensional CFD code. Indeed, CFD calculations are very powerful and most CFD codes are capable of solving non-linear turbulent flow equations in complex three-dimensional geometries. However, solution of non-linear equations in complex geometries requires unstructured grids, sophisticated discretisation schemes and intricate data management, leading to very long computational times.

The forte of a classical CFD approach is component analysis where the focus is on detail in the spatial domain. The work by Van Staden *et. al.* [4] and Becker & Laurien [3] are examples of typical CFD application. Becker and Laurien investigated the temperature effect of misplaced fuel spheres in a pebble bed reactor with a dynamic centre column. Such a three-dimensional model of the reactor is necessary to investigate three-dimensional effects. However, it is not feasible in practice to use a CFD model for the numerous system-level "what-if" studies done during the design process. Becker and Laurien [3] reported, "a main memory of 1GB and about 20h computation time (cpu time) on one processor was necessary". In view of the fact that the PBMR design has changed to a fixed center column [5], misplacement of fuel elements is no longer possible, thereby also diminishing the need for three-dimensional simulations.

An additional consideration is that for a pebble bed, even CFD models assume a porous medium. This causes the flow equations to simplify considerably due to the dominance of the bed resistance. Given this simplification and the fact that the cost of the CFD computational overhead remains, the use of classical CFD offers very little benefit in this case.

Even if a very simplified CFD model is coupled to a system simulation code, information has to be exchanged either with an explicit or semi-implicit interface. This implies considerable programming effort to maintain conservation between the two codes. An explicit interface furthermore severely limits the timestep length in transient simulations[6].

In contrast to the classical CFD approach, the system CFD approach used in Flownex overcomes many of these hurdles. The system CFD approach is based on the classical CFD staggered grid discretisation. This discretisation has the advantage of excellent coupling between pressure and velocity, as scalar values (mass, pressure, temperature) are calculated at control volume centres (nodes), while vector quantities (e.g. velocity) are calculated at control volume faces (elements) [7].

In the system CFD approach, nodes representing fluid volumes or thermal masses are connected with one-dimensional heat and fluid flow elements to represent a thermal system. The type of element determines the pressure drop, mass and heat flow characteristics used in the conservation equations. Examples of elements are pipes, pumps, valves, heat exchangers, orifices, porous media flow resistances and solid conduction elements. The fundamental nature of the modelling approach enables simulation of phenomena such as pressure waves in gas flows, water hammer as well as convection, conduction and radiation heat transfer [8].

Networks can be arbitrarily structured to represent complex real-life situations. As shown in Figure 2, single components can also be modelled as sub-networks of nodes and elements, thereby providing freedom to match the level of detail of all components in a simulation.

The reactor model is a typical example of a component modelled as a sub-network, which is essentially the equivalent of a two-dimensional CFD model, but without the overhead associated with full CFD codes. Figure 4 shows how the reactor is modelled as a sub-network. This method has the advantage of a fully implicit coupling between the reactor and the rest of the system, so that the assembled network is solved as one system with the implicit pressure correction method [9].

Due to the implicit solution algorithm and implicit coupling between sub-networks, there is no timestep length constraint to ensure stability for transient simulations.

By combining different elements in different configurations, numerous topologies are possible to mimic the complex reactor behaviour. In the next section the validity of the current network topology is evaluated by comparison with two other possible topologies.

Current network model of the pebble bed

The current pebble bed network model is shown in Figure 5.

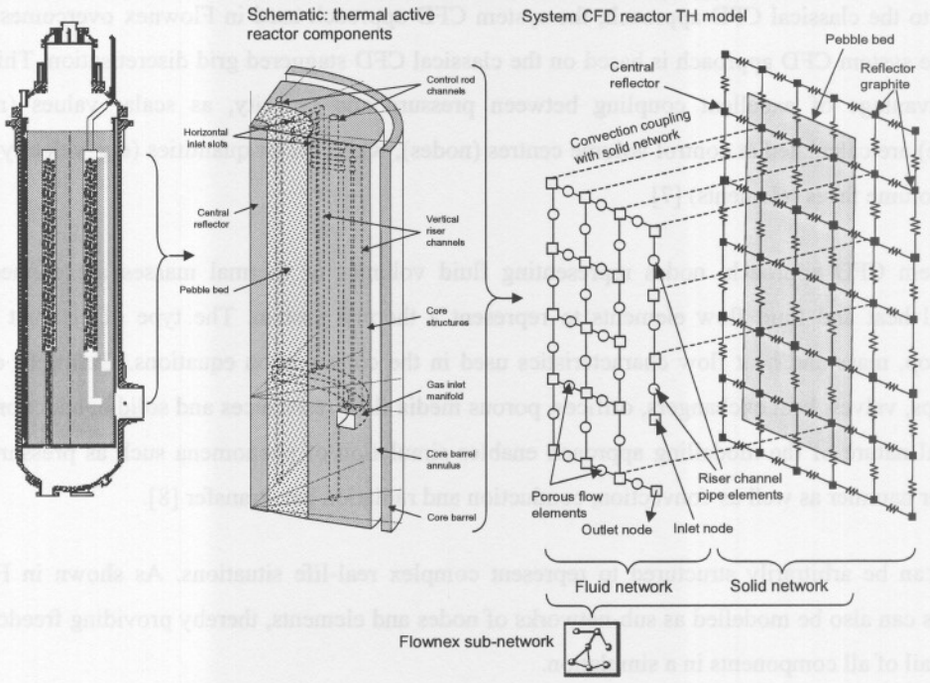


Figure 4: Diagram showing the network modelling approach for the reactor.

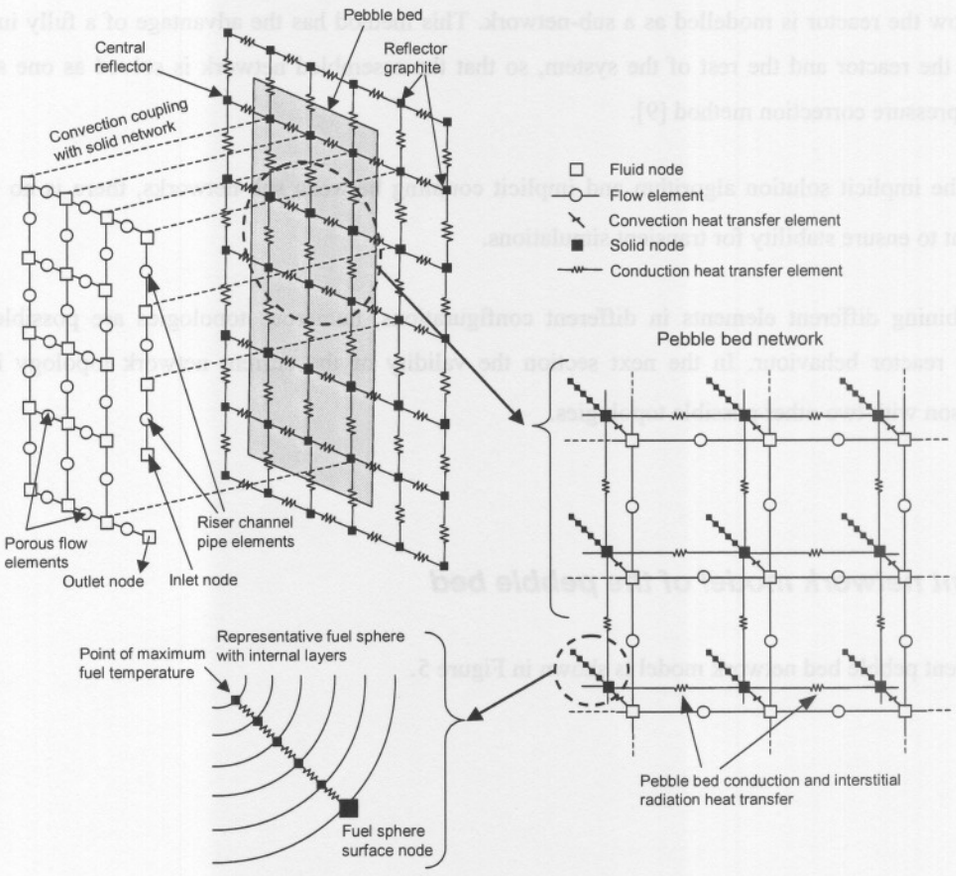


Figure 5: Current network model of the pebble bed core. It is a heterogeneous sphere model.

The current pebble bed reactor core model is the heterogeneous model described by Du Toit *et. al.* [1]. Axial symmetry is assumed, thereby discretising the pebble bed core in two-dimensional control volumes in cylindrical coordinates. The total volume of gas in a control volume is represented by a gas node, which is connected to other gas nodes with porous flow resistance elements. The pebble surface temperatures are represented by one representative solid node per control volume, from which convection to the gas occurs, as well as conduction and radiation within the pebble bed. Connected to each surface temperature node is a string of elements and nodes representing layers in a fuel sphere. This allows the calculation of the maximum fuel temperature within the sphere. The thermal mass of the solids is associated with the nodes in the representative fuel sphere.

A disadvantage of this topology is that the solid thermal mass within the sphere does not form part of the radial and axial heat conduction paths within the bed, so that this network could have an inaccurate transient response associated with a sudden change in temperature gradient across the bed. However, if the conduction resistance inside the spheres is much smaller than the convection resistance between the sphere surface and the fluid, this approach (called the lumped capacity approach) will yield accurate results.

For transient conduction/convection systems, the Biot number is used to test the validity of the lumped capacity approach. The Biot number is an indication of the ratio of surface transfer resistance to internal conduction resistance, calculated as follows:

$$B_i = \frac{hL}{k} \tag{1}$$

with h being the surface convection coefficient, L the characteristic length of the solid and k its thermal conductivity. For the PBMR at full mass flow conditions, B_i is typically in the order of 0,3. Only if B_i is smaller than 0,1 can the sphere be treated as a lumped capacitance [10], so that it has to be subdivided. Aumiller [11] addressed the question as to the number of necessary subdivisions for a plane wall. His research produced the following formula:

$$\frac{1}{\beta_{\max}} = 0.338B_i + 5.2 \tag{2}$$

where $\beta_{\max}$ is the maximum length of the surface node, expressed as a fraction of the characteristic length L as described in Figure 6.

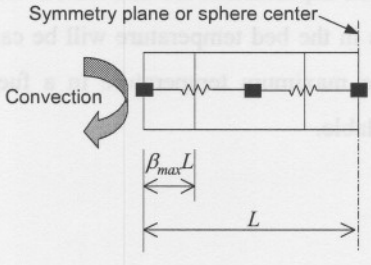


Figure 6: Illustrating the physical meaning of L and β_{max}.

Discretisations that adhere to this guideline can be expected to calculate the cumulative heat transfer within 20% of the analytical value for the full duration of the transient event.

Thus, for pebble bed spheres with a Biot number of 0,3, the surface layer should have a maximum length of $0{,}18L$. In the current discretisation, the fuel sphere is divided radially in five elements, so that the sphere surface node represents only $0{,}1L$ of the conduction length and the requirement is therefore adhered to.

To investigate the validity of the current approach for transient events, some other formulations will be investigated in the next sections.

First alternative

This first alternative is a heterogeneous model, in which the fuel spheres are modelled by a homogeneous porous solid, which is coupled to a coarser gas network by convection heat transfer resistances, as shown in Figure 7.

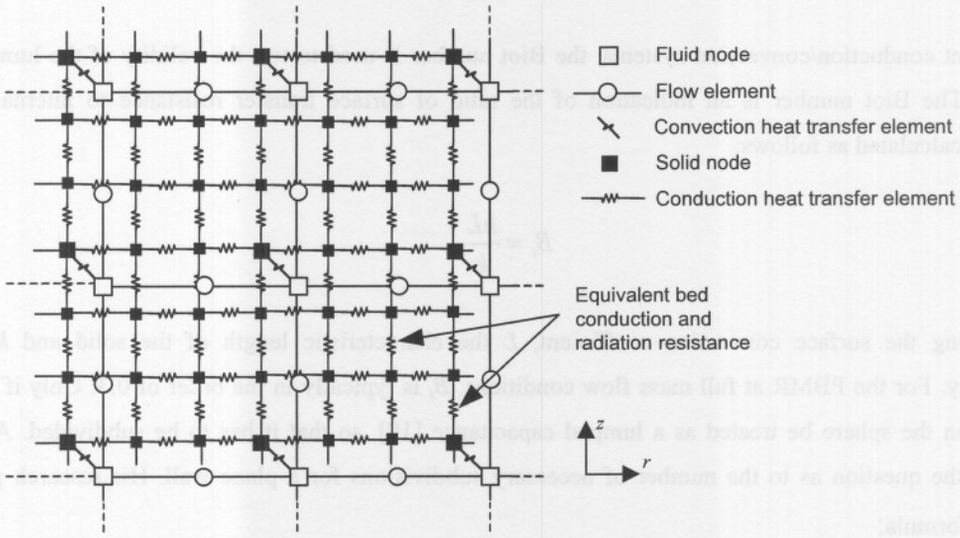


Figure 7: Network model of the core with a homogeneous solid representing the packed bed solids.

The conduction resistances in this topology represent the combined effect of conduction through the spheres, sphere contact resistances and interstitial radiation heat transfer. Because of the homogeneous bed assumption, no characteristic conduction length is applicable.

An advantage of this approach is that the capacitances are distributed within the radial and axial heat transfer paths so that transient response to gradients in the bed temperature will be calculated more accurately. A disadvantage though, is that information about the maximum temperature in a fuel sphere and the temperature difference between center and surface is not available.

Second alternative

This second alternative models the fuel spheres as solid annular rings, coupled to the flow network at the gaps as shown in Figure 8. In this topology, more effort is made with the radial bed conduction path than with the axial

conduction path, as the radial heat flow path is of prime importance for the passive safety of the PBMR. This is due to the fact that radial conduction is the principal means of decay heat removal during loss-of-cooling incidents.

The axial conduction resistances represent combined heat transfer mechanisms in the bed, while the radial conduction path is divided into solid resistances for the layers and resistances across the gaps representing interstitial radiation. The solid layer thickness is equal to the sphere diameter to have the same characteristic length.

This topology has the advantage that the thermal capacitances are distributed within the radial conduction path. Also, some indication is available of the temperature difference in the solids.

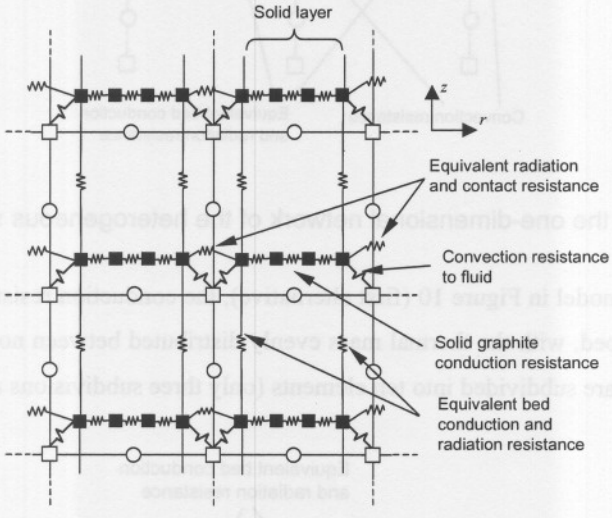


Figure 8: Heterogeneous layer representation of a packed bed.

Assumptions and input parameters

One-dimensional networks will be used to test the transient response, as one-dimensional networks are simple to set up while still having the desired characteristics. The annular pebble bed is thus approximated as a one-dimensional radial system, as the principal temperature gradients occur radially. The annulus is divided into fourteen control volumes, so that each control volume has a similar characteristic length, approximately equal to the diameter of a fuel sphere.

To isolate the effect of network topology, constant thermal conductivity is used throughout. The total thermal capacitance of each network is also the same, although it is differently distributed in each network. Approximating a spherical geometry with Cartesian elements resulted in a maximum difference of 0.94% in overall thermal capacitance between any two networks.

Common to all three topologies is the gas network and its convection coupling to the solid. The convection transfer coefficient is calculated with the correlation presented by Kugeler and Schulten [12]. The correlation by Zehner and Schlünder [13] is employed to determine equivalent bed radiation and conduction resistance.

For the heterogeneous solid sphere model shown in Figure 9 (current model), the resistances between surface nodes represent the combined effect of conduction through spheres, contact resistances and interstitial radiation in the bed. The bed resistances are not subdivided, as no mass is associated with them. Instead, the mass and transfer areas of all spheres in a control volume are associated with the six nodes and interconnecting thermal resistances within the representative sphere.

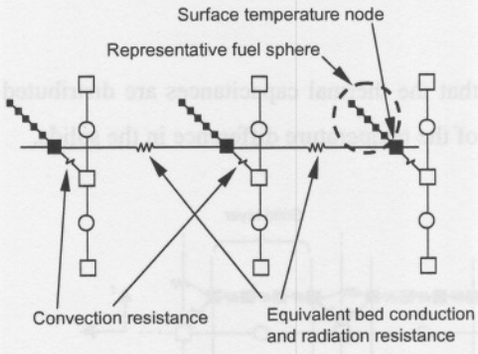


Figure 9: Part of the one-dimensional network of the heterogeneous solid sphere model.

In the homogeneous solid model in Figure 10 (first alternative), the conduction resistances represent the combined heat transfer effects in the bed, with the thermal mass evenly distributed between nodes. The conduction elements between convection points are subdivided into ten elements (only three subdivisions are shown in Figure 10).

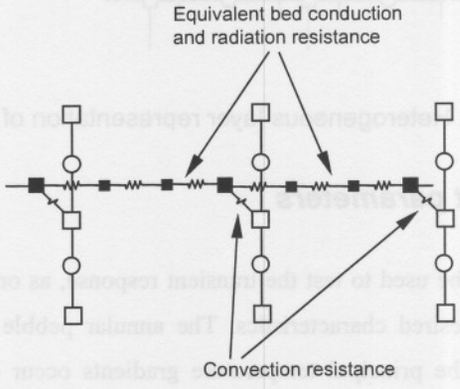


Figure 10: Part of the one-dimensional network with a homogeneous solid.

The heterogeneous layer model (second alternative) has the bed divided into solids and voids. Convection coupling with the gas elements is done at void interfaces, with an equivalent resistance representing interstitial radiation transfer and contact conduction. The solid layers have the same conductivity as solid graphite and are also subdivided in ten elements (only three subdivisions are shown in Figure 11). Thermal resistances are calculated so that the sum of solid and equivalent radiation resistances equal the combined conduction resistance of a packed bed.

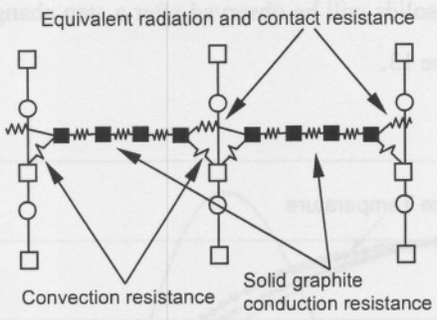


Figure 11: Part of the one-dimensional network of the heterogeneous layer model.

Steady-state results

To assure that the only source of difference in transient response is the network topology, the steady-state conduction of the three topologies have to be the equal. A radial temperature profile under no-flow conditions is shown in Figure 12. Less that 0.03% difference in steady-state radial heat flux was found between the networks.

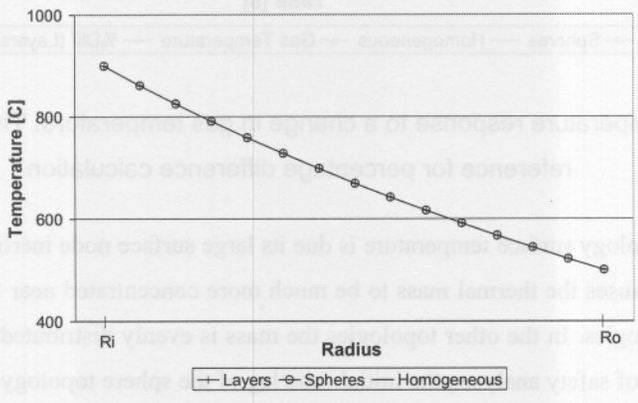


Figure 12: Steady-state radial surface temperature distribution as calculated with all three topologies. No heat generation and a fixed radial temperature difference over the bed.

Transient results

The temperature differences between networks are presented in the following non-dimensional form:

$$\Delta T[\%] = 100 \times \frac{T_1 - T_2}{T_\infty - T_0} \tag{3}$$

T_1-T_2 is the difference between two discretisations at a certain location. T_0 is the steady-state temperature before the event and T_∞ the steady-state temperature after the event. For all cases in this paper, T_∞ - T_0 has a value of 400°C.

There are two conduction paths of which the response is dependant on the thermal mass configuration, the first being conduction from the bed surface into the solids and the second being the core radial conduction path. The

response of the conduction into the solids will be observed after a step change in gas temperature under full mass flow condition, as presented in Figure 13.

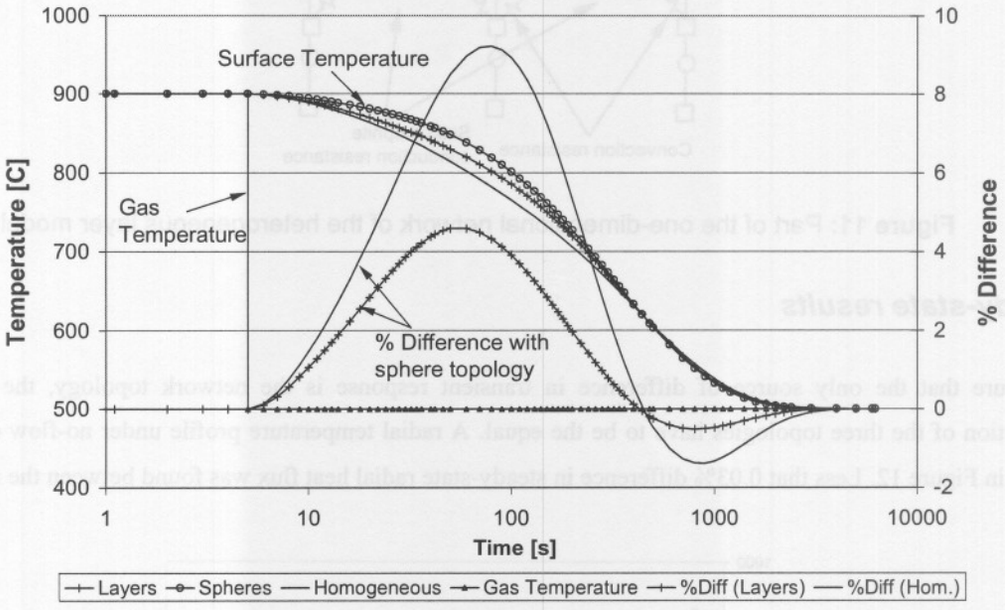


Figure 13: Surface temperature response to a change in gas temperature. The sphere model is used as reference for percentage difference calculation.

The lag of the sphere topology surface temperature is due its large surface node inertia. As illustrated in Figure 17, the spherical geometry causes the thermal mass to be much more concentrated near the convection transfer points than with the other topologies. In the other topologies the mass is evenly distributed in the pebble bed cylindrical geometry. In the context of safety analysis, the initial time lag of the sphere topology is not significant, as repeated real-life transients are much more gradual than the simulated step temperature change.

To test the response of the core radial conduction path, the pebble bed outer temperature is fixed at 500°C, while the pebble bed center temperature is suddenly increased to 900°C under no-flow conditions. Temperatures at several locations in the bed are plotted in Figure 15. Percentage differences between the topologies are shown in Figure 16.

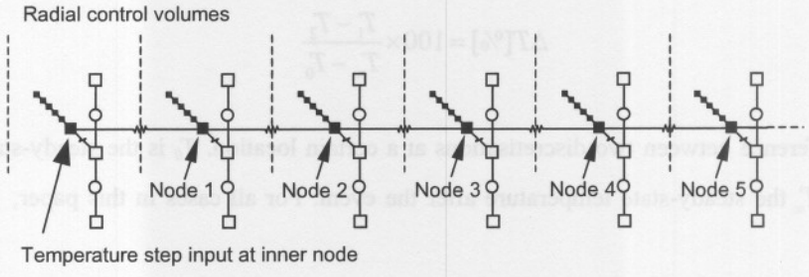


Figure 14: Indication of temperature result locations in Figure 15 (sphere topology shown).

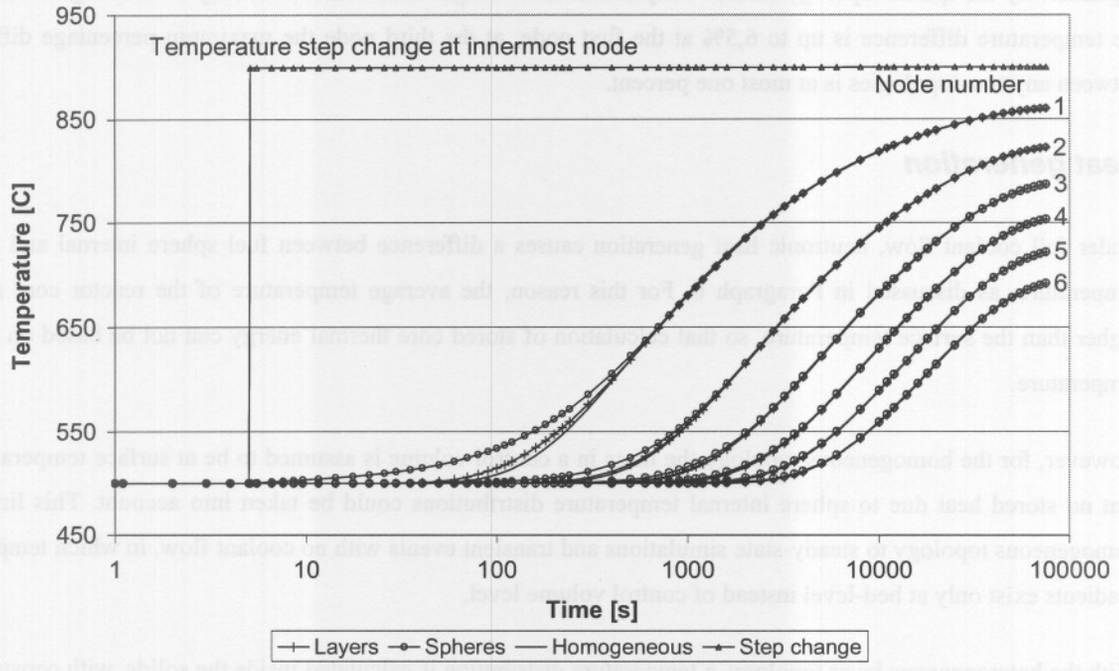


Figure 15: Surface temperature response at different annular layers from the pebble bed center.

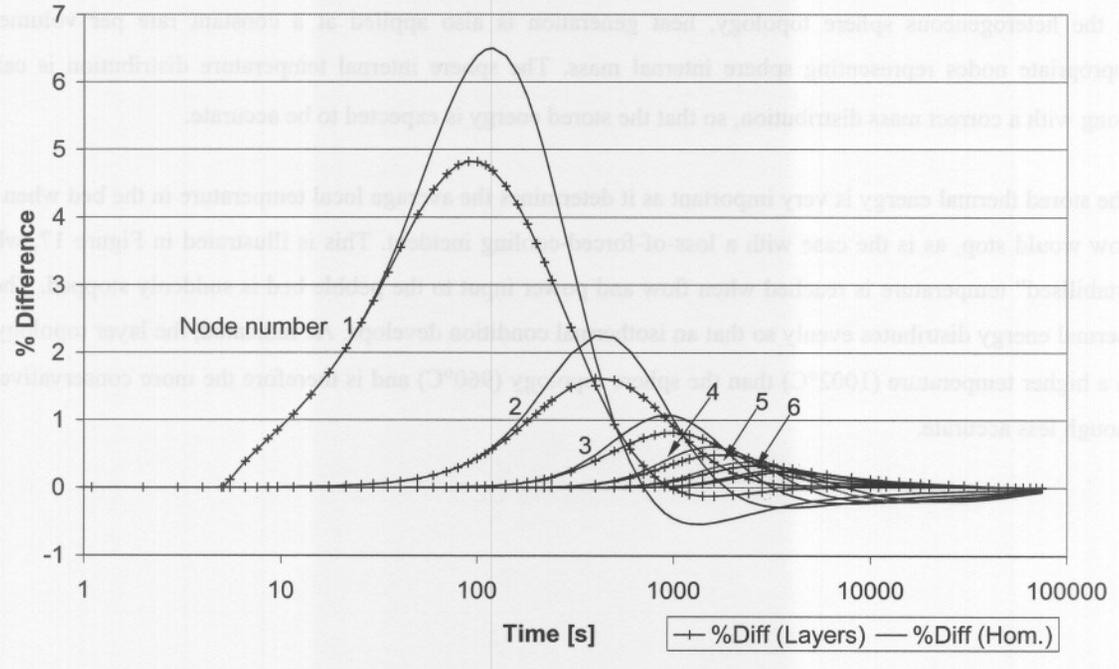


Figure 16: Percentage difference between topologies for the results in Figure 15. The sphere topology is used as reference.

It is seen in Figure 15 that the sphere topology initially has a faster response than the other configurations. This can be expected, as the layer and homogeneous bed topologies have the total thermal mass on the conduction path, while the sphere topology has considerable mass distributed away from the main conduction path. This also

explains why the sphere topology surface temperature takes longer to stabilise, as is only seen in Figure 16. While the temperature difference is up to 6,5% at the first node, at the third node the maximum percentage difference between any two topologies is at most one percent.

Heat generation

Under full coolant flow, neutronic heat generation causes a difference between fuel sphere internal and surface temperature, as discussed in Paragraph 6. For this reason, the average temperature of the reactor core mass is higher than the surface temperature, so that calculation of stored core thermal energy can not be based on surface temperature.

However, for the homogeneous topology the mass in a control volume is assumed to be at surface temperature, so that no stored heat due to sphere internal temperature distributions could be taken into account. This limits the homogeneous topology to steady-state simulations and transient events with no coolant flow, in which temperature gradients exist only at bed-level instead of control volume level.

With the heterogeneous layer topology, a temperature distribution is calculated inside the solids, with constant heat generation per volume applied at all solid nodes. But since the spatial distribution of thermal mass and temperature is not spherical, the stored energy is not expected to be accurate.

In the heterogeneous sphere topology, heat generation is also applied at a constant rate per volume at the appropriate nodes representing sphere internal mass. The sphere internal temperature distribution is calculated along with a correct mass distribution, so that the stored energy is expected to be accurate.

The stored thermal energy is very important as it determines the average local temperature in the bed when coolant flow would stop, as is the case with a loss-of-forced-cooling incident. This is illustrated in Figure 17, where the "stabilised" temperature is reached when flow and power input to the pebble bed is suddenly stopped. The stored thermal energy distributes evenly so that an isothermal condition develops. As indicated, the layer topology results in a higher temperature (1002°C) than the sphere topology (960°C) and is therefore the more conservative option, though less accurate.

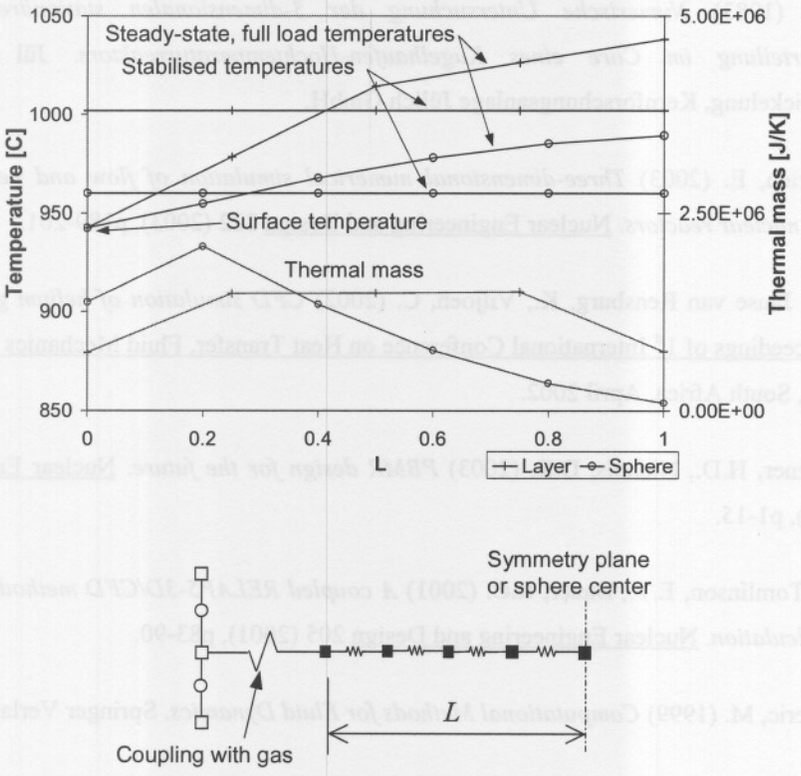


Figure 17: Control volume temperature and mass distributions for the layer and sphere topologies.

Conclusion

The versatility of the system CFD approach was illustrated by showing three different possible topologies for a pebble bed reactor core model. Despite the differences in network layout, the largest temperature difference between any two topologies in a transient simulation without heat generation was 9%. On the basis of the general good agreement between such diverse topologies, all three topologies are accepted as valid models of a pebble bed. However, the homogeneous topology was found to have very limited applicability in cases with heat generation. Of the three topologies, the sphere topology is the most useful as it provides the most information, namely the temperature distribution in the fuel spheres as well as an accurate calculation of stored thermal energy. It is therefore considered the most suitable topology for a reactor core thermal-fluid simulation model.

Acknowledgements

The authors hereby acknowledge the support of PBMR Pty (Ltd), who funded this research.

References

Du Toit, C.G., Greyvenstein, G.P., Rousseau, P.G. (2003) *A Comprehensive reactor model for the integrated network simulation of the PBMR power plant.* Proceedings of the 2003 International Congress on Advances in Nuclear Power Plants (ICAPP'03). Cordoba, Spain, 4-7 May 2003.

Verfondern, K. (1983) *Numerische Untersuchung der 3-dimensionalen stationären Temperatur- und Strömungsverteilung im Core eines Kugelhaufen-Hochtemperaturreaktors.* Jül –1826, Institut für Reaktorentwickelung, Kernforschungsanlage Jülich GmbH.

Becker, S., Laurien, E. (2003) *Three-dimensional numerical simulation of flow and heat transport in high-temperature nuclear reactors.* Nuclear Engineering and Design 222 (2003), p189-201.

Van Staden, M., Janse van Rensburg, K., Viljoen, C. (2002) *CFD simulation of helium gas cooled pebble bed reactor.* Proceedings of 1st International Conference on Heat Transfer, Fluid Mechanics and Thermodynamics, Kruger Park, South Africa, April 2002.

Koster, A., Matzner, H.D., Nichols, D.R. (2003) *PBMR design for the future.* Nuclear Engineering and Design 2800, (2003), p1-15.

Aumiller, D.L., Tomlinson, E.T., Bauer, R.C. (2001) *A coupled RELAP5-3D/CFD methodology with a proof-of-principle calculation.* Nuclear Engineering and Design 205 (2001), p83-90.

Ferziger, J.H., Peric, M. (1999) *Computational Methods for Fluid Dynamics.* Springer Verlag, p158.

Greyvenstein, G.P., Du Toit, C.G. (2001) *FLOWNET Version 5.4 User Manual.* M-Tech Industrial, Potchefstroom, South Africa.

Greyvenstein, G.P. (2002) *An implicit method for the analysis of transient flows in pipe networks.* International Journal of Numerical Methods in Engineering., 53, 1127-1143.

Incropera, F.P., DeWitt, D.P. (1996) *Fundamentals of Heat and Mass Transfer.* 4th ed. John Wiley & Sons.

Aumiller, D.L. (2000) *The effect of nodalisation on the accuracy of the finite-difference solution of the transient conduction equation.* 2000 RELAP5 International Users Seminar, Jackson Hole, Wyoming, September 12-14, (2000). Available at: http://www.inel.gov/relap5/rius/jackson/aumillerconduction.pdf

Kugeler, K., Schulten, R. (1989) *Hochtemperaturreaktortechnik.* Springer-Verlag.

Zehner, P., Schlünder, E.U. (1970) *Wärmeleitfähigkeit von Schüttungen bei mäßigen Temperaturen.* Chemie-Ingenieur Technik, (1970), p933-941

Appendix C:

HEFAT2005. 4th International Conference on Heat Transfer, Fluid Mechanics and Thermodynamics, Cairo, Egypt. Paper number: VH1

ONE-DIMENSIONAL HEAT TRANSFER CALCULATION OF CONDUCTION AND RADIATION THROUGH SOLIDS WITH TRANSVERSE HOLES

H.J. van Antwerpen*, G.P. Greyvenstein
*Author for correspondence
School of Mechanical and Materials Engineering
North West University, Private Bag X6001, Potchefstroom 2520, South Africa
Corresponding author – HJ van Antwerpen: Phone: +27 18 297 0326 Fax: +27 18 297 0318
Email: mgihjva@puk.ac.za

ABSTRACT

In this paper, a semi-empirical heat transfer model is presented for calculating the one-dimensional heat transfer coefficient for a conducting solid with a transverse hole. The interaction between conduction and radiation heat transfer across the hole is taken into account. To calibrate the semi-empirical heat transfer model, experimental data is generated with a computational fluid dynamics (CFD) numerical model. The phenomena encountered here are very efficiently characterised with two non-dimensional parameters, namely the hole radius to block width ratio and the conduction to radiation ratio. The correlated values very accurately follow the CFD results and greatly simplify calculations, making parametric studies and higher level optimisation possible.

INTRODUCTION

Simple approximate calculation methods are more convenient and in many engineering problems, more appropriate than detailed numerical simulations. This is the case when heat conduction perpendicular to holes in a solid has to be calculated as part of a whole thermal system. Correct calculation of this phenomenon is computationally too expensive to perform in a system simulation so that simple inaccurate methods are mostly used. If a simple but accurate method could be found to represent these complex phenomena, it will be of great value.

Such two-dimensional conduction effects are accurately simplified by using conduction shape factors. Hahne and Grigull [1] as well as Lewis [2] presented conduction shape factors for many geometries, but their research did not include the effect of radiation heat transfer across voids. A simple shape factor that takes only conduction into account is not necessarily accurate as the relative contribution of radiation heat transfer across the hole is not quantitatively known.

In addition, the temperature distribution in the solid around the hole is influenced by radiation heat transfer and requires a two-dimensional calculation method. On average however, the temperature gradient over the solid body is one-dimensional and it is therefore considered feasible to create a simple one-dimensional calculation method.

This paper presents a semi-empirical model with the necessary correlations for calculating the one-dimensional heat transfer through a rectangular solid with a transverse hole. The influence of hole radius/block width ratio, as well as the effect of temperature level on overall heat transfer are taken into account. Similar to the approach used by Ganzevles and Van der Geld [3], a numerical model is used to generate data for the correlations.

NOMENCLATURE

AU	heat transfer coefficient [W/K]
b	block height [m]
F	conduction shape factor [m]
g	geometric or radiation multiplier
h	block thickness [m]
k	thermal conductivity [W/mK]
L	length [m]
P	Planck number or conduction-radiation parameter
Q	heat flow [W]
r	radius [m]
T	temperature [K]

Greek Letters

ε	emissivity
σ	*Stefan-Boltzmann constant* *(5.67e-8 W/m²K⁴)*

Subscripts and superscripts

0	*no radiation*
ave	*average*
c	*center*
rad	*radiation*
sb	*side block*
T	*temperature*

PHYSICAL CONSIDERATIONS

The physical layout under consideration is shown in Figure 1. A symmetry plane enables simplification to one half block.

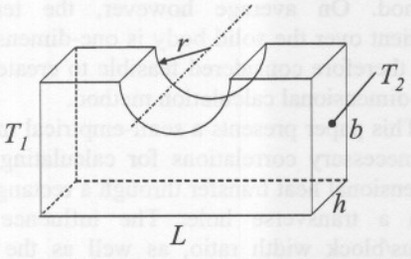


Figure 1: Geometry with dimension symbols.

In reality, there is always fluid present in the hole, which will transport heat by means of convection. With natural convection conditions, the hole axis orientation also comes into play. Furthermore, accurate flow simulation requires turbulence modelling and a fine three-dimensional calculation grid. Therefore, as a starting point, this paper focuses only on the interaction between radiation and conduction, which can be investigated with a two-dimensional grid.

This type of physical problems where radiation and conduction interact, are characterised by the Planck number P as defined for this paper by Eq.(1).

$$P = \frac{k}{\varepsilon \sigma T^3 r} \tag{1}$$

The Planck number characterises the isotherm pattern by means of a ratio between conduction and radiation heat transfer [4]. For a given block and hole size, the geometry is characterised by the ratio of r/b.

NUMERICAL MODEL

Empirical data for this study is obtained with Flo++ version 3.14 computational fluid dynamics (CFD) software. Flo++ solves a finite-volume discretisation of the basic transport equation as well as radiation heat transfer across cavities [5]. For the purpose of this study, only grey, diffuse surface radiation and non-participating gas was considered. Symmetrical cavity boundaries are also treated correctly by the radiation capability, which made symmetry simplification of the problem possible. The calculation grid is shown in Figure 2.

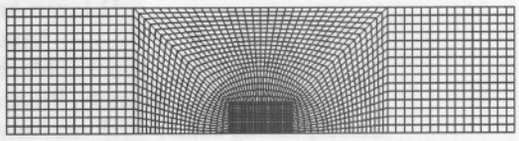


Figure 2: Calculation grid representation of the geometry.

Typical isotherm results obtained with the numerical model are shown in Figure 3. The results shown are for an r/b ratio of 0.5, k = 20 W/mK and b = 0.15m and average temperatures of 400K, 800K and 1200K, corresponding to Planck numbers as shown in Figure 3. The other parameters for this case had the following values: L = 0.6m, h = 0.01m, ε = 0.8.

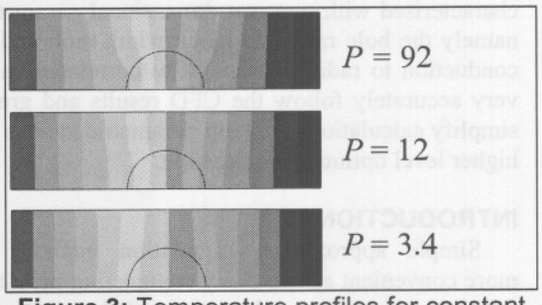


Figure 3: Temperature profiles for constant temperature difference and conductivity with three different average temperatures and therefore values of P.

The numerical model gives the boundary heat flux Q from the fixed temperature boundaries T_1 and T_2, so that the total heat transfer coefficient AU is obtained with Eq.(2).

$$AU = \frac{Q}{(T_2 - T_1)} \tag{2}$$

Other parameters can then be found from AU.

SIMPLE MODELLING APPROACH

A conduction shape factor is only defined for a fixed isotherm pattern, which is in turn characterised

by the Planck number. It is further known that in this case, radiation increases the heat transfer from a basic value, i.e. it will increase the value of the conduction form factor. Therefore, it appears appropriate to introduce a radiation multiplication function g_{rad} into the one-dimensional heat transfer equation, as shown in Eq.(3).

$$Q = kF_0(T_1 - T_2) \times g_{rad} \tag{3}$$

with F_0 being the zero-radiation form factor for a given r/b ratio. g_{rad} represents the effect of radiation heat transfer on the conduction shape factor as a function of Planck number.

The values of F_0 and g_{rad} will change according to physical size and r/b ratio. While g_{rad} is truly dimensionless, F_0 has the dimension of length and can be determined from simulations in which the radiation is switched off, i.e. g_{rad} equals unity.

CONDUCTION ONLY –DETERMINATION OF F_0.

For the zero-radiation case, the geometry shown in Figure 1 is divided into the thermal resistance network shown in Figure 4.

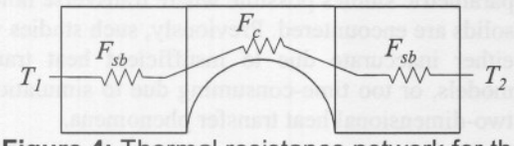


Figure 4: Thermal resistance network for the heat transfer model without radiation.

F_0 is calculated from the numerical results with Eq.(4), in which g_{rad} equals unity.

$$kF_0 g_{rad} = AU \tag{4}$$

From F_0 and the side-block shape factor (Eq.(5)) the central block shape factor F_c is calculated with Eq.(6).

$$F_{sb} = \frac{bh}{L/2 - r} \tag{5}$$

$$F_0 = \frac{1}{\frac{2}{F_{sb}} + \frac{1}{F_c}} \tag{6}$$

Once the center block shape factor F_c is found, the dimensionless conduction-only shape factor g_c is calculated from Eq.(7). In Eq.(7) $hb/2r$ relates the heat transfer to the physical size of the geometry.

$$F_c = \frac{hb}{2r} \times g_c\left(\frac{r}{b}\right) \tag{7}$$

g_c was found to correlate to r/b ratio according to Eq.(8), as shown in Figure 5.

$$g_c = 0.9389 - 0.8432\frac{r}{b}, 0 \le \frac{r}{b} \le 0.9 \tag{8}$$

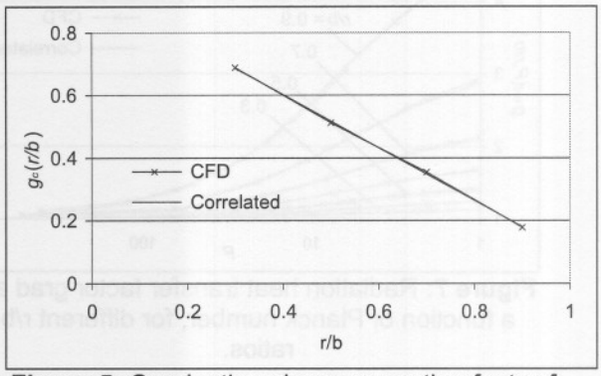


Figure 5: Conduction shape correction factor f_c for the central block.

Application of Eq.(8) gives an overall heat transfer coefficient as shown in Figure 6 (calculated for physical values of L = 1m, b = 0.25m, h = 0.1m, k = 0.025W/mK).

At low values of r/b, CFD slightly overpredicts the heat transfer coefficient, as the grid distortion required to accommodate small hole sizes aggravates numerical diffusion. Because the simple heat transfer model is only semi-empirical, it gives the analytical value at extremities.

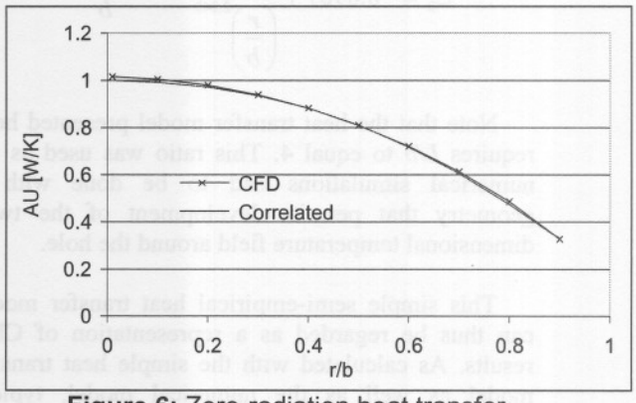


Figure 6: Zero-radiation heat transfer coefficient as a function of r/b ratio.

RADIATION HEAT TRANSFER

Once F_0 is determined as a function of r/b, it is possible to determine g_{rad} as a function of P and r/b from Eq.(4). A series of simulations was done over a large range of average temperatures, emissivities, conductivities, block sizes and several specific r/b values.

The numerically determined as well as the correlated values for g_{rad} are presented in Figure 7.

Given the fact that all possible parameters were varied in the source data for Figure 7, it is evident that g_{rad} correlates very well to P and r/b.

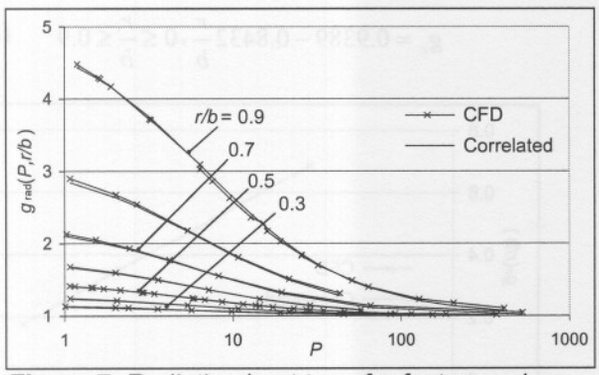


Figure 7: Radiation heat transfer factor grad as a function of Planck number, for different r/b ratios.

g_{rad} is correlated with Eq.(9).

$$g_{rad} = 1 + \frac{1}{C_1 + C_2 P}, \frac{L}{b} = 4, 0.5 \le P \le 1000 \quad (9)$$

with C_1 and C_2 being empirical functions of the r/b ratio as described in Eqs.(10) and (11).

$$C_1 = -0.5618 + \frac{0.6546}{\left(\frac{r}{b}\right)^{2.017}}, 0.3 \le \frac{r}{b} \le 0.9 \quad (10)$$

$$C_2 = -0.0987 + \frac{0.1088}{\left(\frac{r}{b}\right)^{2.042}}, 0.3 \le \frac{r}{b} \le 0.9 \quad (11)$$

Note that the heat transfer model presented here requires L/b to equal 4. This ratio was used as all numerical simulations had to be done with a geometry that permits development of the two-dimensional temperature field around the hole.

This simple semi-empirical heat transfer model can thus be regarded as a representation of CFD results. As calculated with the simple heat transfer model as well as the numerical model, typical variation of total heat transfer coefficient with average temperature is shown in Figure 8 for several r/b ratios (k = 20W/mK, b = 0.15m, h = 1m, L = 0.6, ε = 0.8).

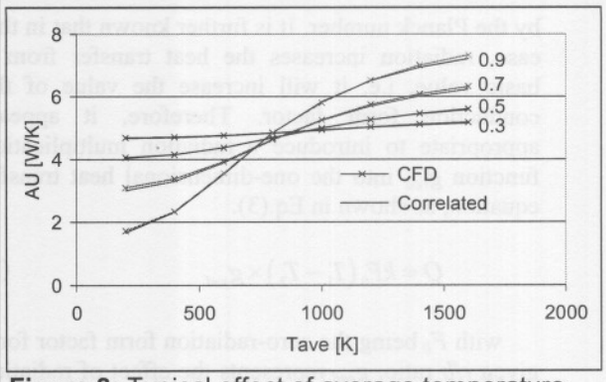


Figure 8: Typical effect of average temperature on heat transfer coefficient for four different r/b ratios.

In general, good agreement is seen between the correlation and the numerically calculated heat transfer values.

CONCLUSION

A simple semi-empirical method has been proposed to calculate the combined conduction and radiation heat transfer through a rectangular solid with a transverse hole. Good agreement is seen between the correlation and its source data.

This simple calculation model makes quick, accurate parametric studies possible where transverse holes in solids are encountered. Previously, such studies were either inaccurate due to insufficient heat transfer models, or too time-consuming due to simulation of two-dimensional heat transfer phenomena.

REFERENCES

[1] Hahne and Grigull (1977). Shape factor and shape resistance for steady multidimensional heat conduction. International Journal of Heat and Mass Transfer Volume 18, Issue 6, June 1975, pp751-767.

[2] Lewis, G.K. (1967) Shape factors in conduction heat flow for circular bars and slabs with various internal geometries. International Journal of Heat and Mass Transfer Volume 11, Issue 6 , June 1968, pp 985-992.

[3] Ganzevles, F.L.A., Van der Geld, C.W.M. (1997) The shape factor of conduction in a multiple channel slab and the effect of non-uniform temperatures. International Journal of Heat and Mass Transfer Volume 40, Number 10, pp2493-2498

[4] Modest, M.F. (2003) Radiative Heat Transfer, 2ndEd.Academic Press.

[5] La Grange, L.A. (2005) Flo++ User Manual, Softflo, Potchefstroom, South Africa. http://www.softflow.com/

Appendix D:

Draft paper submitted and accepted for publication in Nuclear Engineering and Design (2007).

EVALUATION OF A DETAILED RADIATION HEAT TRANSFER MODEL IN A HIGH TEMPERATURE REACTOR SYSTEMS SIMULATION MODEL

H.J. van Antwerpen
Corresponding author: School for Mechanical Engineering, Northwest University, Private Bag X6001, Potchefstroom 2520, South Africa, Fax: +27 18 297 0318 Email: mgihjva@puk.ac.za

G.P. Greyvenstein
Postgraduate School for Nuclear Engineering, North-West University, South Africa

1. Abstract

Radiation heat transfer is a major mode of heat transfer in high temperature gas-cooled reactors because of the high operating temperatures. It is, however, a difficult phenomenon to calculate in full detail due to its geometrical complexity. One has to use either a numerical method or complex analytical view factor formulae. Except the difficulty of view factor calculation, a vast number of calculation elements are required to consider all interacting surfaces around a cavity. A common approximation in systems simulation codes is to connect only directly opposing surfaces with a view factor of one.

The accuracy of this approximation was investigated with a finite volume, two-dimensional axial-symmetric reactor model implemented in the systems simulation code Flownex. A detailed radiation model was developed and also implemented in the Flownex reactor model. This paper also describes the analytical formulae for view factor calculation in this detailed radiation heat transfer model.

The HTR-10 and the 268MW version of the PBMR were used as case studies in which Loss-Of-Flow events without SCRAM were simulated. In these simulations, the time to reach recriticality was used as an indicator of heat removal effectiveness.

With the HTR-10, other nonlinear phenomena in the reactor core constrained the solution process, so that the number of radiation elements had no effect on solution time, while with the 268MW PBMR DLOFC, the use of a detailed radiation model increased solution time with 30 percent.

With both the HTR-10 and the PBMR, the radiation model had negligible effect on the total heat resistance from the reactor, as indicated by the time elapsed until recriticality.

For system simulation codes that focus on transient response of a plant, it is not considered worthwhile to use a detailed radiation model, as the gain in accuracy does not justify the increased solution time or the implementation and verification effort.

2. Nomenclature

Symbol	Unit	Description
A	-	area auxiliary parameter in view factor calculation
B	-	auxiliary parameter in view factor calculation
C	-	auxiliary parameter in view factor calculation
D	-	auxiliary parameter in view factor calculation
F_{ij}	-	view factor from surface i to surface j
H	-	normalised height in view factor calculation
h	m	height
q	W	heat flow
r	m	radius
r_c	m	included cylinder radius
R	-	normalised radius in view factor calculation
T_{sp}	K	spatial temperature
T	K	temperature
Y	-	auxiliary parameter in view factor calculation
α	radians	angle
ε	-	emissivity
σ	W/m^2K^4	Stefan-Boltzmann constant

3. Introduction

High Temperature Gas Cooled Reactors (HTRs) typically operate at reactor outlet gas temperatures of about 900°C. Due to these high temperatures, radiative heat transfer becomes an important heat transfer mechanism. As reactor core components are all made of graphite, opaque, diffuse, gray surface behaviour is assumed for radiation. The reactor core cavities are filled with helium, which has (monatomic) non-polar molecules and therefore does not partake in radiation heat transfer.

Radiation heat transfer between two surfaces in the reactor can thus be calculated with the following equation:

$$q_{12} = \frac{\sigma\left(T_1^4 - T_2^4\right)}{\frac{1-\varepsilon_1}{\varepsilon_1 A_1} + \frac{1}{AF_{12}} + \frac{1-\varepsilon_2}{\varepsilon_2 A_2}} \quad (1)$$

However, as the present state-of-the-art reactor thermal-fluid calculations use discretised domains, each cavity is surrounded by numerous surfaces that exchanges heat with each other. Therefore a radiation exchange network has to be set up, in which the various terms in Eq.(1) are split up into the surface emissivity resistance Eq.(2) and the spatial resistance in Eq.(3).

$$q_1 = \frac{\varepsilon_1 A_1}{1-\varepsilon_1}\sigma\left(T_1^4 - T_{sp1}^4\right) \quad (2)$$

$$q_{sp12} = A_1 F \sigma\left(T_{sp1}^4 - T_{sp2}^4\right) \quad (3)$$

This requires definition of effective surface spatial temperatures T_{sp}. A radiation exchange network is shown in Figure 1. At this point, the only unknown is the geometrical view factor F_{12}, defined as the fraction area A_2 occupies of the total view from area A_1. The details of view factor calculation is discussed later in this paper, under the heading *Calculation model*.

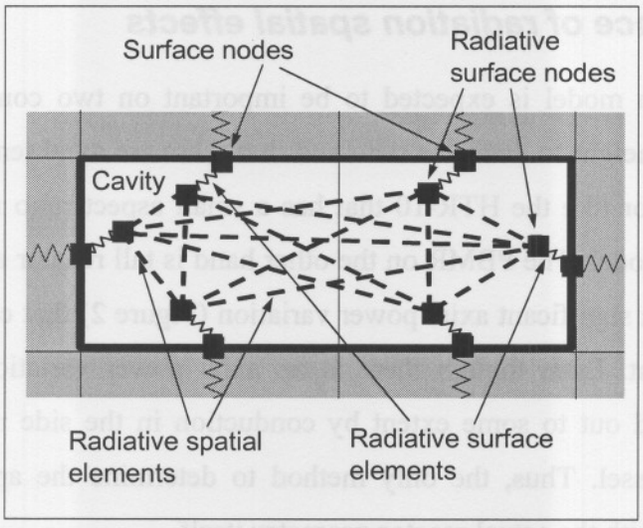


Figure 1. Topology of the radiation element network in a cavity.

The method used in this study for discretising radiation heat transfer domains connects every surface in a cavity to every other surface in the cavity, giving rise to an enormous number of connections. Because of the great number of spatial heat transfer elements necessary for

radiation heat transfer and the difficulty in calculating the view factor, many analysts assume a view factor of 1 and radiation heat transfer only between directly opposing surfaces in cavities. The qualitative effect of this approximation is to retain temperature profiles that would otherwise be smoothed out by spatial radiation connections.

There are thus three possibilities for radiative heat transfer spatial connections, namely to use the full number of spatial connections, to use only a reduced number of significant connections or to connect only directly opposing surfaces.

The effects of these approximations are threefold. Firstly it affects the temperatures of various components adjacent to cavities and secondly it affects the total heat resistance from a reactor. This is of particular importance to HTRs of which the inherent safety feature relies on passive heat removal from the reactor core. Thirdly, it is not known how the number of radiation connections affects solution time in numerical calculations. This is crucial for systems simulations codes as they require fast solution times for doing transient simulations and parametric studies.

Therefore this paper reports on the effect of the radiation heat transfer calculation method on temperature profiles, heat removal rates and solution times for HTR calculations.

4. Significance of radiation spatial effects

A detailed radiation model is expected to be important on two conditions, namely that the reactor has a large height to diameter ratio and that there are axial temperature gradients. This implies that a reactor like the HTR-10 that has a small aspect ratio is not likely to require a detailed radiation model. The PBMR on the other hand is tall reactor and as shown by Reitsma *et al.*(2004), it has a significant axial power variation (Figure 2) that could give rise to an axial temperature gradient. Even though there is an axial power variation, an axial temperature variation is smeared out to some extent by conduction in the side reflector, core barrel and reactor pressure vessel. Thus, the only method to determine the applicability of a detailed radiation model is with the actual reactor geometry itself.

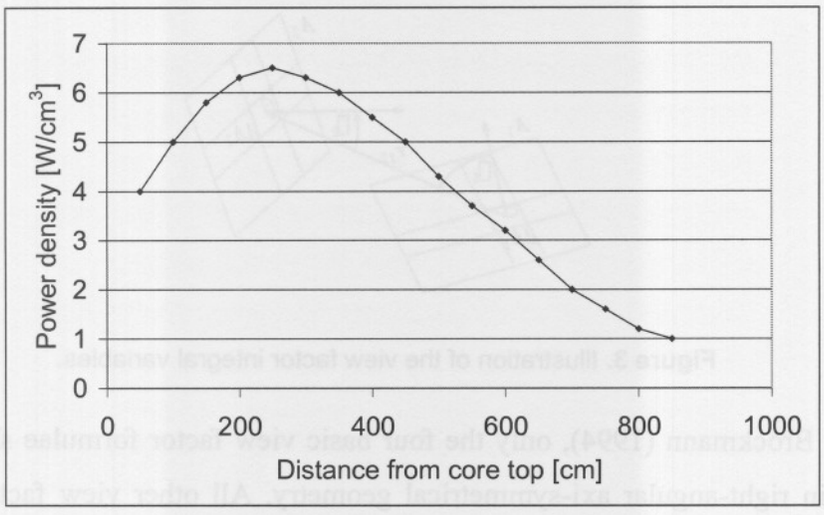


Figure 2. Axial power profile for the 268MW PBMR (Reitsma *et al*, 2004)

5. Calculation model

A two-dimensional, axi-symmetric finite volume thermal-fluid model was implemented in a research version of the systems-CFD code Flownex and was used for this investigation. Due to the unique solution method in Flownex, the flow and heat transfer network can have an arbitrary topology (Greyvenstein, Van Antwerpen, Rousseau, 2004). The capability of Flownex to solve a network with arbitrary topology enabled the implementation of a detailed radiation model in the reactor model, as the radiation model requires a complex network topology as shown in Figure 1. The most challenging aspect of the radiation model is the view factor calculation. The view factor is formally defined by the integral

$$F_{12} = \int_{A_1}\int_{A_2} \frac{\cos\alpha_1 \cos\alpha_2}{\pi r_{12}^2} dA_2 dA_1 \tag{4}$$

with r_{12} being the distance between dA_1 and dA_2 and α_1 and α_2 being the angles between r_{12} and normal vectors on the surfaces of dA_1 and dA_2. All the variables are shown in Figure 3.

Despite the difficulty of analytically evaluating the integral in Eq.(4), many view factors have been evaluated and were compiled by Howell (2001) into a numbered view factor catalogue that is accessible on the Internet. Specifically relevant to HTR radiative heat transfer calculations, Brockmann (1994) presented a complete set of basic view factor formulae for two-dimensional axi-symmetric geometry.

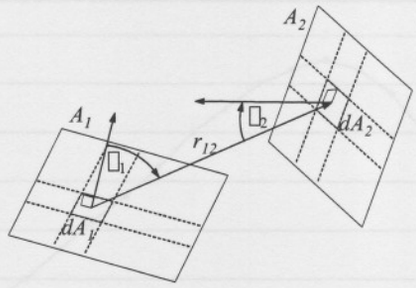


Figure 3. Illustration of the view factor integral variables.

As shown by Brockmann (1994), only the four basic view factor formulae shown in Figure 4 are required in right-angular axi-symmetrical geometry. All other view factors can be found using view factor algebra.

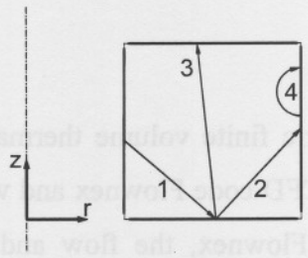


Figure 4. View factors required for radiative heat transfer calculation in two-dimensional right-angular axi-symmetrical geometry.

Because of the difficulty of analytically evaluating the view factor integral, it is only solved for the most simple surface configurations, such as the setup shown in Figure 5.

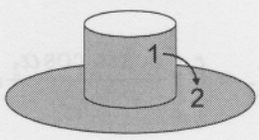


Figure 5. A primitive surface setup for evaluating the view factor integral.

If surfaces 1 and 2 in Figure 5 are subdivided as shown in Figure 6, the basic view factor formula can not be applied directly, but has to be used in conjunction with view factor algebra.

For the sake of completeness, the four basic view factor formulae are quoted from Brockmann (1994) and Howell (2001) before presenting the algebraic formulae that were derived in this study for calculating the view factor between discretised surfaces. The basic view factor formulae are distinguished from other by an overbar symbol, such as basic view factor $\overline{F1}$.

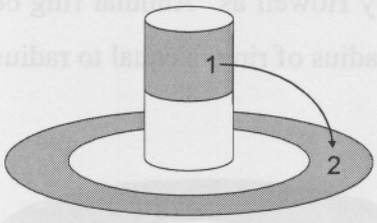


Figure 6. The geometrical setup typically encountered on discretised surfaces.

5.1. Basic view factor $\overline{F1}$: radiation from central cylinder to bottom

The geometry for this view factor is shown in Figure 7.

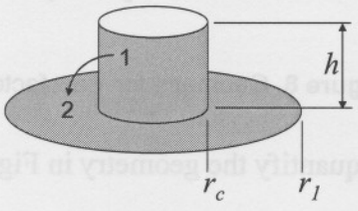


Figure 7. Geometry for view factor $\overline{F1}$.

It is convenient to use the following dimensionless variables to describe the geometry:

$$\begin{aligned} R &= r_c/r_1 \\ H &= h/r_1 \\ A &= H^2 + R^2 - 1 \\ B &= H^2 - R^2 + 1 \end{aligned} \tag{5}$$

with r_c being the included cylinder radius, h the included cylinder height and r_1 the disk outer radius, as shown in Figure 7. The view factor formula is given by

$$\overline{F1} = \frac{B}{8RH} + \frac{1}{2\pi}\left\{\arccos\left(\frac{A}{B}\right) - \frac{1}{2H}\left[\frac{(A+2)^2}{R^2} - 4\right]^{1/2} \times \arccos\left(\frac{AR}{B}\right) - \frac{A}{2RH}\arcsin R\right\} \tag{6}$$

To avoid undefined operations when Eq.(6) is implemented in a computer code, $\overline{F1}$ can be set to zero when $r_1 \leq r_c$ or $h \leq 0$. This situation arises when calculating the view factors between discretised surfaces.

5.2. Basic view factor $\overline{F2}$: radiation from bottom to outside

This view factor is described by Howell as "Annular ring between two concentric cylinders to inside of outer cylinder, inner radius of ring is equal to radius of inner cylinder" as illustrated in Figure 8.

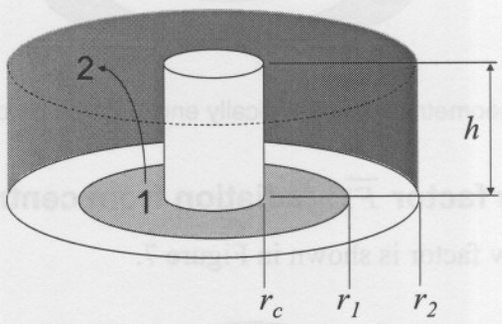


Figure 8. Geometry for view factor $\overline{F2}$.

The dimensionless variables to quantify the geometry in Figure 8 are given by

$$\begin{aligned} R_1 &= r_1/h & A &= R_1^2 - R_c^2 & D &= R_2 - R_1 \\ R_2 &= r_2/h & B &= R_2^2 - R_c^2 & Y &= A^{1/2} + B^{1/2} \\ R_c &= r_c/h & C &= R_2 + R_1 & & \end{aligned} \tag{7}$$

The view factor is then described by

$$\overline{F2} = \frac{1}{\pi A}\left[\begin{aligned} &\frac{B}{2}\left(\pi - \arccos\frac{R_c}{R_2}\right) - 2R_c\left(\arctan Y - \arctan B^{1/2}\right) - \frac{1}{2}\arccos\frac{R_c}{R1} \\ &+\left[\left(1+C^2\right)\left(1+D^2\right)\right]^{1/2}\arccos\left[\frac{\left(1+C^2\right)\left(Y^2-D^2\right)}{\left(1+D^2\right)\left(C^2-Y^2\right)}\right]^{1/2} \\ &-\left\{\left[1+\left(R_2+R_c\right)^2\right]\left[1+\left(R_2-R_c\right)^2\right]\right\}^{1/2}\arctan\left\{\frac{\left[1+\left(R_2+R_c\right)^2\right]\left(R_2-R_c\right)}{\left[1+\left(R_2-R_c\right)^2\right]\left(R_2+R_c\right)}\right\}^{1/2} \\ &-\left(R_2^2-R_1^2\right)\arctan\left[\frac{C}{D}\left(\frac{Y^2-D^2}{C^2-Y^2}\right)^{1/2}\right] \end{aligned}\right] \tag{8}$$

To avoid undefined operations when Eq.(8) is implemented in a computer code, $\overline{F2}$ can be set to zero when $r_1 \le r_c$ or $h \le 0$.

5.3. Basic view factor $\overline{F3}$: radiation from bottom to top

This view factor is between parallel, annular rings at the end of an inscribed cylinder, as shown in Figure 9.

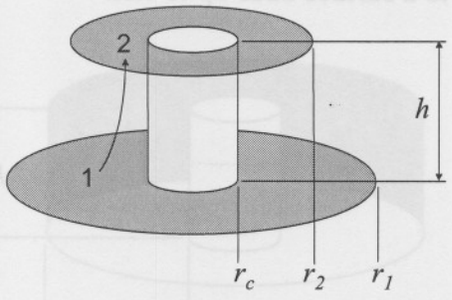


Figure 9. Geometry for view factor $\overline{F3}$.

The geometry in Figure 9 is quantified by the following dimensionless numbers:

$$A = r_c/h \quad B = r_1/h \quad C = r_2/h$$

$$Y = \sqrt{C^2 - A^2} + \sqrt{B^2 - A^2} \tag{9}$$

with the symbols above as defined in Figure 9.

$$\overline{F3} = \frac{1}{\pi\left(C^2 - A^2\right)} \left[\begin{array}{l} \frac{1}{2}\left(C^2 - A^2\right)\arccos\frac{A}{B} \\ +\frac{1}{2}\left(B^2 - A^2\right)\arccos\frac{A}{C} \\ +2A\left\{\arctan\left(\sqrt{C^2 - A^2} + \sqrt{B^2 - A^2}\right) - \arctan\left(\sqrt{C^2 - A^2}\right) - \arctan\left(\sqrt{B^2 - A^2}\right)\right\} \\ -\sqrt{\left[1+(C+B)^2\right]\left[1+(C-B)^2\right]} \times \arctan\left(\sqrt{\frac{\left[1+(C+B)^2\right]\left[Y^2-(C-B)^2\right]}{\left[1+(C-B)^2\right]\left[(C+B)^2-Y^2\right]}}\right) \\ +\sqrt{\left[1+(C+A)^2\right]\left[1+(C-A)^2\right]} \times \arctan\left(\sqrt{\frac{\left[1+(C+A)^2\right][C-A]}{\left[1+(C-A)^2\right][C+A]}}\right) \\ +\sqrt{\left[1+(B+A)^2\right]\left[1+(B-A)^2\right]} \times \arctan\left(\sqrt{\frac{\left[1+(B+A)^2\right][B-A]}{\left[1+(B-A)^2\right][B+A]}}\right) \end{array} \right] \tag{10}$$

To avoid undefined operations when Eq.(10) is implemented in a computer code, $\overline{F3}$ can be set to zero when $h \leq 0$ or $r_2 \leq r_c$ or $r_1 \leq r_c$.

5.4. Basic view factor $\overline{F4}$: radiation from outer surface to itself

This is the view factor from an outer cylinder inner surface to itself with the presence of a concentric inner cylinder. This view factor is necessary for discretised surfaces and to verify that the sum of view factors to a surface adds op to one.

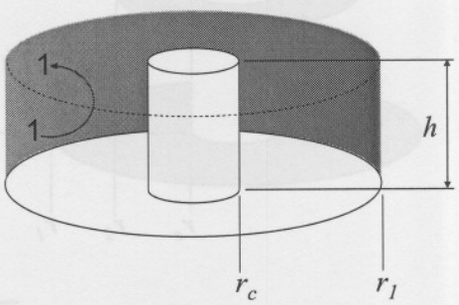


Figure 10. Geometry for view factor $\overline{F4}$.

The dimensionless parameters that quantify the geometry in Figure 10 are

$$A = r_c/h \qquad B = r_1/h \tag{11}$$

with the symbols as defined in Figure 10.

$$\overline{F4} = \frac{1}{\pi B}\left[\begin{array}{l} \pi(B-A) + \arccos\dfrac{A}{B} \\ -\sqrt{\left[1+4B^2\right]} \times \arctan\left(\dfrac{\sqrt{\left[1+4B^2\right]\left[B^2-A^2\right]}}{A}\right) \\ +2A\arctan\left(2\sqrt{\left[B^2-A^2\right]}\right) \end{array}\right] \tag{12}$$

To avoid undefined operations when Eq.(12) is implemented in a computer code, $\overline{F4}$ can be set to zero when $h \leq 0$.

5.5. Derived view factor 1

The view factor from the inner cylinder outer surface to a directly opposing inner surface on the outer cylinder is calculated with view factor $\overline{F1}$ and Eq.(13) as:

$$F_{12} = 1 - 2\overline{F1} \tag{13}$$

with input values to $\overline{F1}$ as defined in Figure 11.

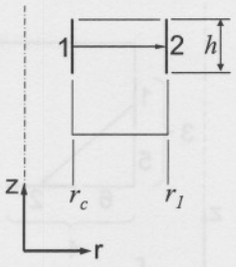


Figure 11. Geometry for derived view factor DF1

5.6. Derived view factor 2

For this case, the coaxial surfaces are not directly opposing as in Figure 11, but are offset axially as shown in Figure 12.

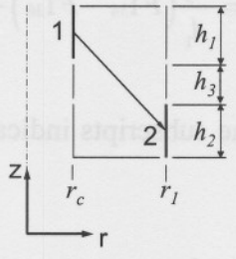


Figure 12. Geometry for calculation of derived view factor DF2

For the geometry in Figure 12, it can be shown that F_{12} is given by:

$$F_{12} = \frac{h_1 + h_3}{h_1}\overline{F1}_{h_1+h_3} + \frac{h_2 + h_3}{h_1}\overline{F1}_{h_1+h_3} - \frac{h_3}{h_1}\overline{F1}_{h_3} - \frac{h_1 + h_2 + h_3}{h_1}\overline{F1}_{h_1+h_2+h_3} \qquad (14)$$

with the subscripts in Eq.(14) indicating the length that should be used when evaluating $\overline{F1}$, i.e. h in Figure 7 should be replaced by the subscripts of $\overline{F1}$ when evaluating the terms in Eq.(14).

5.7. Derived view factor 3

This view factor is from a single discrete surface on the outside of a cylinder to a flat annular ring around the base of the cylinder as shown in Figure 13.

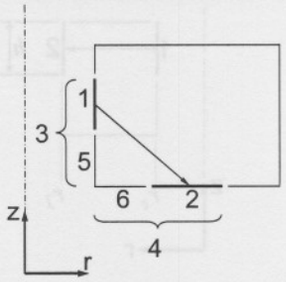


Figure 13. Geometry for derived view factor 3.

With the surfaces as indicated in Figure 13, the view factor F_{12} is calculated by using $\overline{F1}$ in the formula

$$F_{12} = \frac{A_3}{A_1}\left(\overline{F1}_{34} - \overline{F1}_{36}\right) - \frac{A_5}{A_1}\left(\overline{F1}_{54} - \overline{F1}_{56}\right) \tag{15}$$

with A in Eq.(15) being area and the subscripts indicating between which surfaces $\overline{F1}$ should be evaluated.

5.8. Derived view factor 4

This view factor is from a flat annular ring to a single discrete surface on the inside of the outer cylinder, with the presence of an inner cylinder as shown in Figure 14.

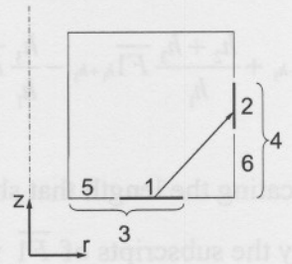


Figure 14. Geometry for derived view factor 4

With the surfaces as indicated in Figure 14, the view factor F_{12} is calculated by using $\overline{F2}$ as follows:

$$F_{12} = \frac{A_3}{A_1}\left(\overline{F2}_{34} - \overline{F2}_{36}\right) - \frac{A_5}{A_1}\left(\overline{F2}_{54} - \overline{F2}_{56}\right) \tag{16}$$

with A in Eq.(16) being area and the subscripts indicating between which surfaces $\overline{F2}$ should be evaluated. The inner cylinder radius is required for calculating this view factor, even though it is not directly associated with any of the surfaces in the calculation.

5.9. Derived view factor 5

This view factor is from one discrete annular ring at the bottom of a cavity to another discrete annular ting at the top of a cavity, with the presence of an inner cylinder as shown in Figure 15.

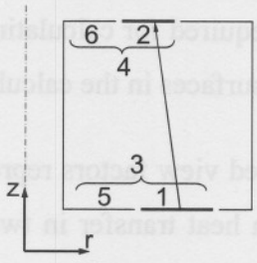


Figure 15. Geometry for derived view factor 5

With the surfaces as indicated in Figure 15, the view factor F_{12} is calculated by using $\overline{F3}$ as follows:

$$F_{12} = \frac{A_3}{A_1}\left(\overline{F3}_{34} - \overline{F3}_{36}\right) - \frac{A_5}{A_1}\left(\overline{F3}_{54} - \overline{F3}_{56}\right) \tag{17}$$

with A in Eq.(17) being area and the subscripts indicating between which surfaces $\overline{F3}$ should be evaluated. The inner cylinder radius is required for calculating this view factor, even though it is not directly associated with any of the surfaces in the calculation.

5.10. Derived view factor 6

This view factor is from a cylinder inner surface to an adjacent surface on the same cylinder.



Figure 16. Geometry for derived view factor 6

With the surfaces as indicated in Figure 16, the view factor F_{12} is calculated by using $\overline{F4}$ as follows:

$$F_{12} = \frac{h_1 + h_2 + h_3}{2h_1}\overline{F4}_{h_1+h_2+h_3} - \frac{h_1 + h_3}{2h_1}\overline{F4}_{h_1+h_3} - \frac{h_2 + h_3}{2h_1}\overline{F4}_{h_2+h_3} + \frac{h_3}{2h_1}\overline{F4}_{h_3} \qquad (18)$$

with the subscripts in Eq.(18) indicating the length that should be used when evaluating $\overline{F4}$, i.e. h in Figure 10 should be replaced by the subscripts of $\overline{F4}$ when evaluating the terms in Eq. (18). The inner cylinder radius is required for calculating this view factor, even though it is not directly associated with any of the surfaces in the calculation.

These basic view factors and derived view factors represent all the formulae that are necessary for accurately calculating radiation heat transfer in two-dimensional axi-symmetric geometry. View factor calculation can be verified by summing the view factors of all spatial connections to a node and ensuring it adds up to one.

6. Case studies

The HTR-10 reactor Pressurised Loss of Forced Cooling (PLOFC) benchmark published by the IAE (2006) was used as case study. For the second case study, a Depressurised Loss Of Forced Cooling (DLOFC) of the 268MW PBMR was used as described by Reitsma *et al.* (2004) for an international calculation benchmarking effort. Cross-sections of the reactors, as well as their discretised representation are shown in Figure 17 and Figure 18.

Both these cases have been widely calculated and well standardised. The PBMR benchmark has many simplifications in order to establish the effects of differences in modelling approach.

For the HTR-10, the LOFC event starts from a steady state power level of 3MW, inlet temperature at 215°C and outlet temperature of 700°C. The event is initiated by shutting off the reactor coolant flow with no control rod movement. The ensuing temperature rise shuts the reactor down by means of a negative reactivity insertion from the negative fuel temperature reactivity coefficient.

The reactor then cools down by means of natural convection in the pebble bed core, conduction through the side reflectors and radiation heat transfer across cavities.

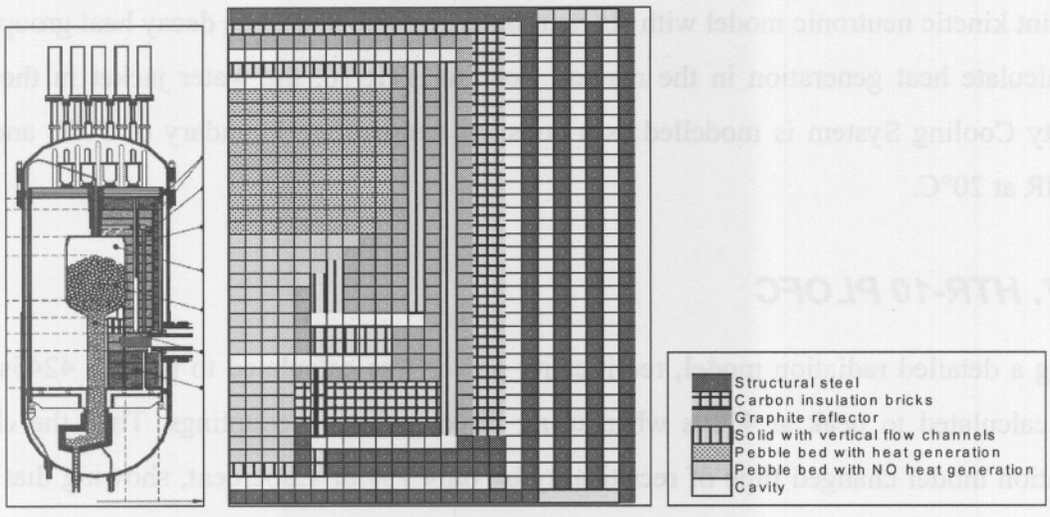


Figure 17. Vertical cross-section of the HTR-10 (left) with zones for describing the reactor geometry and input values (right).

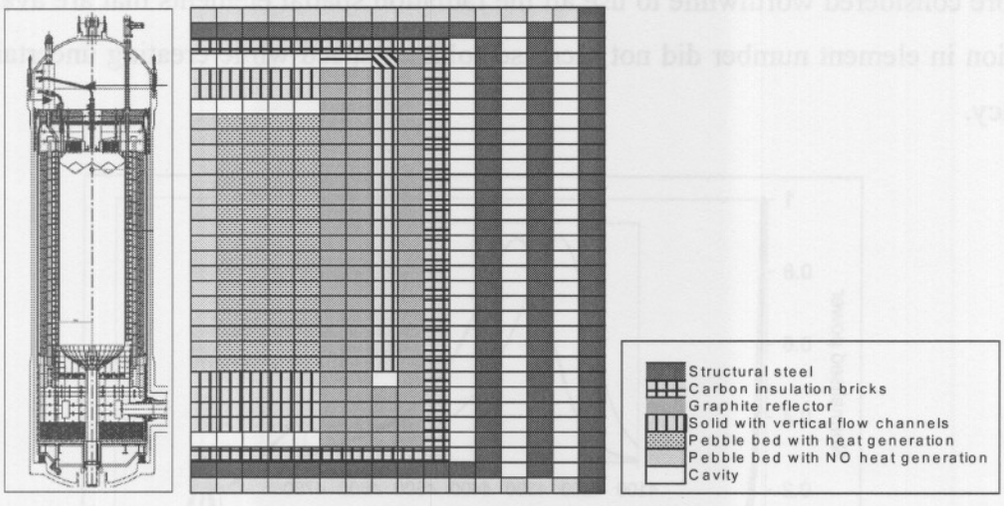


Figure 18. Vertical cross-section of the 268MW version of the PBMR (left) with zones for describing the reactor geometry and input values (right). The zones were used as described by Reitsma *et al.* (2004).

The heat from the reactor is eventually taken up by the water circulating through the reactor cavity cooling system. As the reactor cools down, the negative temperature coefficient again increases reactivity, until criticality is reached again. As the time from coolant flow shutdown to recriticality depends largely on the heat loss from the reactor, this event presents a very good test for a thermal-fluid calculation code.

The PBMR DLOFC is started at 100 percent power and a massflow of 129kg/s at 7000kPa. This decreases to zero kg/s and 100kPa over a timespan of 13s.

A point kinetic neutronic model with six neutron precursors and three decay heat groups is used to calculate heat generation in the reactor. For the HTR-10, the water jacket in the Reactor Cavity Cooling System is modelled as a constant temperature boundary of 50°C and for the PBMR at 20°C.

7. HTR-10 PLOFC

Using a detailed radiation model, recriticality power was calculated to peak at 4245s while it was calculated to peak at 4320s when using direct radiation couplings. Thus the change in radiation model changed time of recriticality by only 75s or 1.8percent, showing that the total heat loss from the reactor is not influenced significantly by the radiation model.

For both cases, simulation duration was 20 minutes for a 6000 seconds simulated time. It is therefore considered worthwhile to use all the radiation spatial elements that are available, as a reduction in element number did not increase solution speed while creating uncertainty on the accuracy.

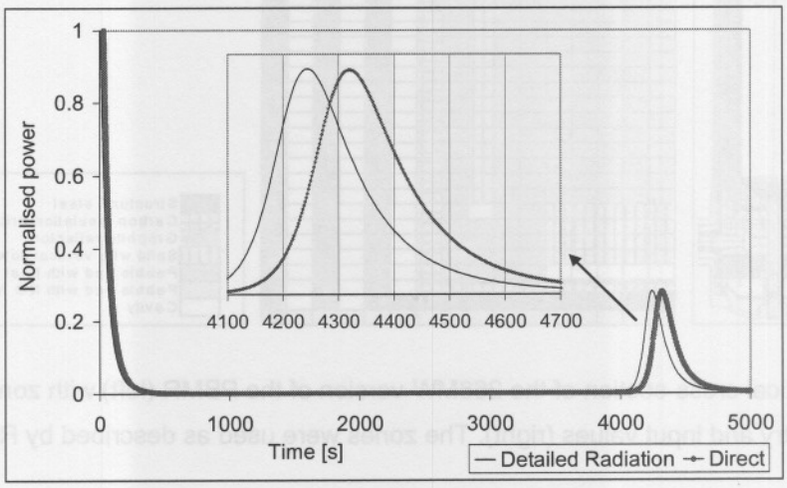


Figure 19. Normalised power as a function of time for detailed and direct radiation models for the HTR-10 PLOFC.

Element number reduction did not increase speed because the size of the energy conservation matrix is determined by the number of nodes, while only the bandwidth of the matrix is determined by the number of elements. As convective heat transfer elsewhere in the reactor has much more nonlinear characteristics, radiation heat transfer is not the constraining parameter on the solution in the case of the HTR-10 PLOFC.

This investigation confirms that modelling radiation heat transfer by linking directly opposing surfaces gives accurate results for the HTR-10 reactor as far as overall heat removal rate is concerned.

8. 268MW PBMR DLOFC

Using a detailed radiation model, recriticality was calculated to occur at 69.2 hours after the DLOFC event. When only directly opposing surfaces were linked with a view factor of one, the recriticality was calculated at 70.2 hours, thus shifting the time of recriticality by only one hour. With the detailed radiation model, it took 475s to calculate 7840 timesteps while the same number of timesteps required only 349s when using only direct radiation elements.

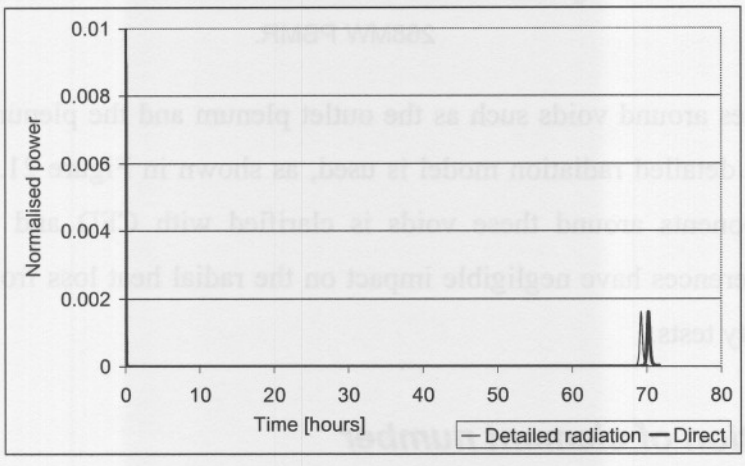


Figure 20. Normalised power as a function of time for detailed and direct radiation models for the 268MW PBMR DLOFC.

Neither the HTR-10 nor the first PBMR case took into account gamma-ray heating of the side reflector. If there is significant heating in the side reflector, the axial temperature profile could be more pronounced, thereby making it more important to have a detailed radiation model. This possibility was investigated by assuming that one percent of the total heat generation is deposited in the side reflector. Under this assumption, recriticality was calculated at 80hours with direct couplings and 79 hours with a detailed radiation model. The assumption of reflector heating thus changed the time of recriticality, but did not change the difference between the direct and detailed radiation models.

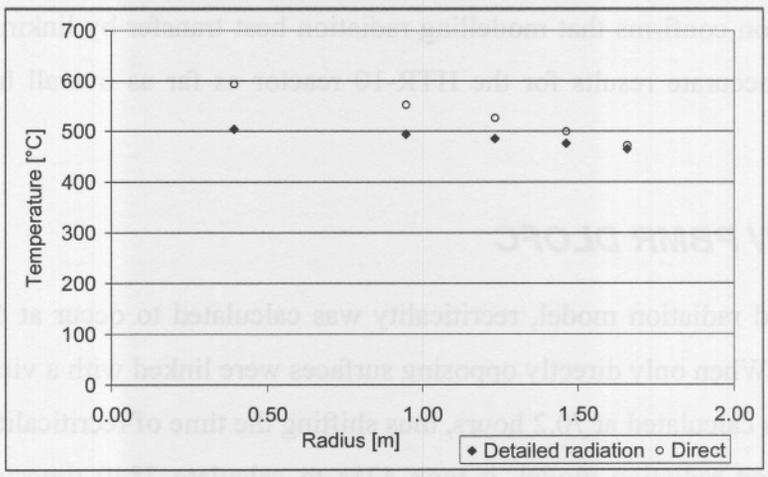


Figure 21. Surface temperatures around the cavity above the pebble bed at the time of recriticality, the zone where there were the greatest difference between the detailed and direct radiation models. 268MW PBMR.

Only temperatures around voids such as the outlet plenum and the plenum above the core are changed when a detailed radiation model is used, as shown in Figure 21. However, the detail design of components around these voids is clarified with CFD and for the PBMR, this temperature differences have negligible impact on the radial heat loss from the core as shown by the recriticality tests.

9. Reduction of element number

Connecting the surfaces around a cavity creates a vast number of elements of which only a relatively small number have any significant contribution to heat transfer. By simply omitting elements with an *AF* below a certain value, the number of elements can be drastically reduced without necessarily losing accuracy. To test how a reduction in radiation element number affects heat transfer and temperature profiles, a very simple geometry was set up to resemble a reactor pressure vessel surface surrounded by a RCCS as shown in Figure 22.

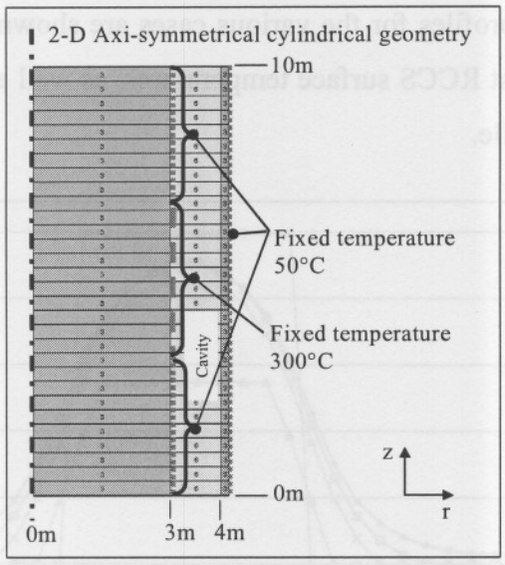


Figure 22. Domain used for testing the effect of spatial radiation elements on temperature profile.

As seen in Figure 22, a 300°C block temperature profile is specified on the RPV outer wall. All other temperature boundary values were fixed at 50°C. A 40mm steel wall was specified for the RCCS in order to observe a well-defined temperature profile on the surface facing the RPV.

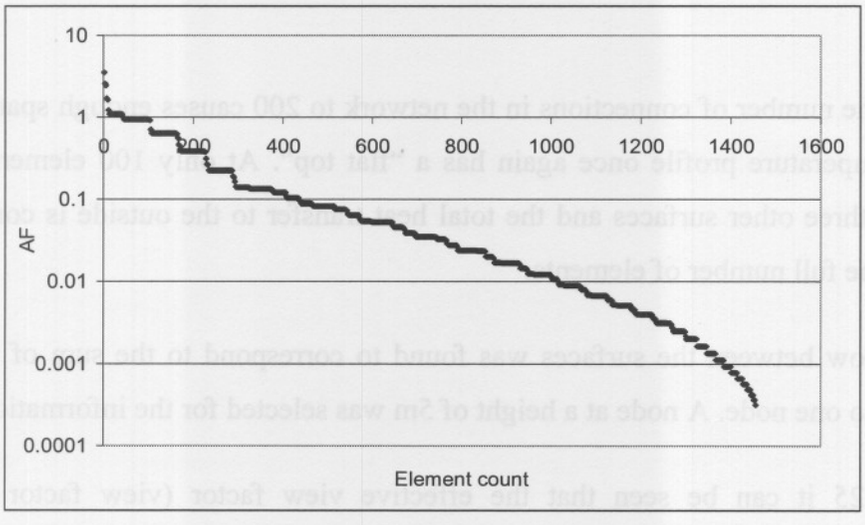


Figure 23. Area/view factor distribution of spatial elements for the domain in *Figure 22.*

The radiation spatial element transfer coefficients for this case is shown in Figure 23 in descending order. To test the effect of the number of elements used, the lower limit on *AF* (referring to Eq.(3)) was set to 0, 0.01, 0.38 (200 elements) and 0.94 (100 elements) as well as connecting directly opposing surfaces with a view factor of one.

The surface temperature profiles for the various cases are shown in Figure 24, with the direct coupling giving the highest RCCS surface temperatures, as well as retaining the exact shape of the RPV temperature profile.

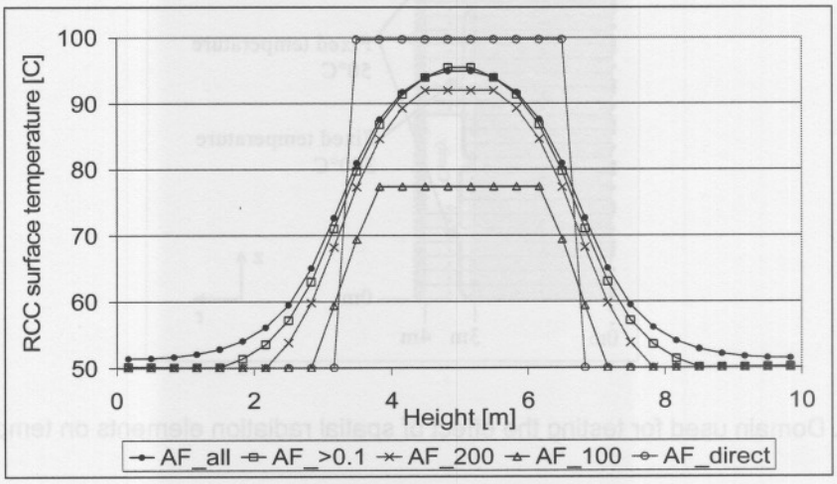


Figure 24. RCCS surface temperature distributions for various sets of radiation spatial elements.

For the full number of radiation elements, the temperature block profile is smoothed out on the RCCS surface. Using only elements with AF>0.1 have minimal impact on temperatures directly across the raised temperature, while temperatures away from the central part are markedly lower.

Reducing the number of connections in the network to 200 causes enough spatial detail loss so that the temperature profile once again has a "flat top". At only 100 elements, each surface faces only three other surfaces and the total heat transfer to the outside is considerably lower than with the full number of elements.

The heat flow between the surfaces was found to correspond to the sum of the view factors connected to one node. A node at a height of 5m was selected for the information in Figure 25.

In Figure 25 it can be seen that the effective view factor (view factor sum) decreases considerably with a decrease in radiation spatial elements, except when linking directly opposing surfaces with a view factor of 1.

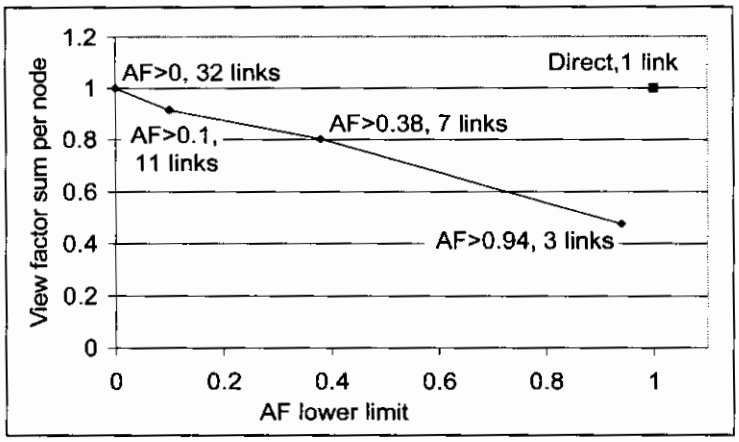


Figure 25. The view factor sum, as well as the count of radiation spatial elements connected to one radiation surface node at a height of 5m in the geometry of *Figure 22*.

10. Conclusion

This paper presented an investigation into the calculation of radiation heat transfer in systems simulation models of high temperature gas-cooled reactors. The complete set of equations for calculating the view factors of a detailed radiation heat transfer model were also presented.

The simplest, and most widely-used method is to couple only directly opposing surfaces with a view factor of one. The second option is using a full detailed radiation model and the third option is to delete radiation connections of which the view factors are smaller than a certain cutoff value.

Regarding deletion of elements, it was found that the total heat transfer between two surfaces is directly dependent on the view factor sum at each node, i.e. ensure that the view factor sum at a node always equal one.

The sophistication of the radiation heat transfer model had a negligible effect on the overall heat removal from the HTR-10 reactor as well as the 268MW PBMR reactor. The PBMR DLOFC case took 30 percent longer to solve using a detailed radiation model.

It is also concluded that when overall heat loss from an integrated system is considered, good accuracy can be obtained when linking only directly opposing surfaces with a view factor of one. However, when local component temperatures are important, as could be the case with metal components above or below the core, a detailed radiation heat transfer model is considered essential, but then, that level of detail falls within the scope of CFD calculations.

For system simulation codes that focus on transient response of a plant, it is not considered worthwhile to use a detailed radiation model, as the gain in accuracy does not justify the increased solution time or the implementation and verification effort.

11. Acknowledgments

The authors wish to thank PBMR (Pty) Ltd., as well as the THRIP programme of the National Research Foundation of South Africa whose financial support made this work possible, as well as M-Tech Industrial (Pty) Ltd., suppliers of the Flownex systems simulation software.

12. References

Brockmann, H. (1994) Analytic angle factors for the radiant interchange among the surface elements of two concentric cylinders. Int. J. Heat Mass Transfer. Vol.37, No. 7. pp1095-1100.

Greyvenstein, G.P., Van Antwerpen, H.J., Rousseau P.G. (2004) The system CFD approach applied to a pebble bed reactor core. International Journal of Nuclear Energy Science and Technology. Inaugural Issue, Vol.1 No.1. 2004.

Howell, J. R., (2001) A Catalog of Radiation Heat Transfer Configuration Factors, 2nd edition. Department Of Mechanical Engineering, The University Of Texas At Austin. Available online at http://www.me.utexas.edu/~howell/

IAEA (2006) CRP-5 Tecdoc. http://www.iaea.org/inis/aws/htgr/abstracts/

Reitsma, F., Strydom, G., De Haas, H., Ivanov, K., Tyobeka, B., Mpahlele, R., Downar, T., Seker, V., Gougar, H.D., Da Cruz. (2004) The PBMR Steady-state and Coupled Kinetics Core Thermal-hydraulic Benchmark Test Problems. HTR-2004, Beijing, China, 2004.

Appendix E:
Additional Radiation View Factor Derivations And Implementation

E.1 Implementation

The most convenient way to make the view factor calculations robust is by adding small values or doing simple tests in the basic view factor functions. For view factor $\overline{F1}$ very small values are added to r_1 and to H. For all the other basic view factors some input values are tested for zero inputs. Before calling even the derived view factor functions it is also necessary to test whether surfaces actually face each other, but this would only be necessary for cavities with complex shapes. Possible layouts for the functions are presented below.

```
function F1(rc, r1, h)
{
      r1+=0.00000000001
      R=rc/r1
      H=h/r1+0.00000000001
      calculate F1
}

function F2(rc, r1, r2, h)
{
      if ((h equals 0) or (rc equals r1))
      {
      return 0
      }
      else
      {
            calculate F2
            return F2
      }
}

function F3(rc, r2, xb, h)
{
      if ((h equals 0) or (r2 equals rc) or (r1 equals rc))
      {
            return 0
      }
      else
      {
            calculate F3
            return F3
      }
```

```
}

function F4(rc, r1 , h)
{
      if (h equals 0)
      {
            return 0
      }
      else
      {
            calculate F4
            return F4
      }
}
```

Considerable bookkeeping is necessary to connect all the surfaces participating in radiation heat exchange across a cavity. The approach used for this bookkeeping is highly dependent upon the programming strategy followed in the rest of the code and is therefore not covered in this report.

E.2 Additional derivations: discretised surfaces

The following rules apply to view factors between two surfaces A_1 and A_2. The first is the so-called reciprocity rule, expressed mathematically as:

$$A_1 F_{12} = A_2 F_{21} \tag{E.1}$$

From the definition of view factor, it follows that for a surface that is enclosed by and faced by n other surfaces, the sum of the view factors equals unity:

$$\sum_{i=1}^{n} F_{1i} = 1 \tag{E.2}$$

The summing rule for view factors also follow from the definition and it states that if A_2 is subdivided into non-overlapping surfaces A_3 and A_4, the following holds:

$$F_{12} = F_{13} + F_{14} \tag{E.3}$$

With the above identities, the necessary view factors are derived from the four basic formulae.

E.2.1 Derived view factor 1

From the fact that the sum of view factors equal unity for a surface it can be stated that for coaxial cylindrical surfaces 1 and 2 in Figure E.1, the view factors to the top and bottom cavity ends have to be deducted to find the view factor.

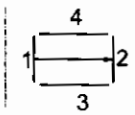


Figure E.1. Geometry for derived view factor 1

From Eq.(E.2):

$$1 = F_{12} + F_{13} + F_{14} \tag{E.4}$$

But $F_{13} = F_{14}$ and both can be calculated with $\overline{F1}$ so that the derived view factor formula follows directly:

$$F_{12} = 1 - 2\overline{F1} \tag{E.5}$$

E.2.2 Derived view factor 2

Derived view factor 2 is an extension of view factor $\overline{F1}$. The notation is different from derived view factors 3,4 and 5 because the view factor is found by an indirect method. It is done by calculating the view factor to an opposing surface as the difference between two other view factors. The process is illustrated in Figure E.2, where surfaces 1 and 2 are of interest, while surfaces 3 to 9 are only used in the derivation of the view factor.

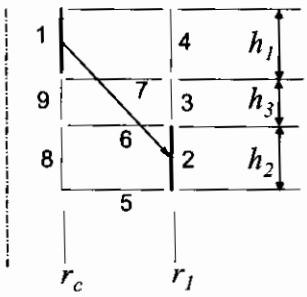


Figure E.2. Geometry for derived view factor 2 with extra surfaces for derivation.

For the geometry in Figure E.2, it follows from the summing rule (Eq.(E.3)) that:

$$F_{12} = F_{16} - F_{15} \tag{E.6}$$

Multiply throughout by A_1 and apply the reciprocity rule to change the right-hand terms:

$$\begin{aligned} A_1F_{12} &= A_1F_{16} - A_1F_{15} \\ &= A_6F_{61} - A_5F_{51} \end{aligned} \tag{E.7}$$

It also holds that

$$F_{6,9+1} = F_{61} + F_{69} \tag{E.8}$$

$$F_{5,1+8+9} = F_{51} + F_{5,8+9}$$

Rearrange and apply the reciprocity rule to the above equations to obtain:

$$A_6F_{61} = A_{9+1}F_{9+1,6} - A_9F_{96} \tag{E.9}$$

$$A_5F_{51} = A_{1+8+9}F_{1+8+9,5} - A_{8+9}F_{8+9,5} \tag{E.10}$$

Substitute Eqs.(E.9) and (E.10) into Eq.(E.7) to obtain:

$$A_1F_{12} = A_{9+1}F_{9+1,6} - A_9F_{96} - A_{1+8+9}F_{1+8+9,5} + A_{8+9}F_{8+9,5} \tag{E.11}$$

All areas in Eq.(E.11) are calculated at the same radius so that only the height remains after division by πr_c. All the view factors on the right-hand side of Eq.(E.11) are calculated with the basic view factor $\overline{F1}$, thus using the same radius so that the following can be stated:

$$F_{12} = \frac{h_1 + h_3}{l}\overline{F1}_{h_1+h_3} - \frac{h_3}{l}\overline{F1}_{h_3} - \frac{h_1 + h_2 + h_3}{l}\overline{F1}_{h_1+h_2+h_3} + \frac{h_2 + h_3}{l}\overline{F1}_{h_1+h_3} \tag{E.12}$$

Rearrangement of the terms gives the equation for derived view factor 2.

E.2.3 Derived view factors 3 to 5

Derived view factors three to five follow the same derivation method, as they have a common zero point each time the basic view factor formula is evaluated. The geometry

for derived view factor three will be used (Cylinder outer surface to a flat annular ring around the base of the cylinder) as shown in Figure E.3.

The approach that will be followed is to write an expression in which all terms on the right-hand side can be calculated with existing view factor formulae. In this case it would be F_{56}, F_{36}, F_{54} and F_{34}. From the summing rule it follows that:

$$F_{12} = F_{14} - F_{16}$$

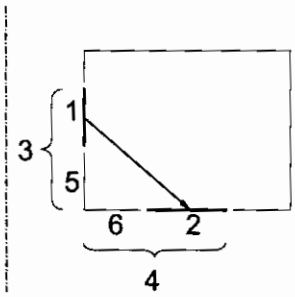


Figure E.3. Geometry for derived view factor 3.

Multiply throughout by A_1 and apply the reciprocity rule to change the right-hand terms:

$$\begin{aligned} A_1F_{12} &= A_1F_{14} - A_1F_{16} \\ &= A_4F_{41} - A_6F_{61} \end{aligned} \tag{E.13}$$

It also holds that

$$F_{43} = F_{41} + F_{45}$$

and

$$F_{63} = F_{61} + F_{65}$$

The above equations are rewritten and the reciprocity rule applied to obtain view factors that can be calculated with the basic formula.

$$A_4F_{41} = A_3F_{34} - A_5F_{54} \tag{E.14}$$

and

$$A_6F_{61} = A_3F_{36} - A_5F_{56} \tag{E.15}$$

Substitute Eqs.(E.14) and (E.15) into Eq.(E.13) to obtain:

$$\begin{aligned} A_1F_{12} &= A_3F_{34} - A_5F_{54} - A_3F_{36} + A_5F_{56} \\ &= A_3\left(F_{34} - F_{36}\right) - A_5\left(F_{54} - F_{56}\right) \end{aligned} \tag{E.16}$$

Rearrangement gives:

$$F_{12} = \frac{A_3}{A_1}\left(F_{34} - F_{36}\right) - \frac{A_5}{A_1}\left(F_{54} - F_{56}\right) \tag{E.17}$$

F_{56}, F_{36}, F_{54} and F_{34} are then calculated with the appropriate basic view factor formulae given in Appendix D.

E.2.4 Derived view factor 6

For derived view factor 6, the view factor for two adjacent surfaces is derived first, according to the geometry in Figure E.4.

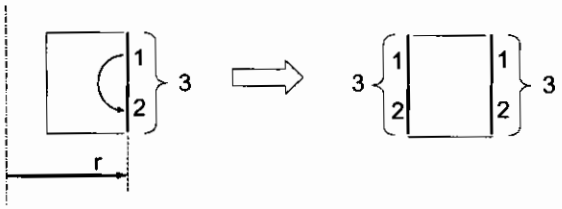


Figure E.4. Conceptual geometry for the first part derivation of derived view factor 6

The following can be stated that for the geometry in Figure E.4:

$$A_3F_{33} = A_3F_{31} + A_3F_{32} \tag{E.18}$$

Both right-hand terms can be rewritten in terms of the parts of their reciprocals:

$$A_3F_{33} = A_1\left(F_{11} + F_{12}\right) + A_2\left(F_{21} + F_{22}\right) \tag{E.19}$$

As $A_1F_{12} = A_2F_{21}$, Eq.(E.19) can be rewritten as:

$$A_3F_{33} - A_1F_{11} - A_2F_{22} = 2A_1F_{12}$$

$$F_{12} = \frac{A_3}{2A_1} F_{33} - \frac{A_2}{2A_1} F_{22} - \frac{1}{2} F_{11} \tag{E.20}$$

As all the areas in Eq.(35)(E.20) are calculated at the same radius, only the height remains after division by πr. All the right-hand view factors in Eq.(35) can be calculated with basic view factor $\overline{F4}$.

$$F_{12} = \frac{h_3}{2h_1} \overline{F4}_{h_3} - \frac{h_2}{2h_1} \overline{F4}_{h_2} - \frac{1}{2} \overline{F4}_{h_1} \tag{E.21}$$

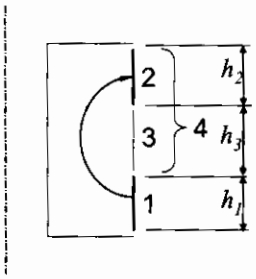


Figure E.5. Geometry for the second part derivation of derived view factor 6.

For the geometry in Figure E.5, the following holds:

$$F_{14} = F_{12} + F_{13}$$

$$\text{i.e:} \qquad F_{12} = F_{14} - F_{13} \tag{E.22}$$

The right-hand terms of Eq.(E.22) can be calculated with Eq.(E.20):

$$F_{14} = \frac{h_1 + h_4}{2h_1} \overline{F4}_{h_1+h_4} - \frac{h_4}{2h_1} \overline{F4}_{h_4} - \frac{1}{2} \overline{F4}_{h_1} \tag{E.23}$$

F_{14} can be expanded further to:

$$F_{14} = \frac{h_1 + h_2 + h_3}{2h_1} \overline{F4}_{h_1+h_2+h_3} - \frac{h_2 + h_3}{2h_1} \overline{F4}_{h_2+h_3} - \frac{1}{2} \overline{F4}_{h_1} \tag{E.24}$$

$$F_{13} = \frac{h_1 + h_3}{2h_1} \overline{F4}_{h_1+h_3} - \frac{h_3}{2h_1} \overline{F4}_{h_3} - \frac{1}{2} \overline{F4}_{h_1} \tag{E.25}$$

Substituting Eqs.(E.24) and (E.25) into Eq.(E.22) gives the formula presented for

derived view factor 6

$$
\begin{aligned}
F_{12} &= \frac{h_1+h_2+h_3}{2h_1}\overline{F4}_{h_1+h_2+h_3} - \frac{h_2+h_3}{2h_1}\overline{F4}_{h_2+h_3} - \frac{1}{2}\overline{F4}_{h_1} \\
&\quad -\left(\frac{h_1+h_3}{2h_1}\overline{F4}_{h_1+h_3} - \frac{h_3}{2h_1}\overline{F4}_{h_3} - \frac{1}{2}\overline{F4}_{h_1}\right) \\
&= \frac{h_1+h_2+h_3}{2h_1}\overline{F4}_{h_1+h_2+h_3} - \frac{h_2+h_3}{2h_1}\overline{F4}_{h_2+h_3} - \frac{h_1+h_3}{2h_1}\overline{F4}_{h_1+h_3} + \frac{h_3}{2h_1}\overline{F4}_{h_3}
\end{aligned}
\tag{E.26}
$$

Rearrangement of the terms gives the formula for derived view factor 6.

Appendix F:

Sphere Discretisation Schemes

Abstract

In this document, pebble bed HTR fuel sphere discretisation schemes are investigated for use in CFD and network-type calculation models.

An existing discretisation scheme is investigated and compared with analytical solutions to point out advantages and deficiencies. Discretisation of temperature-dependent conductivity is also investigated. Two new discretisation schemes are presented that calculates steady-state maximum and average temperatures with no grid dependence and a minimum number of nodes.

Transient average temperature grid dependence is studied for an existing scheme as well as the two new schemes. Two possible dynamic simulations are used for the investigation. The effect of surface layer subdivision, as well as that of sphere internal subdivision is investigated. The effect of surface discretisation on gas temperature response is also tested. It is attempted to cover most aspects of sphere discretisation.

F.1 Abbreviations and acronyms

AS	Analytical Sphere
CFD	Computational Fluid Dynamics
HTR	High Temperature Reactor, generally used for a gas-cooled high temperature nuclear reactor
N	Numerical
PBMR	Pebble Bed Modular Reactor
SV	Staggered Volume

F.2 Nomenclature

English Variables	*Units*	
a		Substitution variable for integration
A	m^2	Conduction area

b		Substitution variable for integration
c	J/kgK	Specific heat or correlation constant
F	m	Conduction form factor
k	W/mK	Conductivity
l	m	Control volume length
m		Number of control volumes in the surface shell
n		Number of control volumes in the heat generating zone
Q	W	Heat flow
q'''	W/m^3	Volumetric heat generation
R	m	Sphere fuel region outer radius, typically 25mm
r	m	Radius
r^*	m	Position where local temperature equals volumetric average temperature
r_s	m	Radius of division between nodes to obtain a correct average temperature from adjacent nodes
r_E	m	Element radius
r_N	m	Node radius
r_q	m	Heat generation control volume boundary radius
R_{sh}	m	Surface shell outer radius
r_v	m	Thermal mass control volume boundary radius
t	s	Time
T	K or °C	Temperature
T^*	K or °C	Volumetric average temperature
T_s	K or °C	Surface temperature
V	m^3	Volume

Greek Variables		
ε		Pebble bed porosity
ρ	kg/m^3	Density

Graph series legends

SV*n*3*m*10: SV: Staggered Volume scheme or N: Numerical scheme;

Number of control volumes *n* in the heat generating zone equals 3;

Number of control volumes *m* in the surface shell equals 10.

F.3 Introduction

In general, the steady-state maximum fuel temperature is the most important parameter that the sphere model in a pebble bed reactor calculation has to calculate, but an accurate average material temperature is also critical for a nuclear reactor as it directly determines the reactivity values used in neutronics calculations. Added to this, the average fuel temperature is a measure of the stored energy in the reactor, and thus the initial conditions to a transient event. This brings up the topic of transient response, which is also highly grid dependent. Therefore, apart from maximum fuel temperature, other parameters such as transient response and average temperature should also be considered when evaluating discretisation schemes.

The most obvious accuracy improvement by means of grid refinement is not necessarily the best, as it comes at great calculation cost. Therefore this document presents research into optimal discretisation schemes for calculating HTR fuel spheres with systems simulation or CFD codes. These schemes are specifically derived to have steady-state analytical accuracy for maximum and average temperatures while being very simple and fast.

F.4 Previous work

Verfondern (1983) described the sphere temperature calculation method used in the simulation code THERMIX. The sphere surface temperature is calculated from the gas temperature and the surface heat transfer coefficient. The sphere itself is divided into ten radial layers and starting from the surface temperature, the inner temperature of each layer is calculated from its outer temperature. The inner temperature of one layer is the outer temperature of the next layer, up to the innermost temperature which is also the maximum temperature. The calculational procedure for transients was not described.

Verkerk (2000) used analytical formulae with constant conductivity to calculate the maximum and average fuel temperatures.

At the time of writing, the PBMR CFD group uses a fuel sphere discretisation in which the graphite shell as well as the internal fuel zone is divided into five layers, giving a total of ten layers per sphere (Viljoen,2004; Hoffmann,2003).

It appears that for all of the existing discretisations the maximum steady-state fuel temperature was used as the most important measure of accuracy and therefore also the prime measure of grid dependency.

F.5 Theory

The first simplifying assumption to create a useful sphere model is spherical symmetry, whereby temperature is only a function of radial position in the sphere. For this situation with heat generation, the transient equation for conservation of energy is given by:

$$\rho c \frac{\partial T}{\partial t} = \frac{1}{r^2}\frac{\partial}{\partial r}\left(kr^2 \frac{\partial T}{\partial r}\right) + q''' \tag{F.1}$$

Temperature and position independent density, ρ and heat capacity, c are assumed. For steady-state Eq.(F.1) simplifies to the following:

$$0 = \frac{1}{r^2}\frac{d}{dr}\left(kr^2 \frac{dT}{dr}\right) + q''' \tag{F.2}$$

For constant conductivity and the center boundary condition of zero temperature gradient, i.e. $\left.\frac{dT}{dr} = 0\right|_{r=0}$, integration of Eq.(F.2) leads to the following expression for the temperature profile in a solid sphere with radius R:

$$T(r) = \frac{q'''}{6k}\left(R^2 - r^2\right) + T_s \tag{F.3}$$

F.6 Geometry

In a typical discrete approach, the conducting elements are treated as passive with all heat generation placed at nodes. For such conducting elements, it is appropriate to apply Fourier's law in the following form:

$$q = -kA\frac{dT}{dr} \tag{F.4}$$

For a spherical shell, $A = 4\pi r^2$ so that with constant conductivity, integration of Eq.(F.4) results in the following:

$$q = \frac{4\pi k}{\frac{1}{r_1} - \frac{1}{r_2}} \times \left(T_1 - T_2\right)$$

This also presents us with the general integrated form of Fourier's law, in which the effect of geometry is represented by the form factor F:

$$q = kF\left(T_1 - T_2\right) \tag{F.5}$$

The analytical form factor for a spherical shell is thus given by:

$$\begin{aligned} F &= \frac{4\pi}{\frac{1}{r_1} - \frac{1}{r_2}} \\ &= \frac{4\pi r_2 r_1}{r_2 - r_1} \end{aligned} \tag{F.6}$$

From the above result it can be seen why the following numerical approximation F_N could be accurate:

$$\begin{aligned} F_N &= \frac{4\pi \times r_{ave}^2}{\delta r} \\ &= \frac{4\pi \times \left(\frac{r_2 + r_1}{2}\right)^2}{r_2 - r_1} \end{aligned} \tag{F.7}$$

With F_N indicating the numerical approximation for the shape factor.

F.6.1 Average temperature location in a spherical shell without heat generation

For creating a discretisation that accurately calculates the average temperature, it will be useful to know the relation between node position and average temperatures. Therefore, this paragraph presents a derivation for the location of the point where the local temperature equals the average temperature in a spherical shell without heat generation. With that in mind, consider the spherical shell in Figure F.8.3:

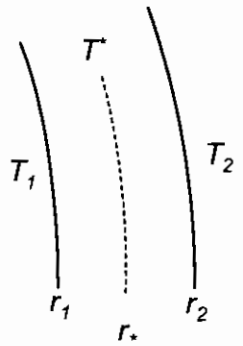


Figure F.8.3. A spherical shell without heat generation. T^* is the average temperature of the shell, located at r^*

At a location r^* between r_1 and r_2 the average temperature T^* is found. It is defined as:

$$T^*(r^*) = \frac{\int_{r_1}^{r_2} T(r) 4\pi r^2 dr}{\frac{4}{3}\pi\left(r_2^3 - r_1^3\right)} \tag{F.8}$$

The temperature profile for a spherical shell without heat generation is given by: (Incropera and DeWitt, 1996)

$$T(r) = T_2 - (T_2 - T_1)\left[\frac{\frac{1}{r} - \frac{1}{r_2}}{\frac{1}{r_1} - \frac{1}{r_2}}\right] \tag{F.9}$$

By defining the following constants in terms of the boundary values, the integration is simplified considerably,

$$a = T_2 + (T_2 - T_1)\left[\frac{\frac{1}{r_2}}{\frac{1}{r_1} - \frac{1}{r_2}}\right]$$
$$b = \frac{(T_2 - T_1)}{\frac{1}{r_1} - \frac{1}{r_2}} \tag{F.10}$$

to obtain the following equation:

$$T(r) = a - \frac{b}{r} \tag{F.11}$$

Substituting the above in the integral gives:

$$T^* = \frac{3}{\left(r_2^3 - r_1^3\right)} \int_{r_1}^{r_2} \left(ar^2 - br\right) dr$$
$$\therefore T^* = a - \frac{3b\left(r_2^2 - r_1^2\right)}{2\left(r_2^3 - r_1^3\right)} \tag{F.12}$$

Equating the above result to the temperature profile formula (F.11) gives an equation solvable for r^*:

$$a - \frac{3b\left(r_2^2 - r_1^2\right)}{2\left(r_2^3 - r_1^3\right)} = a - \frac{b}{r^*} \tag{F.13}$$

Rewriting (F.13) gives

$$r^* = \frac{2\left(r_2^3 - r_1^3\right)}{3\left(r_2^2 - r_1^2\right)} \tag{F.14}$$

Thus, if a node is placed at a radius r^* in a spherical shell of a solid sphere with uniform heat generation, its temperature would equal the average temperature of that shell. This is shown in the left of Figure F.8.4.

F.6.2 Spherical shell in two half control volumes without heat generation

The approach described in the previous paragraph is applicable inside a fuel sphere, but at the surface of a fuel sphere there also has to be a node to communicate with the surrounding fluid and the rest of the pebble bed. Thus, another approach is needed to accurately calculate the average temperature T^* at the surface. Therefore, the volume associated with the nodes at the inner and outer ends of the shell, i.e. V_1 and V_2, can be determined such that the overall average temperature is accurate.

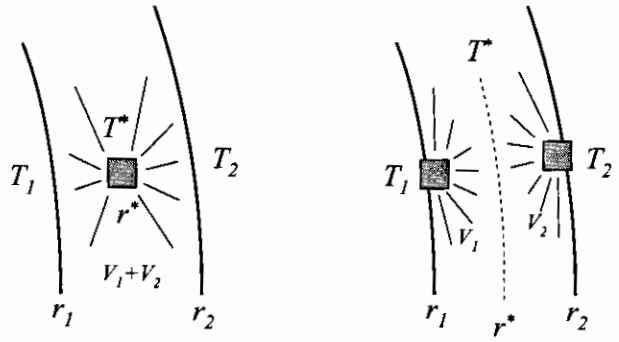


Figure F.8.4. Left: possible sphere internal node placement, right: node placement required at a surface.

In the case of two nodes at the ends of a spherical shell as shown in Figure F.8.4 on the right, the average temperature can be calculated analytically correct by specifying the radius which divides the inner and outer control volumes. In other words, the radius r_s has to be found for which the following equation holds:

$$V_1 T_1 + V_2 T_2 = (V_1 + V_2) T^* \tag{F.15}$$

with V_1 and V_2 being the respective volumes of nodes 1 and 2 in Figure F.8.4. Expanding Eq.(F.15) and dividing by $\frac{4}{3}\pi$ gives:

$$(r_s^3 - r_1^3) T_1 + (r_2^3 - r_s^3) T_2 = (r_2^3 - r_1^3) T^* \tag{F.16}$$

An expression for T^* in terms of r_1 and r_2 is now required. This can be obtained by substituting the formula for r^* into the temperature profile equation for a spherical shell without heat generation:

$$r^* = \frac{2\left(r_2^3 - r_1^3\right)}{3\left(r_2^2 - r_1^2\right)}$$
$$\therefore \frac{1}{r^*} = \frac{3(r_2 - r_1)(r_2 + r_1)}{2\left(r_2^3 - r_1^3\right)} \tag{F.17}$$

In the temperature profile equation:

$$T^* = T_2 - (T_2 - T_1)\left[\frac{\frac{1}{r^*} - \frac{1}{r_2}}{\frac{1}{r_1} - \frac{1}{r_2}}\right] \tag{F.18}$$

$$T^* = T_2 - (T_2 - T_1)\left[\frac{\frac{3(r_2 - r_1)(r_2 + r_1)}{2\left(r_2^3 - r_1^3\right)} - \frac{1}{r_2}}{\frac{r_2 - r_1}{r_2 r_1}}\right] \tag{F.19}$$
$$= T_2 - (T_2 - T_1)\left[\frac{3(r_2 + r_1)r_2 r_1}{2\left(r_2^3 - r_1^3\right)} - \frac{r_2 r_1}{r_2 - r_1}\right]$$

Substituting the above result for T^* into (F.16) and rearranging gives:

$$r_s^3 = r_1^3 + \frac{3}{2}(r_2 + r_1)r_2 r_1 - \frac{r_1\left(r_2^3 - r_1^3\right)}{r_2 - r_1} \tag{F.20}$$

Thus, the average temperature of a spherical layer between two nodes at r_1 and r_2 will be calculated analytically correct if the layer volume between the two nodes is divided at r_s.

F.7 Sphere discretisations

These paragraphs describe three sphere discretisation schemes, namely the newly developed Analytical Sphere scheme, the existing Numerical scheme and the newly developed Staggered Volume scheme.

The existing Numerical scheme is used in this study as reference to evaluate the two newly developed sphere discretisation schemes. The Analytical Sphere scheme can not be subdivided, so that its accuracy is not grid dependent, while the accuracy of the Numerical and the Staggered Grid schemes can be increased by refining the grid.

Therefore, the Numerical and Staggered Grid schemes will be described under the heading F.8 Subdivided sphere discretisation schemes.

F.7.1 Analytical sphere scheme: Form factors for a uniformly heated solid sphere

The first component of the Analytical Sphere scheme is the central heat-generating part which can be treated as a uniformly heated solid sphere for which the constant conductivity temperature equation states that

$$T(r) = \frac{q'''}{6k}\left(R^2 - r^2\right) + T_s$$

with R being the sphere outer radius, r the radial location in the sphere, k the conductivity and T_s the sphere surface temperature. The maximum temperature would be at the sphere center, i.e. where r=0:

$$T_{\max} = \frac{q'''R^2}{6k} + T_s \tag{F.21}$$

The average temperature of the sphere can thus be found from the following integration:

$$\begin{aligned} T_{ave} &= \frac{\int_0^R \left(\frac{q'''}{6k}\left(R^2 - r^2\right) + T_s\right) 4\pi r^2 dr}{\frac{4}{3}\pi R^3} \\ &= \frac{q'''R^2}{15k} + T_s \end{aligned} \tag{F.22}$$

The volumetric heat rate in the above equations can be substituted as follows with the total heat transfer and volume as follows:

$$q''' = \frac{Q}{\frac{4}{3}\pi R^3}$$

The maximum and average temperature equations can thus be rewritten in the following forms:

$$T_{\max} = T_s + \frac{Q}{8\pi Rk} \tag{F.23}$$

$$T_{ave} = T_s + \frac{Q}{20\pi Rk} \tag{F.24}$$

Eqs.(F.23) and (F.24) are rewritten in the form of Fourier`s law:

$$Q = k8\pi R\left(T_{\max} - T_s\right) \tag{F.25}$$

$$Q = k20\pi R\left(T_{ave} - T_s\right) \tag{F.26}$$

In the context of the network approach, the following network can thus be used to directly calculate the maximum temperature. The sphere total heat generation is the input at the left node, while the sphere conduction form factor equals $8\pi R$.

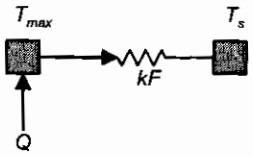


Figure F.8.5. A simple calculational setup for maximum temperature in a sphere with heat generation.

Similarly, the average fuel temperature can also be calculated directly. The two can even be combined so that in one network, the maximum and average temperatures are calculated analytically correct in a numerical solution. The total length of the heat path should have a resistance of $1/(k8\pi R)$, while the heat resistance from the surface to the average sphere temperature node should be $1/(k20\pi R)$. To obtain this, a resistance of $1/\left(k\frac{40}{3}\pi R\right)$ is added between the maximum and average temperature nodes, as shown in Figure F.8.6. When the T_{ave}-node is given the total mass of the sphere, the steady-state stored energy is also calculated analytically correct.

The method described above does have some limitations, of which the most obvious are constant conductivity and the lumped mass at the T_{ave}-node. The lumped mass could decrease transient response accuracy.

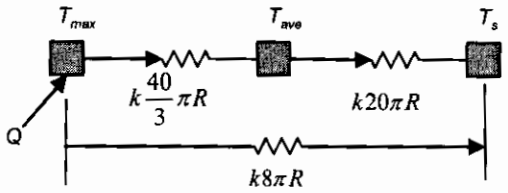


Figure F.8.6. A sphere model that provides maximum and average temperatures analytically in the context of the network approach.

F.7.2 Analytical Sphere scheme: Surface layer discretisation

For the outer graphite shell of the fuel sphere, the method presented in Paragraph F.6.2 can be used. If transient response accuracy requires it, the surface layer can be subdivided by placing such shells successively as shown in Figure F.8.7. Equation (F.20) will have the following form for such a subdivided shell:

$$r_{vi}^3 = r_{i-1}^3 + \frac{3}{2}(r_i + r_{i-1})r_i r_{i-1} - \frac{r_{i-1}\left(r_i^3 - r_{i-1}^3\right)}{r_i - r_{i-1}} \qquad \text{(F.27)}$$

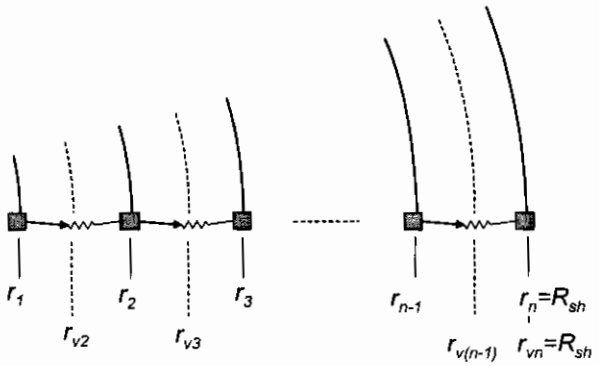


Figure F.8.7. Successive sphere shells without heat generation, if transient simulation accuracy requires it.

F.7.3 Assembly of the Analytical Sphere model

By linking the simple sphere model presented in Paragraph F.7.1 to the surface layer model in Paragraph F.7.2, a complete PBMR fuel sphere can be modelled with analytically correct results for at least steady-state and constant conductivity. The resulting model has the layout shown in Figure F.8.7. It will be shown with the grid dependence studies that one surface layer gives grid independent results, so that the Analytical Sphere scheme uses only four nodes to represent a fuel sphere.

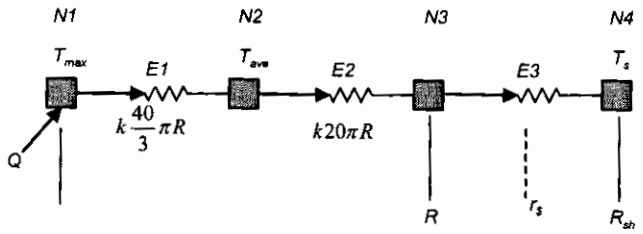


Figure F.8.8. Network layout for a simple analytical fuel sphere model.

The volumes of the nodes are calculated as follows:

$$V_1 = 0$$

$$V_2 = \frac{4}{3}\pi R^3$$

$$V_3 = \frac{4}{3}\pi\left(r_s^3 - R^3\right)$$

$$V_4 = \frac{4}{3}\pi\left(R_{sh}^3 - r_s^3\right)$$

The conduction shape factors for the elements are:

$$F_1 = \frac{40}{3}\pi R$$

$$F_2 = 20\pi R$$

$$F_3 = \frac{4\pi}{\frac{1}{R} - \frac{1}{R_{sh}}}$$

The total heat generation in the sphere is entered at Node 1.

The only error introduced in this sphere model is the discrete handling of conductivity, for which one of the schemes in Paragraph 4.8.2 has to be used.

F.8 Subdivided sphere discretisation schemes

Two subdivided sphere discretisation methods are presented in this paragraph. The first is an industry-standard numerical scheme, while the second is the newly developed scheme "Staggered Volume" scheme. The Numerical scheme is used as benchmark in

this study, in order to have a reference for evaluating the newly developed Analytical Sphere and Staggered Volume schemes.

F.8.1 An existing Numerical scheme

In the Numerical sphere discretisation scheme, denoted by N, the sphere is divided into equally spaced radial control volumes, starting from the centre. Node volumes are calculated from:

$$V_i = \frac{4}{3}\pi\left(r_{Ei}^3 - r_{E(i-1)}^3\right) \qquad i = 0 \text{ to } n \qquad \text{(F.28)}$$

with

$$r_{Ei} = \frac{r_{Ni} + r_{Ni-1}}{2}$$

The node heat sources are calculated from:

$$Q_i = \frac{V_i}{V_{sphere}} Q_{sphere} \qquad i = 0 \text{ to } n \qquad \text{(F.29)}$$

Following Equation (F.7), the conduction element form factor is:

$$F_i = \frac{4\pi r_{Ei}^2}{r_{Ni} - r_{N(i-1)}} \qquad i = 1 \text{ to } n \qquad \text{(F.30)}$$

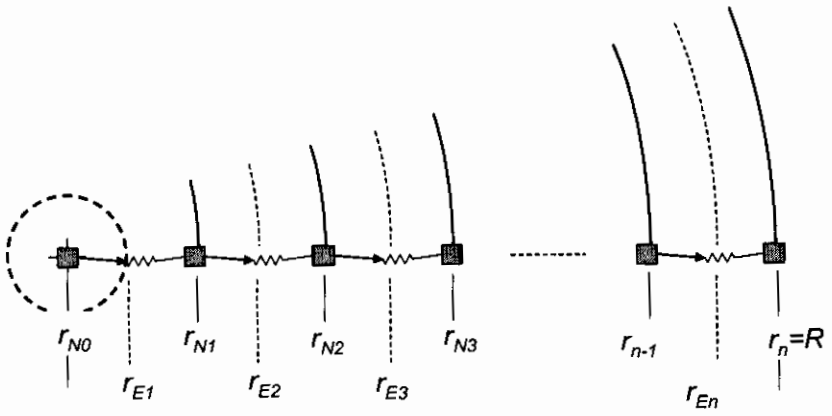


Figure F.8.9. Node and element placement for the Numerical discretisation scheme.

F.8.2 The Staggered Volume discretisation

The development of this scheme started with the correct calculation of stored thermal energy in mind. Therefore a formula was derived to find the location of the correct representative temperature for a control volume (Eq.(F.14) in Paragraph F.6.1). The maximum temperature was calculated completely grid-independent while using the location and form factors for a spherical shell without heat generation. Stored thermal energy was however greatly overestimated. This was corrected by finding the correct volume for a certain temperature, instead of finding the correct average temperature for a volume. An empirical formula for this correction is presented. The name "staggered volume" is derived from this fact that the heat generation control volumes does not coincide with the node mass control volumes. Keep in mind that this discretisation can not span heat-generating and passive zones simultaneously and still produce accurate results.

The Staggered Volume discretisation is done as follows.

1. Firstly, the fuel part of the sphere is divided into equally spaced radial control volumes for calculation of heat generation. The boundaries of the heat generation control volumes are indicated by r_{qi} in Figure F.8.10. The outermost node is an exception; it should have the smallest possible heat generation and volume, as its location at a boundary introduces an error into the average temperature calculation.
2. Temperature node positions are calculated from the r^* equation for a spherical shell without heat generation (F.14). Their positions are indicated by r_{Ni} in Figure F.8.10.
3. The conduction form factor for a spherical shell without heat generation is used between temperature nodes.
4. The energy storage control volumes are calculated from the heat generation control volumes with an empirical formula. Their boundaries are shown by r_{vi} in Figure F.8.10.

This scheme is valid only for three or more nodes! This is caused by the correlation for volume adjustment.

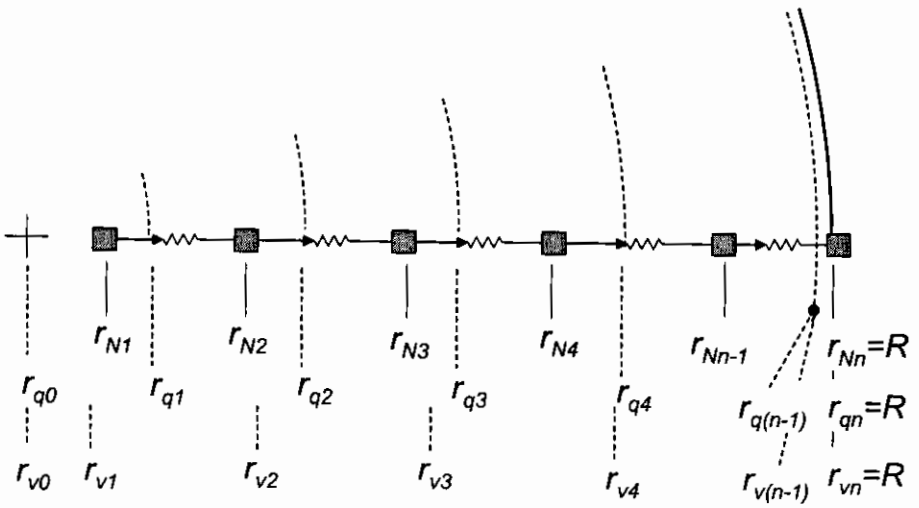


Figure F.8.10. Node and control volume placement for staggered volume discretisation.

With n being the number of temperature nodes, control volume size l is calculated from:

$$l = \frac{R}{n - 1 + 0.0001}, \qquad n \geq 3 \tag{F.31}$$

Heat generation control volumes are calculated from:

$$r_{q(i+1)} = r_{qi} + l \qquad i = 1 \text{ to } (n\text{-}1) \tag{F.32}$$

$$r_{qn} = R$$

The effect of the above formulae is that control volume n has a length of only 0.0001 times the radial length of other control volumes. It was found that maximum temperature grid dependence was further minimised by making the surface control volume as small as possible.

Node radii are calculated as follows, according to Eq.(F.14):

$$r_{Ni} = \frac{2\left(r_{qi}^3 - r_{q(i-1)}^3\right)}{3\left(r_{qi}^2 - r_{q(i-1)}^2\right)} \tag{F.33}$$

The following empirical formula is used for calculating r_{vi} from r_{qi}:

$$r_{vi} = r_{qi} - \frac{l}{2i + \frac{10}{n^{3.5}} - 0.003} \qquad i = 1 \text{ to } (n\text{-}1),\ n \geq 3 \qquad \text{(F.34)}$$

$$r_{v0} = 0$$
$$r_{vn} = R$$

Note that this formula is derived for i counting from the sphere centre to the outside.

The heat generation for each node is calculated with the following formula:

$$Q_i = \frac{r_{qi}^3 - r_{q(i-1)}^3}{R^3} Q_{sphere} \qquad i = 1 \text{ to } n \qquad \textit{(F.35)}$$

Node volumes are calculated from:

$$V_i = \frac{4}{3}\pi\left(r_{vi}^3 - r_{v(i-1)}^3\right) \qquad i = 1 \text{ to } n \qquad \textit{(F.36)}$$

Conduction element form factors are:

$$F_i = \frac{4\pi}{\frac{1}{r_{Ni}} - \frac{1}{r_{N(i+1)}}} \qquad i = 1 \text{ to } (n\text{-}1) \qquad \text{(F.37)}$$

To assemble a complete fuel sphere model, the outermost node in this discretisation forms the inner node of the surface layer model in Paragraph 0.

The sphere models described in this report are mostly used as representative spheres in reactor-scale control volumes much larger than one sphere. For this purpose, the sphere internal properties can be adjusted as follows:

$$Q_i = \frac{r_{qi}^3 - r_{q(i-1)}^3}{R^3} Q_{zone} \qquad i = 1 \text{ to } n \qquad \text{(F.38)}$$

with Q_{zone} being the zone power, specified from the core power distribution profile.

$$V_i = \frac{\left(r_{vi}^3 - r_{v(i-1)}^3\right)}{R^3}(1-\varepsilon)V_{zone} \qquad i = 1 \text{ to } n \qquad \text{(F.39)}$$

with V_{zone} being the reactor zone volume and ϵ being the porosity of that zone. The quantity $\frac{(1-\varepsilon)V_{zone}}{\frac{4}{3}\pi R^3}$ denotes the number of spheres in a reactor core zone.

The form factor is then calculated as follows:

$$F_i = \frac{4\pi}{\frac{(1-\varepsilon)V_{zone}}{\frac{4}{3}\pi R^3}\left(\frac{1}{r_{Ni}} - \frac{1}{r_{N(i+1)}}\right)}, \quad i = 1 \text{ to } (n\text{-}1) \tag{F.40}$$

F.9 Steady-state grid dependence tests

F.9.1 Internal heat generating zone

As a test case, a 25mm fuel sphere with uniform heat generation of 600Watts was simulated. Under the assumptions of spherical symmetry and constant conductivity, analytical expressions for the maximum and average temperatures exist. For temperature dependent conductivity, a grid independent solution was obtained with both the Numerical and the Staggered Volume methods, compared with each other and then used as a reference to evaluate coarser grids. The schemes are compared, for constant conductivity as well as temperature dependent conductivity.

Figure F.8.11 shows the results of a grid dependence study for maximum fuel temperature. A minimum of three nodes was used, as the Staggered Volume scheme is only valid upwards from a minimum of three nodes. The Analytical Sphere scheme was not included in the constant temperature calculations, as it is simply a rearrangement of the analytical expressions

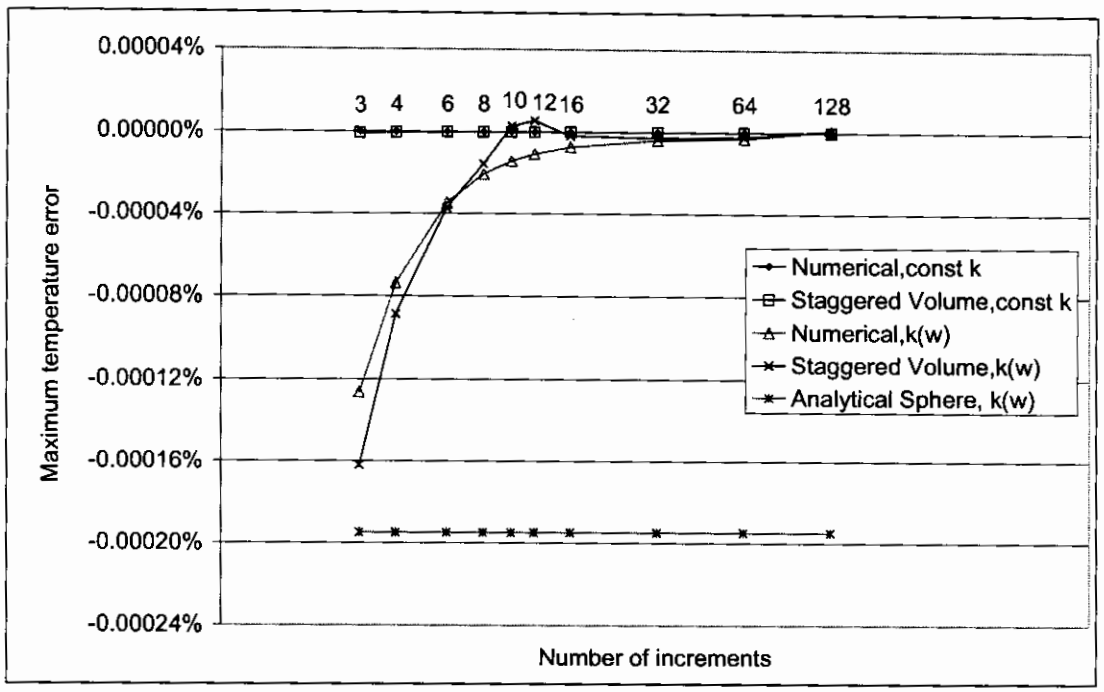


Figure F.8.11. The negligible grid dependence of the maximum fuel temperature as calculated with the Numerical and Staggered Volume schemes. k(w) denotes the weighted method for temperature dependent conductivity.

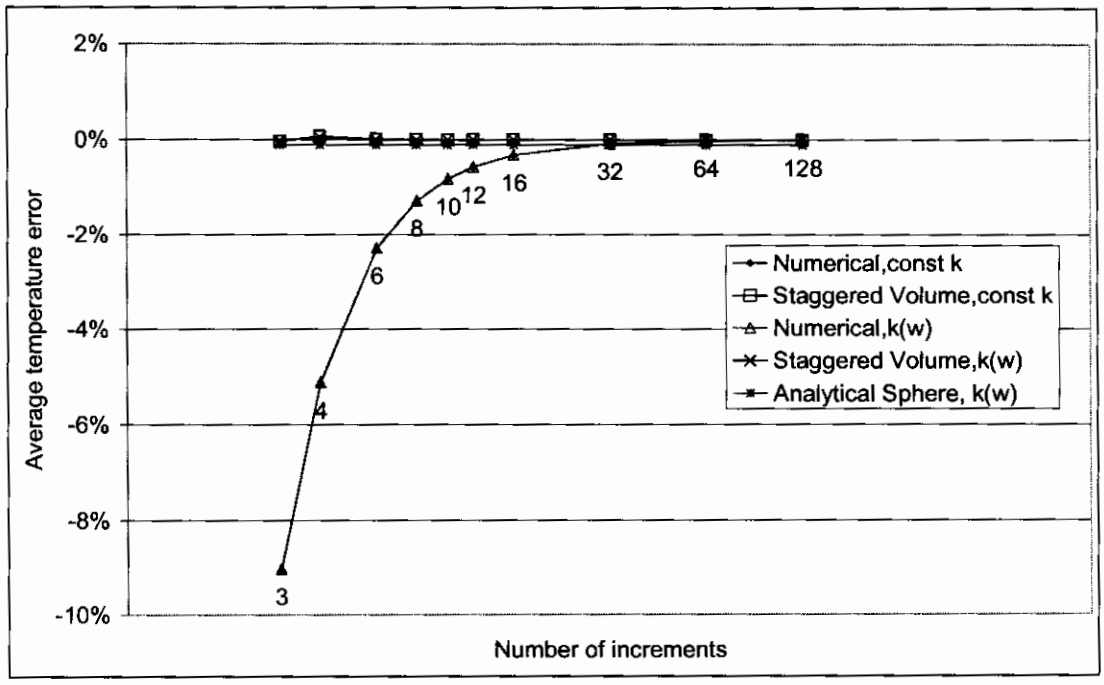


Figure F.8.12. Average temperature grid dependence for three sphere modelling approaches, as well as constant and temperature dependent conductivity.

As seen in Figure F.8.11, the maximum normalised deviation of maximum temperature for all the schemes in the comparison was less than 0.0002 percent. Thus, for the discretisation schemes at hand, the maximum fuel temperature can not be used as a selection criterion, but rather the average temperature. Average temperature errors are shown in Figure F.8.12.

For both constant and temperature dependent conductivity, the Numerical discretisation underpredicts the average temperature when using coarse grids. The error is less than 5 percent only after using at least six nodes. The Staggered Volume and Analytical Sphere schemes show negligible grid dependence, as they were derived specifically to have this property.

Based on the steady-state analyses, the Analytical Sphere scheme appears to be the best to use on account of being the simplest possible scheme while still being accurate. The Staggered Volume scheme requires only three nodes for grid independence.

F.9.2 Surface layer

The properties of surface layer discretisation were also investigated, with the most significant results presented in Figure F.8.13. A spherical layer with inner radius 25mm and outer radius 30mm and no heat generation was simulated with the Numerical and Analytical Layer methods (Paragraph 0). The average temperature shown in the figure was only calculated for the sphere shell.

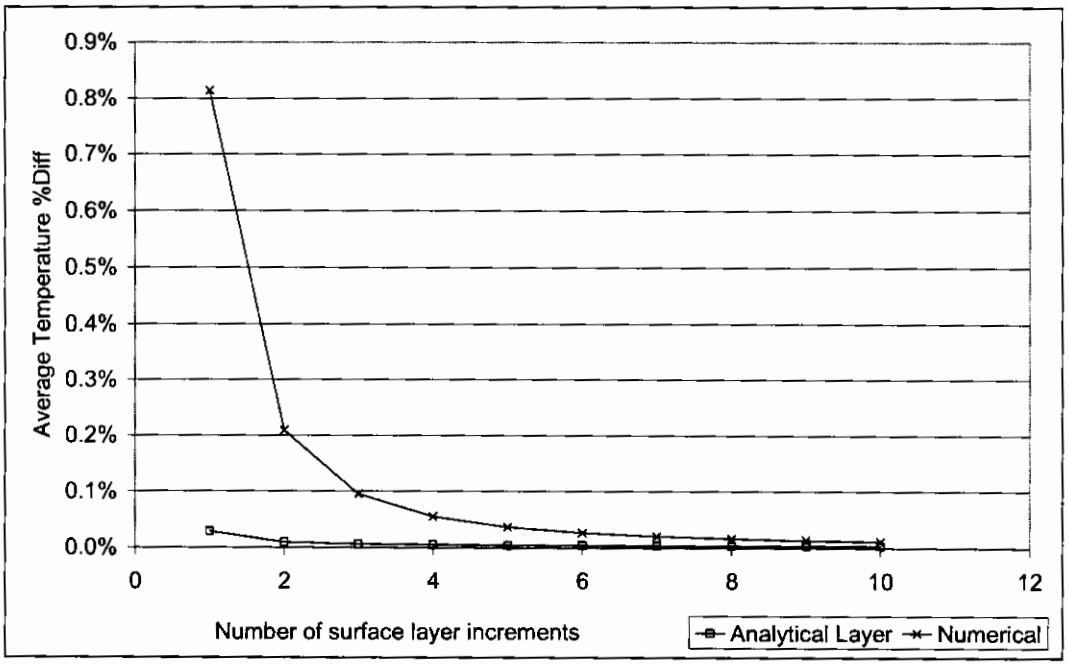


Figure F.8.13. Surface layer average temperature grid dependence for two discretisation schemes. The test is for a spherical layer between 25mm and 30mm without heat generation.

The reference value for the grid dependence study was calculated with 128 divisions with both the Numerical and the Analytical Layer discretisations. The surface layer division had no effect on the maximum temperature, while it did have a small effect on layer average temperature, as shown in Figure F.8.13. Except for the effect of temperature-dependent conductivity, the Analytical Layer method is grid independent for any number of subdivisions. This shows that for steady-state analyses, the error is at most 0.8 percent for the Numerical discretisation and less than 0.03 percent for the Analytical Layer discretisation. Transient analyses could however require finer division and will be investigated in the next section.

F.10 Transient grid dependence tests

The sphere model has to respond to two possible types of transients, namely a change in neutronic power, or a change in coolant temperature, i.e. a change in surface temperature. The transient response to a change in gas temperature is known to be very much dependent upon sphere surface discretisation.

Such transient conduction/convection systems are characterised by the Biot number, which is the ratio of surface transfer resistance to internal conduction resistance, calculated as follows:

$$Bi = \frac{hL}{k}$$

with h being the surface convection coefficient, L the characteristic length of the solid heat path and k its thermal conductivity. If Bi is smaller than 0.1 the sphere can be treated as a lumped capacitance (Incropera and DeWitt,1996), but for the PBMR at full mass flow conditions, Bi is typically in the order of 5 (with h=3400 W/m^{2}K, k=20W/mK and L=0.03m). This means that the sphere model has to be subdivided, which is already the case with all the schemes compared in this study.

To compare the various schemes, three transient events are simulated. In the first case a step change in gas temperature is simulated with no heat generation in the spheres. In the second case, heat generation in the sphere is switched off from maximum and internal temperature left to stabilise under constant gas temperature, while in the third case, the response to a step increase in power was calculated.

A second-order semi-implicit (Crank-Nicholson) time discretisation was used for all simulations. A timestep of 0.1 was found to give timestep-independent results.

The volume averaged temperature was used to compare schemes because it is an indication of the stored heat and it determines the cross-sections or reactivity used in neutronic power calculations. Surface temperature or maximum temperature could have been used, but they do not have such important simulation effects as the average temperature. In all the figures, the Staggered Volume scheme is denoted by *SV* and the Numerical scheme by *N*. n is the number inner sphere divisions and m the number of surface layer divisions as shown in Figure F.8.14.

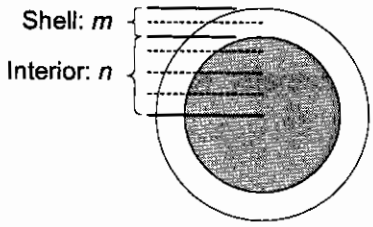


Figure F.8.14. Sphere subdivision, with *n* the number of inner divisions and *m* the number of shell divisions.

F.10.1 Reference case and temperature dependent conductivity

To establish a reference case, a fuel sphere with temperature dependent conductivity was simulated using ten surface and 20 inner divisions, with both the Staggered Volume and the Numerical schemes. A step increase of 100°C in gas temperature with no heat generation in the spheres was simulated.

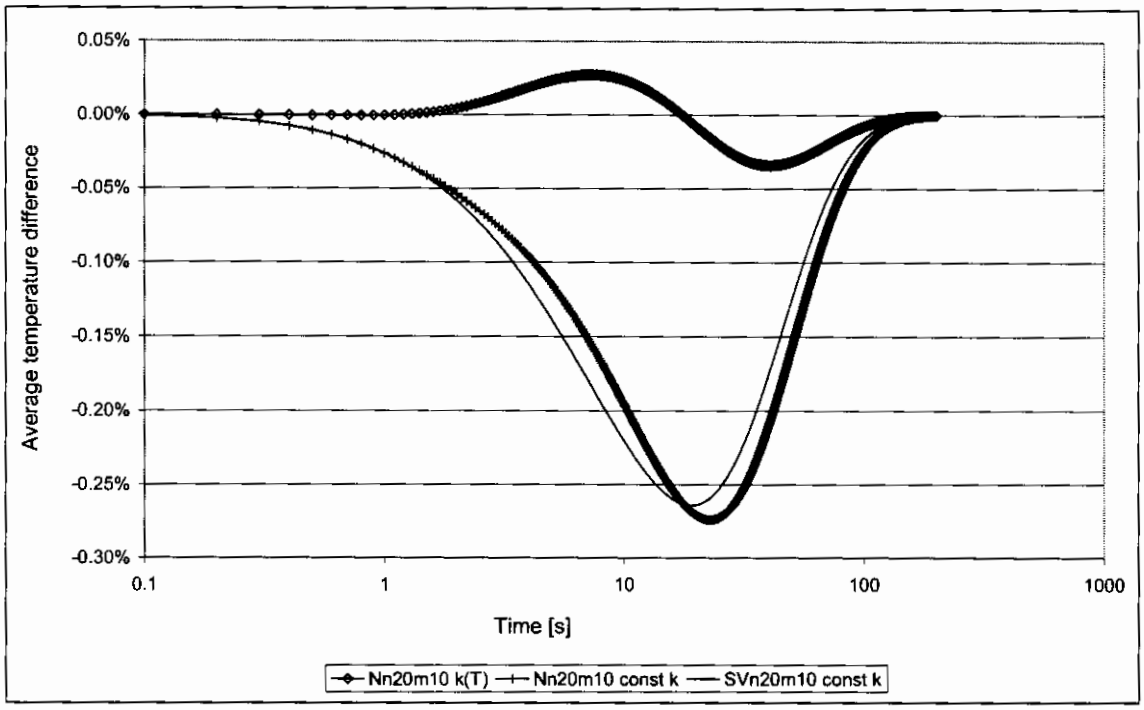


Figure F.8.15. The average temperature percentage difference with a reference case. The Staggered Volume scheme is denoted by SV and the Numerical scheme by N. Results from a SVn20m10 simulation with temperature dependent conductivity were used as reference.

The percentage difference between the two cases is shown in Figure F.8.15. The effect of assuming constant conductivity was tested as well, with the results also shown in Figure F.8.15. It shows that if conductivity is calculated at an appropriate temperature

for the transient event, the error introduced by using a constant conductivity can be small, less than 0.3 percent. But because an appropriate temperature is usually not known beforehand, it is still better to use a temperature dependent conductivity if possible.

F.10.2 Gas temperature step

As seen in Figure F.8.16, the surface layer discretisation has the largest effect during the start of the event, below about eight seconds. The inner discretisation of the sphere has its effect on accuracy during the greatest part of the event, from about seven seconds up to about 90 seconds. This is clearly seen in cases like Nn3m1 and Nn3m10, which are more or less equal from about 40 seconds on, while differing largely during the first half of the event, because of their difference in surface discretisation.

In general, the Staggered Volume has error peaks at a later stage in the transient than the Numerical Scheme. This is due to the difference in mass distribution among sphere internal nodes.

The Analytical Sphere scheme provided the unexpected result that with one surface layer node, the maximum normalised difference with the reference case was only 1.2 percent. When more surface nodes are used with this scheme, a slightly larger undershoot is found later on in the event. The best results with the Analytical Sphere scheme are found with two surface layer divisions, i.e. m=2.

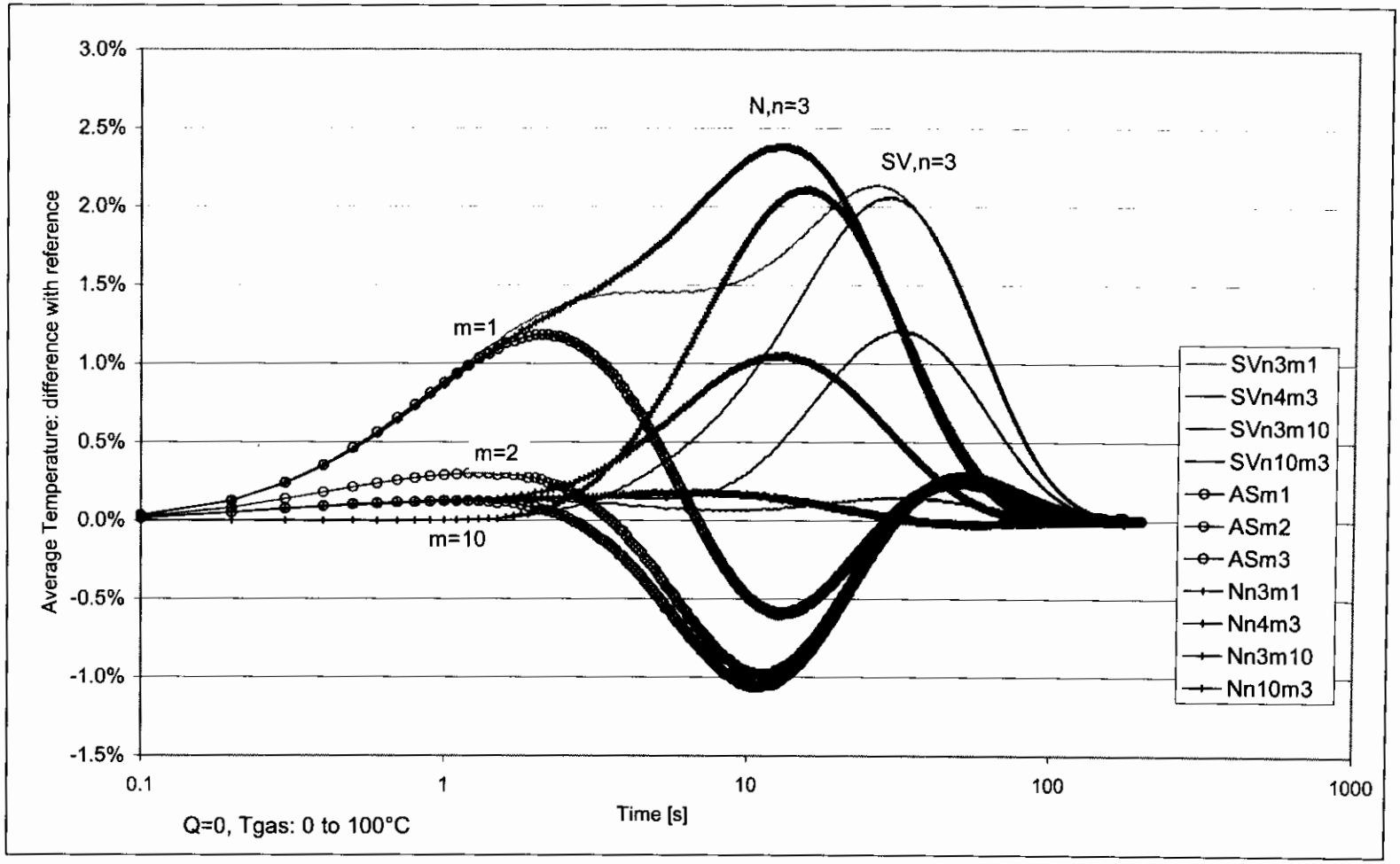


Figure F.8.16. The average temperature response relative difference with reference case SVn20m10 for a sudden step in gas temperature. Conductivity is temperature dependent. AS denotes the Analytical Sphere model. Surface division (*m*) has the largest effect on the initial response.

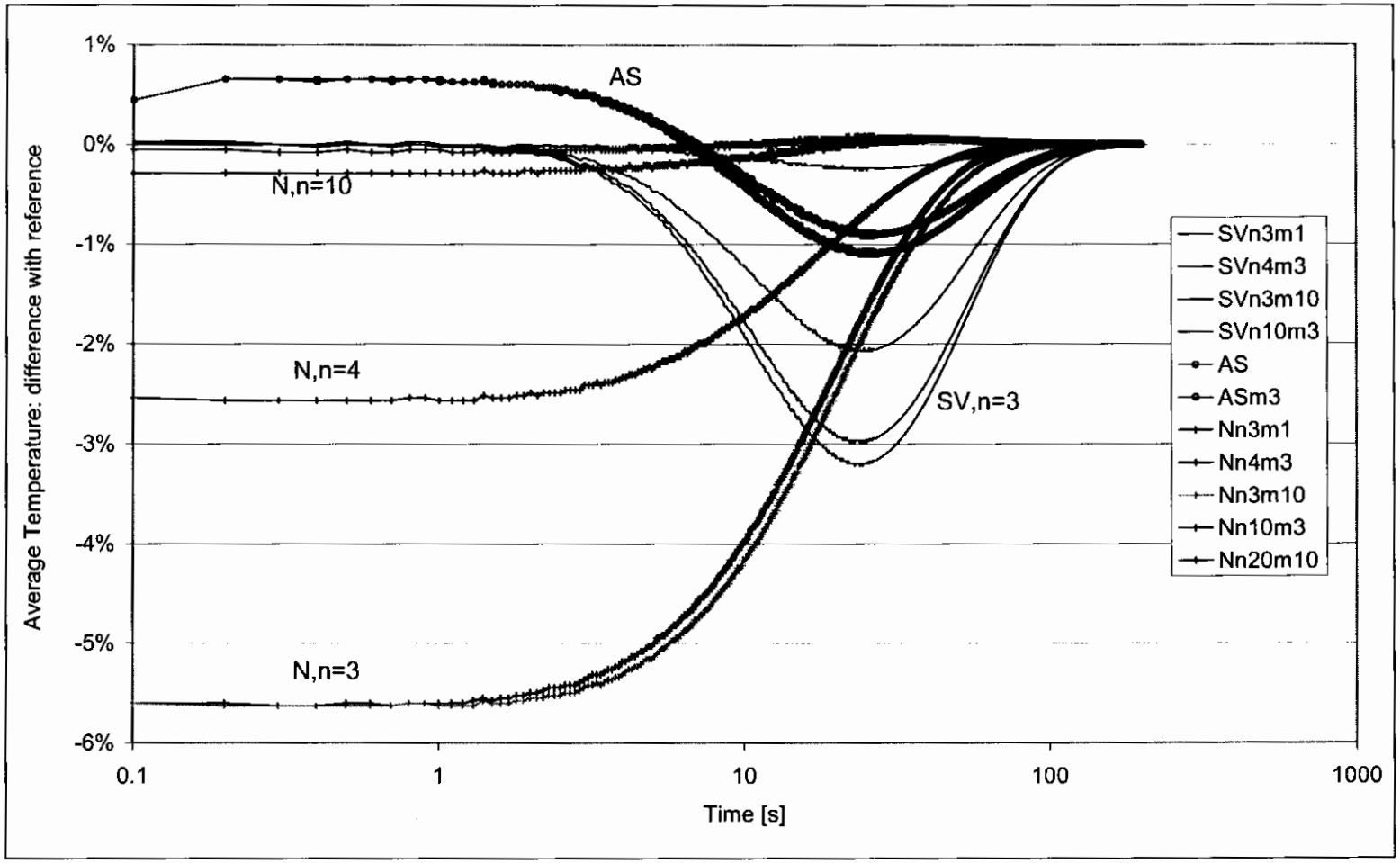


Figure F.8.17. The average temperature response relative difference with reference case SVn20m10 for a sudden drop in power with constant gas temperature. Conductivity is temperature dependent.

F.10.3 Step decrease in heating

In this case, the heating in the sphere was decreased from 600W to 0W and the sphere temperature left to stabilise. Gas temperature was kept constant throughout the event.

Somewhat less grid dependence was observed for the Numerical scheme average temperature in the transient results as opposed to its steady-state results. This is due to the fact that the transient simulation includes the passive sphere surface layer, of which the average temperature is not as grid dependent as the inner part of the sphere.

In this transient, the surface discretisation had a negligible effect on the average temperature response, while the sphere inner discretisation determined not only the starting temperature, but also the percentage deviation in the rest of the event. For coarse discretisations (n = 3 or 4), the Staggered Volume scheme deviated during the latter part of the event with a maximum difference with the reference in the order of three percent.

The Analytical Sphere model has the lowest overall deviation, with a maximum difference with the reference of just over one percent. The deviation at the start of the event is due to the discrete approximation of temperature dependent conductivity.

F.10.4 Step increase in heating

In this case, the heating in the sphere was increased from 0W to 600W and the sphere temperature left to stabilise. The gas temperature was kept constant throughout the event.

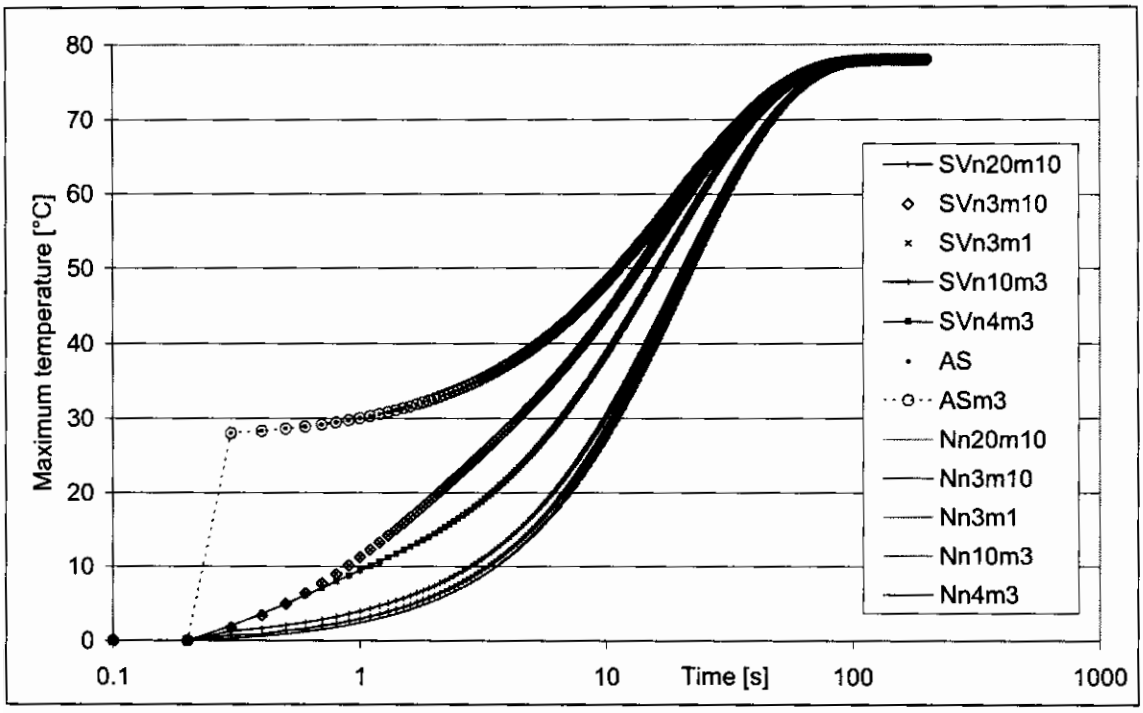


Figure F.8.18. Maximum temperature response to a step power increase. Conductivity is temperature dependent and a reference of 700°C is used, i.e. conductivity at 40°C on the graph is calculated at 740°C.

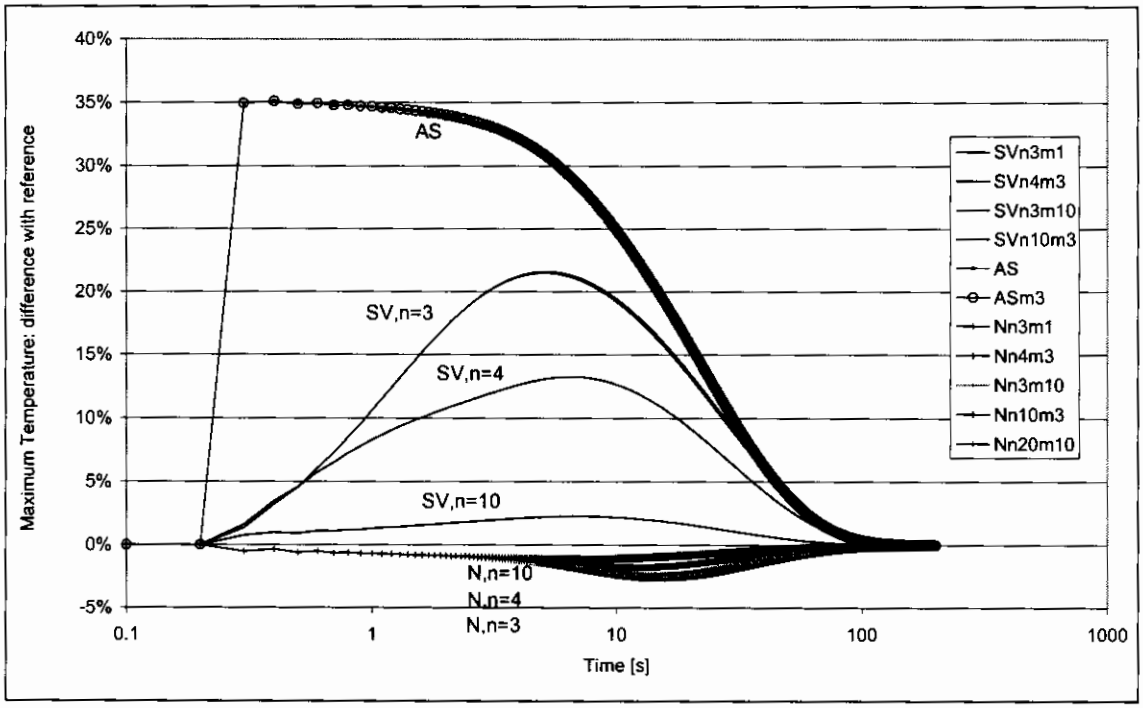


Figure F.8.19. Maximum temperature response, difference with the SVn20m10 reference case.

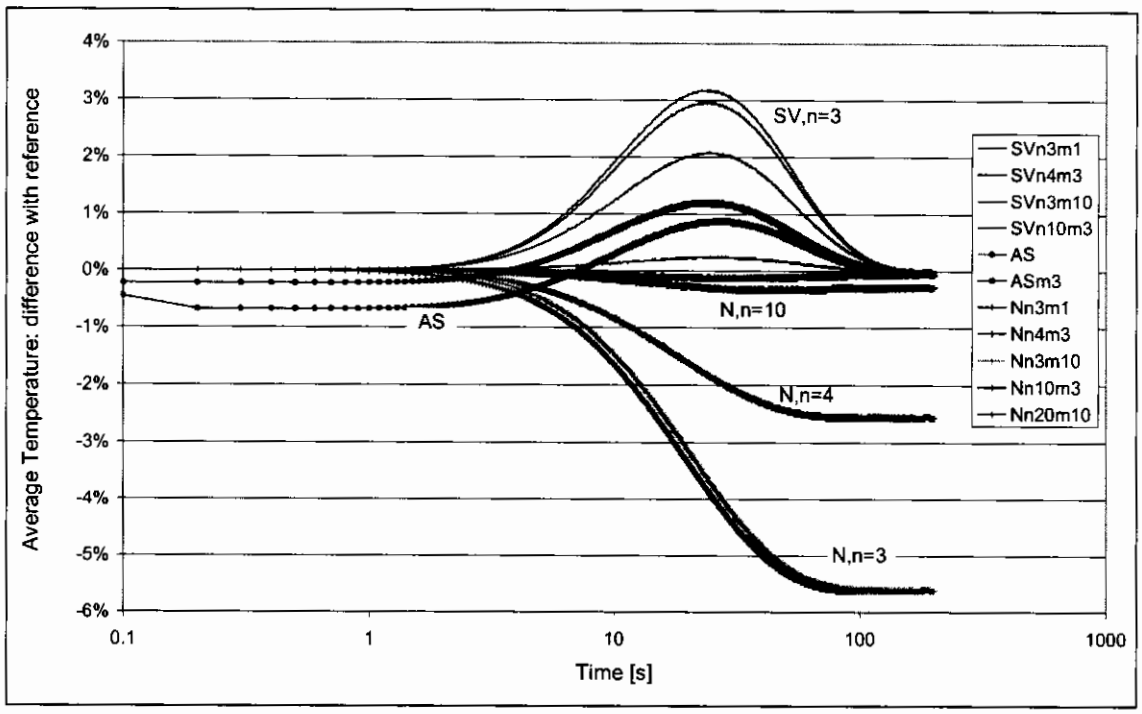


Figure F.8.20. The average temperature response relative difference with reference case SVn20m10 for a step increase in power with constant gas temperature.

Figure F.8.18 shows the maximum temperature history of the event while Figure F.8.19 shows that the Analytical Sphere scheme maximum temperature has a difference of about 35 percent with the reference case. The Staggered Volume scheme maximum temperature difference with the reference case is 22 percent while the numerical schemes are all quite accurate on the maximum temperature, with the maximum difference with the reference being 2.5 percent.

The reason for the large difference maximum temperature result of the Analytical Sphere model, is that the node for calculating maximum temperature has no mass assigned to it, i.e. the Analytical Sphere model calculates maximum fuel temperature accurate only under steady-state and slow transient conditions.

Figure F.8.20 shows that the magnitude of average temperature differences with the reference case is the same as for the step decrease in power. For the Analytical Sphere scheme with one surface layer, the average temperature difference with the reference case is still less than one percent. This affirms the strength of the Analytical Sphere model with regards to average fuel temperature, the input parameter required by neutronic calculations.

As with the step decrease in power, the surface discretisation has a negligible effect on the average temperature response, while the sphere inner discretisation determined the percentage

deviation. For coarse discretisations (n = 3 or 4), the Staggered Volume scheme differed maximum three percent with reference during the latter part of the event.

F.10.5 Gas temperature response

In the gas temperature step simulation (Figure F.8.16 in Paragraph 0), the initial response of the average temperature is seen to be most sensitive to the surface layer division. This is due to the fact that the surface temperature response is very grid dependent, which in turn affects the sphere average temperature.

As the convection heat transfer is a function of the (grid dependent) temperature difference between solid surface and gas, it is expected that the gas temperature response could also be grid dependent. To ascertain this, a sphere in contact with a gas control volume was simulated, with the gas inlet temperature undergoing a sudden change. The ratio of gas to sphere volume was the same as in an actual pebble bed reactor core, corresponding to a porosity of 0.39.

The gas outlet temperature response was calculated for two different sphere surface discretisations, namely one increment (m=1) and ten increments (m=10). For the central part of the sphere, a three-node Staggered Volume discretisation was used and the results are presented in Figure F.8.21.

The maximum difference in gas temperature between the two setups is less than 1 percent, showing that for one control volume, the effect of surface discretisation on gas temperature response is negligible.

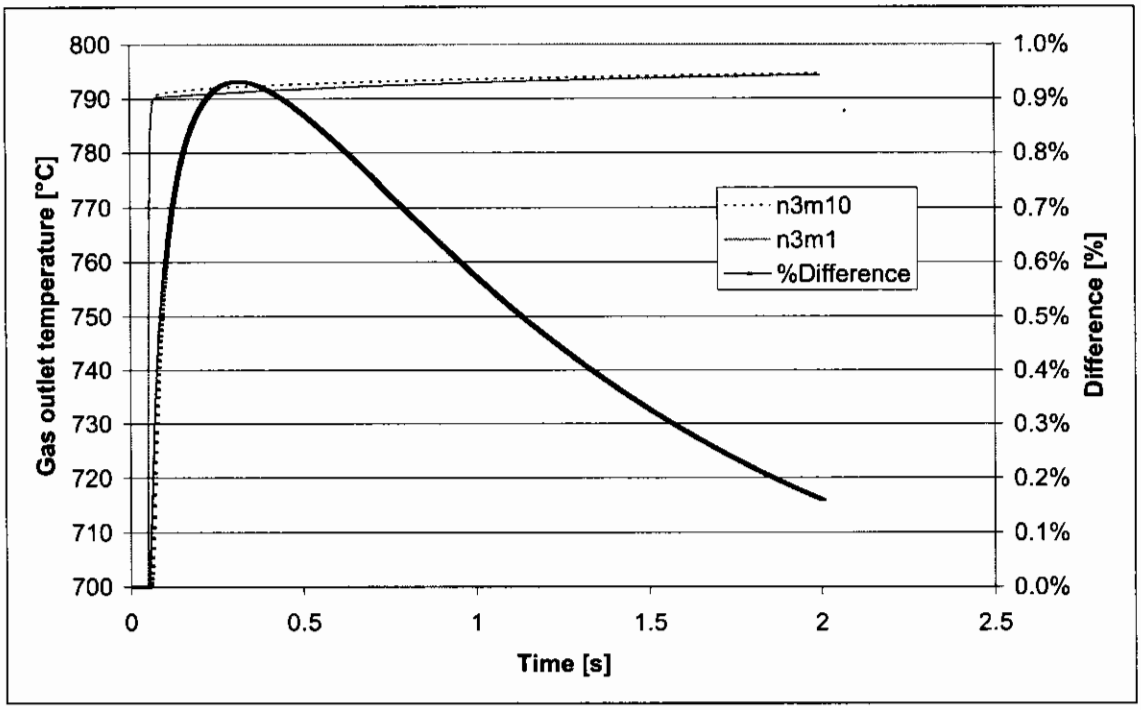


Figure F.8.21. Gas outlet temperature transient response and relative difference between one and ten surface layer increments, showing negligible difference.

F.11 Summary and conclusions

Pebble bed HTR fuel sphere discretisation schemes were investigated for use in CFD and network-type calculation models.

An existing discretisation scheme was investigated and compared with analytical solutions to point out advantages and deficiencies. Discretisation of temperature-dependent conductivity was also undertaken. Two new discretisation schemes were presented that calculates steady-state maximum and average temperatures with no grid dependence and a minimum number of nodes.

Transient average temperature grid dependence was studied for the existing scheme as well as the two new schemes. This was done by simulating three possible transient events. The effect of surface layer subdivision, as well as that of sphere internal subdivision was investigated. The effect of surface discretisation on gas temperature response was also tested.

All of the proposed methods require only pre-processing, thereby adding no additional burden to the solver. If fewer control volumes are required, it will actually shorten the solution time.

For the material used in the PBMR fuel spheres, the discrete modelling of temperature dependent conductivity did not seem to introduce significant errors in temperature. The best method to use was the "weighted" method that takes geometry into account, with second best being to calculate the conductivity at the average temperature.

From the steady-state grid dependence tests it was found that if only steady-state maximum temperature is important, the Numerical scheme is adequate. However, if average temperature is important (as is the case in a nuclear reactor), considerably more subdivisions are required to obtain the same accuracy with the Numerical scheme as with the Staggered Volume or Analytical Sphere schemes.

From the transient investigations, it was concluded that if a transient event does not involve sharp changes in gas temperature, the surface layer discretisation does not appear to be as important as the sphere inner discretisation. However, for sharp changes in gas temperature, the sphere surface layer needs to be subdivided depending on the required accuracy. The sphere discretisation was also found to have a negligible effect on the gas outlet temperature response.

The overall best performer was considered to be the Analytical Sphere model as it accurately calculated average temperatures for all cases tested. Maximum fuel temperature was however not calculated accurately directly after a step increase in power. Therefore maximum temperature results from this discretisation have to be interpreted with discretion.

F.12 Bibliography

Hoffmann, J.E. 2003. Software V&V: Subroutine Pebble Validation and Verification Report. PBMR document: PP260-018666-3715

Patankar, S.V. 1980. Numerical Heat Transfer and Fluid Flow. McGraw-Hill, New York.

Incropera, F.P., Dewitt, D.P. 1996. Fundamentals of Heat and Mass Transfer. John Wiley&Sons.

Van Rensburg, P.A.J. 2003. Flownet Uncertainty Analysis for a DLOFC. PBMR document: MR000-018726-3180

Verfondern, K. 1983. Numerische Untersuchung der 3-dimensionalen stationären Temperatur- und Strömunsverteilung im Core eines Kugelhaufen-Hochtemperaturreaktors, Jül-1826, Institut für Reaktorentwicklung, Kernforschungsanlage Jülich GmbH.

Verkerk, E.C. 2000. Dynamics of the Pebble-Bed Nuclear Reactor in the Direct Brayton Cycle. Ph.D. Thesis, Delft University of Technology.

Viljoen, Carel. 2004. Personal communication